Using shear wave velocity and microstructure for investigation of Champlain clay anisotropy

by

Amin TORABI POUR

THESIS PRESENTED TO ÉCOLE DE TECHNOLOGIE SUPÉRIEURE
IN PARTIAL FULFILLEMENT FOR THE DEGREE OF
DOCTOR OF PILOSOPHY
Ph.D.

MONTREAL, NOVEMBER 30, 2025

ÉCOLE DE TECHNOLOGIE SUPÉRIEURE
UNIVERSITÉ DU QUÉBEC

BOARD OF EXAMINERS (THESIS PH.D.)

THIS THESIS HAS BEEN EVALUATED

BY THE FOLLOWING BOARD OF EXAMINERS

Mr. Yannic Ethier, Thesis Supervisor
Department of Construction Engineering, École de technologie supérieure

Mr. Mourad Karray, Thesis Co-supervisor
Department of Civil Engineering and Building Engineering, Université de Sherbrooke

Mr. Vladimir Brailovski, Chair, Board of Examiners
Department of Mechanical Engineering, École de technologie supérieure

Mr. François Duhaime, Member of the jury
Department of Construction Engineering, École de technologie supérieure

Mr. Pascal Locat, External Evaluator
Ministère des Transports et de la Mobilité durable du Québec

THIS THESIS WAS PRENSENTED AND DEFENDED

IN THE PRESENCE OF A BOARD OF EXAMINERS AND PUBLIC

OCTOBER 30, 2025

AT ÉCOLE DE TECHNOLOGIE SUPÉRIEURE

ACKNOWLEDGMENTS

The completion of this thesis represents not only years of dedicated research and writing but also the culmination of support, guidance, and encouragement from numerous individuals to whom I am deeply indebted.

First and foremost, I would like to express my profound gratitude to my supervisor, Yannic Ethier, whose expert guidance, support, and constructive criticism have been instrumental in shaping both this thesis and my development as a researcher. Your dedication to academic excellence and your ability to challenge my thinking while providing encouragement have been invaluable.

I am equally grateful to my co-supervisor, Mourad Karay, for their insightful comments, technical expertise, and the countless hours spent reviewing my work. Your unique perspective and detailed feedback have significantly enhanced the quality of this research.

To my beloved family members in Iran, words cannot fully express my gratitude for your unconditional love, endless patience, and constant support throughout this journey. Your belief in my abilities, even during the most challenging times, has been my foundation. Thank you for understanding the challenges of long-distance separation, missed occasions, and the emotional roller coaster that came with this endeavor.

I would like to extend my heartfelt thanks to my love, Dena, whose unwavering support, understanding, and encouragement have been my anchor throughout this process. Your ability to bring light to my life and your constant reassurance have made this journey possible.

To my friends and technicians in the department, thank you for stimulating discussions, technical assistance, and for creating an environment conducive to research and personal growth. The camaraderie we shared made this journey not only bearable but enjoyable.
This achievement is as much yours as it is mine.

Utilisation de la vitesse des ondes de cisaillement et de la microstructure pour l'étude de l'anisotropie de l'argile de Champlain

Amin TORABI POUR

RÉSUMÉ

La mesure de la vitesse des ondes de cisaillement constitue un outil puissant pour étudier le comportement dynamique des sols, notamment le module de cisaillement maximal (rigidité élastique). La compréhension de la relation entre la rigidité élastique, la vitesse des ondes de cisaillement, la contrainte effective et l'indice des vides améliore la fiabilité de la conception sismique et de l'interprétation dans la pratique géotechnique. Les mesures en laboratoire de la vitesse des ondes de cisaillement permettent un suivi parallèle des caractéristiques mécaniques au moyen d'appareils géotechniques conventionnels comme un œdomètre standard.

Cette thèse porte sur l'investigation des propriétés directionnelles de l'argile marine molle de Champlain sous essais de consolidation unidimensionnelle. Les dépôts de sols cohésifs naturels présentent une anisotropie allant de légère à prononcée. Pour caractériser l'anisotropie des dépôts d'argile marine molle, une nouvelle méthode de laboratoire a été développée et employée pour permettre des mesures de directionnalité. À l'aide d'un système de transducteurs, les vitesses d'ondes de cisaillement ont été mesurées sur des échantillons non remaniés dans un œdomètre instrumenté équipé de jauges de déformation latérales pour la mesure des contraintes K_0, tout en appliquant des contraintes verticales effectives allant jusqu'à 1000 kPa.

Les vitesses des ondes de cisaillement ont augmenté avec le niveau de contrainte, atteignant jusqu'à 200 m/s dans le plan vertical-horizontal et 220 m/s dans le plan horizontal-horizontal à la contrainte maximale appliquée. Ces mesures ont été utilisées pour calculer la rigidité cross-anisotropique à différents niveaux de contrainte. Les résultats ont révélé que les argiles de Champlain intactes présentent des rapports d'anisotropie faibles à modérés (1,10-1,30), avec des variations plus importantes observées à des niveaux de contrainte plus faibles, particulièrement en dessous de la pression de préconsolidation. L'effet des caractéristiques des couches de stratification a également été étudié en taillant et en préparant des échantillons à différents angles, de 90 à 0 degrés. Les résultats démontrent un modèle cohérent où les valeurs d'anisotropie à des angles intermédiaires comblent l'écart entre les directions verticale et horizontale.

Un autre point d'intérêt dans cette étude était de développer les investigations d'anisotropie de ces échantillons d'argile à l'échelle microscopique. La position des plaquettes d'argile et leur réarrangement ont été étudiés dans des échantillons intacts et consolidés, respectivement. La microscopie électronique à balayage (MEB), en tant que technique d'imagerie, a été utilisée pour prendre des images numériques de haute qualité de la surface d'argile utilisée dans les

tests de consolidation unidimensionnelle. Un script basé sur MATLAB a également été développé pour quantifier l'orientation de la structure argileuse à l'aide d'images MEB, en appliquant deux méthodes différentes de quantification (FOCM-I et FOCM-II). Les échantillons d'argile Champlain intacts montrent une association orientée aléatoirement à faiblement orientée selon la classification d'anisotropie (l'indice d'anisotropie varie de 0,145 - 0,17). Les orientations initialement aléatoires des particules dans les échantillons intacts s'alignent progressivement perpendiculairement à la contrainte verticale appliquée au cours du processus de consolidation unidimensionnelle.

Une étude paramétrique a été menée pour examiner les effets des paramètres clés du MEB, notamment la tension d'accélération (10-30 kV) et le grossissement (1000-7000x), sur les écarts dans les calculs d'anisotropie de la structure argileuse. Une technique d'imagerie a été employée pour améliorer la fiabilité de la quantification de l'anisotropie par l'analyse d'images MEB tout en minimisant les incertitudes dans les calculs de directionnalité. Une comparaison de la détermination de l'anisotropie avec des données publiées à l'échelle macro et microscopique a révélé la relation et la dépendance de l'anisotropie au rapport de surconsolidation et à l'historique des contraintes des argiles marines et glaciaires.

Mots-clés : argiles marines molles de Champlain, vitesse des ondes de cisaillement, anisotropie transverse, piézoélectrique ring-actuateur technique (P-RAT), essai de consolidation unidimensionnelle, microscopie électronique à balayage, traitement d'images

Using shear wave velocity and microstructure for investigation of Champlain clay anisotropy

Amin TORABI POUR

ABSTRACT

Shear wave velocity measurement is a powerful tool to study the dynamic behavior of soils, including maximum shear modulus (elastic stiffness). Understanding the relationship between elastic stiffness, shear wave velocity, effective stress and void ratio enhances the reliability of seismic design and interpretation in geotechnical practice. The laboratory measurements of shear wave velocity allow parallel monitoring of mechanical characteristics by means of conventional geotechnical apparatuses like a standard oedometer device.

This dissertation focuses on the investigation of directional properties of the Champlain soft marine clay under 1D-consolidation testing. Naturally occurring cohesive soil deposits exhibit anisotropy ranging from slight to pronounced degrees. To characterize the anisotropic nature of soft marine clay deposits, a novel laboratory method was developed and employed to enable directionality measurements. Using a transducer system, shear wave velocities were measured on undisturbed specimens within an instrumented oedometer equipped with lateral strain gauges for K_0 stress measured, while applying effective vertical stresses up to 1000 kPa.

The shear wave velocities increased with stress level, reaching up to 200 m/s in the vertical-horizontal plane and 220 m/s in the horizontal-horizontal plane at maximum applied stress. These measurements were used to calculate cross-anisotropic stiffness at different stress levels. The results revealed that intact Champlain clays exhibit low to moderate anisotropy ratios (1.10-1.30), with higher variations observed at lower stress levels, particularly below the pre-consolidation pressure. The effect of bedding layer characteristics was also studied through trimming and preparing specimens at different angles from 90 to 0 degrees. Results demonstrate a consistent pattern where anisotropy values at intermediate angles bridge the gap between vertical and horizontal directions.

Another point of interest in this study was to develop the anisotropy investigations of these clay samples on a microscale. The clay platelets position and their rearrangement were studied in intact and consolidated specimens, respectively. Scanning electron microscopy as an imaging technique was conducted to take high-quality digital images from the clay surface utilized in 1D-consolidation tests. A MATLAB-based script was developed to quantify clay fabric orientation using SEM images, applying two different methods of quantification (FOCM-I and FOCM-II). Intact Champlain clay samples show a randomly oriented to low-oriented association based on the anisotropy classification (anisotropy index ranges around 0.145 and 0.17). Initially random particle orientations in intact samples progressively align perpendicular to the vertical applied stress through 1D-consolidation process.

A parametric study was conducted to examine the effects of key SEM parameters, including accelerating voltage (10-30 kV) and magnification (1000-7000x), on clay fabric anisotropy calculations discrepancies. An imaging technique was employed to enhance the reliability of anisotropy quantification through SEM image analysis while minimizing uncertainties in directionality calculations. A comparison of anisotropy determination with published data in both macro- and microscale revealed the relationship and dependency of anisotropy on overconsolidation ratio and stress history of marine and glacial clays.

Keywords: Champlain soft marine clays, shear wave velocity, cross-anisotropy, piezoelectric ring actuator technique (P-RAT), one-dimensional consolidation test, scanning electron microscopy, image processing

TABLE OF CONTENTS

Page

INTRODUCTION 1

CHAPTER 1 STATE OF ART 7
1.1 Sedimentology of Champlain clays 7
1.2 Clay microstructure and consolidation effects 11
1.2.1 Clay structure and fabric 12
1.2.2 Effects of compression on clay microstructure 13
1.3 Lateral strain determination 17
1.4 Digital imaging and morphology 18
1.4.1 Image processing 19
1.5 Summary 22
1.6 Isotropic small strain stiffness 23
1.6.1 Shear wave propagation 25
1.6.2 Stiffness measurement 26
1.7 Laboratory approach of V_s measurement 31
1.7.1 Resonant Column Test 31
1.7.2 Piezoelectric Transducer System 33
1.7.3 P-RAT interpretation method 38
1.8 Summary 42
1.9 Anisotropy 43
1.9.1 Transverse isotropy (Cross-anisotropy) 43
1.9.2 Cross-anisotropy constitutive model 44
1.9.3 Anisotropic stiffness correlations 46
1.9.4 Anisotropy literature review 49
1.10 Discussion 60

CHAPTER 2 RESEARCH OBJECTIVES AND CONTRIBUTION 63
2.1 Overview and motivation 63
2.2 Objective 63
2.2.1 Laboratory setup for directional V_s 64
2.2.2 SEM imaging and clay particles arrangement 64
2.2.3 Bedding orientation effect on anisotropy degree 65
2.3 Contribution of this study 66

CHAPTER 3 VERTICAL MEASUREMENT OF V_s 67

CHAPTER 4 USE OF SHEAR WAVE VELOCITY TO ASSESS CHAMPLAIN MARINE CLAY FABRIC ANISOTROPY 73
4.1 Introduction 75
4.2 Experimental program 79
4.2.1 Clay soil information 80

4.2.2 Shear wave measurement 81
4.2.3 Lateral strain measurement 85
4.2.4 Scanning electron microscopy 87
4.3 Results and discussion 92
4.4 Conclusion 101

CHAPTER 5 INFLUENCE OF SEM IMAGING PARAMETERS ON CLAY FABRIC ANISOTROPY 105
5.1 Introduction 107
5.2 Sample preparation and image acquisition 110
5.3 Image processing 114
5.4 Segmentation and porosity calculation 114
5.4.1 First fabric orientation calculation method (FOCM-I) 117
5.4.2 Second fabric orientation calculation method (FOCM-II) 118
5.5 Numerical results and discussion 121
5.5.1 Script validation 121
5.5.2 Parametric studies 123
5.6 Conclusion remarks 142

CHAPTER 6 BEDDING LAYER INCLINATION EFFECTS ON CHAMPLAIN CLAY ANISOTROPY 145
6.1 Introduction 147
6.2 Material and testing procedure 150
6.2.1 Directional *Vs* testing with P-RAT 151
6.3 Result and discussion 156
6.3.1 Bedding layer characteristics 156
6.3.2 Stress history effects 161
6.3.3 Clay morphology 168
6.4 Conclusion 182

CONCLUSION 185

RECOMMENDATIONS 191

ANNEX I LABORATORY MEASUREMENT APPROACH FOR ANISOTROPY IN CHAMPLAIN CLAYS 195

APPENDIX A STRAIN GAUGES FUNDAMENTAL 213

APPENDIX B SEM IMAGES OF PARAMETRIC STUDY- CHAPTER 5 221

LIST OF BIBLIOGRAPHICAL REFERENCES 243

LIST OF TABLES

Page

Table 1.1 Geotechnical Characteristics of Champlain clays 11

Table 1.2 Overview of wave propagation techniques utilized to assess the stiffness of soils 28

Table 1.3 Influential parameters in G_{max} determination 47

Table 1.4 Proposed material constants and void ratio functions in $Gmax$ correlations 48

Table 2.1 Scientific publication in geotechnical journals and proceedings 65

Table 3.1 Clay samples characteristics 67

Table 3.2 Empirical Correlations of V_s for different utilized samples 69

Table 4.1 Characteristics of Champlain clay block sample 81

Table 5.1 Characteristics of Champlain clay specimen 110

Table 5.2 Comparison of anisotropy index of the SEM image according to different methods 123

Table 5.3 Anisotropy indices of the intact samples S3 and S7 using two different accelerating voltage values 135

Table 5.4 Percent difference between anisotropy analysis results based on FOCM-I approach for different SEM image formations 135

Table 5.5 Anisotropy analysis based on the grid-view image and randomly taken images from the surrounding area (magnification 3000×) 139

Table 5.6 Anisotropy analysis based on the full-view image and randomly taken images from the surrounding area (magnification 3000×) 139

Table 6.1 Compression index values of the conducted 1D-consolidation tests 158

Table 6.2 Different clays utilized in stiffness anisotropy studies from various sites 165

Table 6.3 Anisotropy assessment of SEM specimens of Beauharnois clay 176

Table 6.4 Comparison of anisotropy index of the SEM images of St- Marcel clay 176

Table 6.5 Anisotropy assessment of SEM images of London clay 181

Table A I.1 Common laboratory experimental programs utilized for Champlain clay anisotropy 197

Table A I.2 Anisotropy ratio of Champlain marine clays 209

Table A A.1 Calibration of installed strain gauges with air pressure 220

LIST OF FIGURES

Page

Figure 1.1 a) Winter overflow; b) Summer heavy density flow into glacial lakes....8

Figure 1.2 The arrangement and association of Champlain clays from undisturbed to consolidated specimen....10

Figure 1.3 Schematic view of clay fabric structure....13

Figure 1.4 Effect of compaction on one-dimensional consolidation of clays....15

Figure 1.5 Rearrangement of clay particles due to the applied stress....16

Figure 1.6 Samples for the SEM observations, a) samples for observation and stress state; b) horizontal plane; c) vertical plane....19

Figure 1.7 Method of analysis and image processing....20

Figure 1.8 CAT scan imaging for visualization of stratification and bedding layers, a) stratigraphy details; b) CPTU and CAT scan image....20

Figure 1.9 Relationship between shear modulus and shear strain....24

Figure 1.10 Propagation of seismic waves in the soil body: a) P-waves, b) S-waves....25

Figure 1.11 Typical resonant column test apparatus: (a) top view of loading system, and (b) profile view of loading system and soil specimen....32

Figure 1.12 Two types of piezoceramic bender elements: (a) series connected and (b) parallel connected....34

Figure 1.13 Bender elements employed for the purpose of anisotropic shear wave velocity measurements....36

Figure 1.14 P-RAT at ETS soil mechanics laboratory, a) Non-encapsulated P-RAT with porous stone; b) Encapsulated P-RAT with alloy inner parts used in the current study....37

Figure 1.15 Face-to-face test of P-RAT in different laboratory conditions....42

Figure 1.16 Schematic representation of cross-anisotropic soil fabric due to the bedding layers 44

Figure 1.17 $G_{max(ij)}$ against stress ratio for anisotropically consolidated a) reconstituted specimen b) intact specimen.....51

Figure 1.18 Relationship between G_{max} and mean effective stress: a) London Clay; b) Gault Clay 52

Figure 1.19 Comparison of G_{hh} and G_{vh} of published experimental results to London and Gault clays.....53

Figure 1.20 Obtained directional shear modulus by means of BE tests during K_0 reconsolidation, a) Ghh; Ghv; Gvh, b) stiffness ratio 55

Figure 1.21 Results of BE tests: a) G_{vh} versus mean effective stress during consolidation testing; b) anisotropy ratio for shallow block samples; c) anisotropy ratio for deep block samples.....57

Figure 1.22 Computed settlement troughs for trial tunnel in London clays.....58

Figure 3.1 V_s-consolidation curves of f tested clay specimens with $\sigma_p' \approx 150 - 165$ kPa.....70

Figure 3.2 V_s-consolidation curves of tested clay specimens with $\sigma_p' \approx 85 - 145$ kPa.....71

Figure 3.3 V_s-consolidation curves of tested clay specimens with $\sigma_p' \approx 145 - 265$ kPa.....72

Figure 4.1 Modified oedometer equipped with P-RAT and strain gauges for measuring shear wave velocity and lateral strain, respectively.....79

Figure 4.2 Illustration of vertical and horizontal specimens: a) trimming path, b) cross-anisotropy assumption.....80

Figure 4.3 a) Mounted P-RAT within an oedometer cell and the associated data acquisition setup; b) Theoretical fit-curve for evaluating the dynamic response of the transducer system; c) Temporal traces of input and output waves; d) Illustration of V_s measurement interpretation procedure 84

Figure 4.4 a) Consolidation ring equipped with strain gauges; b) Hoop stress illustration in a cross-section of the consolidation ring subjected to internal pressure 85

Figure 4.5 Calibration curve of strain gauges subject to uniform air pressure.....87

Figure 4.6 Microstructure of vertically oriented intact sample (a-1 and c-1) and vertically consolidated (b-1 and d-1) samples and their corresponding directionality analysis results (a-2 and c-2) and (b-2 and d-2), respectively 90

Figure 4.7 Microstructure of horizontally oriented intact sample (a-1 and c-1) and horizontally consolidated (b-1 and d-1) samples and their corresponding 91

Figure 4.8 Consolidation curves of the eight tests on a) vertically consolidated (VC) samples, b) horizontally consolidated (HC) samples, and c) average curves for both orientations.....92

Figure 4.9 Temporal traces of output wave in the vertical-horizontal (vh) and horizontal-horizontal (hh) propagation-polarization plane, considering the gradual effects of the consolidation stress.....95

Figure 4.10 V_s-consolidation average curves for vertically and horizontally consolidated clay samples (vh and hh, respectively) 96

Figure 4.11 Vertically and horizontally consolidated specimens: a) measured horizontal effective stress during 1D-consolidation test, b) Estimated K_0 based on vertical and horizontal stresses 99

Figure 4.12 Normalized V_s correlations considering vertical and mean effective stresses, relative to a) vertical-horizontal (vh) plane and b) horizontal-horizontal (hh) plane.....101

Figure 5.1 Particle size gradation of Champlain clay soil 111

Figure 5.2 A visual representation of the sample preparation procedures employed for digital imaging 113

Figure 5.3 SEM images of the Champlain marine clay microstructure, a) magnitude of 4000×; b) magnitude of 7000× 114

Figure 5.4 Original SEM image utilized for the threshold analysis representation (magnification at 5000 ×) 115

Figure 5.5 Three different applied threshold levels (T = 3 to T = 5) for distinguishing particles zone from pore spaces, a) contours of segmented pores, b) contours of segmented particles.....116

Figure 5.6 Schematic view of fitting ellipse for the identified particles.....118

Figure 5.7 Illustration of directionality of the clay particles based on the original SEM image, a) Polar graph; b) Rose diagram 119

Figure 5.8 Schematic representation of directionality analysis of the original SEM image with the ellipse-fitting method, a) Ellipse fitting in cartesian coordinates; b) Ellipse fitting for rose diagram of identified particles.....121

Figure 5.9 SEM images from previous studies for verifying the fabric orientation calculation procedure. a and b) FOCM-I by Martinez-Nistal et al. (1999) and Mitaritonna et al. (2014), respectively; c) FOCM-II by Tovey and Dadey (2002) 122

Figure 5.10 Effect of voltage on SEM imaging of the intact samples of S3 and S7 based FOCM-I approach; a) 1000×; b) 2000×, c) 3000×, d) 4000× 124

Figure 5.11 Effect of applied voltage on SEM imaging of the intact sample S3 based on ellipse-fitting method considering four different magnifications: a) 1000×; b) 2000×, c) 3000×, d) 4000× 125

Figure 5.12 Effect of applied voltage on SEM imaging of the intact sample S7 based on ellipse-fitting method considering four different magnifications: a) 1000×; b) 2000×, c) 3000×, d) 4000× 126

Figure 5.13 Magnification analysis of the intact sample S3 and S7 by FOCM-I method, through usage of different voltage, a) 10 kV, b) 15 kV, c) 20 kV, d) 25 kV, e) 30 kV.....127

Figure 5.14 Influence of magnification with ellipse-fitting methods and different voltages for intact sample S3, a) 10 kV, b) 15 kV, c) 20 kV, d) 25 kV, e) 30 kV.....128

Figure 5.15 Influence of magnification with ellipse-fitting methods and different voltages for intact sample S7, a) 10 kV, b) 15 kV, c) 20 kV, d) 25 kV, e) 30 kV.....129

Figure 5.16 Analysis of the effect of applied voltage on SEM imaging of the consolidated sample S3 based on FOCM-I considering four different magnifications: a) 1000×; b) 2000×, c) 3000×, d) 4000× 130

Figure 5.17 Analysis of the effect of applied voltage on SEM imaging of the consolidated sample S3 based on ellipse-fitting method considering four different magnifications: a) 1000×; b) 2000×, c) 3000×, d) 4000× 131

Figure 5.18 Magnification analysis of the consolidated sample S3 by FOCM-I method, through usage of different voltage, a) 10 kV, b) 15 kV, c) 20 kV, d) 25 kV, e) 30 kV....132

Figure 5.19 Magnification analysis of the consolidated sample S3 by ellipse-fitting method, through usage of different voltage, a) 10 kV, b) 15 kV, c) 20 kV, d) 25 kV, e) 30 kV....133

Figure 5.20 Grid view and full view of SEM images for intact sample S3 with voltage of 15 kV; a) quarter images at magnification of 3000×; b) Grid-view image at magnification of 3000×; c) Full-view image at magnification of 1500×....137

Figure 5.21 Random images (R1 to R5) of the surface of the S3 sample with voltage of 15 kV, from surrounding areas of a) Grid-view zone at magnification of 3000×; and b) Full-view zone at magnification of 1500×....138

Figure 5.22 Anisotropy illustration through polar graphs for intact (a-1 to c-1) and consolidated (a-2 to c-2) sample of S3: a) 10 kV-3500×, b) 10 kV-2000× and c) 20 kV-3500×....140

Figure 5.23 Anisotropy illustration through polar graphs for intact (a-1 to c-1) and consolidated (a-2 to c-2) sample of S7: a) 10 kV-2500×, b) 15 kV-5000×, c) 15 kV-3000×....141

Figure 6.1 (a) Assembled instrumented oedometer setup with clay specimen. (b) Components: lateral strain gauge, pedestal base equipped with P-RAT, and fabricated sensor....151

Figure 6.2 Specimen and transducer setup for shear wave velocity tests....152

Figure 6.3 Frequency and phase response of the P-RAT....154

Figure 6.4 Void ratio versus vertical effective stress relationship for 1D consolidation of Beauharnois clay specimens at different bedding plane orientations; (a) $\theta = 0°$, (b) 30°, (c) 45°, (d) 60°, and (e) 90°....157

Figure 6.5 Shear wave, $V_s(\theta h)$, measurements at 45° under 253 kPa vertical stress using four input signals: a) time-domain waveforms, b) frequency-dependent phase shifts, and c) amplitude response and phase velocity....159

Figure 6.6 Empirical correlations of normalized V_s, over void ratio for different bedding plane orientations....160

Figure 6.7 Normalized shear wave velocity versus bedding layer angle at various stress levels 162

Figure 6.8 Variation in anisotropy ratio as a function of bedding layer inclination angle under increasing consolidation stress 163

Figure 6.9 Normalized G_θ for various clay deposits: (a) Lightly OCR, (b) Heavily OCR; stiffness anisotropy degree: (c) OCR and (d) Heavily OCR 167

Figure 6.10 Intact structure of Beauharnois clay at magnifications of 3000× and 7000× 170

Figure 6.11 SEM images from different stages of 1D-consolidation test of clay from St Marcel site at orientation of 90 degree (Delage and Lefebvre, 1984) 171

Figure 6.12 SEM images from different stages of 1D-consolidation test of clay from St Marcel site at orientation of zero degree (Delage and Lefebvre, 1984) 172

Figure 6.13 Rose diagram of fabric orientation analysis of SEM specimens at 90 degrees (a) intact and (b) consolidated at 1014 kPa 173

Figure 6.14 Rose diagram of fabric orientation analysis of SEM specimens at 0 degree (a) intact and (b) consolidated at 1014 kPa 175

Figure 6.15 Quantification of fabric anisotropy of vertically trimmed St Marcel clay under different 1D-consolidation stresses; (a) Intact, (b) 124 kPa, (c) 421 kPa and (d) 1452 kPa 177

Figure 6.16 Quantification of fabric anisotropy of horizontally trimmed St Marcel clay under different 1D-consolidation stresses; (a) Intact, (b) 124 kPa, (c) 421 kPa and (d) 1452 kPa 178

Figure 6.17 SEM images of heavily overconsolidated London clay captured by Gasparre et al. (2011) (Zones: C, B2 and A3) and Hight et al. (2003) (Zones: B2) 179

Figure 6.18 Intact London clay (a) and (b), SEM images by Gasparre et al. (2011) (c) and (d), SEM images by Hight et al. (2003) 180

Figure A I.1 Modified oedometer for the purpose of stiffness anisotropy identification 202

Figure A I.2 Consolidation curve of vertically and horizontally trimmed specimens 205

Figure A I.3	Interpretation of shear wave signals captured at 127 kPa vertical effective stress during consolidation	207
Figure A I.4	Vertical and horizontal G_{max} of tested specimens versus mean effective stress	208
Figure A A.1	Stress state in thin-walled circular cylinders	214
Figure A A.2	Waterproof strain gauge (KFWB) specifications	217
Figure A A.3	Strain gauge bonding procedure	218
Figure A A.4	Principles of strain gauges measurements	219
Figure A B.1	Different applied threshold levels (T = 1 and T = 2) for distinguishing of particles zone from pore spaces, a) gray scale level and the determined limit; b) segmented pores; c) segmented particles	222
Figure A B.2	Different applied threshold levels (T = 3 and T = 4) for distinguishing of particles zone from pore spaces, a) gray scale level and the determined limit; b) segmented pores; c) segmented particles	223
Figure A B.3	Different applied threshold levels (T = 5 and T = 6) for distinguishing of particles zone from pore spaces, a) gray scale level and the determined limit; b) segmented pores; c) segmented particles	224
Figure A B.4	SEM images of the intact S3 sample at 10 kV	225
Figure A B.5	SEM images of the intact S3 sample at 15 kV	226
Figure A B.6	SEM images of the intact S3 sample at 20 kV	227
Figure A B.7	SEM images of the intact S3 sample at 25 kV	228
Figure A B.8	SEM images of the intact S3 sample at 30 kV	229
Figure A B.9	SEM images of the intact S7 sample at 10 kV	230
Figure A B.10	SEM images of the intact S7 sample at 15 kV	231
Figure A B.11	SEM images of the intact S7 sample at 20 kV	232
Figure A B.12	SEM images of the intact S7 sample at 25 kV	233
Figure A B.13	SEM images of the intact S7 sample at 30 kV	234

Figure A B.14 SEM images of the consolidated S3 sample at 10 kV.....235

Figure A B.15 SEM images of the consolidated S3 sample at 15 kV.....236

Figure A B.16 SEM images of the consolidated S3 sample at 20 kV.....237

Figure A B.17 SEM images of the consolidated S3 sample at 25 kV.....238

Figure A B.18 SEM images of the consolidated S3 sample at 30 kV.....239

Figure A B.19 Grid view and full view of SEM images for intact S7 with voltage of 15 kV; a) quarter images at magnification of 3000×; b) Grid-view image at magnification of 3000×; c) Full-view image at magnification of 1500×.....240

Figure A B.20 Random images (R1 to R5) of the surface of intact S7 sample with voltage of 15 kV, from surrounding areas, Grid-view zone at magnification of 3000×.....241

Figure A B.21 Random images (R1 to R5) of the surface of intact S7 sample with voltage of 15 kV, from surrounding areas, Full-view zone at magnification of 1500×.....242

LIST OF SYMBOLS

V_s	Shear wave velocity (m/s)
V_{s1}	Normalized shear wave velocity (m/s)
V_{ph}	Phase velocity (m/s)
Vh	Vertical-Horizontal (propagation-polarization) plane
hh	Horizontal-Horizontal (propagation-polarization) plane
Vs_{ij}	Anisotropic shear wave velocity in principal planes
f_0	Resonant frequency (kHz)
ζ/D	Damping ratio (%)
G_{max}	Maximum shear modulus (kPa)
G_{oij}	Anisotropic shear modulus in principal planes
E_{max}	Initial Young modulus (kPa)
I_α	Anisotropy index
AR or α	Anisotropy ratio
$\bar{L}$	Anisotropy index based on FOCM-II
D_i	Major length of the ellipse fitted in particles
D_j	Minor length of the ellipse fitted in particles
θ	Angle of particles
cc	Clay content (%)
I_p	Plasticity index
ω_l	Liquid limit
ω_p	Plastic limit

I_l	Liquidity index
ω_n	Water Content
OCR	Overconsolidation ratio
e	Void ratio
F(e)	Void ratio function
σ'_m	Mean effective stress (kPa)
σ'_v	Vertical effective stress (kPa)
σ'_p	Preconsolidation pressure (kPa)
σ_t	Hoop, or tangential stress (kPa)
ε_t	Hoop, or tangential strain
σ_r	Radial stress (kPa)
σ_a	Axial stress (kPa)
K_0	Coefficient of earth pressure at rest
σ'_h	Horizontal effective stresses (kPa)
P_a	Atmospheric pressure (kPa)
ρ	Bulk density (kg/m^3)
υ	Poisson ratio coefficient
P_i	Internal pressure (kPa)
S	Thickness of Oedometer ring (mm)
d_i	Internal diameter of Oedometer ring (mm)
r_e	External Oedometer ring radii (mm)
r_i	Internal Oedometer ring radii (mm)

INTRODUCTION

It is widely recognized that natural clays are frequently formed in horizontal strata and then exposed to anisotropic stress due to the sedimentation process, resulting in preferentially oriented particles. It can be stated that natural clay deposits have an intrinsic anisotropic structure ranging from weak to heavy that leads to variations in the deformation-strength characteristics of the soil medium. The understanding of soil anisotropy and its significance in geotechnical engineering is an extensive study that can be conducted in both laboratory and field-testing setups. Since 2000, there has been an increasing recognition of the importance of clay soil anisotropy in engineering practice. Zdravković et al. (2002) and Franzius et al. (2005) conducted computational analyses that emphasized the significance of accounting for anisotropy in anticipating deformations caused by embankments and tunnelling, respectively. Sedimentary soils like clays are anticipated to exhibit cross-anisotropic behavior, characterized by consistent stiffness in horizontal directions but varying stiffness in the vertical direction. The directional variability of stiffness characteristics is being assessed in two principal planes: the vertical-horizontal and the horizontal-horizontal. This anisotropic behavior is also pronounced in marine clays, owing to the preferred orientation of their plate-like minerals. In discussions of the anisotropic response of soft marine clays, two types of anisotropy might be involved: I) inherent anisotropy and II) stress-induced anisotropy. The microstructure and fabric of clay exclusively determine the first type. The second type is caused by unequally applied external stresses in different principal directions. Marine clays, especially Champlain, has a soft and compressible nature that can exhibit stress-induced anisotropy in addition to fabric anisotropy. Stress-induced factors have the potential to alter the clay specimen's microstructure. Specimens respond differently when loaded perpendicular versus parallel to their main fabric direction.

Through a gradual sedimentation approximately 12,000 to 10,000 years ago, Champlain marine clay is commonly found along the St. Lawrence Lowlands regions in the provinces of Ontario and Quebec in eastern Canada (Karrow, 1961). Weak particle bonds and high-water contents are important factors in the soil matrix of Champlain clays (Quigley et al. 1983),

making this soil critical for stress-induced anisotropy evaluation besides the fabric assessment. Champlain marine clays are reportedly problematic in geotechnical phenomena including landslides and large settlements which increase the importance of anisotropy recognition in this soil (Crawford, 1961; Penner and Burn, 1978, Demers et al. 2014). Anisotropy study of this clay is helpful to provide a more precise vision for calculation and anticipation of analyses attributed to this fine soil, like stability analysis and bearing capacity of foundations. This capability minimizes the inaccuracy of isotropic investigations, ultimately promoting more efficient and sustainable testing methods.

The literature on Eastern Canadian clays, particularly Champlain clay, primarily focuses on characterizing their isotropic properties. Their anisotropy phenomenon can be studied through mechanical and dynamic characteristics of soil, including shear strength, electrical resistance, permeability, and shear wave velocity testing. Current research focused on experimental phase that integrated Piezoelectric Ring Actuator Technique, P-RAT, into an oedometer cell setup to study dynamic characteristics as shear wave velocity and maximum shear modulus. This integration allowed for precise measurements of shear wave velocity under controlled conditions. A series of 1D-consolidation tests were conducted to ensure a reliable anisotropic characterization of clay specimens. Determining key parameters such as shear wave velocity and subsequently calculating maximum shear modulus facilitates the investigation of anisotropy degree. Understanding the directionality of linear elastic stiffness in clays, along with factors such as applied stress, void-ratio, and stress state, enables development of empirical correlations for clay anisotropic response. They can be employed in underground geotechnical projects where anisotropy can be a crucial aspect.

The study adapts laboratory instrumentation including transmitter-receiver transducer sensors, and lateral strain gauges in a standard oedometer apparatus to evaluate anisotropy in Champlain marine clays across varying porosity levels and applied stresses during 1D-consolidation testing. Scanning electron microscopy (SEM) complements this testing regime by characterizing clay fabric anisotropy at the microscale, providing multi-level insights into the directional properties of these Eastern Canadian deposits. This integrated approach gives a

comprehensive assessment of the soil behavior from both macroscopic mechanical responses and microstructural arrangements.

This dissertation includes seven chapters.

Chapter 1

This chapter presents a literature review and methodology overview, divided into several key sections:

This chapter begins by introducing Champlain clays and their fundamental properties, followed by an examination of clay microstructure. The stiffness anisotropy through measurements of shear wave velocity is presented. Both laboratory and field-testing methods are explained for the purpose of anisotropy. The final sections cover the cross-anisotropy assumption, its constitutive models, existing empirical relationships, and a review of significant studies on anisotropic behavior of clays and its implication.

Chapter 2 outlines the research objectives and establishes the overall framework of the dissertation, which follows a manuscript-based structure composed of three papers. Each paper is presented as an independent yet complementary study, progressively advancing the investigation of anisotropy in Champlain marine clays. These papers encompass distinct methodologies, results, and discussions, but are thematically connected to form a coherent narrative on the characterization of anisotropic behavior from both macro- and microscale perspectives. This chapter also emphasizes the significance and original contributions of this research project to the field of geotechnical engineering, particularly regarding the anisotropic behavior of Champlain marine clays.

Chapter 3

The experimental results begin with a chapter on laboratory testing with isotropic assumption (considering only the vertical direction). This groundwork phase establishes testing protocols, validates fabricated sensor performance, and acquire technical expertise with Champlain clay

samples. These foundational attempts build gradual progression toward the more complex anisotropic investigations that form the main research focus.

Chapter 4

This chapter presents the experimental framework developed to characterize cross-anisotropy in Champlain marine clay through laboratory measurements. A modified oedometer apparatus, instrumented with a P-RAT and high-precision strain gauges, was employed to measure directional shear wave velocities and lateral stresses under controlled consolidation conditions. The study focuses on evaluating the stiffness response in the vertical-horizontal (vh) and horizontal-horizontal (hh) planes, enabling quantitative assessment of anisotropic behavior. The experimental results establish the foundation for correlating shear wave velocity, effective stress, and void ratio regarding anisotropy understanding (Paper I).

Chapter 5

This chapter investigates clay fabric anisotropy using SEM imaging, examining both intact morphology and consolidation effects. Two quantification approaches are presented for fabric anisotropy assessment. To minimize SEM imaging errors, a parametric analysis was conducted and an improved imaging method proposed for the determination of anisotropy index from microstructure of the soil. The outcome is the proposal of an optimized imaging and processing method that improves the accuracy and reproducibility of microscale anisotropy characterization in Champlain marine clays (Paper II).

Chapter 6

This chapter explores the influence of bedding layer inclination on the anisotropic behavior of Champlain soft marine clay. The study investigates how the depositional fabric orientation affects stiffness anisotropy by testing specimens trimmed at various angles (from 90° to 0°) relative to the natural bedding plane. Using directional shear wave velocity measurements obtained through the P-RAT system under controlled consolidation stresses, the chapter establishes the relationship between bedding orientation, overconsolidation ratio, and

anisotropy degree. The findings provide valuable insights into how sedimentary layering and stress history govern the directional stiffness of marine clays (Paper III).

The final section presents conclusions drawn from the investigations and offers recommendations for future research. This part is followed by a bibliography.

CHAPTER 1

STATE OF ART

1.1 Sedimentology of Champlain clays

This fine soil, which is deposited in the Champlain Sea arm of the Atlantic Ocean, is predominantly marine post-glacial sediment created by retreating ice sheets during the closure of the last glacial period. The distinct engineering characteristics of the Champlain clay make it of geotechnical interest. This clay is characterized as being highly sensitive ($8 < St \leq 16$) and quick ($St > 16$) clay based on the classification proposed reported in the Canadian Foundation Engineering Manual (CGS, 2023). The natural occurrence of quick and highly sensitive clays is generally restricted to formerly glaciated regions that have been subjected to isostatic uplift due to retreating ice sheets. These clays frequently exist in the area along the St. Lawrence Seaway in the northeast of North America and in certain parts of Alaska. Champlain clays [also named Leda clays (Crawford, 1961)], are a notable formation of soft sensitive clays found in Eastern Canada, including parts of the major cities of Montreal, Quebec City, and Ottawa. This marine deposit was formed approximately 12,000 years ago (Fulton and Richard, 1987).

Marine clays in Canada formed through three primary sedimentation processes (Quigley, 1980):

1. Waterlaid tills are stratified deposits formed under shallow floating ice sheets, characterized by minimal grain size sorting. Their depth varies significantly, from 1 meter in Alberta to 30 meters in Sarnia, Ontario. They typically overlay harder till deposits.
2. Lacustrotills are sediments deposited in lake environments, often including waterlaid tills. When these submarine mudflows had sufficient momentum, they could be transferred by underwater and form turbidity current deposits, which became interlayered with varved deposits along the shores.
3. Varved clay deposits are formed through seasonal deposition patterns (Figure 1.1):

Summer Deposition:

- Cold inflow (0-6°C) with ice melting of high density (≥ 1 g/L) created heavy density flows
- These flows could travel extensively even across flat lake floors
- Resulted in graded deposits of silt and sand
- Deposition periods varied from days to brief daily intervals

Winter Deposition:

- Low sediment density in inlet flow led to overflow conditions
- Resulted in undisturbed clay particle sedimentation

The structure of annual varved layers includes:

- A silt layer (80% > 2 μm)
- A transition layer
- A clay layer (80% < 2 μm)
- High moisture content due to open flocculation of clay structure.

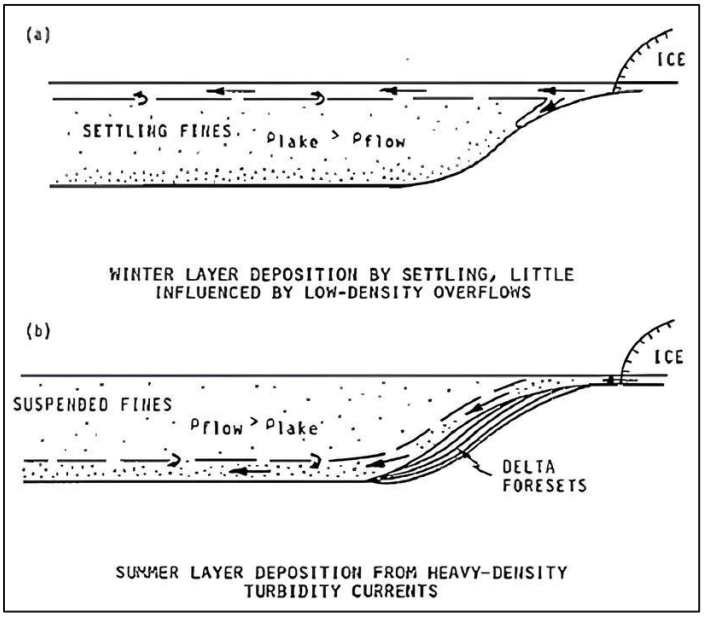

Figure 1.1 a) Winter overflow; b) Summer heavy density flow into glacial lakes
Taken from Quigley (1980, p. 271)

The depositional environment of Champlain clays, particularly the seasonal varving and the density-driven flows, produced a layered microstructure where coarse silt layers alternate with finer clay-rich horizons. During deposition, the plate-like clay minerals tended to align horizontally, reflecting the direction of sedimentation. This preferential particle orientation, combined with the stratified layering, gives rise to a fabric that is inherently anisotropic. As a result, Champlain clays exhibit markedly different stiffness and strength in the vertical and horizontal directions, a feature that must be accounted for in their geotechnical characterization.

The behavior of sensitive and quick clays can be influenced by variations in soil fabrics, according to empirical studies (Gillot, 1970; Quigley and Thompson, 1966; Penner, 1963). As hundreds of documented landslides in the area indicate, they are vulnerable to destruction and sudden strength loss (Brooks, 2014; Demers et al., 2014). According to Quigley and Thompson (1966), two components of soil structure were identified: the intrinsic strength of cementation bonds that hold the soil particles together, and the geometrical arrangement of the soil particles, or "fabric".

Lessard and Mitchell (1985) reported that Champlain clay contains various predominant clay minerals, including illite, quartz, feldspar, amphibole, and calcite, using X-ray diffraction technique on six samples from the La Baie, Quebec, region. Quigley and Thompson (1966) investigated the qualification of the fabric and soil particle arrangements on undisturbed Champlain clay specimens indicating card-house or random fabrics association; however, with increasing consolidation stress, parallelism occurs in these platy particles, as shown in Figure 1.2.

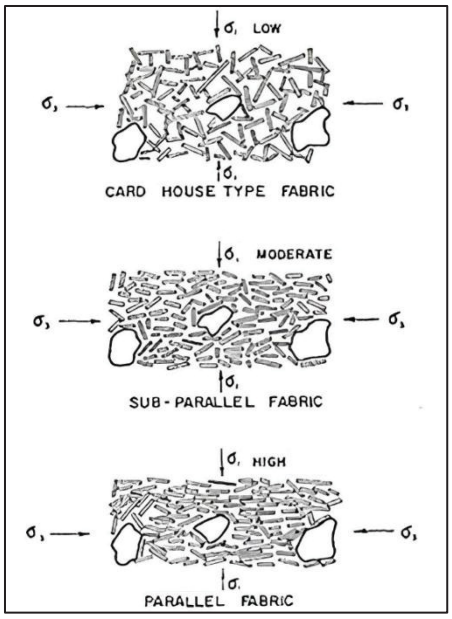

Figure 1.2 The arrangement and association of Champlain clays from undisturbed to consolidated specimen
Taken from Quigley and Thompson (1966, p. 62)

The geotechnical properties of Champlain clays from different regions are presented in Table 1.1. Various studies, including Delage and Lefebvre (1984), Philibert (1984), Leroueil et al. (1990), Ethier (2009), and the ÉTS laboratory (Dion, 2019; Elbeggo, 2023), have utilized this clay type for experimental purposes. According to the literature, the natural water content of sensitive marine clays is commonly high, and the liquid limit shows a lower range of values than the natural water content. Sensitivity generally increases with increasing liquidity index, with highly sensitive or quick clays often having liquidity index values greater than 1 (1.5 or 2) as reported by Holtz et al. (2011). Based on these properties, this clay can be classified as high plasticity clay (CH) according to the Unified Soil Classification System (ASTM D2487-17).

The clay platelets play an important role in the fabric of the soil, as evidenced by the high percentage of clay content reported in different studies. The overconsolidation ratio (OCR) of Champlain clays ranges from light to moderately overconsolidated (Leroueil et al., 1990), with values ranging from 1.3 to 8.9.

Table 1.1 Geotechnical Characteristics of Champlain clays

Studies	ω (%)	ω_P (%)	ω_L (%)	Clay content (%) (<2 µm)	Depth (m)	OCR	Region
Delage and Lefebvre (1984)	80	25	60	80	5.2	2.3	St. Marcel
Philibert (1984)	77	28	56	74	3.8	1.8	Gloucester
	45	23	40	53	6.35	8.9	St. Alban
	50	20	45	60	5.65	7.3	St. Barnabe
	81	25	60	80	5.15	2.3	St-Marcel
	77	27	60	72	8.8	2.3	Ottawa (NRC)
	64	25	66	80	7	3.1	Varennes
	66	28	65	76	8.5	4.8	Ottawa (SP)
Leroueil et al. (1990)	72	30	68	80	9.2	-	Louiseville
	78	28	64	65	5.9	-	St. Esprit
	89	26	74	78	3.4	-	St. Esprit
	75	25	45	75	2.5	-	St. Alban
Ethier (2009)	76	40	59	76	8	1.4	St. Hilaire
ÉTS Laboratory (Elbeggo, 2023; Dion, 2019)	90	43	69	89	4.5	1.3	Abitibi
	61	32	56	74	7.93	3.3	Montreal-East
	80	36	61	71	6.5	2.2	Beauharnois

1.2 Clay microstructure and consolidation effects

Clay microstructure plays a crucial role in determining the engineering properties and behavior of clay soils. The arrangement of clay particles, their interactions, and the resulting pore

structure significantly influence the mechanical and hydraulic characteristics of clay. This section explores the fundamental aspects of clay microstructure and the effects of consolidation on its evolution.

1.2.1 Clay structure and fabric

Clay structure refers to the combined effect of clay fabric and inter-particle bonding (Lambe and Whitman, 1969). Clay fabric specifically describes the geometric arrangement of clay particles, including their orientation and distribution. The fabric of clay is largely influenced by the depositional environment, sediment source, and related environmental conditions (Bennett, 1976).

Several types of clay fabrics have been identified and studied over the years. The concept of a honeycomb structure was first proposed in the 1920s, where clay particles stick to each other at points of contact, forming a structure that can hold large amounts of water within its voids. Lambe (1953) later introduced the cardhouse fabric, which consists of essentially single-particle arrangements.

As research progressed, more complex fabric arrangements were identified. Aylmore and Quirk (1960) described the turbostratic arrangement, consisting of domains or stacks of clay particles. Sloane and Kell (1966) proposed the 'book house' fabric, which is similar to the turbostratic fabric but with a more open structure. These various fabric types are illustrated in Figure 1.3, showing the cardhouse, bookhouse, honeycomb, flocculated, turbostratic, and stack fabrics.

The type of fabric present in a clay soil significantly influences its engineering properties. For instance, flocculated structures typically exhibit higher shear strength, higher void ratios, and lower compressibility compared to dispersed structures. The orientation of clay particles are also an effective aspect, with parallel arrangements in dispersed systems and more random orientations in flocculated systems (Lambe, 1953; Barden and Sides, 1971).

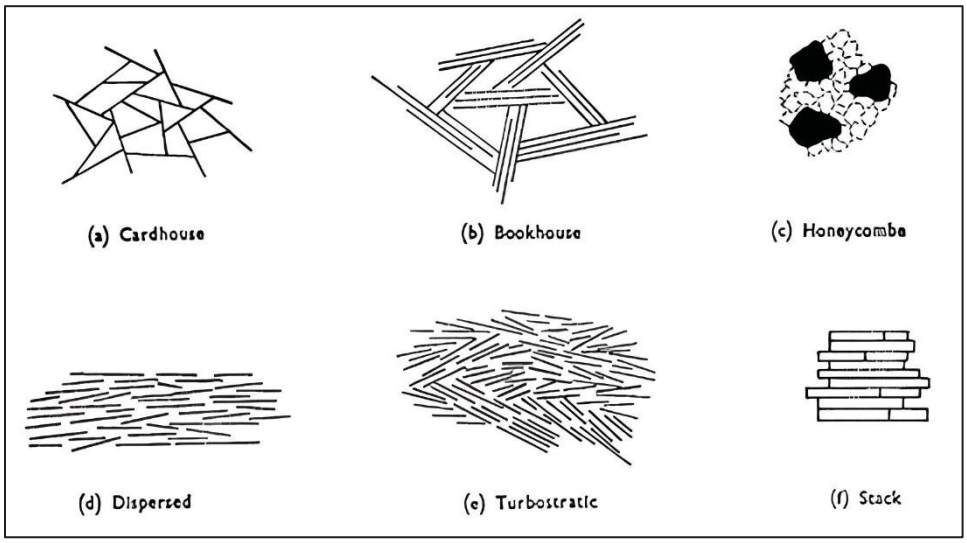

Figure 1.3 Schematic view of clay fabric structure
Taken from Barden and Sides (1971, p. 212)

1.2.2 Effects of compression on clay microstructure

The application of compressive stress, whether one-dimensional (K_0 state) or isotropic, leads to significant changes in clay microstructure, primarily affecting the clay fabric and pore structure.

- **One-dimensional compression**

During one-dimensional compression, clay particles tend to reorient themselves perpendicular to the direction of the applied stress. Smart (1967) observed that unconsolidated clay samples initially exhibit random particle arrangements. As vertical stress increases, there is a progressive increase in the average degree of particle orientation, leading to the development of areas with highly oriented fabric. Figure 1.4 illustrates the evolution of the cardhouse fabric during one-dimensional compression.

Initially, the fabric consists of randomly arranged edge-to-face domains. As consolidation stress increases, these domains start to form and grow in size. Under higher consolidation stress

levels, the domains become fully oriented in face-to-face contact. This reorientation of clay particles during one-dimensional compression has been observed by different researchers. Tchalenko (1967) and Delage and Lefebvre (1984) found that one-dimensional compression orientates clay particles normal to the maximum principal stress.

Crawford (1961) and Quigley and Thompson (1966) observed little to no particle reorientation before reaching the pre-consolidation pressure, but an abrupt increase in particle parallelism occurred once this threshold was exceeded. The evolution of pore structure during one-dimensional compression (Figure 1.4) is characterized by the progressive collapse of larger pores. Delage and Lefebvre (1984) demonstrated that primarily the largest existing pores collapse under a given effective stress, while small intra-aggregate pores remain largely unaffected until very higher levels are applied. This finding has been corroborated by subsequent studies (Tanaka and Locat, 1999; Yu et al., 2016), which show that the reduction in void ratio during compression is mainly due to the closing of inter-aggregate pore spaces.

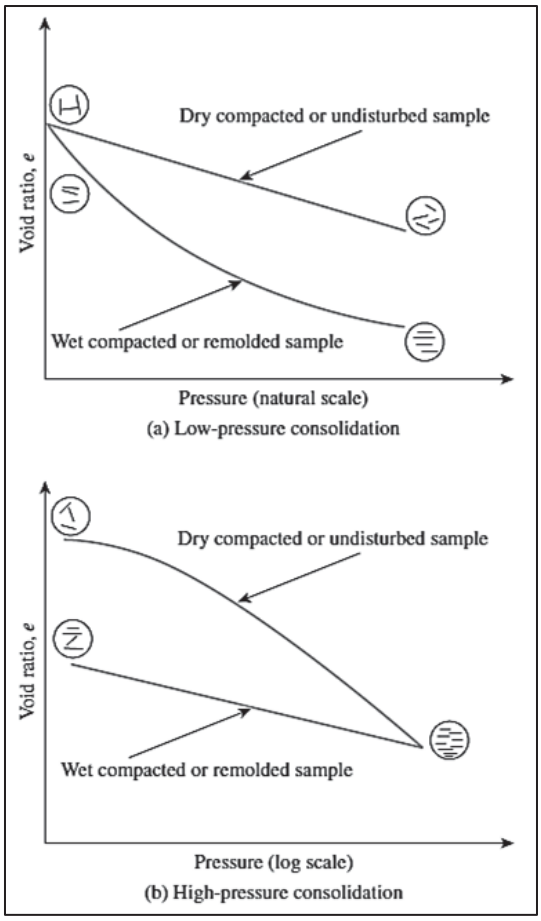

Figure 1.4 Effect of compaction on one-dimensional consolidation of clays
Taken from Das and Sobhan (1990, p. 164)

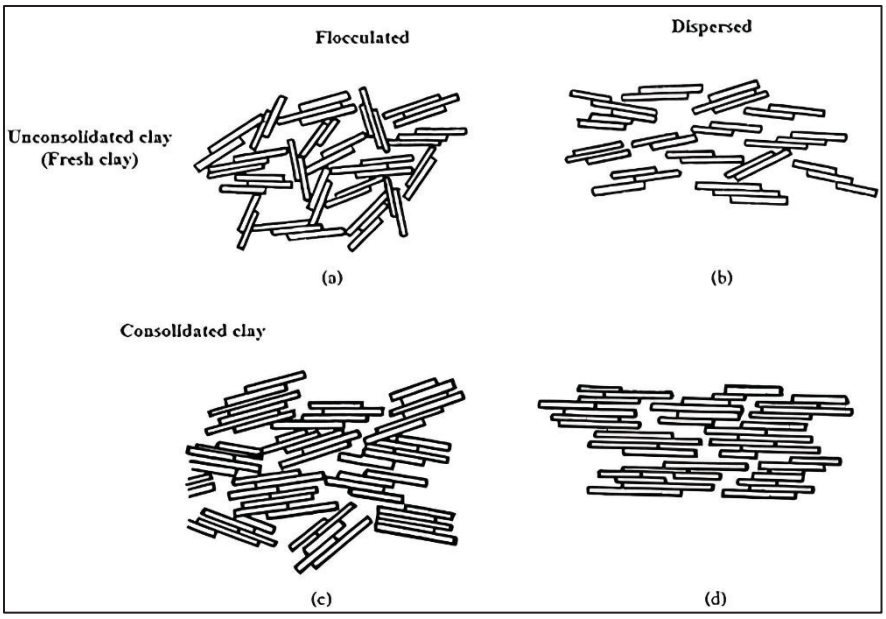

Figure 1.5 Rearrangement of clay particles due to the applied stress
Taken from Lambe and Whitman (1969, p. 73)

- **Isotropic compression**

In contrast to one-dimensional compression, isotropic compression generally leads to a more random particle arrangement, reducing the overall orientation of the clay fabric. Kirkpatrick and Rennie (1972) observed that kaolin clay compressed under isotropic conditions possessed an isotropic fabric with randomly oriented particles, in contrast to the strongly oriented fabric produced by anisotropic compression. Hattab and Fleureau (2010) used the term 'depolarization' to describe the process by which isotropic compression leads to a more random orientation of particles. They found that as isotropic compression proceeded, the initial preferential orientation of particles disappeared. However, the degree of fabric randomization depends on the magnitude of the applied isotropic stress relative to the previous one-dimensional consolidation stress. Hicher et al. (2000) and Mitaritonna et al. (2014) found that an isotropic loading about three to four times greater than the initial one-dimensional consolidation stress was necessary to produce a fully isotropic particle orientation. The evolution of pore structure during isotropic compression is similar to that observed in one-dimensional consolidation. Yu et al. (2016) and Guglielmi et al. (2018) found that isotropic compression primarily affects the inter-aggregate pores, while intra-aggregate pores remain

largely unchanged. The deformation response during isotropic compression is thus controlled mainly by aggregate-to-aggregate interactions rather than particle-to-particle interactions.

While both one-dimensional and isotropic compression lead to significant changes in clay microstructure, there are some notable differences in their effects. In terms of pore structure evolution, both compression types primarily affect the inter-aggregate pores. However, Guglielmi et al. (2022) suggested that isotropic compression may be more effective in reducing inter-aggregate porosity and can lead to faster microstructure evolution compared to one-dimensional compression. Guglielmi et al. (2018) compared the pore-size distribution changes induced by isotropic and one-dimensional compression in reconstituted Pappadai clay. While both compression paths resulted in a shift of the incremental pore-size distribution curve towards smaller pores and a reduction in the size of dominant pores, the isotropically compressed sample showed slightly fewer inter-aggregate pores when compressed to the same void ratio as the one-dimensionally compressed sample.

1.3 Lateral strain determination

According to literature, the measurement of anisotropic behavior in clays has been mostly reported by utilizing triaxial apparatus, where both vertical and horizontal stresses can be independently controlled and measured (either K_0 stress state or isotropic stress state). However, when considering the adaptation of this measurement technique to an oedometer, a significant challenge arises due to the inability to directly measure lateral pressures. Unlike the triaxial apparatus, the oedometer's rigid ring constrains lateral deformation while allowing vertical loading, creating a K_0 stress state where lateral stresses develop in response to vertical loading. To bridge this gap and enable accurate anisotropy measurements in oedometer testing, the installation of high precision strain gauges on the outer surface of the oedometer ring presents a practical solution (Silvestri and Morgavi 1982; Kolymbas and Bauer 1993). These gauges can measure the minute deformations of the ring wall caused by the lateral earth pressure (K_0 state) exerted by the confined soil sample. Through a careful calibration, the measured ring deformation can be converted into lateral pressure values, thereby providing the

critical stress state information needed for anisotropy analysis. This adaptation extends the capability of standard oedometer testing equipment while maintaining the fundamental advantages of its simple design and operation.

1.4 Digital imaging and morphology

The ability to peer inside soils and examine their internal structures has revolutionized geotechnical engineering and soil science over the past century. Among the most powerful tools in modern materials characterization, SEM and X-ray Computed Tomography (CT) stand out as complementary techniques that provide researchers with insights into soil structures across multiple scales.

SEM has revolutionized our ability to visualize and understand material structures at the microscopic scale. Since its early development in the 1930s and commercial introduction in the 1960s, SEM has become an indispensable tool for materials science, engineering, and research across numerous fields. SEM machine employs a focused beam of electrons to generate high-resolution images of a sample's surface topography with magnifications ranging from 10x to over 500,000x.

X-ray computed tomography (CT), in contrast, enables non-destructive visualization of internal structures in three dimensions. By rotating a sample while collecting X-ray projection images, CT systems can reconstruct detailed 3D models of internal features, voids, and defects (Taina et al., 2008). While X-ray CT has become an essential tool in soil research, it faces certain challenges. The analysis of soil solid phases can be complicated due to similar X-ray attenuation values of different solid constituents. However, researchers have addressed this limitation through techniques such as multiple X-ray energy levels, which facilitated better discrimination of minerals in soil (Taina et al.2008).

1.4.1 Image processing

The field of clay microstructure investigation has undergone substantial transformation since the mid-1980s. The foundation was established through pioneering spectral analysis work, with Fourier transformation techniques being implemented to evaluate particle distributions and orientations (Sergeyev et al. 1985). This mathematical approach opened new avenues for quantitative assessment of clay structures, moving beyond purely descriptive methods.

The transition to digital image analysis marked a significant breakthrough in the early 1990s. Researchers developed innovative approaches for translating complex structural patterns into measurable data, with the introduction of rose diagrams providing a revolutionary way to visualize fabric orientation patterns (Tovey and Krinsley, 1992). This visualization technique remains influential in modern analysis methods (Fig. 1.6).

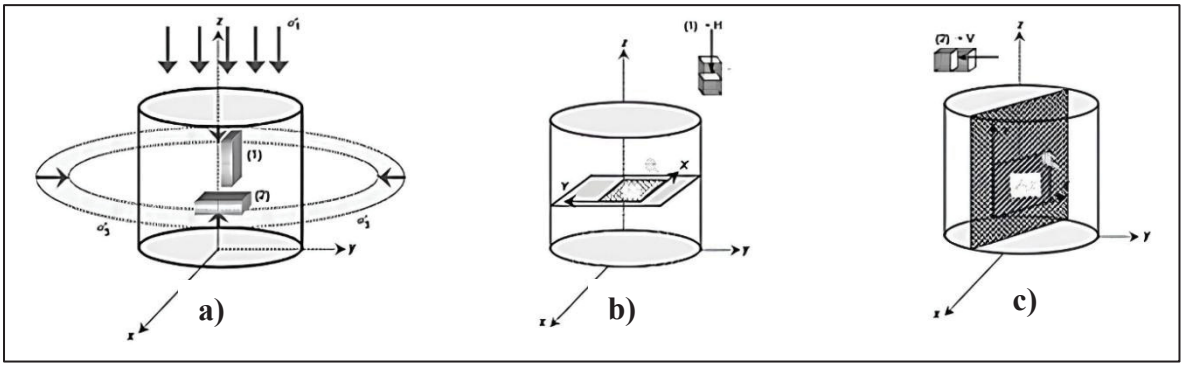

Figure 1.6 Samples for the SEM observations,
a) samples for observation and stress state; b) horizontal plane; c) vertical plane
Taken from Hattab and Fleureau (2010, p. 325)

A notable development came from research incorporating manual particle identification techniques for SEM imagery (Hicher et al., 2000). This approach was subsequently refined to include detailed orientation distribution analysis, particularly focusing on quantifying side particle arrangements relative to their directional positioning (Shown in Fig. 1.7).

Recent methodological advances have centered on pixel-based analysis techniques. Building earlier work by Martinez-Nistal et al. (1999), researchers have developed sophisticated

brightness threshold analyses for examining various clay types (Guglielmi et al. 2022). This pixel-intensity approach has proven particularly valuable for distinguishing structural features in complex clay formations. Recent studies have demonstrated the effectiveness of advanced computational tools, particularly in examining pore structures and their responses to mechanical stress (Zhao et al. 2020; Dai et al., 2021). The cornerstone of modern clay analysis lies in advanced pore segmentation methodologies. Contemporary approaches utilize an 8-bit grayscale system, with threshold values spanning 0-255 for porosity assessment (Moyano et al., 2012). A significant innovation in this field has been the development of adaptive threshold selection methods, utilizing cumulative histogram analysis of grayscale intensities. Research indicates optimal threshold ranges typically fall between 50-80, though this varies based on image characteristics (Wang et al., 2011).

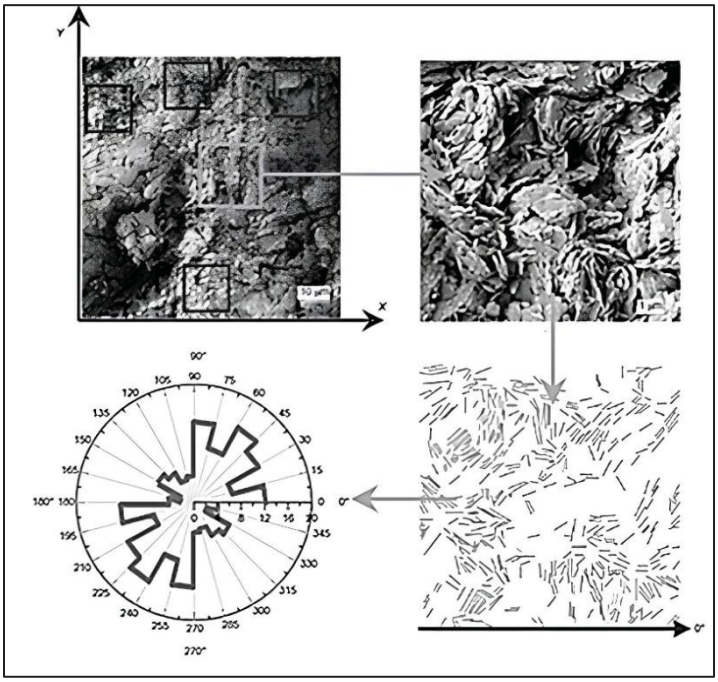

Figure 1.7 Method of analysis and image processing
Taken from Hattab and Fleureau (2010, p. 325)

Due to the significance of microstructure of clays, the bedding layers play an important role in the microstructure and mechanical behavior of Champlain clays, influencing their deformation response and susceptibility to failure. Locat et al. (2017) utilized CAT (Computerized Axial

Tomography) scan imaging as a non-destructive method to investigate the internal structure and stratification of Champlain clays within the landslide debris at the Saint-Jude site in Québec. The CAT scans provided high-resolution cross-sectional images of undisturbed core samples, enabling the visualization of bedding layers, density variations, and deformation patterns within the clay (Figure 1.8). This imaging technique allowed researchers to correlate microstructural layering with in-situ geotechnical observations, offering a three-dimensional understanding of how the clay fabric and stratification contributed to the landslide's failure mechanisms. CAT scanning was particularly valuable for identifying zones of folded, inclined, and sheared strata, which could not be easily detected through conventional sampling or optical core logging. These CAT scan results confirmed that bedding inclination and stratigraphic discontinuities played a crucial role in defining the shear surface and controlling the movement of the landslide mass.

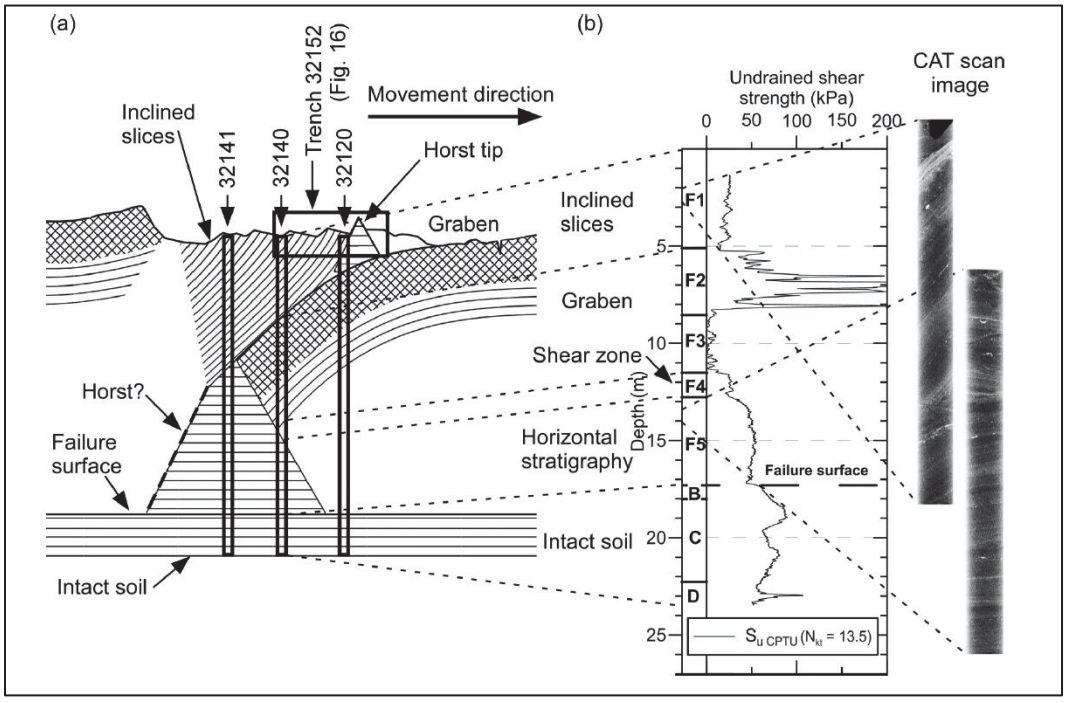

Figure 1.8 CAT scan imaging for visualization of stratification and bedding layers, a) stratigraphy details; b) CPTU and CAT scan image
Taken from Locat et al. (2017, p. 1371)

1.5 Summary

The review of Champlain clays and their microstructural behavior highlights the significance of understanding their anisotropic nature in geotechnical engineering applications. These sensitive clays, which are prevalent in Eastern Canada, exhibit complex behavior that stems from their unique formation history and microstructural characteristics. The transition from their initial depositional fabric to their current state, influenced by post-depositional processes and stress history, creates inherent and stress-induced anisotropy that can affect their engineering behavior.

The microstructural arrangement of clay particles, particularly their orientation and packing, plays a crucial role in determining the mechanical and dynamic response of these soils. As demonstrated in the literature, the fabric of Champlain clays can vary from random arrangements to moderate oriented patterns depending on the stress history and loading conditions. This structural evolution directly influences important engineering properties such as strength (Mitchell 1970), permeability (Leroueil et al. 1990) and shear waves (Hicher et al. 2000 and Gasparre et al. 2011).

Clay microstructure, with its distinct fabric arrangements exhibits different responses to stress conditions. 1D-consolidation induces anisotropic fabric development, necessitating the measurement of both vertical and horizontal stress components. The application of high-precision strain gauges on oedometer rings effectively addresses this limitation of conventional oedometers, enabling accurate lateral stress determination during consolidation testing.

Digital imaging and morphological analysis like SEM provide valuable insights into clay microstructure across multiple scales. The evolution of image processing techniques-from early Fourier transformation methods to modern pixel-based analyses and threshold selection methodologies-has significantly improved engineering ability to quantify fabric orientation patterns and structures.

Analysis of current imaging methodological limitations suggests several priority areas for research:

- Development of standardized procedure for threshold determination
- Implementation of robust procedures less sensitive to image quality variations
- Integration of multi-scale imaging data for comprehensive fabric characterization

1.6 Isotropic small strain stiffness

In geotechnical engineering, soil stiffness is a fundamental parameter governing its deformation response under loading. The relationship between shear modulus and shear strain is especially significant and typically follows a nonlinear trend, as shown in Figure 1.9. As shear strain increases, soil stiffness decreases in a non-uniform manner, highlighting the strain-dependent nature of soil stiffness. Of particular interest is the soil's behavior at very small strain levels those below 0.001%. In this range, often referred to as the 'very small strain' range, the soil behaves elastically. The stiffness in this elastic range is characterized by the small strain shear modulus, G_{max} (also known as G_0). This parameter represents the maximum stiffness of the soil and is of great importance in geotechnical analyses. Interestingly, the value of G_{max} can be derived from the principles of shear wave propagation through isotropic elastic media assumption, linking soil mechanics to wave theory in elastic solids. The maximum shear modulus is a key soil property in engineering. It's crucial for accurately predicting soil behavior and analyzing geotechnical problems like settlements and soil-structure interaction. This parameter is used in numerical models for foundations, piles, excavations, and tunnels. It's also vital in soil dynamics for predicting ground movement during earthquakes, explosions, and machine vibrations.

In the context of an isotropic elastic medium, the theory of shear wave propagation provides a formula for calculating the soil's G_{max}. This relationship is expressed as:

$$G_{max} = \rho V_s^2 \tag{1.1}$$

Where:

G_{max} is measured in (Pa)

ρ represents the particle's density, (kg/m³)

V_s denotes the velocity of shear waves traveling through the soil, (m/s)

Equation (1.1) demonstrates that the maximum shear modulus is directly proportional to the particle's density and to the square of the shear wave velocity.

Isotropy means a soil's properties are similar in all directions. Isotropic elastic soil is defined by two key parameters: Young's modulus (E) and Poisson's ratio (ν). These parameters are used to create the soil's stiffness matrix, which defines its elastic behavior. Using Hooke's law, two additional properties (k and G) can be derived: volumetric modulus (resistance to uniform compression) and shear modulus (resistance to shear deformation), respectively.

$$k = \frac{E}{3(1-2\vartheta)} \tag{1.2}$$

$$G = \frac{E}{2(1+\vartheta)} \tag{1.3}$$

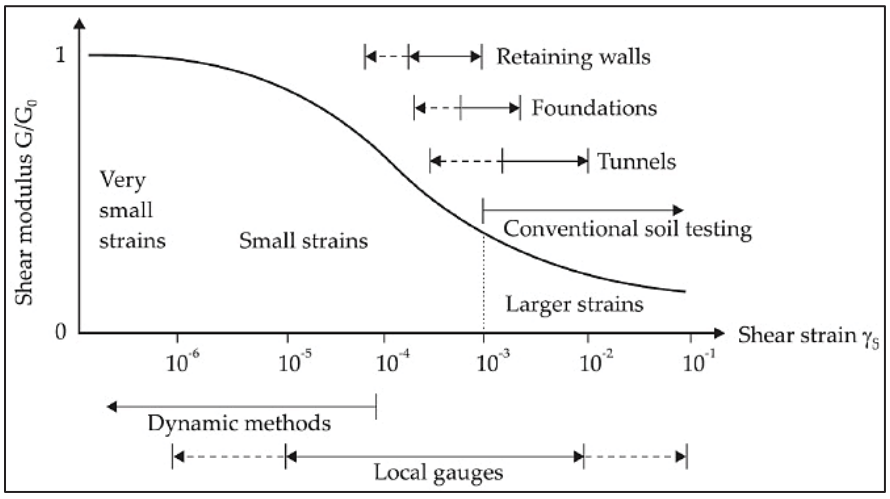

Figure 1.9 Relationship between shear modulus and shear strain
Taken from Atkinson (2000, p. 488)

These derived properties can be expressed in terms of E and ν, allowing for characterization of the soil's elastic behavior.

1.6.1 Shear wave propagation

Seismic waves are categorized into two main types: body waves and surface waves (Kramer, 1996; Ishihara, 1996). Body waves are further divided into compressional waves and shear waves as shown in Figure 1.10. The compressional wave, also known as the primary wave (P-wave), moves particles in a direction parallel to the wave's path. In contrast, shear waves, also known as secondary waves (S-waves), induce deformations through shearing as they propagate through a material. S-waves show particle motion that is perpendicular to their path of propagation.

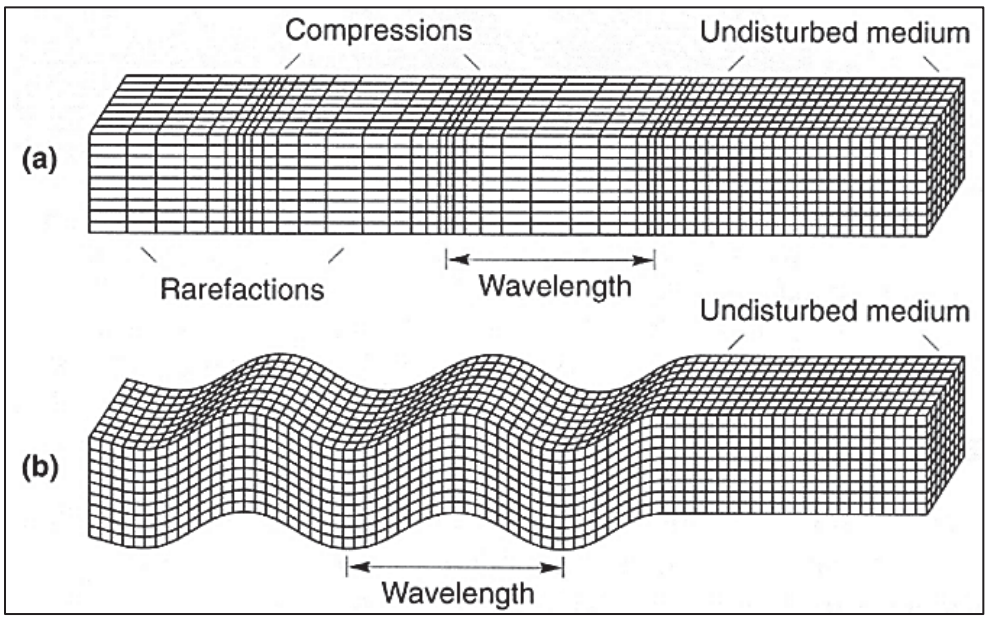

Figure 1.10 Propagation of seismic waves in the soil body: a) P-waves, b) S-waves
Taken from Kramer (1996, p. 19)

Shear waves can propagate in different orientations: vertically with horizontal polarization or particle motion (VH waves), horizontally with vertical particle motion (HV waves), or horizontally with horizontal particle motion (HH waves). Shear waves can be utilized to

estimate the linear elastic stiffness (maximum shear modulus), G_{max}. Shear waves cannot travel through fluids; hence the presence of water does not impact shear wave velocities in saturated soils.

The relationship between the velocities of the body waves and stiffness assumes that the soil behaves as a uniform and elastic material that is isotropic. An isotropic soil medium has consistent properties in all directions, indicating that its mechanical features, including stiffness, are constant regardless of direction. The homogeneity of soil behavior simplifies the analysis since it ensures a consistent response to stress and strain, regardless of orientation. Equation (1.4) shows the relationship between shear wave velocity and maximum shear modulus of the soil structure.

$$V_s = \sqrt{\frac{G_{max}}{\rho}} \tag{1.4}$$

This elastic theory was originally proposed by Hardin and Richart (1963).

1.6.2 Stiffness measurement

Reliable measurements of stiffness, ranging from small to large strains, have been increasingly recognized as important in both static and dynamic analyses for the past two decades. The local displacement transducer was utilized in the static triaxial test to measure local axial strains (Goto et al., 1991; Atkinson, 2000). The resonant column and torsional shear devices have been employed for several years to investigate the cyclic and dynamic characteristics of geomaterials within a strain range of 10-4 to 0.1% (Drnevich, 1985; Saada, 1988). The stiffness of soil has traditionally been assessed using triaxial and resonant column tests for several years. Despite these approaches, the wave propagation techniques both in the laboratory and in the field are widely accepted due to the non-destructive, and low-cost assessment and interpretation methods. Table 1.2 represents the available laboratory and field techniques for

measuring shear wave velocity in soils. This table comprehensively outlines various methods including:

1. Bender elements
2. Resonant column
3. Seismic Cross-Hole
4. Seismic Down-Hole
5. Seismic Cone Penetration
6. Spectral Analysis of Surface Waves (SASW)
7. Modal Analysis of Surface Waves (MASW)

Each of these methods has specific applications and advantages in determining soil stiffness properties. The selection of an appropriate method depends on various factors including the project requirements, site conditions, and the specific parameters needed for analysis.

Table 1.2 Overview of wave propagation techniques utilized to assess the stiffness of soils adapted from Sawangsuriya (2012, p. 162)

Experimental approach	Testing description	References
Bender elements	Bender elements testing is a geotechnical laboratory method used to measure the shear wave velocity and, consequently, the shear modulus of soil. In this test, small piezoceramic transducers (bender elements) are inserted into a soil specimen. One element as a transmitter generates shear waves that travel through the soil and are detected by the other element as a receiver. By analyzing the travel time and distance between the element's tips, the shear wave velocity is determined, which helps in evaluating the soil's stiffness and dynamic properties.	Shirley & Hampton (1978); Dyvik & Madshus (1985); Fam & Santamarina (1995); Viggiani & Atkinson (1995); Jovicic & Coop (1998); Santamarina et al. (2001); Pennington et al., (2001); Clayton et al., (2004); Lee & Santamarina, (2005); Yamashita et al., (2009).
Resonant column	The resonant column test is a laboratory technique used to determine the dynamic properties of soils, such as shear modulus and damping ratio. In this test, a cylindrical specimen is subjected to torsional or flexural vibrations, and its natural frequency and response to these vibrations are measured. By analyzing the resonant frequency and amplitude, the material's stiffness and energy dissipation characteristics can be derived.	Hardin & Black, (1968); Edil & Luh (1978); Isenhower (1980), Kim & Novak, (1981); Chung et al., (1984); Drnevich (1985), Presti & Jamiolkowski, (1998).

Table 1.2 Overview of wave propagation techniques utilized to assess the stiffness of soils adapted from Sawangsuriya (2012, p. 162) (continued)

Experimental approach	Testing description	References
Seismic Cross-Hole	Seismic cross-hole testing is a geophysical method used to determine the shear and compressional wave velocities of soils. This test involves generating seismic waves at one borehole and detecting them at one or more adjacent boreholes equipped with geophones. By measuring the travel time of the seismic waves between boreholes, the wave velocities can be calculated, providing insights into the stiffness, density, and layering.	ASTM-D4428M-25; Ballard, (1976); Butler & Curro, (1981); Campanella, (1994)
Seismic Down-Hole	Seismic down-hole testing is a geophysical technique used to measure the shear and compressional wave velocities of subsurface soils. In this test, seismic waves are generated at the surface and detected by a geophone lowered incrementally down a borehole. By recording the travel times of the waves at different depths, the wave velocities can be calculated, offering detailed information about soil's properties, including stiffness and layering.	ASTM D7400M-19; Richart (1977); Campanella (1994); Ishihara (1996).
Seismic Cone Penetration	Seismic Cone Penetration Testing (SCPT) is a field investigation technique that combines the capabilities of cone penetration testing (CPT) with seismic wave measurements to assess both static and dynamic properties of subsurface soils. During the test, a cone penetrometer equipped with geophones or accelerometers is pushed into the ground at a consistent rate, continuously measuring parameters like tip resistance, sleeve friction, and pore water pressure. Periodic pauses allow for the generation and capture of seismic waves, from which shear (V_s) and compressional (V_p) wave velocities are derived.	Robertson et al., (1986); Sully, (1991); Robertson et al., (1992).

Table1.2 Overview of wave propagation techniques utilized to assess the stiffness of soils adapted from Sawangsuriya (2012, p. 162) (continued)

Experimental approach	Testing description	References
Spectral Analysis of Surface Waves (SASW)	Spectral Analysis of Surface Waves (SASW) is a non-invasive geophysical method used to evaluate the stiffness profile of subsurface soils by analyzing surface wave propagation. The technique involves generating surface waves using a seismic source, such as a sledgehammer or mechanical shaker, and recording the resulting ground motion with an array of geophones or accelerometers placed at varying distances. The recorded signals are transformed from the time domain to the frequency domain using Fourier analysis, allowing the creation of dispersion curves that relate wave velocity to frequency. These curves are interpreted and inverted to develop a shear wave velocity profile, which provides detailed information about the stiffness, density, and stratification of subsurface layers	Nazarian & Stokoe, (1986); Addo & Robertson, (1992).
Modal Analysis of Surface Waves (MASW)	The MASW method makes it possible to isolate and identify the different Rayleigh wave modes contributing to the signals recorded in the field. It also makes it possible to define the dispersion curve for the fundamental mode and for the higher modes of Rayleigh waves. The MASW technique requires different equipment for its implementation, including an impact source, a trigger and 16 sensors to identify the different modes.	Lefebvre & Karray, (1998); Karray, (1999); Karray & Lefebvre, (2009).

1.7 Laboratory approach of V_s measurement

Laboratory methods play a vital role in quantifying anisotropy, with vertical and horizontal sampling techniques forming the foundation of these measurements. The process of obtaining and preparing samples for anisotropy testing is a critical step that directly impacts the quality and reliability of the results.

Vertical and horizontal sampling methods are designed to capture the inherent or stress-induced anisotropy present in clays due to their depositional history and particle arrangement. Vertical sampling involves extracting specimens along the direction perpendicular to the bedding plane or along the depositional direction, typically corresponding to the in-situ vertical orientation. This method provides insights into the clay properties as experienced by vertically propagating waves or loads in the field. Horizontal sampling, on the other hand, requires a more time-consuming procedure to obtain specimens oriented parallel to the bedding planes or perpendicular to the principal stress direction.

By comparing measurements from vertically and horizontally oriented specimens, researchers can quantify the degree of anisotropy and develop a more comprehensive understanding of the clay's behavior under various loading conditions. This approach is fundamental to several laboratory testing methods, including resonant column tests, bender element tests, triaxial and oedometer tests modified for anisotropy measurements. In the following, a summary of common dynamic laboratory testing for the purpose of stiffness anisotropy will be discussed.

1.7.1 Resonant Column Test

The Resonant Column (RC) test is a widely used laboratory technique for measuring the dynamic properties of soils, particularly G_{max} and soil damping ratio (D). This method has been standardized by ASTM D4015-21.

The basic principle of the RC test involves exciting a cylindrical soil specimen in its fundamental mode of vibration. The test typically uses a Stokoe-type fixed-free configuration,

where the bottom of the specimen is fixed, and the top is free to rotate (Drnevich, 1985). The apparatus consists of a drive system attached to the top of the specimen, which includes a set of electromagnetic coils and magnets that apply torsional or flexural excitation. An accelerometer mounted on the drive plate measures the response of the system (As shown in Figure 1.11).

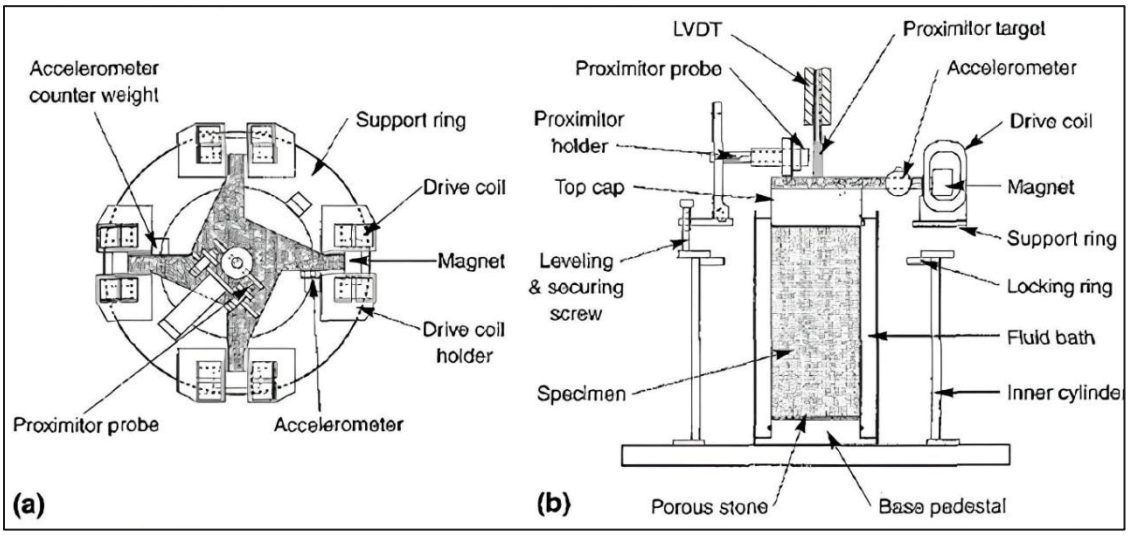

Figure 1.9 Typical resonant column test apparatus: (a) top view of loading system, and (b) profile view of loading system and soil specimen
Taken from Kramer (1996, p. 216)

To perform the test, the soil specimen is first consolidated to the desired effective stress state. Then, a series of sinusoidal torsional excitations at different frequencies are applied to the specimen. The frequency at which the measured acceleration amplitude reaches a maximum is identified as the resonant frequency (f_r) of the system (Cascante et al., 1998). Using this resonant frequency, the shear wave velocity (V_s) can be calculated using the following equation:

$$V_s = 2\pi f_r \frac{H}{\beta} \tag{1.5}$$

Where H is the height of the specimen, and β is a parameter that depends on the mass polar moment of inertia of the specimen and the drive system (Richart et al., 1970).

Once the shear wave velocity is determined, the shear modulus (G_{max}) can be calculated using Eq. (1.4).

The RC test allows for measurements over a range of shear strains, typically from about $10^{-4}\%$ to $10^{-1}\%$. This enables the investigation of the nonlinear stress-strain behavior of soils, including the degradation of shear modulus with increasing strain amplitude (Drnevich, 1985). One of the significant advantages of the RC test is its ability to measure anisotropy in soil stiffness. By testing specimens cut in different orientations (e.g., vertical and horizontal), researchers can assess the degree of anisotropy in the small-strain stiffness of the soil (Pennington et al., 1997). However, the RC test is not without limitations. The interpretation of results can be complicated by equipment-generated damping and inertial effects, especially at higher strains. Additionally, the test is limited in the maximum strain it can apply, which is typically lower than what many geotechnical structures experience in the field (Clayton, 2011).

1.7.2 Piezoelectric Transducer System

- **Bender elements**

Piezoelectric transducers have become an important tool for measuring soil stiffness at very small strains in geotechnical laboratory testing. These sensors allow for the measurement of shear wave velocities, which can be used to determine the G_{max} of soil samples. The use of these transducers, bender elements, in soil testing was first introduced by Shirley and Hampton in 1978. Dyvik and Madshus (1985) then applied this technique to saturated soils,

demonstrating good agreement between G_{max} values measured using bender elements and those obtained from resonant column tests.

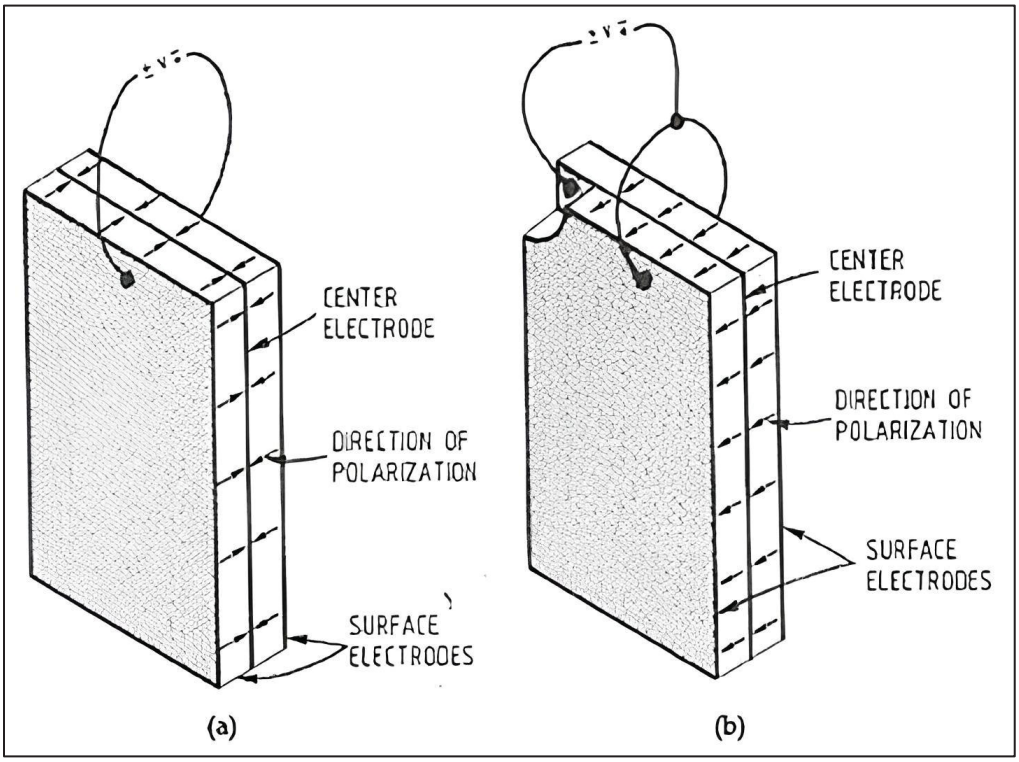

Figure 1.10 Two types of piezoceramic bender elements: (a) series connected and (b) parallel connected
Taken from Dyvik and Madshus (1985, p. 2 & 3)

Bender elements are small transducers that undergo deformation in response to the application of electrical pulse, and in turn, produce an electrical charge when deformed. They have the capability to both stimulate and measure shear and compression waves that travel short distances in soil samples. Bender elements can have varying dimensions, normally between the range of 8 to 15 mm in width and length. Bender elements consist of two piezoelectric ceramic elements that are adhered to a metal shim (Fig. 1.12). Bender elements are mounted on a support, such as the specimen end cap, with a portion extending into the soil to allow wave transmission. Applying voltage to the bender element results in one side lengthening and the other side shortening, which causes the element to bend. The bending of the element generates shear and compression waves. The detection of wave arrival is accomplished by

utilizing an additional bending element that is securely fastened to an alternate support structure.

Despite the widespread adoption of bender element testing for investigating soil anisotropy, several challenges and limitations have been identified in the literature. Lee and Santamarina (2005) conducted a detailed study on the effect of particle cementation on bender element measurements. They found that cementation could significantly affect wave propagation characteristics, potentially leading to misinterpretation of results if not properly accounted for. Clayton (2011) provided a comprehensive review of sources of error in bender element testing, including issues related to sample preparation, coupling between the bender elements and the soil, and near-field effects. He emphasized the importance of careful experimental techniques and interpretation to obtain reliable results.

A key advantage of the transducer technique is that it allows multiple measurements to be taken on the same sample under different stress conditions. This makes it particularly useful for investigating stress-dependence and anisotropy of soil stiffness. Conventional piezoelectric setups typically only allow measurement of vertically propagating, horizontally polarized shear waves ($V_s(vh)$). However, researchers have developed techniques to measure shear waves propagating and polarizing in different directions.

Pennington et al. (1997) developed a multi-directional bender element technique capable of measuring $V_s(vh)$, $V_s(hv)$, and $V_s(hh)$ on the same triaxial sample (Fig. 1.13). This allowed for a more complete characterization of the anisotropic stiffness of soils. The ability to measure shear wave velocities in multiple directions has been crucial in evaluating the stress-induced and inherent anisotropy of soils. Researchers have used these multi-directional measurements

to investigate how factors like void ratio, stress state, and stress history influence the anisotropic stiffness of different soil types.

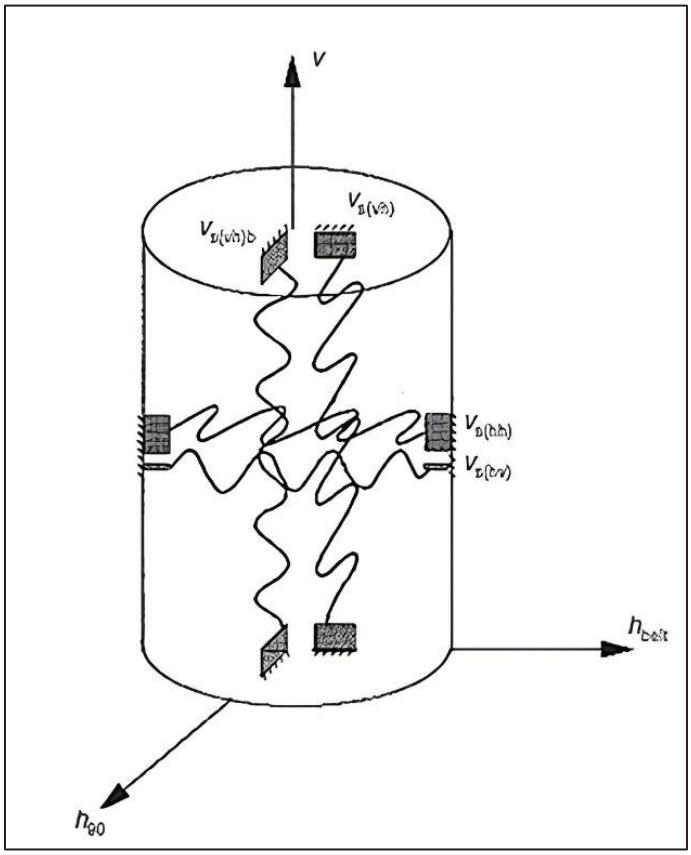

Figure 1.11 Bender elements employed for the purpose of anisotropic shear wave velocity measurements
Taken from Pennington et al. (1997, p. 399)

- **Piezoelectric ring actuator technique (P-RAT)**

The Piezoelectric Ring-Actuator Technique method is used to determine V_s in the experimental program of this research project. This method has been developed and improved over the past 18 years to minimize or eliminate difficulties associated with sample installation and interpretation of signals recorded by transducers (Gamal El Dean, 2007; Ethier, 2009; Karray et al. 2015; Mhenni et al. 2015; Elbeggo et al. 2019; Karray et al. 2019). This technique can be incorporated into most conventional geotechnical apparatuses and offers the advantage of testing various types of geomaterials (Karray et al. 2015).

The P-RAT uses a piezoelectric element in the form of a ring that deforms radially. The wiring and assembly of the piezoelectric rings are similar to those used in piezoelectric bimorphs. To make these piezoelectric rings waterproof before use, several layers of epoxy glue were applied. However, since the rings do not penetrate the soil, their use minimizes the reflection of emitted waves and improves received signals. Additionally, these rings are commercially available and adaptable for installation in conventional geotechnical apparatuses (Ethier, 2009).

The design of P-RAT sensors improves coupling with the tested sample and ensures axisymmetric stress distribution. However, Mhenni et al. (2015) and Karray et al. (2019) found that results can be affected by compression waves due to Poisson's ratio effects. To address this, these authors reduced the impact of compression waves by encapsulating the sensors in a stainless-steel cell, as shown in Figure 1.14. This encapsulation absorbs the longitudinal deformations of the piezoelectric ring and offers better stress distribution on the sample (Karray et al. 2019).

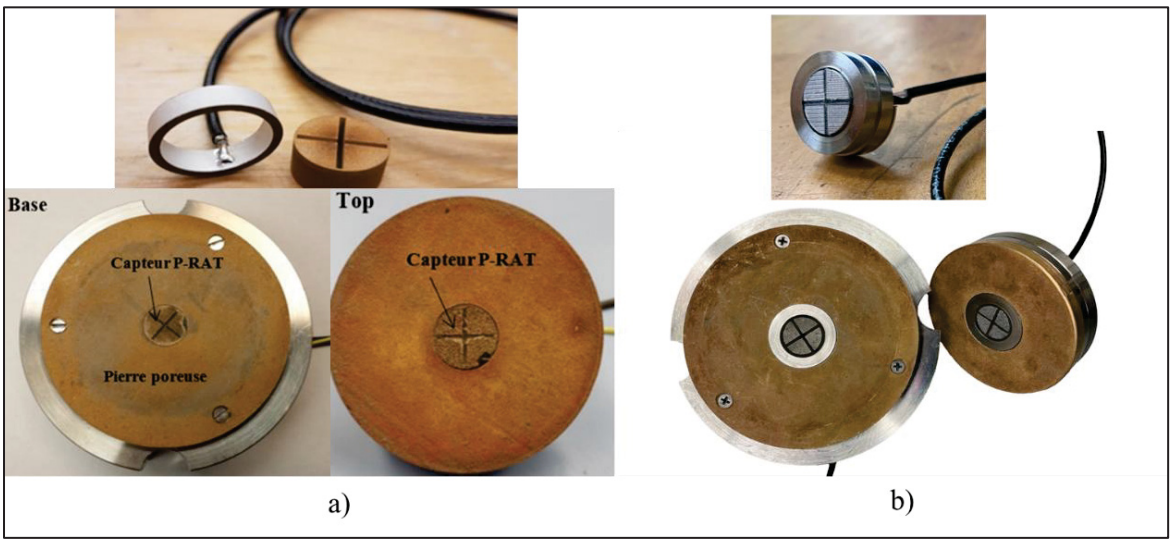

Figure 1.12 P-RAT at ETS soil mechanics laboratory,
a) Non-encapsulated P-RAT with porous stone
Taken from Elbeggo et al. (2023, p. 3);
b) Encapsulated P-RAT with alloy inner parts used in the current study

1.7.3 P-RAT interpretation method

The interpretation of signals produced with P-RAT is carried out in the frequency domain (FD) following an introduced procedure by Karray et al. (2015) and Hussien and Karray, (2021). This approach is preferred over time domain (TD) technique due to its ability to reduce subjectivity and provide more consistent results in V_s determination.

- **Fundamental assumptions**

The interpretation methodology is based on two key assumptions:

a) The shear wave velocity remains constant along the height of typical laboratory soil specimens.

b) V_s is a characteristic soil property that should not vary with frequency. While the measured phase velocity $V_{ph}(f)$ may vary with frequency, the actual V_s should remain constant.

- **Phase velocity calculation**

The initial phase velocity is calculated from the experimental phase function $\varphi_{exp}(f)$ obtained through cross-correlation between transmitted and received signals:

$$t_{ph}(f) = \frac{\varphi_{exp}(f)}{2\pi f} \tag{1.6}$$

where:

$t_{ph}(f)$ is the phase velocity travel time (s)

$\varphi_{exp}(f)$ is the experimental phase function (rad)

(f) is the frequency (Hz)

- **Phase shift decomposition**

The experimental phase function $\varphi_{exp}(f)$ can be decomposed into two components:

$$\varphi_{exp}(f) = \varphi_{th}(f) + \varphi_{corr}(f) \tag{1.7}$$

where:

$\varphi_{th}(f)$ is the theoretical phase shift corresponding to constant V_s

$\varphi_{corr}(f)$ is the correction function needed to account for system effects.

- **Travel time analysis**

The theoretical phase shift corresponds to a constant travel time (t):

$$t = \frac{\varphi_{th}(f)}{2\pi f} \tag{1.8}$$

This relationship can be extended to consider multiple frequencies (f_i, f_j):

$$\frac{\varphi_{exp}(f_i)}{2\pi f_i} = t + \frac{\varphi_{corr}(f_i)}{2\pi f_i} \tag{1.9}$$

$$\frac{\varphi_{exp}(f_j)}{2\pi f_j} = t + \frac{\varphi_{corr}(f_j)}{2\pi f_j} \tag{1.10}$$

- **Correction function determination**

By eliminating the travel time between equations, the correction function can be determined:

$$\varphi_{corr}(f_i) = \varphi_{exp}(f_i) - (\frac{f_i}{f_j})\cdot[\,\varphi_{exp}(f_j) - \varphi_{corr}(f_j)] \tag{1.11}$$

This equation shows that the entire correction function can be constructed if one reliable value $\varphi_{corr}(f_j)$ is known.

- **Experimental validation**

As demonstrated in Figure 1.15, face-to-face tests can be used to validate the correction function. It presents the normalized energy and phase delay curves obtained from face-to-face tests on three piezoelectric transducers, small ring 1, small ring 2, and the medium ring designed with different inner configurations and materials. These tests provide insight into the intrinsic mechanical behavior of the transducers and are used to construct the correction curve of the phase velocity $\varphi_{corr}(f_i)$.

For small ring 1 (Fig. 1.15A), which includes a partially cut steel inner disc, the energy curve reveals two resonant peaks at approximately 20 kHz and 36 kHz, corresponding to distortion and shear vibration modes, respectively, as confirmed by 3D numerical simulations (Mhenni et al. 2016). The local minimum between 27 and 32 kHz indicates antiresonance caused by interference between the two vibration modes. The shear mode exhibits a damping ratio of about 6%.

When the inner steel disc is fully cut (small ring 2, Fig. 1.15B), the response becomes smoother, with the antiresonance effect notably reduced and the amplitude response improved. The dominant shear mode occurs at 32 kHz with a damping ratio of 16%.

In contrast, the medium ring (Fig. 1.15C), equipped with a softer copper insert, behaves as a simple single-degree-of-freedom (SDOF) system with a single shear mode around 29 kHz and 9% damping. The softer material suppresses the distortion mode, leading to a clearer, more stable frequency response.

These tests reveal that:

a) The transducer system produces negligible phase delay (≈ 0) at frequencies below half the resonant frequency
b) Phase delay approaches 2π at frequencies higher than the resonant frequency

c) The experimental phase shifts align well with theoretical predictions for single degree of freedom (SDOF) systems

- **Application to soil testing**

a) The normalized energy spectrum is analyzed to identify the frequency range of reliable measurements.
b) The phase shift is calculated and compared with theoretical predictions.
c) The correction function is applied to obtain a constant phase velocity.

- **Result verification**

The interpretation method's reliability was verified by:

a) Checking that corrected phase velocities approach constant values near the system's resonant frequency.
b) Comparing results across different cell sizes and sensor configurations (Elbeggo et al. 2019; Hussien and Karray, 2021).
c) Normalizing velocities with respect to effective vertical stress [$V_{s1} = V_s(\frac{100}{\sigma_v'})^{0.25}$].

The methodology has proven robust across different soil types, sensor configurations, and testing conditions, as evidenced by the consistent results obtained for both granular and fine soil samples.

The successful implementation of this methodology requires careful consideration of: Sample characteristics; Sensor configuration; Input signal selection; System resonant frequency; Phase shift characteristics. Through this process, the P-RAT interpretation method provides a reliable and objective means of determining shear wave velocity in laboratory soil testing.

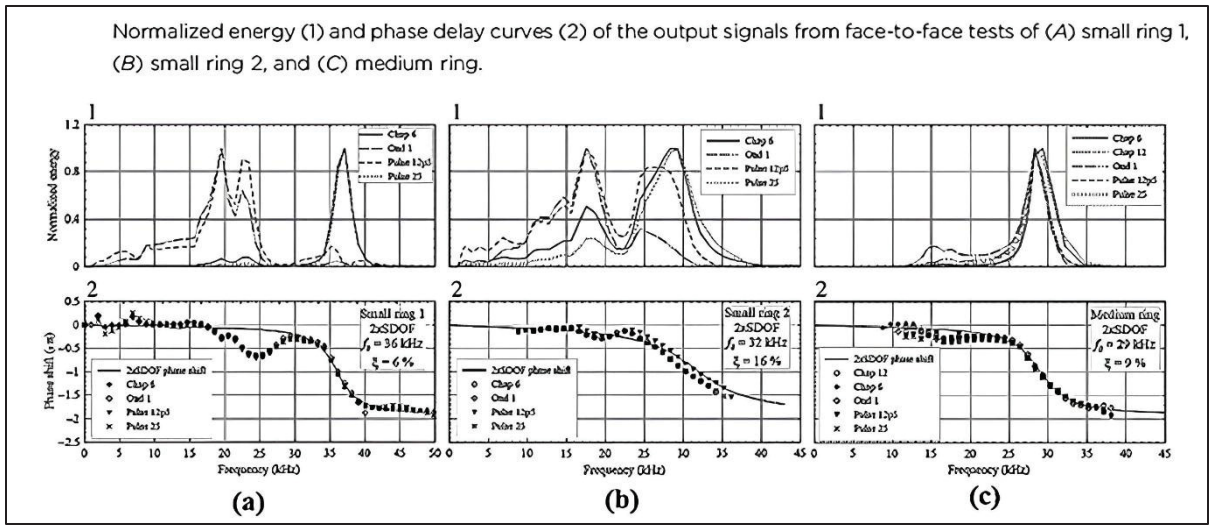

Figure 1.13 Face-to-face test of P-RAT in different laboratory conditions
Taken from Hussien and Karray (2021, p. 211)

1.8 Summary

The measurement of maximum shear modulus (G_{max}) is fundamental to anisotropy investigation. The G_{max} (low strain level, 0.001%) is directly related to shear wave velocity through the equation, $G_{max} = \rho V_s^2$. This relationship provides a non-destructive means of evaluating soil stiffness by measuring wave propagation.

Different laboratory methods have been developed for measuring V_s, including resonant column tests, bender element techniques, and the more recent, P-RAT. The method offers reported advantages over former approaches by minimizing sample disturbance, providing more uniform wave generation, and producing high quality signals.

The frequency domain interpretation method used with P-RAT provides a more objective approach to determining V_s compared to time domain techniques, resulting in more consistent and reliable measurements across different soil types and testing conditions.

1.9 Anisotropy

Anisotropy refers to the variation of a material's properties in different directions. In soil mechanics, two types are recognized. Inherent anisotropy arises naturally from the soil's structure and fabric due to its stress history and sedimentation, independent of external stresses; it can be assessed under isotropic stress conditions (Jovicic and Coop, 1998; Yimsiri and Soga, 2011). Induced anisotropy develops when shearing alters particle alignment, creating a directional microstructure. Consequently, soils respond anisotropically to directional stress changes. Studies show that V_s and G_{max} are influenced only by stress components in the wave propagation plane, not by perpendicular components (Roesler, 1979; Wang and Mok, 2008).

1.9.1 Transverse isotropy (Cross-anisotropy)

Independence of soil parameters from the direction is defined by the term "isotropy." There are two fundamental parameters, E and ϑ, that describe an isotropic elastic soil. These are necessary for establishing the stiffness matrix and defining the elastic behavior of the soil.

An anisotropic soil, which exhibits different mechanical properties in different directions, is characterized by its elastic stiffness matrix, also known as the stiffness tensor. This matrix is a key component in describing the soil's response to stress and strain. For an anisotropic soil, the stiffness matrix is a 6x6 symmetric matrix, which means it has 21 independent components due to symmetry. By simplifying assumption in constitutive modeling, the bedding layers consider the soil structure system cross anisotropic. In other words, the soil medium is considered to be isotropic in horizontal planes and anisotropic in vertical planes, for this reason it is also known as transverse isotropy. As shown in Fig 1.16, transverse isotropy or cross-anisotropy occurs in soils whose properties are identical in all directions within a particular plane, but different in the direction perpendicular to this plane. This behavior is very common in soils that have been deposited vertically and subjected to uniform horizontal stresses, resulting in a vertical axis of symmetry. Typically, the plane of isotropy is horizontal.

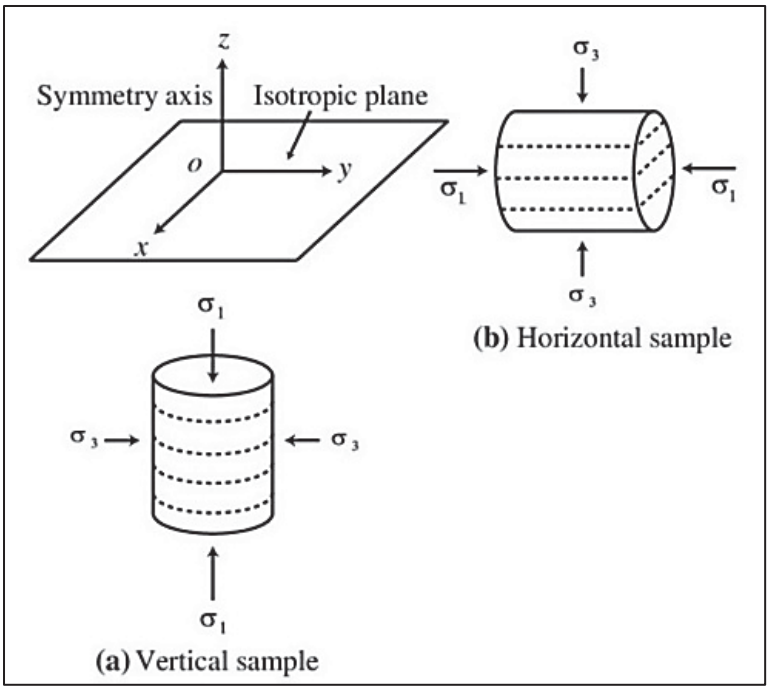

Figure 1.14 Schematic representation of cross-anisotropic soil fabric due to the bedding layers
Taken from Kong et al. (2013, p. 670)

1.9.2 Cross-anisotropy constitutive model

The cross-anisotropy assumption comprises five distinct elastic parameters that are independent of each other. The compliance matrix presented by Crampin (1981) demonstrates these parameters. Equation (1.12) describes the relationship between strain and stress for a material, including soil, that has a single vertical axis of symmetry. The stress increments and strain increments are measured using rectangular Cartesian axes, with the z-axis representing the vertical direction. This allows for differentiation between horizontal directions but indicates that the material properties are identical in both horizontal directions.

$$\begin{bmatrix}\varepsilon_{xx}\\ \varepsilon_{yy}\\ \varepsilon_{zz}\\ \gamma_{yz}\\ \gamma_{zx}\\ \gamma_{xy}\end{bmatrix}=\begin{bmatrix}\begin{bmatrix}\frac{1}{E_h} & \frac{-\vartheta_{hh}}{E_h} & \frac{-\vartheta_{vh}}{E_v}\\ \frac{-\vartheta_{hh}}{E_h} & \frac{1}{E_h} & \frac{-\vartheta_{vh}}{E_v}\\ \frac{-\vartheta_{hv}}{E_h} & \frac{-\vartheta_{hv}}{E_h} & \frac{1}{E_v}\end{bmatrix} & 0 & \\ & \frac{1}{G_{hv}} & \\ 0 & & \frac{1}{G_{vh}} \\ & & \frac{1}{G_{hh}}\end{bmatrix}\begin{bmatrix}\sigma_{xx}\\ \sigma_{yy}\\ \sigma_{zz}\\ \tau_{yz}\\ \tau_{zx}\\ \tau_{xy}\end{bmatrix} \tag{1.12}$$

The components of the stiffness matrix are related to the material's elastic constants as follows:

E_v: Young's modulus in the vertical direction.

E_h: Young's modulus in the horizontal plane.

ϑ_{vh}: Poisson's ratio for horizontal strain from vertical stress.

ϑ_{hh}: Poisson's ratio for horizontal strain from horizontal stress.

ϑ_{hv}: Poisson's ratio for vertical strain from horizontal stress.

G_{vh}: Shear modulus in the vertical plane.

G_{hh}: Shear modulus in the horizontal plane.

- **Symmetrical requirements for the stiffness matrix**

1. Plane of Isotropy: In transversely isotropic materials, there is a plane (often the x-y plane) where properties are identical in all directions. The z-axis is perpendicular to this plane and has different properties. All seven parameters are not considered independent. Because the horizontal plane is a plane of isotropy, the term G_{hh} is a dependent parameter related to E_h and ϑ_{hh} as shown below:

$$G_{hh}=\frac{E_{hh}}{2(1+\vartheta_{hh})} \tag{1.13}$$

2. Symmetry in the x-y Plane: Due to the isotropy within the x-y plane, the stiffness matrix components related to this plane must reflect the same properties in both x and y directions.

$$\frac{\vartheta_{vh}}{E_{vh}} = \frac{\vartheta_{hv}}{E_{hv}} \tag{1.14}$$

3. Shear Coupling: The shear moduli in the planes that include the z-axis should be equal due to the material's rotational symmetry around the z-axis.

$$G_{vh} = G_{hv} \tag{1.15}$$

The elastic stiffness matrix for a transversely isotropic soil captures the directional dependencies of the soil properties, reducing the complexity of analysis by leveraging symmetry. By expressing the matrix components in terms of Young's moduli, Poisson's ratios, and shear moduli, the stiffness matrix facilitates accurate modeling and prediction of the mechanical behavior of anisotropic layered structures material such as clays.

The anisotropy degree describes the ratios of the shear modulus terms as follows:

$$I_\alpha = \frac{G_{hh}}{G_{vh}} \tag{1.16}$$

$I_\alpha > 1$	Soil particles are stiffer horizontally than vertically.
$I_\alpha < 1$	Soil particles are stiffer vertically than horizontally.

The degree of anisotropy in soils quantifies the extent to which its properties vary with direction. For transversely isotropic soils, this involves comparing the mechanical properties in the isotropic plane (x-y plane) with those in the perpendicular direction (z-axis). The factor I_α may be used as a rational measure of soil anisotropy degree.

1.9.3 Anisotropic stiffness correlations

The maximum shear modulus of soils is dependent on different factors. In addition to the inherent characteristics of the clay fabric including mineralogy and particle shape, the

condition and deformation history of the soil, as determined by factors like the over-consolidation ratio (*OCR*), void ratio (*e*), and effective stress (p'), has been shown to significantly affect the stiffness of soils.

Table 1.3 Influential parameters in G_{max} determination

Parameter	**Dependency**	**Typical value**	**Reference**
S	Fabric or microstructure of soil	Regression analysis for individual test results	-
k	Plasticity index (PI)	Vary from 0 to 0.5 (For PI< 40, k = 0 PI >40, k = 0.5)	Hardin and Black (1968), Hardin and Drnevich (1972)
$f(e)$	Properties of packing and density	Variable	-
n	Contact between particles and strain amplitude	Approximately 0.5 at very small strains	Hardin and Richart (1963), Hardin and Black (1968), Seed and Idriss (1970), Hardin and Drnevich (1972)

In order to provide a more accurate description of effective parameters, several formats of empirical correlations are suggested as follows:

For isotropic formations, the relationship is expressed as:

$$G = Sf(e)G(OCR)h(\sigma') \tag{1.17}$$

The equations and parameters have been validated through extensive research by multiple investigators, including Hardin and Richart (1963), Hardin and Black (1968), Seed and Idriss (1970), and Hardin and Drnevich (1972).

These correlations provide a practical framework for estimating G_{max} when direct measurements are not available or as a verification tool for experimental results.

Table 1.4 Proposed material constants and void ratio functions in G_{max} correlations
Taken from Sawangsuriya (2012, p. 178)

Soil type	S	$f(e)$	n	Reference
Round-grained Ottawa sand	6900	$\frac{(2.17-e)^2}{1+e}$	0.5	Hardin and Black (1968)
Angular-grained crushed quartz	3270	$\frac{(2.97-e)^2}{1+e}$		
Clean sand	41600	$\frac{0.67-e}{1+e}$	0.5	Shibata and Soelarno (1975)
Clean sand	9000	$\frac{(2.17-e)^2}{1+e}$	0.4	Iwasaki et al. (1978)
Toyoura sand	8400	$\frac{(2.17-e)^2}{1+e}$	0.5	Kokusho (1980)
Clean sand	7000	$\frac{(2.17-e)^2}{1+e}$	0.5	Yu and Richart (1984)
Ticino sand	7100	$\frac{(2.27-e)^2}{1+e}$	0.4	Lo Presti et al. (1993)
Clean sand	9300	$e^{-1.3}$	0.5	Lo Presti et al. (1997)
Reconstituted NC Kaolinite (PI = 20) and undisturbed NC clays	3270	$\frac{(2.97-e)^2}{1+e}$	0.5	Hardin and Black (1968)
Reconstituted NC Kaolinite (PI = 35)	4500	$\frac{(2.97-e)^2}{1+e}$	0.5	Marcuson and Wahls (1972)
Remolded clay (PI = 0 ~ 50)	2000 ~ 4000	$\frac{(2.97-e)^2}{1+e}$	0.5	Zen et al. (1978)
Undisturbed NC clay (PI = 40~85)	90	$\frac{(7.32-e)^2}{1+e}$	0.6	Kokusho et al. (1982)
Clay deposits (PI = 20 ~150)	5000	$e^{-1.5}$	0.5	Shibuya and Tanaka (1996)
Remolded clay (PI = 20 ~ 60)	24000	$(1+e)^{-2.4}$	0.5	Shibuya et al. (1997)
Undisturbed clay (PI = 20 ~ 40)	-	$e^{-1.3}$	0.5	Jamiolkowski et al. (1995)

For anisotropic formations, relationships become more complex, accounting for directional dependencies:
The general form:

$$G_{ij} = S_{ij} f(e) OCR^k P_a^{1-n_i-n_j} \sigma_i^{'n_i} \sigma_j^{'nj} \tag{1.18}$$

Structure parameter (S_{ij}): A dimensionless parameter representing the soil's fabric or microstructure, including particle arrangement and orientation.

For vertical-horizontal behavior:

$$G_{vh} = S_{vh} f(e) OCR^k P_a^{1-n_v-n_h} \sigma_v^{'n_v} \sigma_h^{'nh} \tag{1.19}$$

For horizontal-horizontal behavior:

$$G_{hh} = S_{hh} f(e) OCR^k P_a^{1-2n_h} \sigma_h^{'nh} \sigma_h^{'nh} \tag{1.20}$$

According to table 1.3 and 1.4, these parameters combine empirical equations to provide a comprehensive framework for estimating G_{max}. The variations in parameter values across different soil types and conditions reflect the complex nature of soil behavior and the importance of considering site-specific characteristics when applying these correlations.

The empirical correlations demonstrate that soil stiffness is not only dependent on current state (void ratio and effective stress) but also on soil type, structure, and stress history (*OCR*).

1.9.4 Anisotropy literature review

The determination of soil anisotropy through shear wave measurements has become increasingly important in geotechnical engineering, as it provides good insights into the directional dependency of soil stiffness. Laboratory studies have consistently demonstrated

that natural clays exhibit significant stiffness anisotropy, particularly at small strains. This anisotropy is characterized by different elastic properties in vertical and horizontal directions, with most soils showing higher stiffness in the horizontal direction compared to the vertical direction.

The following literature review presents key findings from several studies that have contributed to our understanding of anisotropy in glacial and marine clays.

Pennington et al. (1997) involved using horizontally mounted bender elements in the triaxial cell to propagate shear waves with both vertical and horizontal polarization. This configuration allowed measurement of G_{hh} and G_{hv} in addition to the conventional determination of G_{vh}. Tests were conducted on both intact and reconstituted specimens under different confining stresses.

Figure 1.17 presents one of the most important findings of the study, showing the variation of normalized G_{max} with p' for both intact and reconstituted samples. The graph demonstrates the anisotropic nature of Gault Clay, with G_{hh} consistently higher than G_{vh}. The degree of anisotropy, expressed as G_{hh}/G_{vh}, ranged from 1.5-2.5 for intact samples and was close to 1 for reconstituted samples. This highlights the importance of soil fabric in determining stiffness anisotropy, a finding that aligns with other studies on natural clays. Lings et al. (2000) later confirmed these findings, and they estimated a ratio of G_{hh}/G_{vh} equal to 2.25 under anisotropic stresses.

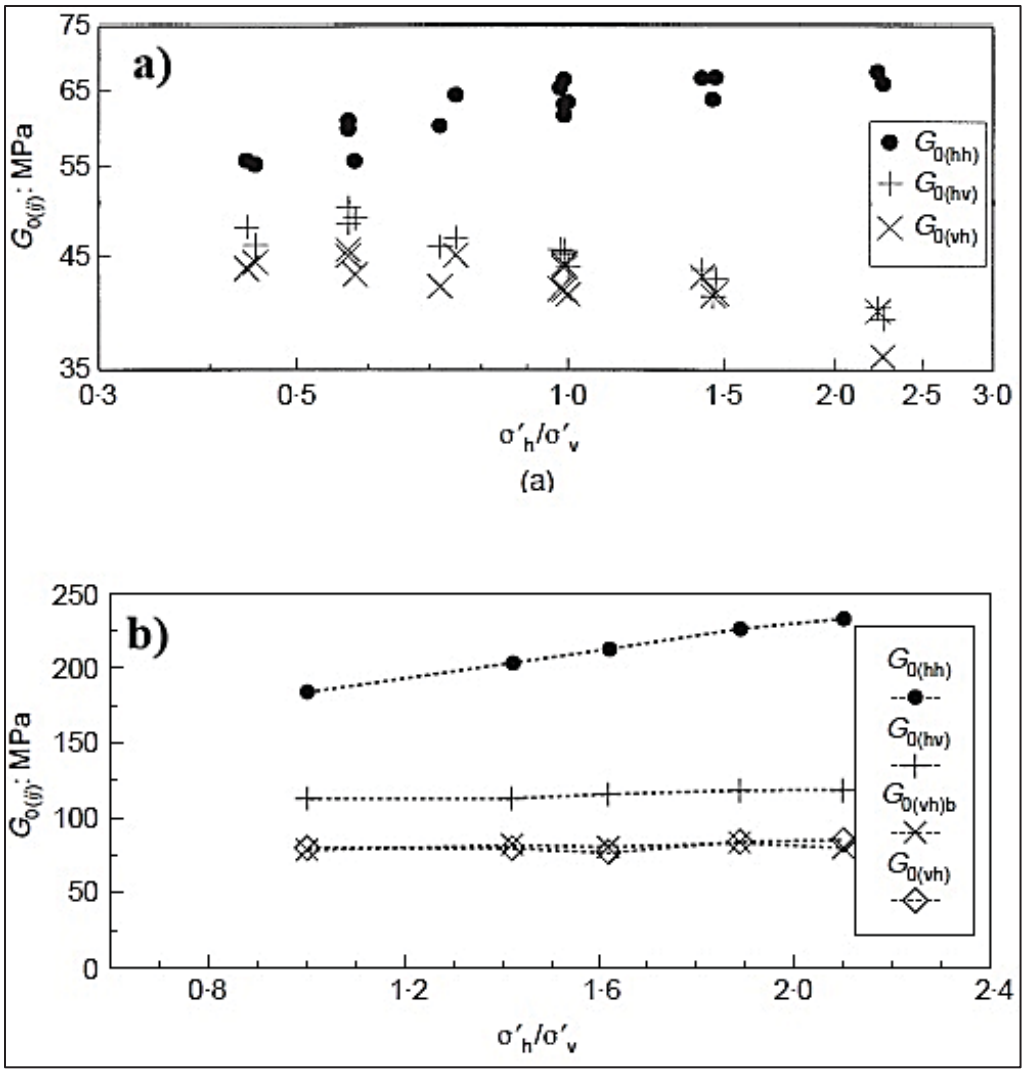

Figure 1.15 $G_{max(ij)}$ against stress ratio for anisotropically consolidated a) reconstituted specimen b) intact specimen
Taken from Pennington et al. (1997, p. 396)

More recent research, Yimsiri and Soga (2011) conducted an experimental study on the cross-anisotropic elastic parameters of two heavily overconsolidated clays: London Clay and Gault Clay through an identical laboratory setup reported by Nakagawa et al. (1996). The methodology involved conducting isotropically consolidated drained compression tests and shear wave velocity measurements on both vertically and horizontally cut specimens, providing a thorough investigation of the inherent anisotropic characteristics of the clays. As illustrated in Figure 1.18, which depicts the relationships between G_{vh} and G_{hh} and p' for both

London Clay and Gault Clay. The data is fitted using the empirical equation proposed by Hardin and Black (1968), allowing for a clear visualization of the anisotropic behavior. This figure demonstrates that both clays exhibit higher stiffness in the horizontal direction compared to the vertical direction, a characteristic typical of sedimentary clays due to their depositional history and stress state (Atkinson, 1975). The results show that Gault Clay exhibits a higher degree of anisotropy under isotropic stress conditions compared to London Clay, with higher ratios of E_h/E_v and G_{hh}/G_{vh}. This difference is attributed to the larger overconsolidation ratio of Gault Clay.

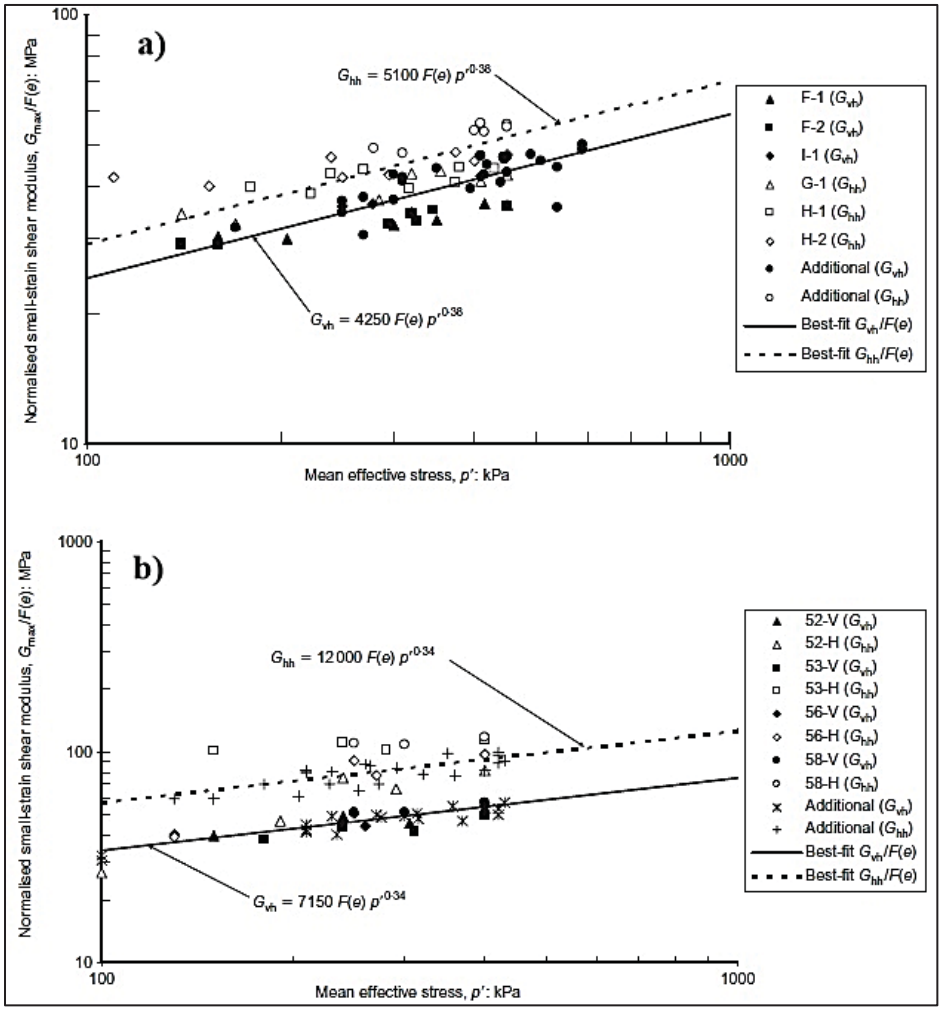

Figure 1.16 Relationship between G_{max} and mean effective stress:
a) London Clay; b) Gault Clay
Taken from Yimsiri and Soga (2011, p. 811)

Figure 1.19 provides a comparison of the normalized shear modulus with void-ratio function through published experimental results from different laboratory investigation attempts on London and Gault clays including Viggiani and Atkinson (1995), Pennington et al. (1997), Jovicic and Coop (1998) and Gasparre et al. (2007a). This comparison highlights the consistency of the current study's results with previous findings, particularly for London Clay, where the data aligns with that reported by Jovicic and Coop (1998). However, some discrepancies are noted, such as the lower values reported by Gasparre et al. (2007a), which are attributed to differences in the lithological units tested. This can underscore the importance of considering site-specific variations in characterization of the soil behavior.

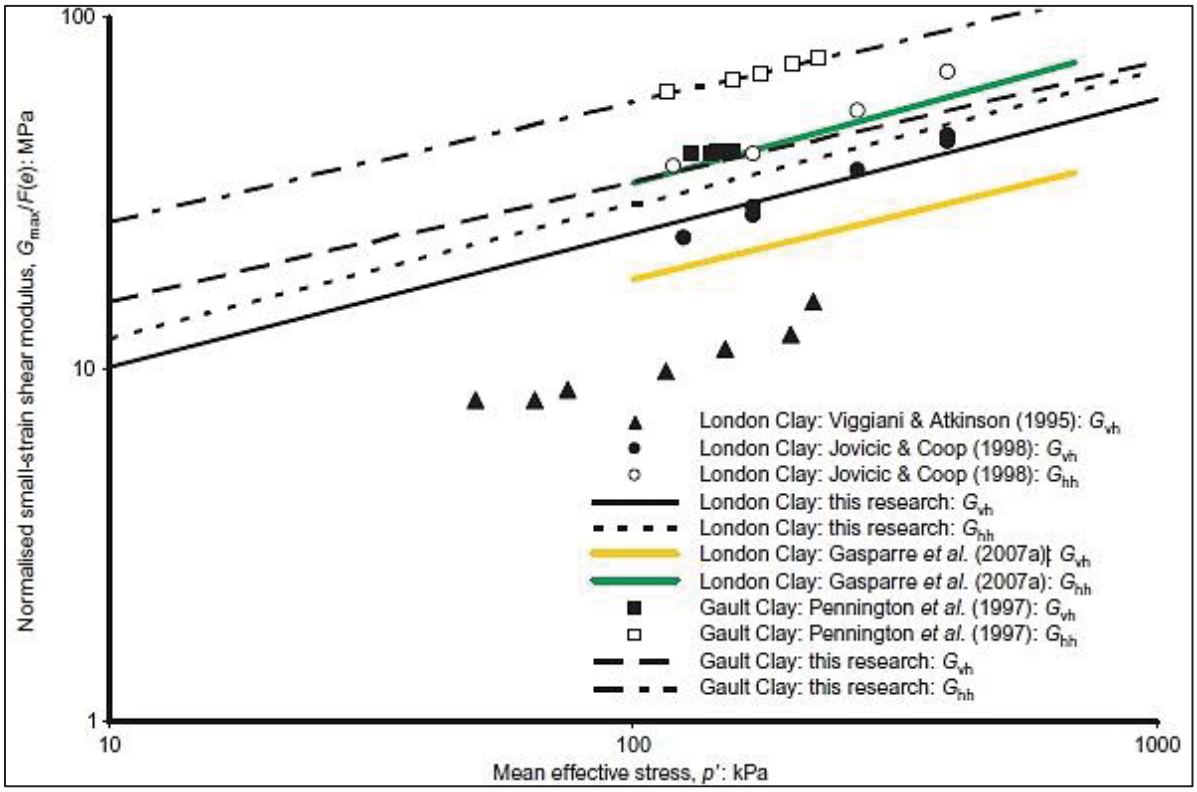

Figure 1.17 Comparison of G_{hh} and G_{vh} of published experimental results related to London and Gault clays
Taken from Yimsiri and Soga (2011, p. 812)

On the other side, Jamiolkowski et al. (1995) examined the anisotropy of G_{max} in six different Italian clay samples with low *OCR* ranges. These clay soils possess low to medium-high

plasticity and were deposited during different geological periods (ranging from Holocene to Pliocene) and under various sedimentation mechanisms (such as lacustrine, marine, estuarine, and alluvial). The measurement of G_{max} was conducted using both the RC and oedometer apparatuses, which were equipped with both vertical and horizontal bender BE. The observed anisotropy, represented by the G_{hh}/G_{vh} ratio, resulted from the combined influence of fabric and stress-induced anisotropy, which ranged from 1.4 to 1.5 for the six clays.

Study conducted by Cho and Finno (2010) and Kim and Finno (2012) explores the anisotropic behavior of compressible Chicago glacial clays. Both studies rely on laboratory measurements of anisotropic behavior of natural glacial clays and its evolution during different loading paths. Their findings underscore the importance of considering stress-induced anisotropy and recent stress history when predicting soil behavior, especially for applications involving small-strain deformations including excavations or tunneling.

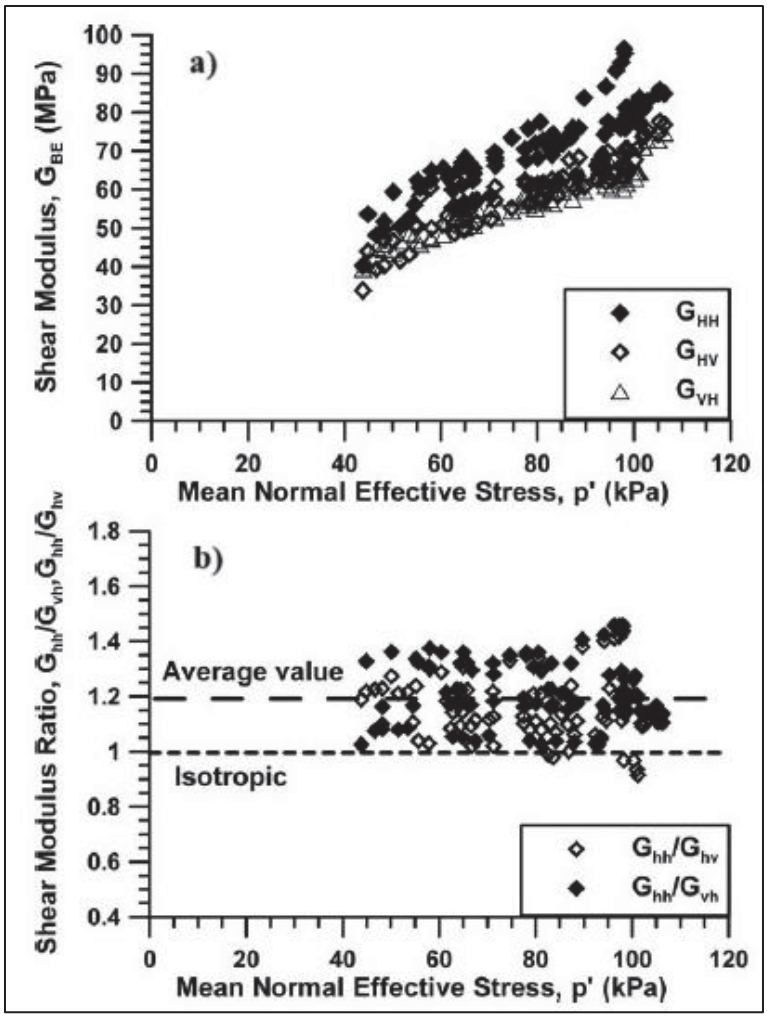

Figure 1.20 Obtained directional shear modulus by means of BE tests during K_0 reconsolidation, a) G_{hh}; G_{hv}; G_{vh}, b) stiffness ratio
Taken from Cho and Finno (2010, p. 182)

According to Cho and Finno (2010), the results indicated that the Chicago glacial clays exhibit a relatively low degree of initial anisotropy. The G_{hh}/G_{vh} ratio varied from 1 to 1.4, with an average of 1.18 and a standard deviation of 0.03. This value is close to the lower bound of reported values for lightly overconsolidated clays, which typically range from 1.2 to 1.7. The similarity between G_{hh}/G_{hv} and G_{hh}/G_{vh} further supports the conclusion that these clays are slightly cross-anisotropic in terms of their dynamically measured moduli. As shown in Figure 1.20a, it is found that $G_{hh} \geq G_{hv} \geq G_{vh}$ throughout the K_0 reconsolidation process. This pattern is consistent with the expected behavior of cross-anisotropic clays that have experienced one-

dimensional deposition. To quantify the degree of anisotropy, the modulus ratios G_{hh}/G_{vh} and G_{hh}/G_{hv} are employed as shown in Figure 1.20b.

A key aspect of the study by Kim and Finno (2012), was the characterization of initial anisotropy using bender element tests during K_c recompression to in-situ stresses. The results, presented in Figure 1.21, demonstrate that the Chicago glacial clay exhibits cross-anisotropic behavior, with G_{hh}/G_{vh} ratios of 1.2 and 1.1 for shallow and deep samples, respectively. These values are at the lower end of the range typically reported for normally consolidated and lightly overconsolidated clays, which are consistent with the geological history of the deposits. Additionally, in-situ SCPT were used to validate the shear wave velocities obtained from BE tests in both studies.

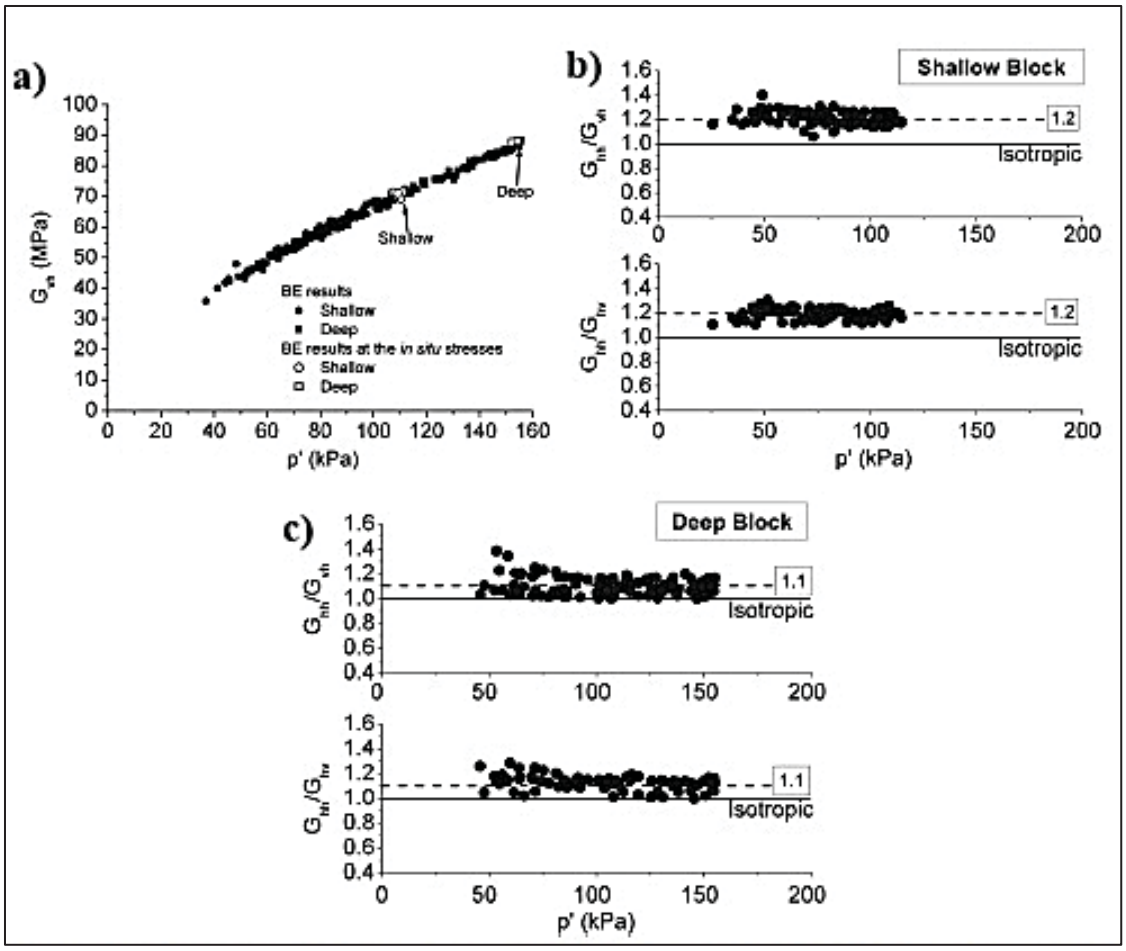

Figure 1.18 Results of BE tests: a) G_{vh} versus mean effective stress during consolidation testing; b) anisotropy ratio for shallow block samples; c) anisotropy ratio for deep block samples
Taken from Kim and Finno (2012, p. 160)

Research on soil anisotropy has been predominantly conducted on glacial and marine clays with a pronounced deficiency of investigations focusing on Eastern Canadian clays. This geographic disparity in anisotropy studies creates a significant knowledge gap regarding the directional variations in dynamic properties of Champlain clays beside physical, hydraulic, and mechanical properties.

The practical implications of soil anisotropy in geotechnical engineering have become increasingly recognized, particularly in the analysis and prediction of ground movements. Multiple studies have demonstrated that incorporating anisotropy in numerical analyses can

significantly impact calculated deformations and improve prediction accuracy. For instance, in the context of tunneling, Simpson et al. (1996) found that including shear modulus anisotropy in the analysis of the Heathrow Express trial tunnel produced settlement trough predictions that matched field observations much better than isotropic models. Their study showed that cross-anisotropic models with G_{hh}/G_{vh} ratios of 1.66 to 2.0 generated settlement profiles significantly closer to measured values compared to isotropic analyses (As shown in Fig 1.22).

1. Line A: Results from highly non-linear but isotropic BRICK model.
2. Line B: Results from linear elastic and orthotropic model with $G_{vh} = 0.6\ G_{hh}$ ($G_{hh}/G_{vh} \approx 1.67$).
3. Line C: Results from BRICK model with anisotropy where $G_{vh} = 0.5\ G_{hh}$ ($G_{hh}/G_{vh} = 2$)

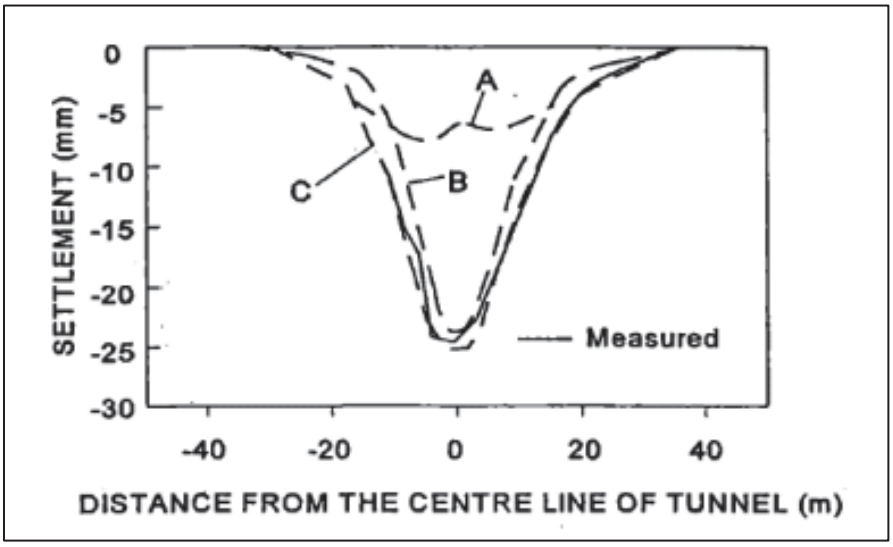

Figure 1.19 Computed settlement troughs for trial tunnel in London clays
Taken from Simpson et al. (1996, p. 594)

The assumption of soil isotropy in engineering analyses can lead to substantial errors in displacement predictions. Rowe and Booker (1981) demonstrated that ignoring anisotropy could result in settlement overestimates of up to 45% or underestimates of up to 16%.

1. For soils with $E_h/E_v = 0.5$ (horizontal modulus less than vertical modulus), neglecting anisotropy led to underestimates of settlement by 13-16%.

2. For soils with $E_h/E_v = 2$ (horizontal modulus greater than vertical modulus), neglecting anisotropy led to overestimates of settlement by 30-45%. The maximum overestimate occurred for deep crusts resting on relatively homogeneous soil.
3. For typical soil profiles with crusts (where horizontal modules are greater than vertical in crust but less than vertical below crust), neglect of anisotropy could lead to errors up to 33 (i.e., overestimates).

This finding has been corroborated by other researchers, Hooper (1975) showed that cross-anisotropy could reduce predicted total settlements by about 40% under undrained conditions and differential settlements by 5-20% under drained conditions. Similarly, Gazetas (1981a) and Gazetas (1982) suggested that highly anisotropic soils may experience settlements up to 50% smaller than those computed using classical isotropic theories.

More recent research has highlighted the importance of properly characterizing and modeling soil anisotropy in geotechnical applications. Modern numerical analyses incorporating anisotropy along with non-linear elasticity have shown improved capabilities in predicting ground response to construction activities. Wongsaroj et al. (2011) demonstrated that anisotropic 3D models could better capture not only surface settlements but also horizontal movements and pore pressure responses around tunnels. However, researchers emphasize that successful implementation requires appropriate constitutive models that account for non-linearity, path-dependent stiffness, and anisotropic behavior with different responses in perpendicular directions (Masin and Herle, 2005).

1.10 Discussion

The literature review demonstrates that significant advances have been made in understanding clay anisotropy, particularly in glacial deposits of different origins where anisotropy ratios typically range from 1.1 to 2.5. However, a knowledge gap remains for Eastern Canadian clays, as Champlain marine deposits, which have received comparatively limited investigation. This is despite their recognized influence on geotechnical hazards, highlighting the need for a better understanding of their directional behavior.

Reported anisotropy investigations frequently employ triaxial apparatus with bender elements or resonant column devices. While these methods have proven valuable, practical challenges remain in both implementation and interpretation. A key limitation in oedometer-based studies has been the inability to directly measure lateral stresses during K_0 consolidation, conventionally constraining anisotropy characterization within this simpler, more accessible framework.

The application of high-precision strain gauges mounted on an oedometer ring addresses this fundamental limitation by enabling indirect but reasonable lateral stress determination. This approach transforms the conventional oedometer into a capable apparatus for stress-state characterization during 1D-consolidation, extending its functionality while preserving the fundamental advantages of simplicity and widespread equipment availability.

For directional stiffness measurements, advances in piezoelectric transducer systems offer promising solutions. The P-RAT represents a significant methodological improvement through its unique interpretation approach in the frequency domain. Its high accuracy and reliability allow the evaluation of anisotropy in soils, providing consistent and precise measurements of directional shear wave velocity under laboratory conditions.

Early qualitative observations by Quigley and Thompson (1966) and Delage and Lefebvre (1984) demonstrated that particle orientation in these clays evolves during consolidation,

transitioning from random card house arrangements to increasingly parallel configurations under increasing stress. Advanced digital imaging techniques, particularly scanning electron microscopy with automated image processing, now offer opportunities for fabric quantification beyond qualitative description.

Studies demonstrate that neglecting anisotropy can produce prediction errors in design and calculations of different geotechnical problems. For Champlain clays, the absence of adequate anisotropy database represents a gap affecting design reliability for infrastructure projects throughout Eastern Canada.

CHAPTER 2

RESEARCH OBJECTIVES AND CONTRIBUTION

2.1 Overview and motivation

Champlain clays developed their inherent anisotropic characteristics during marine deposition, where the settling process established a preferential orientation of clay particles. This structural arrangement results in directional variations in engineering properties, including strength, hydraulic conductivity, and consolidation behavior.

Despite these well-documented characteristics, existing literature has predominantly characterized these soils using isotropic frameworks. Laboratory testing methods routinely assume uniform response regardless of loading direction and bedding orientation, particularly evident in shear wave velocity measurements and dynamic property assessments. While this approach simplifies testing procedures, it fundamentally overlooks the directional dependencies that govern actual field performance.

This research investigates the stiffness anisotropy of intact Champlain clay by integrating macroscale testing and analysis in different orientations with a complementary microscale fabric study. To achieve these objectives, the research was divided into three parts, each forming the subject of a scientific article (Table 2.1) presented in chapters 4, 5, and 6 of this thesis.

2.2 Objective

Anisotropy characterization was categorized into macro and micro-scale investigation in tested clay specimens.

Macro-scale investigation employs a modified oedometer apparatus incorporating fabricated P-RAT to measure shear wave velocity across different orientations. This innovation enables reliable measurement especially for two principal cross-anisotropic V_s under K_0 consolidation stress conditions:

- Vertically propagated-horizontally polarized waves [$V_{s(vh)}$]
- Horizontally propagated-horizontally polarized waves [$V_{s(hh)}$]
- Angularly propagated-horizontally polarized waves [$V_{s(\theta h)}$]

Micro-Scale Investigation utilized SEM imaging techniques and image processing to characterize the morphological properties of both intact and consolidated clay samples. This approach provides detailed visualization of:

- Pore matrix configurations
- Particle associations in intact samples
- Structural rearrangements following consolidation

2.2.1 Laboratory setup for directional V_s

The primary objective of chapter 4 is to develop and validate a comprehensive experimental methodology for simultaneously measuring the coefficient of lateral earth pressure at rest (K_o) and shear wave velocity during one-dimensional consolidation of Champlain marine clay. This integrated approach employs a modified oedometer cell equipped with P-RAT sensors and high-precision strain gauges to capture both dynamic and static soil responses. The study aims to establish empirical correlations between K_o, V_s, and consolidation stress, providing fundamental data on stress-dependent behavior that will serve as the foundation for subsequent anisotropy investigations.

2.2.2 SEM imaging and clay particles arrangement

Recognizing the critical role of SEM imaging in the microstructural analysis conducted in Chapter 4, this chapter aims to develop a standardized methodology for quantifying soil fabric anisotropy from SEM images. The primary objective is to investigate how SEM imaging parameters specifically accelerating voltage and magnification influence calculated anisotropy indices using distinct fabric orientation calculation methods. Through parametric studies and the utilization of an imaging technique that analyzes multiple random areas, this study seeks

to establish best practices for achieving reliable and reproducible anisotropy measurements from SEM analysis, thereby enhancing the accuracy of microstructural characterization methods of anisotropy degree determination.

2.2.3 Bedding orientation effect on anisotropy degree

Chapter 6 aims to extend the understanding of Champlain clay anisotropy by investigating the influence of bedding layer orientation on mechanical properties at intermediate angles beyond the principal directions examined in Chapter 4. The objective is to characterize how shear wave velocity and consolidation behavior vary as specimens are trimmed at angles of 0°, 30°, 45°, 60°, and 90° relative to the horizontal bedding plane. By combining the P-RAT measurement techniques from Chapter 3 with the validated SEM analysis methods from Chapter 5, this study seeks to develop the directional-dependent behavior, comparing Champlain clay's anisotropic response with other clay types to understand how stress history and overconsolidation ratio influence the development of fabric anisotropy across different geological settings.

Table 2.1 Scientific publication in geotechnical journals and proceedings

Paper	Title	Journal	Status
I	Use of Shear Wave Velocity to assess Champlain Marine Clay Fabric Anisotropy.	Canadian Geotechnical journal https://doi.org/10.1139/cgj-2024-0163	Accepted & published
II	Influence of SEM Imaging Parameters on Clay Fabric Anisotropy	Journal of Testing and Evaluation (ASTM)	Submitted (18-Feb-2025)
III	Bedding layer inclination effects on Champlain clay anisotropy	Journal of Geotechnical and Geoenvironmental Engineering (ASCE)	Submitted (08-Sep-2025)
IV	Laboratory Measurement Approach for Anisotropy in Champlain Clays	GeoManitoba 2025 (78th Annual CGS Conference and 9th Canadian Permafrost Conference)	Accepted (09-Jul-2025)

2.3 Contribution of this study

In this study, a multi-aspect laboratory approach was employed to investigate the anisotropic behavior of Champlain clays using a conventional oedometer device (Chapter 4).
The stress response and inherent anisotropy of the soils were experimentally studied through a laboratory testing setup (Chapter 4). Empirical correlations were then proposed for the anisotropic shear wave velocity and maximum shear modulus of the tested Champlain clays (Chapters 4 and 6).

A threshold analysis was conducted based on four hundred images captured from the intact and consolidated surfaces of the clay samples (Chapter 5), alongside the development of an experimental protocol for SEM imaging designed to minimize digital imaging errors in the assessment of the anisotropy index (Chapter 5). Image processing techniques were applied to quantify the microscopic anisotropy index of the clay particle arrangements, based on fabric orientation calculation methods (Chapters 5 and 6). The effectiveness of the proposed methodology was experimentally validated through case studies and comparison with previous experimental works (Chapters 5 and 6). Finally, the shear wave velocity and maximum shear modulus were determined in multiple directions ($\theta = 0, 30, 45, 60$, and $90°$), taking into account the characteristics of the bedding layers (Chapter 6).

This work introduces a cost-effective method for evaluating stiffness anisotropy by adapting standard laboratory equipment. The findings demonstrate that directionality influences the mechanical and deformation characteristics of Champlain marine clays, highlighting the need to account for bedding orientation during testing and interpretation. By emphasizing orientation as a key parameter in testing either laboratory or field, this work promotes more accurate and site-specific soil characterization, ultimately leading to design reliability and performance prediction in anisotropic clay deposits.

CHAPTER 3

VERTICAL MEASUREMENT OF V_s

This chapter examines the relationship between shear wave velocity, stress history, and void ratio in Champlain clay samples under one-dimensional consolidation conditions. The investigation focuses on vertical-horizontal (vh) plane measurements to develop empirical correlations for these sensitive clay deposits. Clay samples were cylindrical with dimensions of 100 mm in height and 67 mm in diameter were subjected to 1D-consolidation testing.

Table 3.1 indicates variations in the geotechnical properties of tested Champlain clay specimens from Quebec region. The natural water content (ω_n) ranges from 47% to 73%, while plasticity index (I_p) values vary between 20 and 43, indicating moderate to high plasticity. Liquid limits (*LL*) span from 41 to 63, and plastic limits (*PL*) from 20 to 24. Clay content (CC) percentages range from 60% to 75%, with preconsolidation pressures (σ_p') between 85 kPa and 265 kPa. According to the Unified Soil Classification System, the samples are classified as either CL (low plasticity clay) or CH (high plasticity clay), with most samples falling into the CH category.

Table 3.1 Clay samples characteristics

Specimen	**ω_n(%)**	***I_p***	***LL***	***PL***	***CC* (%)**	**σ_p' (kPa)**	**Classification**	**Depth (m)**
4098	47	20	41	20	60	150	CL	12.33-12.43
3062	59	32	56	24	69	165	CH	18.08-18.18
4098#2	56	28	49	21	63	145	CL	12.13-12.23
3024	73	40	61	21	75	145	CH	10.30-10.40
Tm-1#5	61	32	54	23	75	265	CH	1.90-2.00
3143	73	43	63	22	70	85	CH	5.37-5.47

The tests were conducted with effective vertical stresses reaching up to 600 kPa. For the isotropic measurements of shear wave velocity ($V_{s(vh)}$) in the vertical-horizontal plane, piezoelectric sensors, P-RAT, were employed. P-RAT sensors utilized in these testing, were not encapsulated due to the relatively low levels of applied stress.

Shear wave velocity measurements by means of non-encapsulated P-RAT provided reliable measurements in the small-strain domain. The consolidation curves and corresponding shear wave velocity relationships are illustrated in Figures 3.1, 3.2, and 3.3. These figures demonstrate the classical S-shaped compression curves in the void ratio-effective vertical stress ($e - \sigma'_v$) plots and the progressive increase in shear wave velocity with increasing effective stress. A notable feature in all samples is the distinct change in slope at the preconsolidation pressure, reflecting the transition from overconsolidated to normally consolidated states.

The measured V_s values obtained at each loading stage were utilized to calculate the normalized shear wave velocity (V_{s1}) according to Equation (3.1). Subsequently, Equation (3.2) establishes a relationship between normalized V_s and soil characteristics, expressed as a function of void ratio *f(e)* and overconsolidation ratio (*OCR*). The function *f(e)* follows an exponential form with constants A and B, as shown in Equation (3.3), while the exponent K represents the power of *OCR* in the relationship.

$$V_{s1} = V_S \left[\frac{P_a = 100\ Kpa}{\sigma'_v}\right]^{0,25} \tag{3.1}$$

$$V_{s1} = F(e).OCR^k \tag{3.2}$$

$$f\ (e) = Ae^{-B} \tag{3.3}$$

These three constants (*A, B*, and *K*) were determined through Linear Regression Multiple Variables analysis to develop a correlation model specific to Champlain clays. To facilitate this regression analysis, the relationship (Eq. 3.2) was transformed into logarithmic form, as expressed in Equation (3.4):

$$ln\, V_{s1} = ln\, A + B(ln\, e) + K\ (ln\, OCR) \tag{3.4}$$

As presented in Table 3.2, the exponent K varies between 0.181 and 0.243 across the different samples, with the complete empirical correlations provided therein.

Table 3.2 Empirical Correlations of V_s for different utilized samples

Sample N°	**K**	**A**	**B**	**R^2**	$\boldsymbol{V_{s1} = Ae^{-B}OCR^{K}}$
4098	0,186	118,72	0,403	0,982	$118{,}72e^{-0{,}403}OCR^{0{,}186}$
3062	0,181	118,15	0,377	0,998	$118{,}15e^{-0{,}377}OCR^{0{,}181}$
3143	0,205	119,26	0,476	0,943	$119{,}26e^{-0{,}476}OCR^{0{,}205}$
3024	0,190	118,71	0,338	0,836	$118{,}71e^{-0{,}338}OCR^{0{,}190}$
4098#2	0,243	107,77	0,106	0,996	$107{,}77e^{-0{,}106}OCR^{0{,}243}$
Tm-1#5	0,226	107,27	0,104	0,989	$107{,}27e^{-0{,}104}OCR^{0{,}226}$

Graphs of $e - \sigma_v'$ may not be clear in determination of σ_p' point. In all measurements, the breaking point of preconsolidation pressure seems to be adequately clear in $V_s - \sigma_v'$ graphs due to the steep slope of the curve. The maximum value of $V_{s(vh)}$ varies between the domain of 155 to 175 m/s. Notably, sensor-soil contact issues prior to reaching σ_p' created P-wave interference, affecting the clarity of initial $V_s - \sigma_v'$ relationships. This technical limitation explains why some of the $V_s - \sigma_v'$ curves appear less defined in the low-stress region.

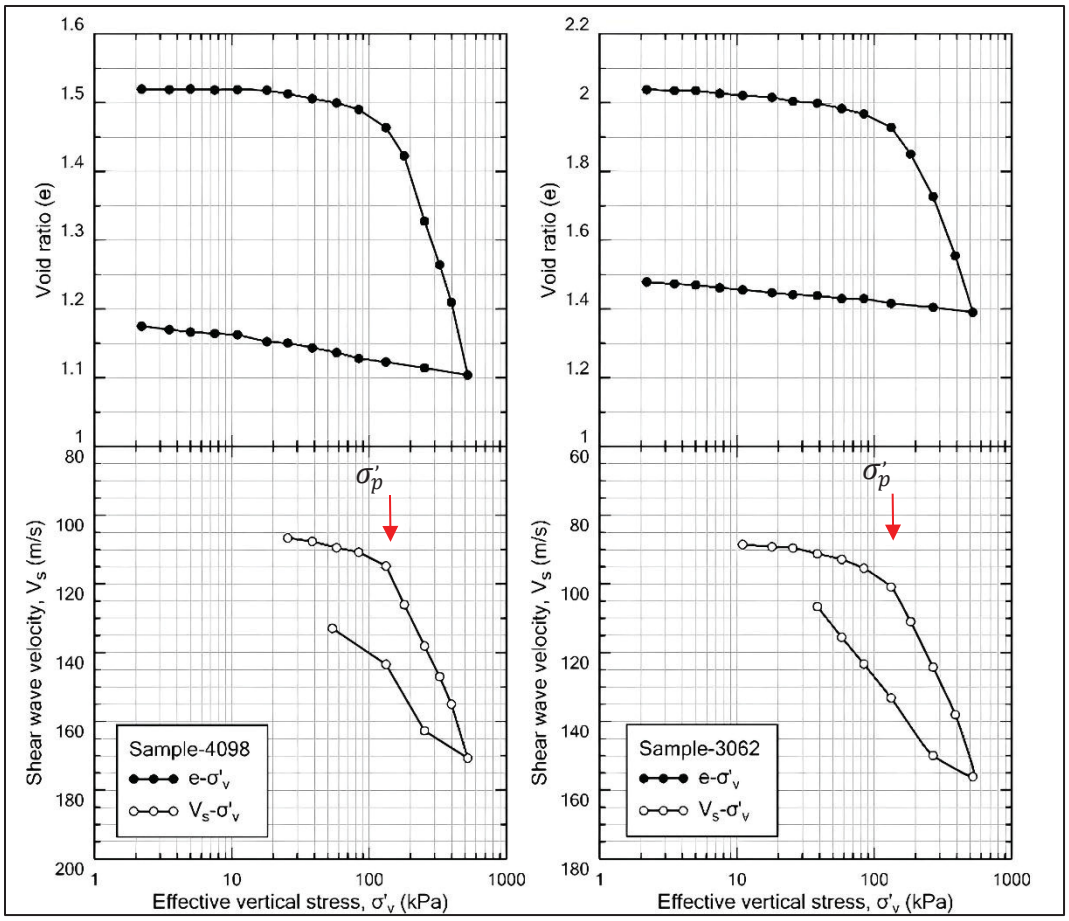

Figure 3.1 V_s-consolidation curves of tested clay specimens with $\sigma'_p \approx 150 - 165$ kPa

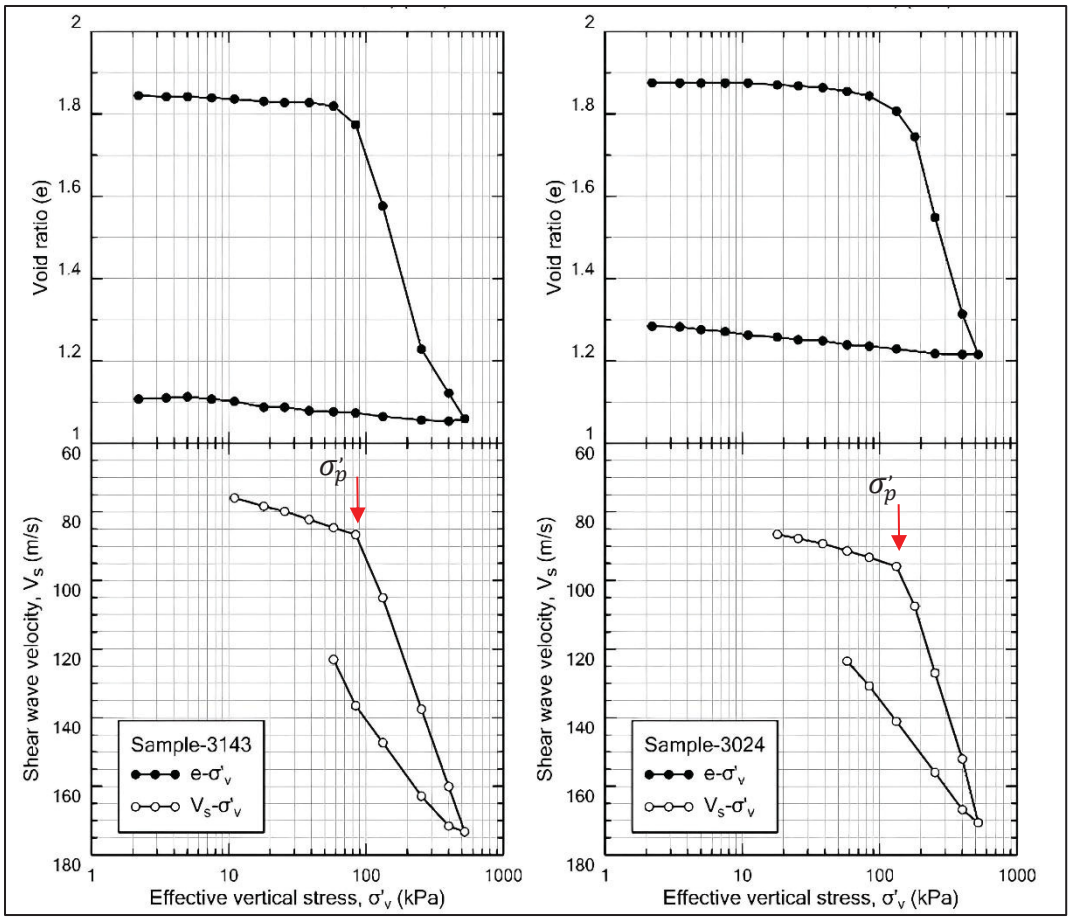

Figure 3.2 V_s-consolidation curves of tested clay specimens with $\sigma'_p \approx 85 - 145$ kPa

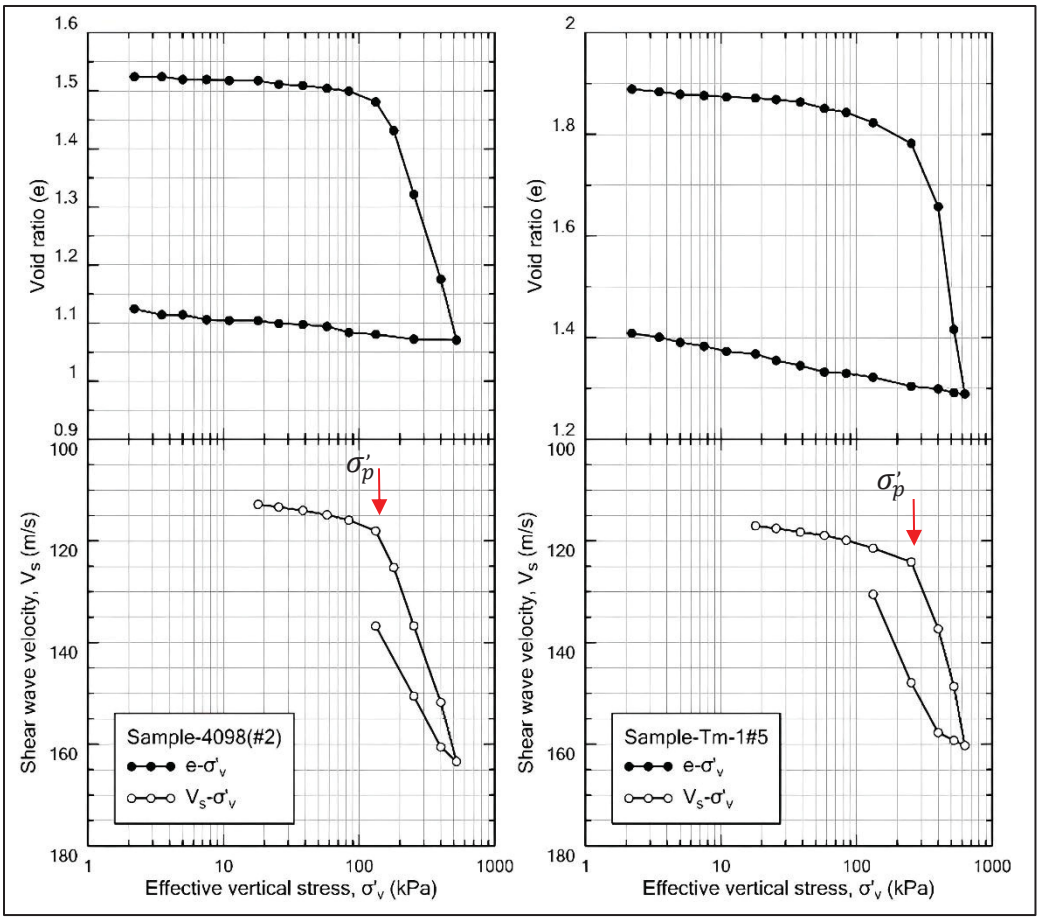

Figure 3.3 V_s-consolidation curves of tested clay specimens with $\sigma_p' \approx 145 - 265$ kPa

The empirical correlations developed in this chapter assume isotropic conditions specific to the vertical-horizontal plane. This simplification provides a practical approach for estimating shear wave velocities in Champlain clays based on conventional geotechnical parameters. However, it is important to recognize that natural clay deposits often exhibit anisotropic behavior due to their depositional history and stress conditions. Subsequent chapters will expand this analysis to address anisotropic behavior, providing a more comprehensive characterization of directional shear wave velocity dependencies in Champlain clays of Beauharnois site under higher stress levels.

CHAPTER 4

USE OF SHEAR WAVE VELOCITY TO ASSESS CHAMPLAIN MARINE CLAY FABRIC ANISOTROPY

A. Torabipour [a], Y. Ethier [b], M. Karray [c],

[a, b] Department of Construction Engineering, École de technologie supérieure,
1100 Notre-Dame West, Montreal, Québec, Canada H3C 1K3
[c] Department of Civil Engineering and Building Engineering, Université de Sherbrooke,
Sherbrooke, Québec, Canada

Paper published in *Canadian Geotechnical Journal*, January 2025

Abstract

This paper investigates the anisotropic characteristics of Champlain marine clay soil using a combination of laboratory techniques. A modified oedometer cell with a piezoelectric ring actuator technique was used to measure shear wave velocity during consolidation stages. The axisymmetric design of the oedometer allowed for the determination of shear wave velocity in both the vertical and horizontal planes. The preliminary findings reveal that the sensitive marine clay is inherently anisotropic, with lower preconsolidation pressure for horizontally consolidated specimens and faster propagation of shear waves in the plane parallel to the bedding layer. High-precision strain gauges integrated into the consolidation ring were used to evaluate horizontal stress during the one-dimensional consolidation test. The ability to determine mean effective stress enables the normalization of shear wave velocities using this stress, providing more coherent empirical correlations in terms of shear wave velocity. Scanning electron microscopy was used to examine the microstructure of clay specimens, providing qualitative and quantitative insight into the restructuring and reorientation of clay platelets under consolidation stress. The consistency of the results through both micro and macro-scale analyses confirms the reliability of the experimental approach, highlighting its potential for future studies on the anisotropy of Champlain marine clay fabrics.

Keywords

Champlain marine clay; Shear wave velocity; Strain gauge; Anisotropy; One-Dimensional Consolidation; Scanning Electron Microscopy.

4.1 Introduction

Anisotropy is a fundamental characteristic of clay materials, resulting from their distinct mineralogical compositions and particle structures. This property leads to various mechanical responses depending on the direction of measurement or external load. Clay anisotropy originates from the depositional processes and the geological history of clay materials. Factors such as gravitational forces, particle shape, colloidal properties, and water flow dynamics cause clay particles to align in specific orientations during sedimentation. The soil fabric alignment results in the development of a low to high preferred orientation, consequently inducing anisotropic behavior (Douglass and Voight, 1969; Mitchell, 1972). This characteristic encompasses two types: stress-induced (external constraint anisotropy), which is caused by the principal stress states, and inherent (soil structure anisotropy), which is caused by the morphology of the soil particles resulting from their genesis (Clayton, 2011).

Various laboratory techniques exist to assess the anisotropy feature of soils, especially for clays. The anisotropy of clays has been quantified reportedly through several laboratory approaches, including electrical conductivity measurements (Anandarajah and Kuganenthira, 1995; Bryson and Bathe, 2009), thermal conductivity measurements (Mitchell and Kao, 1978; Dao et al., 2014; Lu et al., 2020), dielectric dispersion (Arulanandan, 1991) and shear wave measurements (Roesler, 1979; Jamiolkowski et al., 1995; Pennington et al., 1997; Jovičić and Coop, 1998; Teachavorasinskun and Lukkanaprasit, 2008; Nishimura, 2014; Zapata-Medina et al. 2020). Numerous anisotropy studies have been conducted using transducer systems like Bender Elements (BE) in triaxial devices (Roesler, 1979; Pennington et al., 1997; Jovičić and Coop, 1998; Teachavorasinskun and Lukkanaprasit, 2008; Ng and Yung, 2008; Clayton, 2011; Nishimura, 2014), and modified oedometers (Jamiolkowski et al., 1995; Teachavorasinskun and Lukkanaprasit, 2008; Lee et al., 2008; Kang et al., 2014).

Directional measurement of shear wave velocity (V_s) by an instrumented oedometer shows the combined effects of inherent and stress-induced anisotropy on samples. The oedometer apparatus intrinsically imposes an anisotropic stress state, namely at-rest (K_0) stress condition

(Lefebvre and Philibert, 1979; Silvestri and Morgavi, 1982). The parameter K_0, defined as the ratio of horizontal to vertical stress ($\frac{\sigma'_h}{\sigma'_v}$), has been estimated through in-situ tests such as self-boring pressuremeter (Hamouche et al., 1995b), hydraulic fracturing (Lefebvre et al., 1991; Hamouche et al., 1995), total pressure cell and pressuremeter testing (Tavenas et al., 1975), and dilatometer testing (Hamouche et al., 1995). However, the impact of field instrument disturbance on the soil stress state is noticeable (Mesri and Hayat, 1993). The oedometer setup demonstrates specific limitations in directly assessing σ'_h as the other principal stress component. Previous laboratory works (including Lee et al., 2008; Kang et al., 2014) show the effect of the two involved principal stresses on anisotropic wave propagation and particle polarization planes.

Large oedometer apparatuses were used to provide the possibility of measurements of V_s in horizontal path through mounted horizontal BEs (Teachavorasinskun and Lukkanaprasit, 2008; Lee et al., 2008; Kang et al., 2014). The utilization of a large oedometer ring remarks the importance of side-wall friction effect on the distribution of lateral stress within the soil specimen, potentially leading to non-uniform stress states and complicating the interpretation of V_s measurements. Roesler (1979) primarily proposed a methodology used by Jamiolkowski et al. (1995) in the oedometer with cubic clay specimen for determining the V_s relative to their bedding planes by orienting the specimen along the principal stress directions. By considering trimmed specimens in both the normal and parallel directions to the bedding planes, a conventional oedometer ring can also be used to examine anisotropic behavior. This approach allows the assessment of anisotropy influences on V_s measurements relative to the bedding plane throughout the consolidation process. The axisymmetric condition of 1D-consolidation assumes that the vertical-horizontal (vh) and horizontal-vertical (hv) planes have identical properties, including permeability, compressibility, and stiffness. Therefore, the anisotropy in 1D-consolidation is cross-anisotropy, which refers to the variation or difference in soil characteristics between vh and hh planes (Jovičić and Coop, 1998; Atkinson, 2000).

The literature on the anisotropic characteristics of Champlain marine clay mainly focused on using other laboratory methods, including hydraulic conductivity testing (Leroueil et al., 1990;

Benabdallah, 2006), triaxial testing (measurement of strength characteristics) (Yong and Silvestri, 1979; Silvestri and Morgavi, 1982), and visual investigation of gradual realignments of the soil fabric by electron microscopy (Delage and Lefebvre, 1984). A series of anisotropic hydraulic conductivity laboratory testing were conducted on different sensitive marine clays from several regions by Leroueil et al., (1990) and Benabdallah, (2006). Normally consolidated Champlain marine clays exhibit a ratio of less than 1.2 between their vertical and horizontal hydraulic conductivities (Leroueil et al., 1990). Benabdallah (2006) confirmed weak anisotropy of Lachenaie clays (as Champlain marine clay) that exhibits the similar trend of vertical and horizontal permeabilities with no significant distinction in oedometer test.

The triaxial testing demonstrated that the sensitive marine clay exhibits also this anisotropic behavior in its stress-strain response and strength properties. The elastic moduli and undrained shear strength are directionally dependent, with the vertical direction being higher than the horizontal one due to the presence of horizontal laminations and cemented bonds in the clay fabric (Yong and Silvestri, 1979).

In addition to macroscopic properties measurements, which provide insight into the soil response system, a microscopic assessment is also required for the evaluation of the soil structure. Advancements in imaging techniques have revolutionized the study of geomaterials, revealing details and providing a deeper understanding of their properties and behavior. Employing imaging techniques such as scanning electron microscopy (SEM), transmission electron microscopy (TEM), and X-ray diffraction allowed studying materials at various scales, ranging from micron to nano levels (Moore and Reynolds, 1989; Kang et al. 2003).

Among these imaging techniques, SEM has gained widespread adoption in academia, research, and industry due to its ability to deliver high-resolution imaging, compositional information, and efficient material analysis. Its ease of use and straightforward image interpretation further contribute to its popularity across diverse fields (Ul-Hamid, 2018). However, the analysis of clay microstructure presents several challenges arising from factors such as small particle size and strong water bonding. Conventionally, mercury intrusion porosimetry (Delage and

Lefebvre, 1984) has been employed to investigate Champlain clay microstructure, although other techniques, including x-ray diffraction, have been suggested as well (Klug, 1974; Yong and Silvestri, 1979; Moore, 1989). Nevertheless, SEM remains a prevalent method for examining clay microstructure (Delage et al., 1982; Hicher et al., 2000; Delage, 2010; Romero, 2013, Locat et al. 2025). SEM enables the investigation of soil microstructure characteristics at various magnifications, ultimately leading to a more comprehensive understanding of the complex interplay between clay microstructure and its mechanical behavior under different stress conditions (Delage et al., 1982; Hicher et al., 2000; Delage, 2010; Chow and Wang, 2019).

This research investigates the mechanisms behind the anisotropic responses of a sensitive marine clay, including particle reorientation, fabric changes, and stress-strain behavior, by following a multi-faceted laboratory methodology. The study specifically assesses Champlain marine clay fabric anisotropy during 1D-consolidation testing by considering horizontal and vertical trimming path clay samples. Two different techniques were employed to characterize clay specimens and examine their anisotropic behavior under K_0 stress conditions. The study relied on a modified oedometer cell that enables simultaneous measurement of V_s and continuous monitoring of K_0 during a conventional oedometer test. The experimental methodology includes the use of P-RAT (Ethier, 2009; Karray et al., 2015; Elbeggo et al., 2019; Hussien and Karray, 2020) for V_s measurements as covered in more details in following section. At the same time, high-precision strain gauges implemented on the consolidation ring were used to estimate the K_0 coefficient. Additionally, SEM imaging was utilized to capture the microstructure condition and particle arrangement, providing a detailed view of clay platelet conditions pre- and post-1D-consolidation testing.

V_s measurements and SEM imaging process allowed the clay anisotropy mechanism in macro and micro scales, respectively. The similarity in clay fabric association and small difference between measured anisotropic V_s in both planes emphasize the low anisotropy feature of this site. The findings are outlined in different forms including consolidation curves, consolidation-V_s, rose diagram of particle intensity distribution and anisotropic empirical correlations. The

proposed correlations show the efficiency of mean effective stress (σ'_m) allowing for more accurate V_s estimations by considering the effect of both σ'_v and σ'_h stress components in the plane of propagation and polarization.

4.2 Experimental program

The experimental approach followed in this study involved performing two tests on each specimen: i) a conventional oedometer test conducted using a modified oedometer cell that integrated two P-RAT sensors, enabling the measurement of V_s at each loading stage. Simultaneously, four strain gauges are incorporated onto the consolidation ring to monitor the horizontal pressure during the 1D-consolidation test, and ii) two SEM tests were performed on each sample before (intact fraction) and after (consolidated fracture) the oedometer test. These SEM tests allowed for a qualitative and quantitative assessment of the directionality of particle arrangement. Fig. 4.1 illustrates the configuration of the modified oedometer cell setup with the clay specimen used in this study.

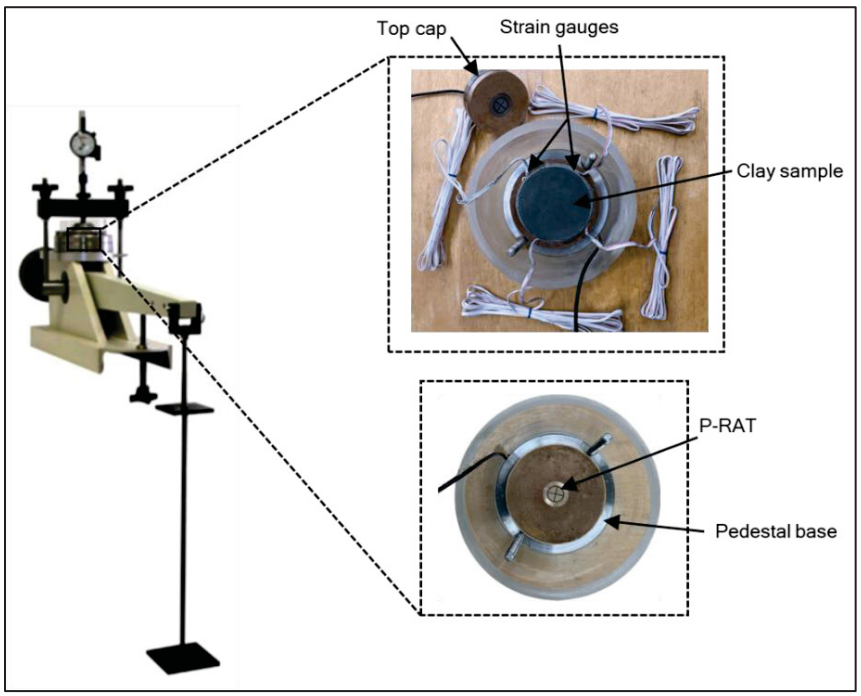

Figure 4.1 Modified oedometer equipped with P-RAT and strain gauges

for measuring shear wave velocity and lateral strain, respectively

4.2.1 Clay soil information

Consolidation tests were conducted on specimens obtained from a large block sample of Champlain marine clays. This soil originates from marine deposits formed gradually, almost 12,000 years before present, during the glacial era. This sensitive marine clay is predominantly found in eastern Canada, particularly in Québec province. The undisturbed block sample of the clay was extracted using the Laval University clay sampler (La Rochelle et al., 1981). This sampling technique enables the examination of the clay in its natural state and the analysis of its undisturbed properties (Elbeggo et al., 2023). The 22 × 15 cm (diameter × height) intact block sample was collected from the Saint-Étienne-de-Beauharnois region of Quebec at a 6.8 to 7 m depth. Eight consolidation tests were performed on prepared clay specimens, considering both normal alignments and the 90-degree rotation of the cutting (Fig. 4.2). The specimen size for the conventional 1D-consolidation test is 63.5 × 19 mm in accordance with ASTM D2435-11.

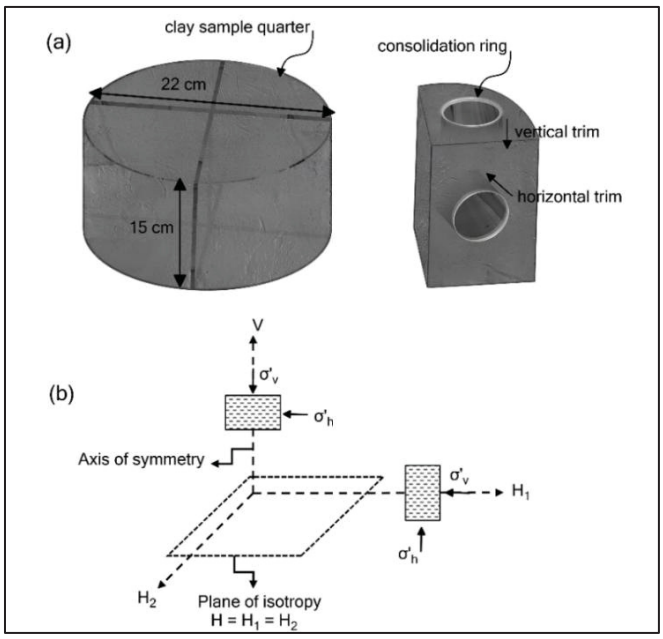

Figure 4.2 Illustration of vertical and horizontal specimens:
a) trimming path, b) cross-anisotropy assumption

Table 3-1 presents the key mechanical properties of the Champlain clay sample, including the liquid limit, plastic limit, clay content, and natural water content, measured across four quarters of the sample block. The average values indicate that the clay has a relatively high plasticity and moisture content, consistent with Champlain clay characteristics (Leroueil et al. 1983). Based on the unified soil classification system (USCS), the soil is categorized as a highly plastic clay (CH). The OCR of this block clay sample is 2.24.

Table 4.1 Characteristics of Champlain clay block sample

Property (%)	**Quarter I**	**Quarter II**	**Quarter III**	**Quarter IV**	**Average**	**Standard**
Liquid Limit (ω_l)	67	64	61	68	65	ASTM D4318-17e1
Plastic Limit (ω_p)	24	25	20	23	23	
Clay Content (cc) (< 2 μm)	71	74	66	70	70	ASTM D7928-16
Water Content (ω_n)	82	74	73	83	78	ASTM D2216 − 19

4.2.2 Shear wave measurement

V_s measurement was performed using P-RAT, illustrated in Fig. 4.2a. This technique was initiated at Université de Sherbrooke (UdeS) through a series of experimental and numerical studies (Ethier, 2009; Karray et al., 2015; Mhenni et al., 2015) and subsequently adopted by École de Technologies Supérieure (ÉTS) (Elbeggo et al., 2019). In a comparative study conducted by Elbeggo et al. (2019), the authors evaluated the agreement and consistency of results between ÉTS and UdeS laboratories, thereby demonstrating the applicability and accuracy of the P-RAT method for measuring V_s.

The P-RAT can be integrated into the oedometer top cap and base pedestal, enabling continuous measurement of V_s throughout the consolidation process (Fig. 4.3a). The P-RAT

sensor consists of various components, including a piezoelectric ring actuator manufactured by APC International, which is covered with epoxy, and four alloy quarters separated by thin silicone layers. The epoxy coating waterproofs the piezoelectric component, while the clear silicone connects the individual quarters and facilitates radial movements. The dimensions of the piezoelectric ring actuator are 19 × 3.5 mm (outer diameter × height). The fabricated sensor is encased within a stainless-steel (SS grade 304) capsule for this consolidation testing procedure. Using high-resistance material, this encapsulation ensures uniform stress distribution across the sensor components and reduces longitudinal shear at the boundary between the inner parts and the epoxied ring actuator (Mhenni et al., 2016). This design effectively enhances the sensor durability and performance under varying environmental conditions and stress levels, making it suitable for a wide range of geotechnical applications. In this study, the measurement setup includes a generator-oscilloscope (Handyscope-HS3), an amplifier (7602M type, KROHN-HITE), and a data acquisition system controlled with TiePie software (Fig. 4.3a).

The P-RAT system can use both main approaches to interpret signals: time domain and frequency domain analysis. Though both methods are available, the frequency domain approach is considered because it's less affected by input signal variations and provides deeper insights into the transducer-soil system response (Karray et al., 2015; Hussein and Karray, 2020). This contrasts with time domain analysis, which faces challenges in precisely determining through arrival of shear waves (Brignoli et al., 1996). The frequency content dependency of emitted signals (Arulnathan et al. 1988) lead to considering the frequency domain interpretation method. This work involved analyzing the experimental phase shift identification and correction between transmitter and receiver sensors, which was calculated based on the theoretical phase shift (Blewett et al., 1999; Greening and Nash, 2004; Brandenberg et al., 2008). This analysis assumed a single degree of freedom mass-spring system, with the experimental and theoretical phase distortion agreement shown in Fig. 4.3b. Through this frequency domain analysis, two fundamental dynamic properties of the system were determined: a resonant frequency of 35 kHz and a damping ratio of 8%. The dynamic characteristics of the transducer system (transmitter-receiver) were identified through a face-

to-face test using various input waveforms including i) rounded half-sine, ii) half-sine, and iii) wavelet.

The frequency domain analysis procedure implemented in this study is presented in Fig. 4.3d, building upon established methodologies (Karray et al., 2015; Hussein and Karray, 2020). This approach, as demonstrated in the analysis of generated signals (Fig. 4.3c), provides a framework of phase velocity for V_s determination in frequency domain. Accordingly, the measured phase velocity $V_{ph}(f)$ differs from the actual shear wave velocity V_s due to mechanical system phase shifts and soil dispersion. The method relies on applying a correction function $\varphi_{corr}(f)$ to the experimental phase function $\varphi_{exp}(f)$, which can be expressed as $\varphi_{exp}(f) = \varphi_{th}(f) + \varphi_{corr}(f)$.

Where $\varphi_{th}(f)$ corresponds to the constant V_s. The system exhibits predictable behavior with negligible phase delay at low frequencies and approximately 2π delay above resonant frequency.

Measured V_s utilized input signals with different shapes and frequency content allows for a thorough evaluation and reflects the true physical properties of the soil, independent of the dynamic effects, equipment limitations, and signal-processing factors (Karray et al., 2015).

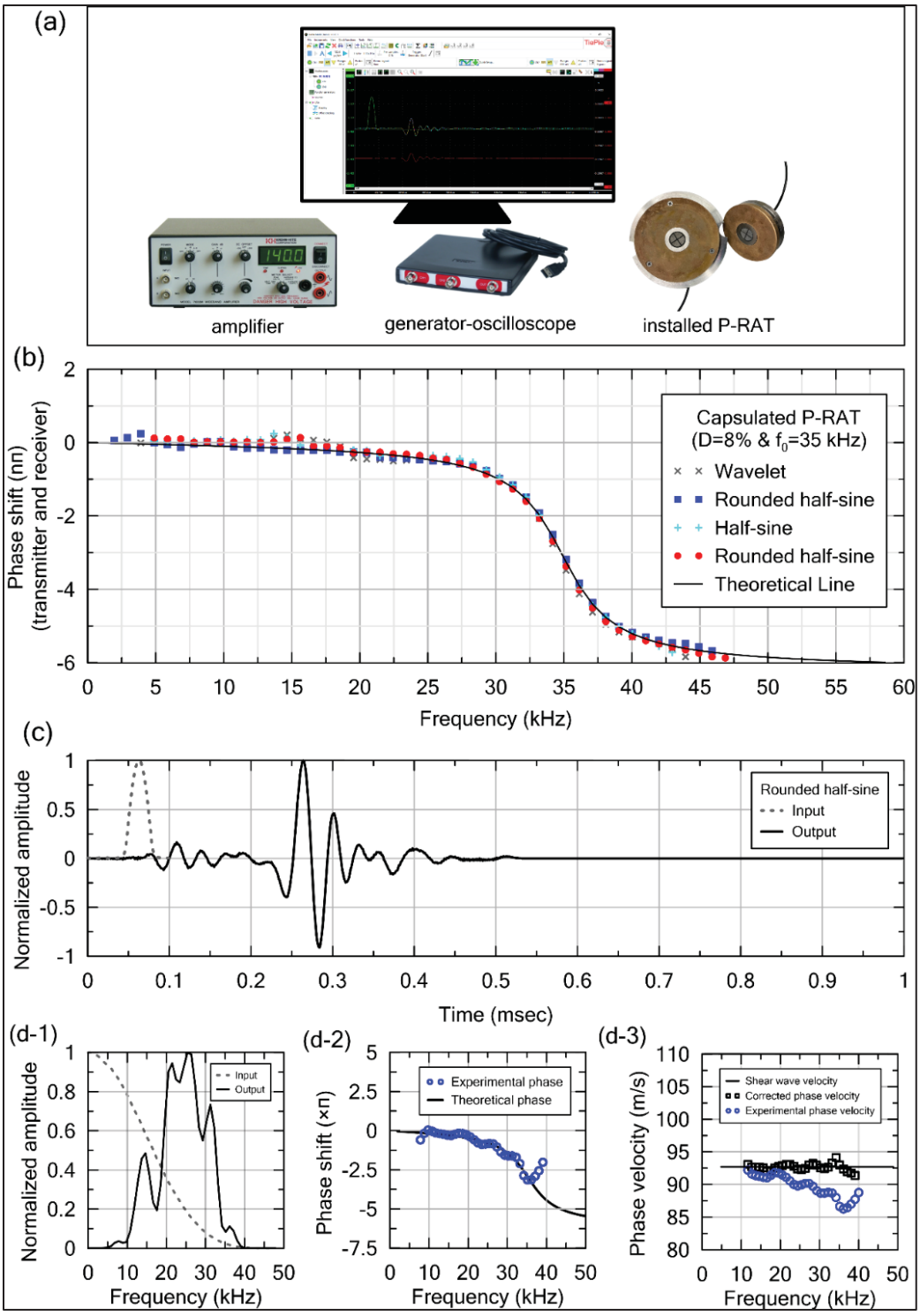

Figure 4.3 a) Mounted P-RAT within an oedometer cell and the associated data acquisition setup; b) Theoretical fit-curve for evaluating the dynamic response of the transducer system; c) Temporal traces of input and output waves; d) Illustration of V_s measurement interpretation procedure

4.2.3 Lateral strain measurement

Strain gauges measure the change in electrical resistance as a function of applied forces, allowing for the measurement of strain values on the exterior or interior surface of an instrumented component. In this study, four high-precision strain gauges manufactured by KYOWA were mounted on the exterior side of the standard stainless-steel consolidation ring, as shown in Fig. 4.4. The strain gauge model KFWB-5-120-C1 was utilized for this study (Fig. 4.4a). It is a waterproof strain gauge with a length of 5 mm, a resistance of 120 Ω, and a uniaxial pattern on one end. The sensors installation followed the manufacturer guidelines, with a special adhesive (CC-33A) employed to bond the strain gauge to the clean and neutralized surface of the metal ring. An acquisition data system (S-5000) controlled and recorded all measurement processes during 1D-consolidation tests. At the end of each consolidation stage, strain values were recorded and converted to pressure according to the material stiffness. As a result of the pressure applied to the interior wall of the oedometer cylindrical ring, three types of pressure can be generated: i) radial (σ_r), ii) hoop, or tangential (σ_t), and iii) axial (σ_a).

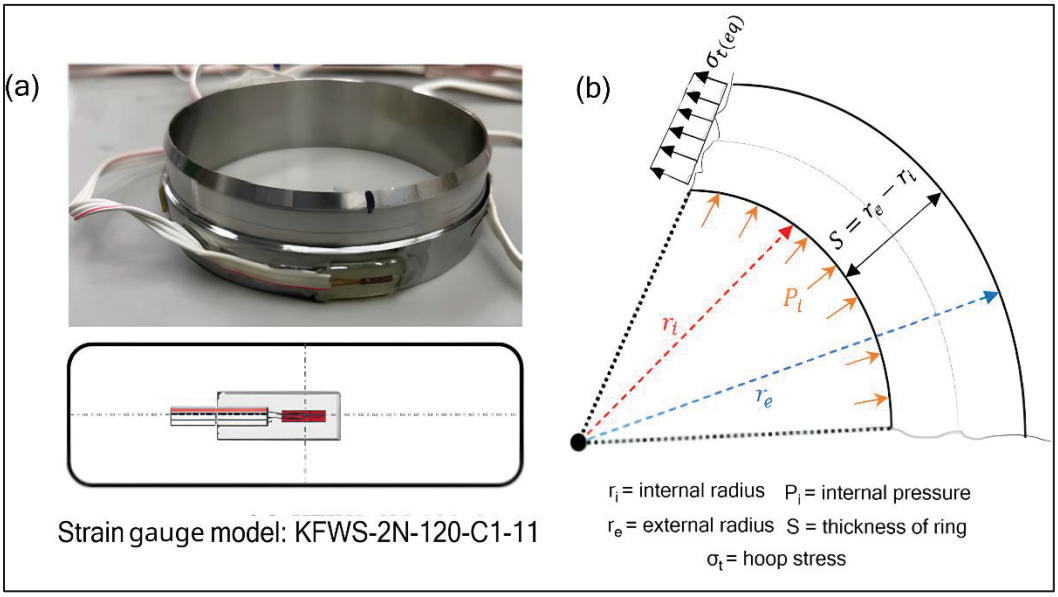

Figure 4.4 a) Consolidation ring equipped with strain gauges; b) Hoop stress illustration in a cross-section of the consolidation ring subjected to internal pressure

In a consolidation ring, σ_t is the stress component is considered for the measurement of horizontal stress (Vullo, 2014). For a hollow cylinder subjected to internal pressure (P_i), σ_t is a radius (r) function, the differences between inner and outer radii values are negligible for thin-walled frames. The ring utilized in this study is considered thin due to its thickness-to-internal diameter (S/d_i) ratio being less than 5%. σ_t is attributed to the maximum internal value ($\sigma_{t,i}$) based on the assumption of a uniform distribution of stress. The measured strains (ε_t) are converted to the hoop stress through Young's modulus of stainless steel (E), as written in Eq. (4.1). The lateral pressure can then be calculated according to σ_t based on the external and internal ring radii (r_e, r_i, respectively). Eq. (4.2) is applied for experimental investigation due to the reasonable agreement (Vullo, 2014). phase velocity $V_{ph}(f)$

$$\sigma_{t,i} = \mathrm{E} * \varepsilon_t \tag{4.1}$$

$$\sigma_h = \frac{\ln\left(\frac{r_e}{r_i}\right)^2 \times \sigma_{t,i}}{2} \tag{4.2}$$

Strain gauges must be calibrated before being utilized in consolidation tests. Calibration was accomplished by applying uniform pressure distribution using air pressure. As illustrated in Fig. 4.5, the consolidation ring was placed between two plates, with four bolts providing stability and ensuring proper alignment. Two rubber portions between aluminum plates sealed the air circulation inside the ring. The inner surface of the odometer ring was lubricated with low-friction silicon grease and filled with water before applying internal pressure. The air pump could generate pressures up to 600 kPa (Fig. 4.5). The obtained calibration curve is shown in Fig. 4.5, testifying to the efficient workability of installed strain gauges on monitoring K_0.

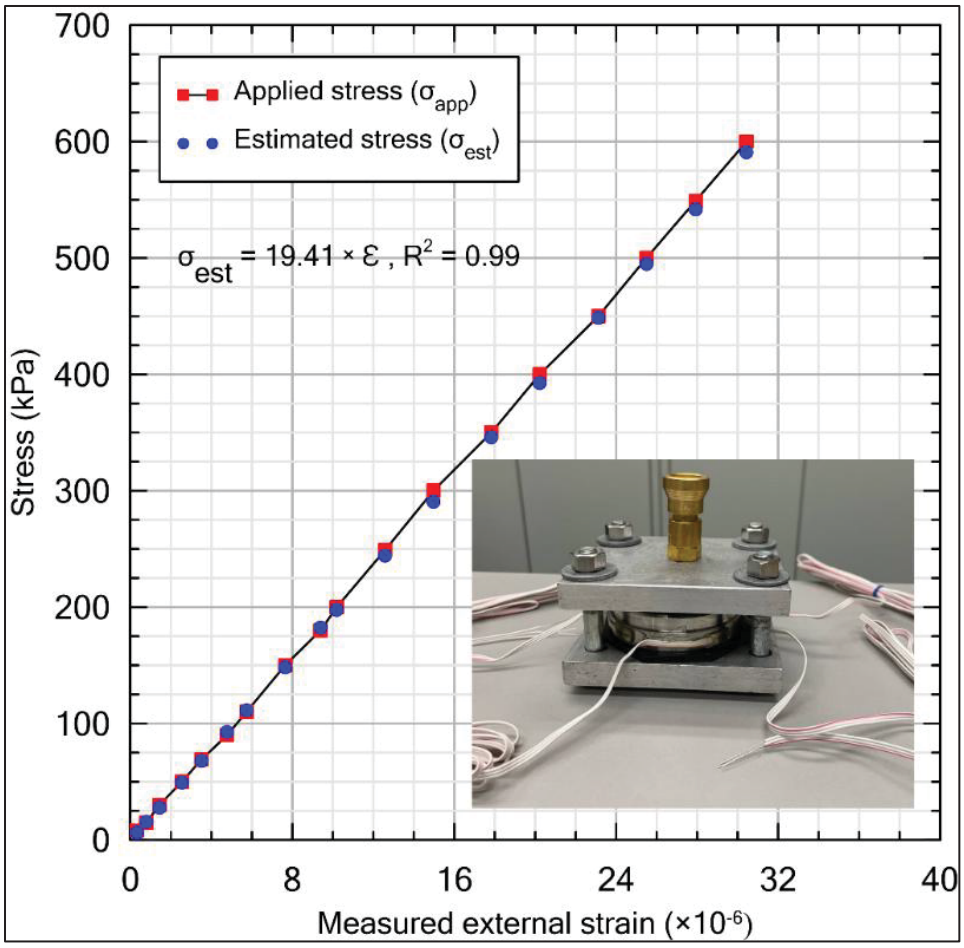

Figure 4.5 Calibration curve of strain gauges subject to uniform air pressure

4.2.4 Scanning electron microscopy

Clay minerals are typically composed of particles within the nanometer to micrometer range. Consequently, electron microscopy offers a suitable approach for investigating clays and clay minerals. The SEM images enable the observation and analysis of the material structure of tested clays at the micrometer scale, revealing details about the fabric anisotropy and the directional variation of clay platelets. Sample preparation for SEM primarily involves the removal of pore water to enable smooth observation of the soil surface. Dehydration of the moisture in a sample is commonly achieved using oven-drying and freeze-drying methods. The oven-drying approach is not suitable for moist clay soils, as it can result in significant shrinkage

and potentially alter the soil structure (Delage and Lefebvre, 1984; Krizek et al., 1975; Kang et al., 2003; Hattab et al., 2013).

Instead, lyophilization, or freeze-drying, is a drying technique that simultaneously employs vacuum pressure (≤ 0.2 mbar) and heat to prepare a sample for SEM analyses. In this approach, the drying process involves sublimation, a process in which the water transitions from the solid phase (ice) to the gaseous phase (vaporized water). The sublimation process requires a pre-frozen soil sample. SEM samples also termed soil sticks of 10 mm per 10 mm with a thickness of 2 mm, as Delage and Pellerin (1984) recommended a thickness of less than 3 mm for sensitive marine clays to ensure uniform and efficient freezing and drying during the lyophilization process. The horizontal and vertical sections of SEM samples were prepared to examine the bedding layers and particles that were taken from the top sides of the cut soil from the natural sample (in the trimming process for the 1D consolidation test) and subsequently from its consolidated one. It is based on initial sampling orientation as shown in figure 4.2, that the vertical direction is identical to the initial sampling orientation, while horizontal refers to 90 degrees rotation.

These samples were pre-frozen using liquid nitrogen, which has a boiling point of -195.8℃. The drying process is performed using a freeze-dryer device manufactured by Labconco Corp., which requires three days for these samples. The freeze-dryer can maintain the clay sticks under high vacuum pressure (0.2 mbar) while the temperature remains at -105°C. The soil sticks, pre-frozen using liquid nitrogen, were placed in flasks connected to the drying chamber of the freeze-dryer. To prevent crystallization, both the flasks and the clay sticks were pre-frozen. This process helps preserve the integrity of the clay structure during the drying process. An image processing is implemented in MATLAB to analyze the orientation of clay particles from taken SEM images based on pixel intensity and labeled regions of similar particles. An algorithm of calculation employs imaging processing techniques, including image segmentation of clay particles to isolate the particles from the image contents and image thresholding techniques to differentiate the bright, elongated regions, which are the particles, from the dark background regions as pores. The segmentation procedure, the Otsu's method,

grouped the regions of interest of particles based on the established threshold limit as level of four for these images. As shown in Figs. 4.6 and 4.7, the high resolution of images allows for the differentiation of individual clay particles and the discernment of their alignment. The degree of anisotropy ($\bar{L}$) and the mean direction of all the vectors (θ) can be determined based either directly from equations based on the length and direction of identified particles through major axis length or directly from polar graph of frequency distribution. A polar diagram can represent the lengths of major axis of identified particles, l_i, for each direction range, θ_i, with an interval of 10. Particle distributions were illustrated in the form of rose diagrams (Figs. 4.6 and 4.7). The calculation of $\bar{L}$ and θ are as follows:

$$\theta = tan^{-1}\left[\frac{\sum_{i=0}^{n} l_i \times sin\theta_i}{\sum_{i=0}^{n} l_i \times cos\theta_i}\right] \tag{4.3}$$

$$\bar{L} = \frac{\sqrt{(\sum_{i=0}^{n} l_i \times sin\theta_i)^2 + (\sum_{i=0}^{n} l_i \times cos\theta_i)^2}}{\sum_{i=0}^{n} l_i} \tag{4.4}$$

Using the derived $\bar{L}$ values, the fabric orientation is classified into various categories to describe the uniformity of particle alignment within the clay material, ranging from maximum iso-orientation to random oriented fabric (Martinez-Nistal, 1999). The proposed classification is as follows:

$\bar{L}$ =1	maximum degree of iso-orientation
0.21 < $\bar{L}$ < 1	highly oriented fabric
0.15 < $\bar{L}$ < 0.21	weakly oriented fabric
$\bar{L}$ < 0.15	randomly oriented fabric

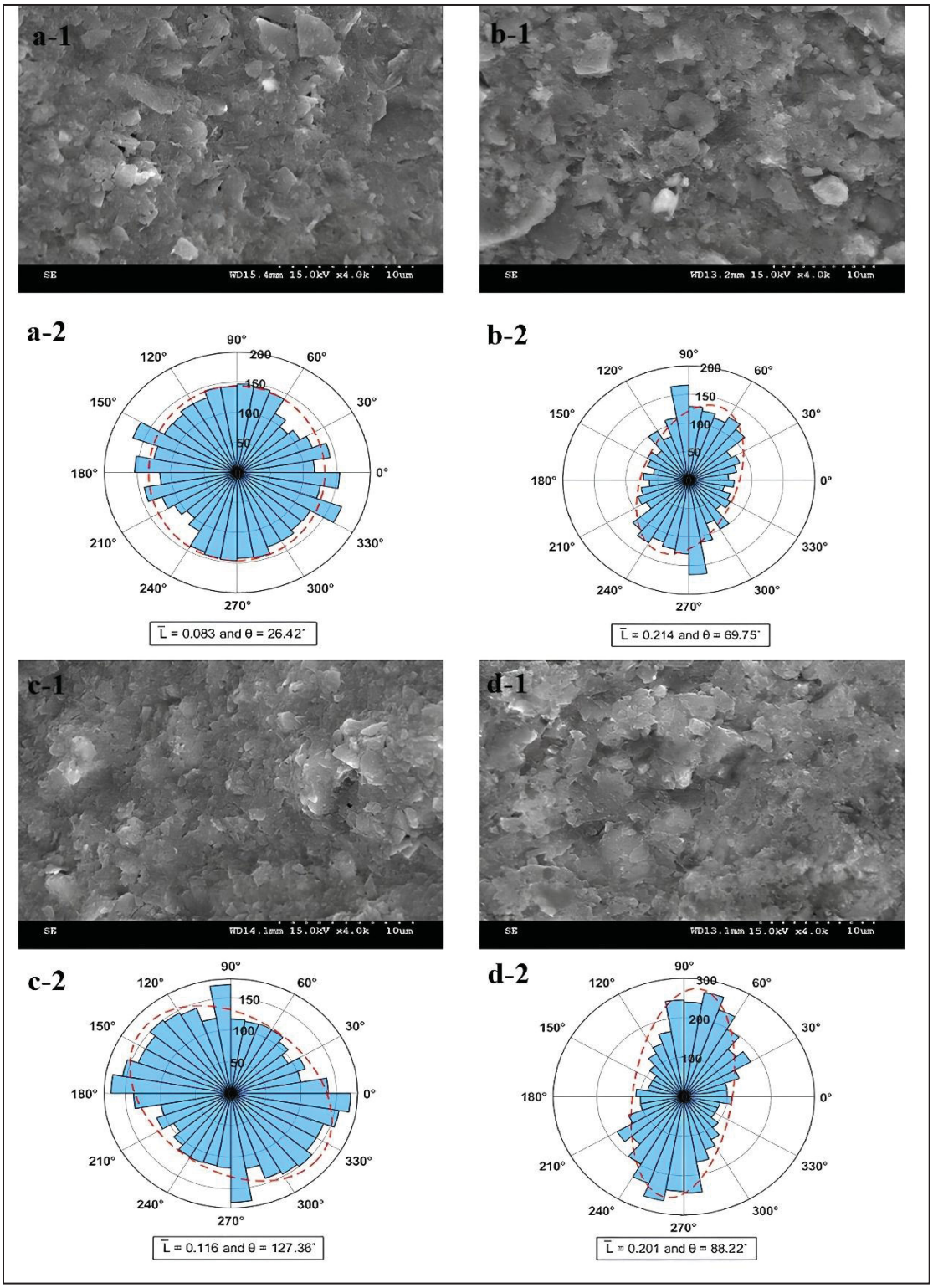

Figure 4.6 Microstructure of vertically oriented intact sample (a-1 and c-1) and vertically consolidated (b-1 and d-1) samples and their corresponding directionality analysis results (a-2 and c-2) and (b-2 and d-2), respectively

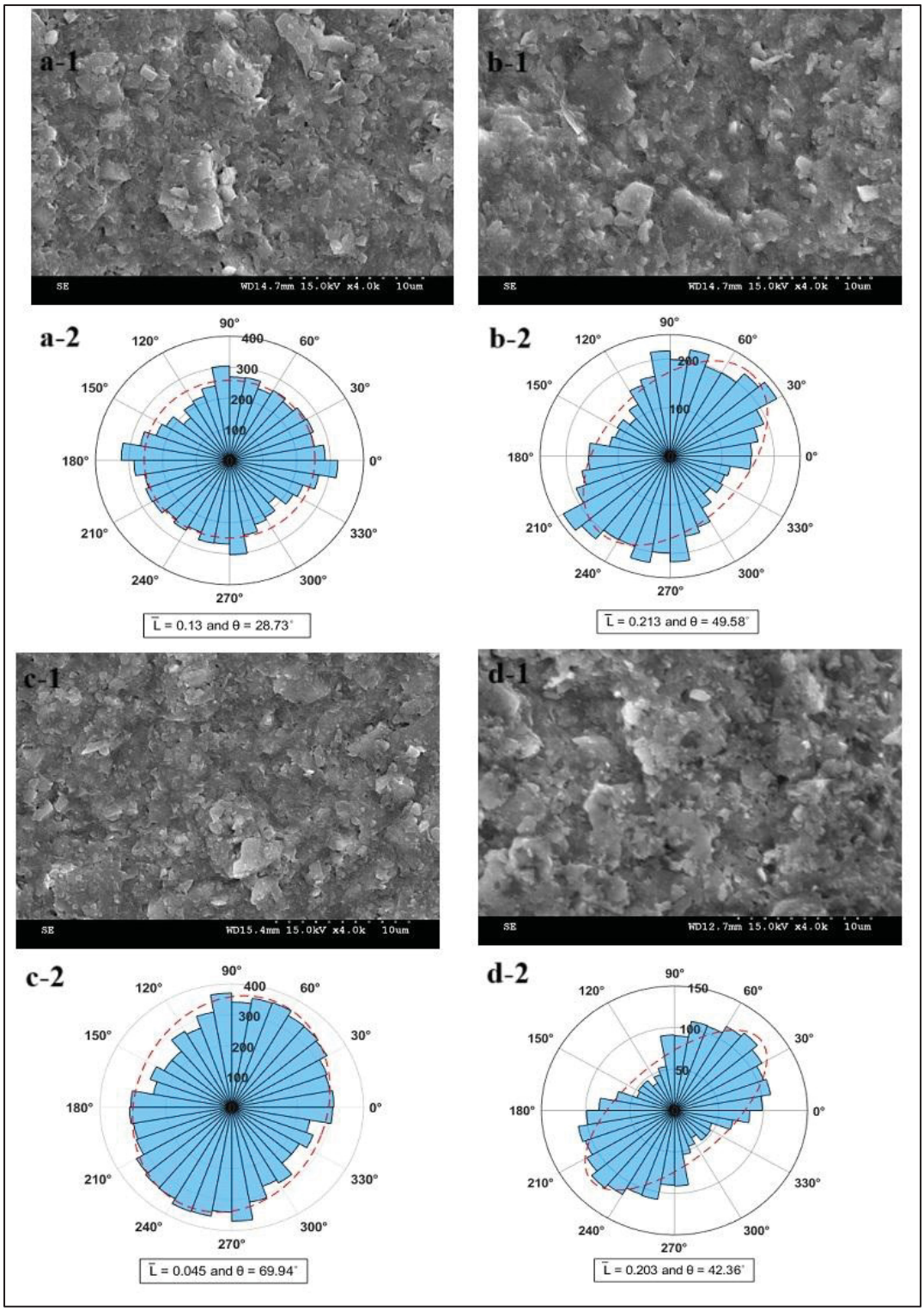

Figure 4.7 Microstructure of horizontally oriented intact sample (a-1 and c-1) and horizontally consolidated (b-1 and d-1) samples and their corresponding directionality analysis results (a-2 and c-2) and (b-2 and d-2), respectively

4.3 Results and discussion

The consolidation curves obtained for both vertically consolidated (VC), and horizontally consolidated (HC) specimens are shown in Fig. 4.8. HC specimens were prepared with a trimming path rotated 90° compared to VC specimens to examine the directional properties of the studied clay. In agreement with the literature (Silvestri and Aubertin, 1988; Lefebvre et al., 1991), the findings highlight these directional properties with HC specimens exhibiting a distinctly lower σ_p' compared to VC specimens for Champlain clays. The mean consolidation curves of vertical and horizontal planes are illustrated based on arithmetic average of the void ratio for a given orientation (Figure 4.8 c). The average value of preconsolidation pressure (σ_p') of VC and HC specimens were also determined at 60 kPa and 45 kPa, respectively.

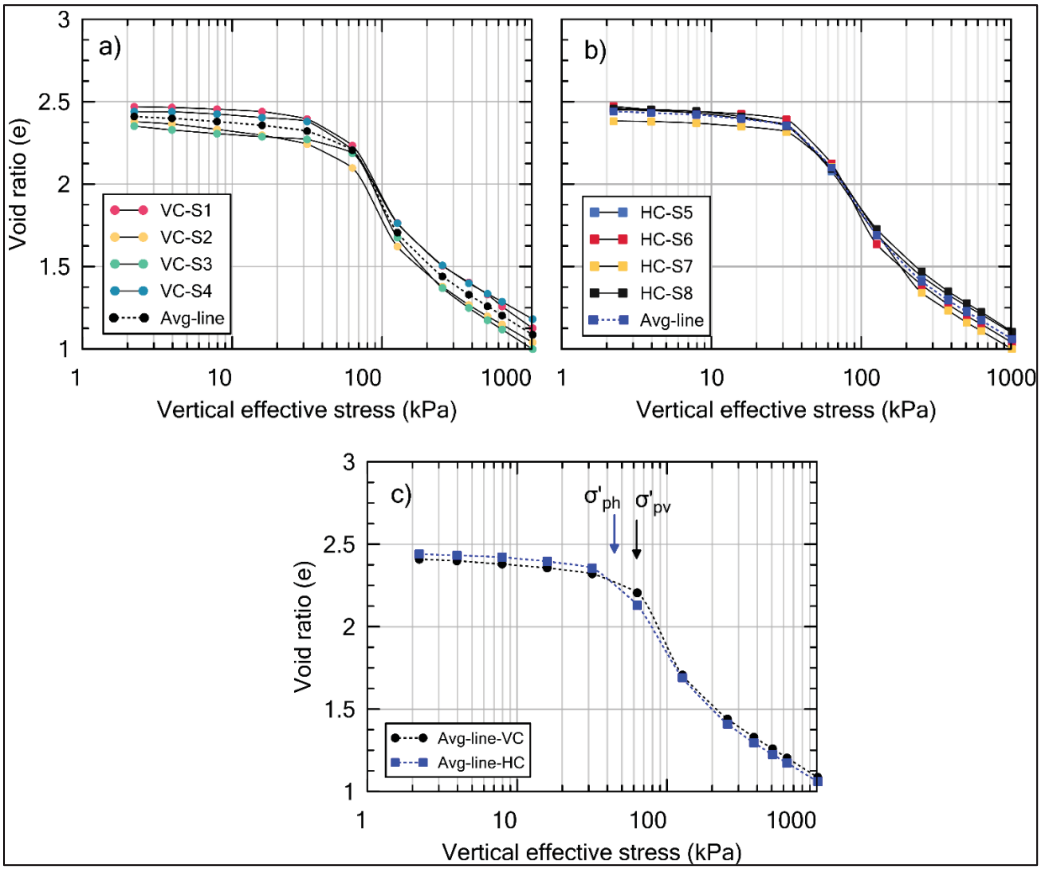

Figure 4.8 Consolidation curves of the eight tests on a) vertically consolidated (VC) samples, b) horizontally consolidated (HC) samples, and c) average curves for both orientations

SEM images shown in Figs. 4.6 and 4.7 were performed with high resolution considering a high voltage equal to 15 kW at 4000× magnifications and a range of working distance of 13 to 15 mm, to ensure constant factors of image visibility and reasonable coverage of particle numbers. The visual analysis of these images reveals the fabric geometry with similar formation and association in both directions. It confirms the inherently random arrangement of clay platelets before consolidation corresponding to the intact conditions (Figs. 4.6a-1, 4.6c-1, 4.7a-1, and 4.7c-1) in oriented samples in horizontal (S6 and S7) and vertical (S1 and S3) directions. After consolidation (Figs. 4.6b-1, 4.6d-1, 4.7b-1, and 4.7d-1), for both VC or HC samples, preferred orientation and parallelism are visible. This comparative analysis between pre- and post-consolidation states indicates the soil fabric adaptation to the consolidation stress at a microscopic scale and highlights that anisotropy is a progressive phenomenon (Delage and Lefebvre, 1984) with a shift from a random to a more oriented soil fabric throughout the consolidation process. The initial inherent anisotropy can be attributed to depositional conditions, geology, mineralogy, and soil history, where individual platelets naturally have formations and associations, including face-to-face and edge-to-face (Tessier et al., 1992).

Microstructural examinations indicate that the interparticle connections and clay fabric undergo disruption upon exceeding σ_p', forming distinct aggregates with groups of clay fabric that attain new equilibrium positions. The incremental consolidation stress alters soil particle arrangement, porosity, and clay platelet interactions following a sequential pattern: i) below σ_p', a rearrangement and realignment of initially randomly disposed clay fabric as a group of clay platelets with reversible deformation, ii) exceeding σ_p' up to the end of primary consolidation stage, causes a greater degree of rearrangement of clay fabric and individual platelets start to reorientate irreversibly, initiating pseudo-anisotropy, and iii) beyond primary consolidation stage, a further intensification of fabric and platelet orientation accompanied by an irreversible reduction in clay fabric volume, resulting in secondary compression effects.

Anisotropy visualization through rose diagrams provides a quantitative assessment of the structural patterns and the evolution of anisotropy in both VC and HC intact samples (Figs.

4.6a-2, 4.6c-2, 4.7a-2, and 4.7c-2) and consolidated (Figs. 4.6b-2, 4.6d-2, 4.7b-2, and 4.7d-2). The count density of particles is expressed as a fraction of utilized pixels in the image, representing the intensity distribution across specific directions with intervals of 10 degrees. Narrow-fitting ellipses indicate visually aligned fabrics, as evident in consolidated samples, contrasting with wide-fitting ellipses representing a uniform intensity distribution, corresponding to a random anisotropy characteristic of the intact fabric. According to the classification of anisotropy stage by Martinez-Nistal, (1999), before consolidation, $\bar{L}$ shows a variation of less than 0.15, confirming the random intensity distribution between 0 and 360 degrees. Upon conducting consolidation tests under high-stress levels, polar histograms reveal preferential and dominant peaks demonstrating a significant reorientation of platy particles. This reorientation leads to a more parallel alignment of clay platelets, predominantly exposing their flat faces (face-to-face position), and results in a centralized distribution of particle orientation for both VC and HC samples, mainly converging to parallelism. The analyses of SEM images reveal a low degree of anisotropy between the two principal directions, as the value of $\bar{L}$ for consolidated soil is approximately less than 0.21 based on the anisotropy classification.

Fig. 4.9 represents an illustration of the temporal traces of shear waves at distinct consolidation stages for VC-S2 and HC-S6 clay specimens (from a similar quarter of the block sample), using a rounded half sine as an input. Independent of the propagation-polarization plane, V_s increases proportionally with the applied consolidation stress, manifested by a progressive shift of output signals to the input signal pick with incremental load application. Despite using the P-RAT interpretation approach (Fig. 4.3), based on the first peak arrival time method, which identifies the first peak within the input signal (marked with a red dot for VC and a blue dot for HC in Fig. 4.9), a systematic decrease in the time difference for shear wave arrival between vh and hh planes is observed. Upon exceeding 500 kPa, the two picks merge, resulting in nearly identical V_s values in both plane orientations. This trend highlights that the tested soil exhibits uniform anisotropic behavior under significant consolidation pressure, leading to the same fabric structure and similar platelet rearrangement. The time-domain graph was used for an illustrative purpose, the measurements were obtained using P-RAT interpretation method.

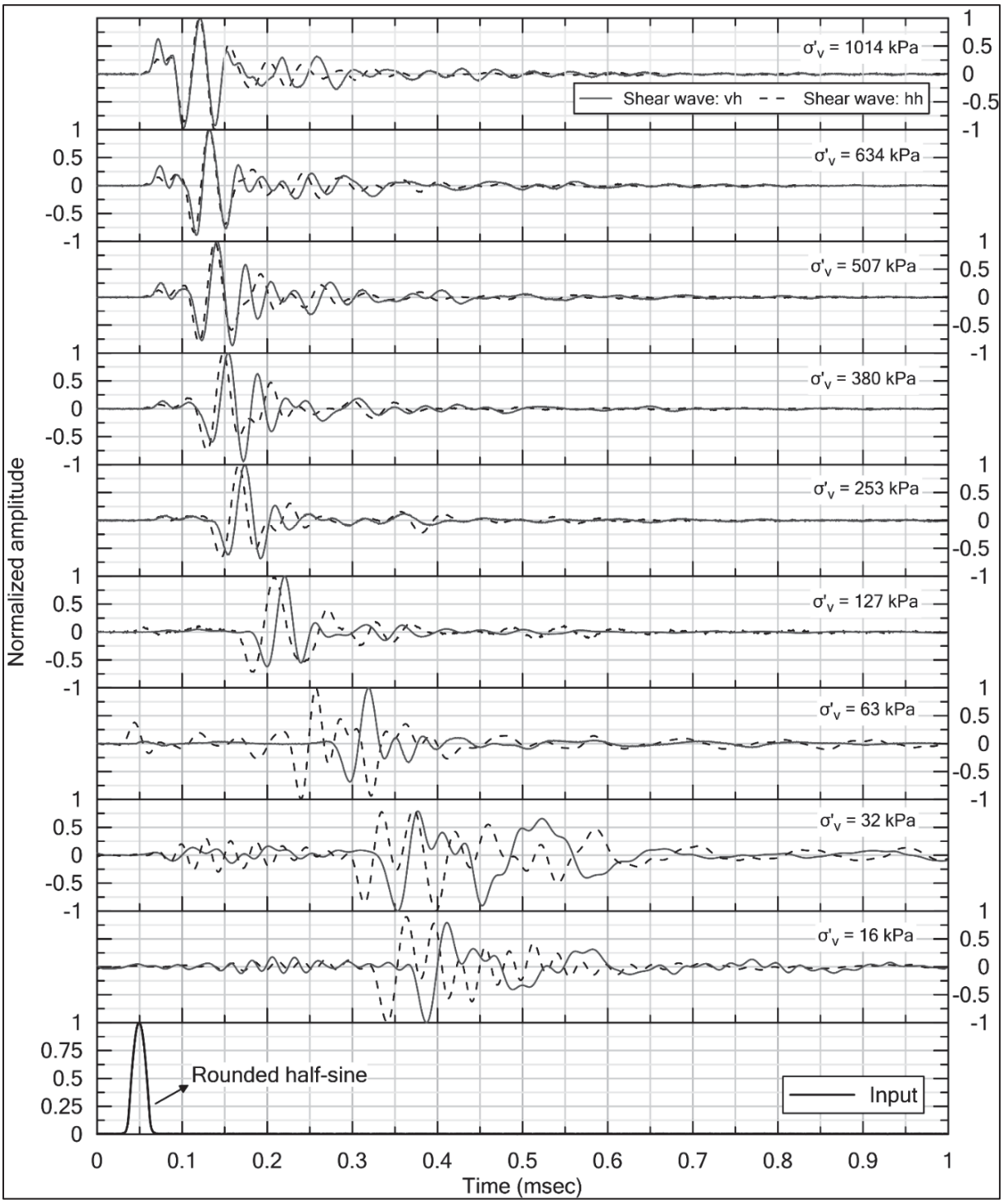

Figure 4.9 Temporal traces of output wave in the vertical-horizontal (vh) and horizontal-horizontal (hh) propagation-polarization plane, considering the gradual effects of the consolidation stress

As shown in Fig. 4.10, V_s-consolidation curves illustrate the variation of V_s as a function of consolidation stress. V_s exhibits a proportional increase with applied consolidation stress, particularly when exceeding σ'_p value where a distinct change in the slope of the consolidation curves is observed. The consistency in V_s-consolidation curves and σ'_p values estimation obtained from the different tests, confirm the high quality of tested specimens and the effectiveness and repeatability of the testing procedures. The σ'_{pv} and σ'_{ph} values estimated from the V_s-consolidation curves as the intersection points of the two linear segments in Fig. 4.10, align with the values estimated from conventional consolidation curves and the Casagrande approach to determine the preconsolidation pressure shown in Fig. 4.8. The observed discrepancies in $V_{s\,(vh)}$ and $V_{s\,(hh)}$values at lower consolidation pressures are attributed to the initial soil fabric and inherent anisotropy and the stress history effect on the alignment of clay platelets. Beyond σ'_p, $V_{s\,(vh)}$ and $V_{s\,(hh)}$values converge, confirming a transition of the soil fabric towards a unified fabric, regardless of the consolidation pressure load direction. This convergence indicates the tendency of sensitive marine Champlain clay to reorganize its microstructural and mechanical properties in response to consolidation loading, leading to a consistent fabric and behavior across different loading orientations.

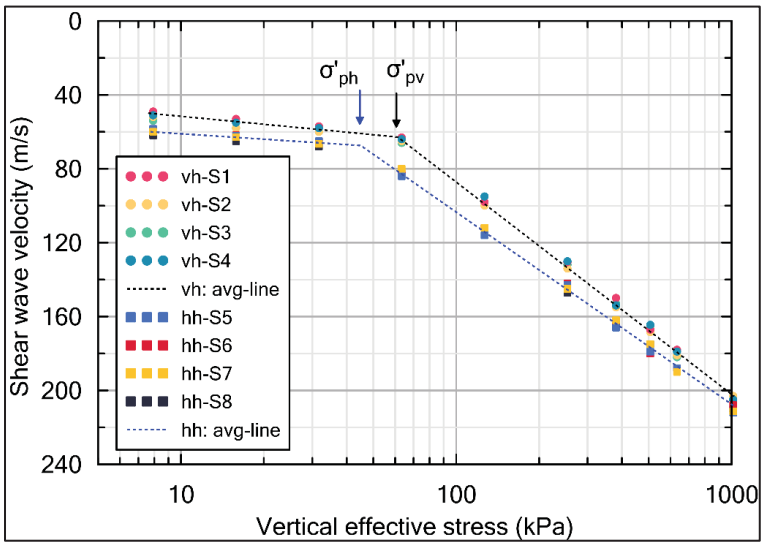

Figure 4.10 V_s-consolidation average curves for vertically and horizontally consolidated clay samples (vh and hh, respectively)

During an oedometer test, the stress state is anisotropic, and the consolidation stress directly affects the degree of anisotropy. Based on cross-anisotropy assumption (Pennington et al., 1997; Jovičić and Coop, 1998; Teachavorasinskun and Lukkanaprasit, 2008; Jamiolkowski et al., 1995; Teachavorasinskun and Lukkanaprasit, 2008; Zapata-Medina et al., 2020), $G_{\max}$, on the axisymmetric planes of vh and hv, were assumed to be equivalent ($G_{\max\,(vh)} = G_{\max\,(hv)}$). As a result, the horizontal shear modulus ($G_{\max\,(hh)} = \rho V_{s(hh)}^2$) was higher than the perpendicular one for bedding layers ($G_{\max\,(vh)} = \rho V_{s(vh)}^2$).To quantify the degree of anisotropy and to allow the comparison with previous studies that report their results in terms of $G_{\max}$ (Jamiolkowski et al., 1995; and Jovičić and Coop, 1998), The anisotropy ratio (AR), as defined by Eq. 4.5, was calculated.

$$\text{AR} = \frac{G_{max(hh)}}{G_{max(vh)}} = \frac{\left(V_{s\,(hh)}\right)^2}{\left(V_{s\,(vh)}\right)^2} \tag{4.5}$$

AR values range from 1.28 to 1 for normally consolidated sections and exhibit variability for overconsolidated sections at consolidation pressure lower then σ_p'. The variability of this clay is attributable to two factors: i) OCR and ii) initial random fabric anisotropy. In studies conducted by Jamiolkowski et al. (1995), Kim and Finno (2012), and Nishimura (2014) on normally consolidated and lightly overconsolidated natural clays of different locations, $\frac{G_{max(hh)}}{G_{max(vh)}}$, were reported, with variations ranging from 1.1 to 1.4, showing relatively low change in the stiffness of the soil in two principal directions. Tested Champlain clay with OCR < 4 (Chen and Kulhawy, 1993), as lightly overconsolidated clays, reportedly show a similar trend of anisotropic behavior.

The incremental application of effective vertical stress (σ_v') induces progressive alterations in the fabric anisotropy due to stress-induced mechanisms (K_0 stress condition), ultimately leading to a preferential alignment of clay platelets in the horizontal plane (Jovičić and Coop, 1998; Zapata-Medina et al., 2020). As a result, the reported AR exhibits a narrower range of variations at high pressures.

Roesler (1979) states that body waves, including V_s, are affected by the elastic properties of a medium and depend on the principal effective stresses acting in both the direction of wave propagation and particle motion orientation. Therefore, the role of lateral and axial stresses with respect to the plane of shear wave propagation and its polarization was assessed in this study through K_0 measurement (Figure 4.11). This was achieved during consolidation testing for both vertically and horizontally oriented specimens, by monitoring horizontal pressure using installed lateral strain gauges. At low effective vertical stresses (below 200 kPa), K_0 value is relatively high (≥ 0.8), but it gradually decreases and stabilizes around 0.6-0.65 at higher stresses. Stabilization at higher stresses represents the normally consolidated state of the soil, while at lower stresses it might reflect the lightly overconsolidated behavior. The fitted line ($R^2 = 0.94$) was adopted for subsequent calculations of normalized V_s correlations in both vh and hh planes. This approach was justified by the minimal variation observed between vertically and horizontally consolidated specimens. The estimated K_0 based on measured lateral pressure, enabled the expression of measured shear wave velocity in terms of σ'_m and allowed investigation of mean effective stress influence on V_s normalization.

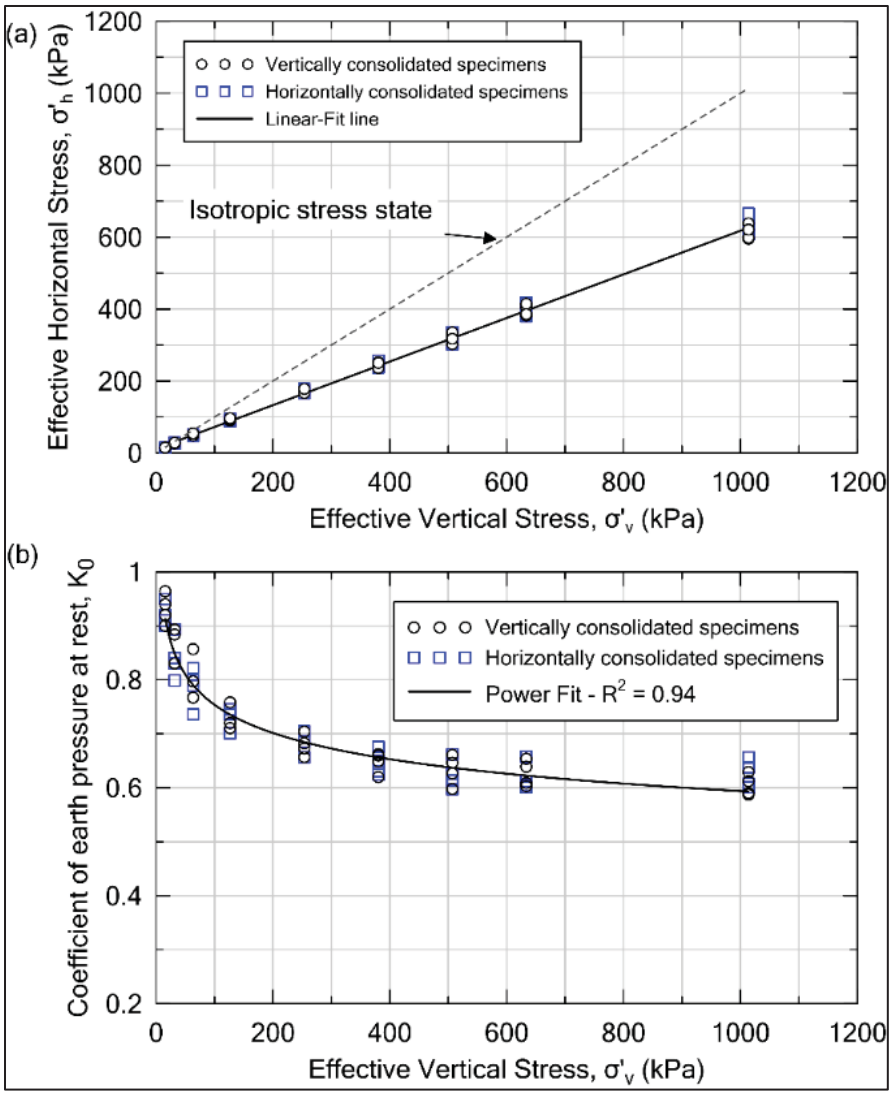

Figure 4.11 Vertically and horizontally consolidated specimens:
a) measured horizontal effective stress during 1D-consolidation test;
b) Estimated K_0 based on vertical and horizontal stresses

Fig. 4.12 shows the best-fitting line for the obtained $V_{s(hh)}$ and $V_{s(vh)}$ values and the proposed correlations taking anisotropy into account for the studied sensitive marine clay.

The empirical correlation for estimating V_s based on experimental data and theoretical analyses proposed by Hardin and Black (1969) indicate that V_s (e, σ'_m) is predominantly influenced by void ratio (e) and effective confining pressure (σ'_m).

$$V_s = AF(e)\ OCR^k \sigma_m'^{0.25} \tag{4.6}$$

Where $F(e)$ is a function of the void ratio, k is an exponent depending on the plasticity index of the soil (Viggiani and Atkinson, 1995), and A is a constant considering the influence of other factors such as geological and microstructural ones. As proposed by Youd et al. (2001), V_s normalization can be formalized as Eq. 4.7 in order to remove the effect of effective stress using an overburden correction factor (Karray et al. 2011).

$$V_{s1} = V_s(P_a/\sigma_v')^{0.25} \tag{4.7}$$

Based on the V_s-consolidation results, a comparison between V_{s1} with respect to different stress components revealed the stress-dependent nature of soil behavior. Normalized V_s to σ_m' show higher values compared to those normalized to σ_v' in the virgin compression zone for both directions. The measured K_0 for the examined clay is less than 1 in this zone and consequently results in lower σ_h' values compared to σ_v' values. Additionally, the normalized V_s is also less scattered when considering σ_m' in proposed correlations. This difference is less pronounced in the vh plane with a higher coefficient of determination (R^2= 0.97). σ_m' incorporates both σ_v' and the effect of lateral pressure and provides a comprehensive representation of the stress conditions in the plane of wave propagation and particle polarization, allowing for more accurate estimations of V_s.

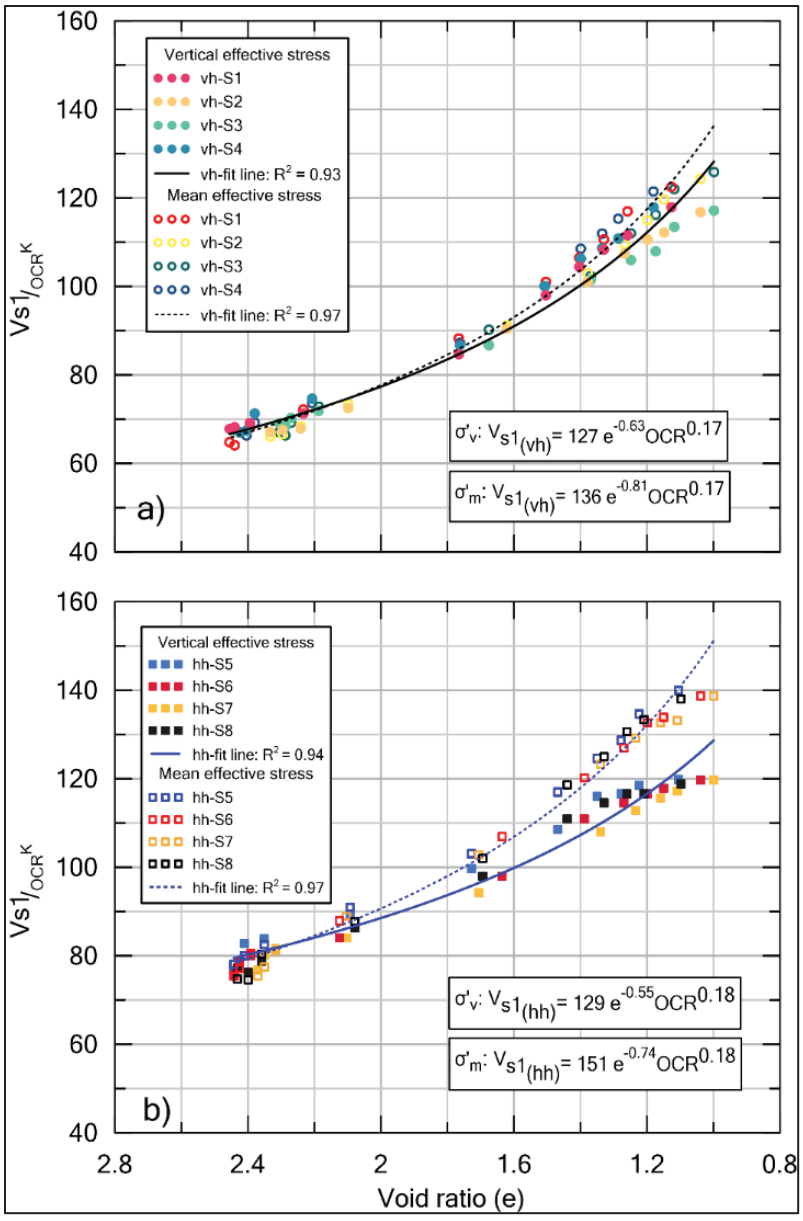

Figure 4.12 Normalized V_s correlations considering vertical and mean effective stresses, relative to a) vertical-horizontal (vh) plane and b) horizontal-horizontal (hh) plane

4.4 Conclusion

This study employed a combination of complementary experimental techniques, including P-RAT for Vs measurement, SEM for microscopic imaging, and high-precision strain gauges for lateral deformation measurement, to investigate the microstructural properties and anisotropy of clay soil at different scales. The proposed approach was established to characterize and

quantify the microstructural properties of clay samples simultaneously with a series of conventional 1D-consolidation tests. Within the testing process, K_0 coefficient was also monitored using strain gauges. SEM imaging was performed on the intact and consolidated sample before and after each test. The findings drawn from the study are summarized as follows:

1. The established procedure stands out for its efficiency, repeatability, and multiple-faceted approach in investigating clay soil behavior at macro and micro scales. Combination of V_s measurement and SEM imaging technique proceed the clay fabric structure changes through the effect of inherent and stress induced anisotropy.
2. The consolidation process of the clay specimens induced systematic changes in the microstructure soil fabric. The increase of the applied stress level results in the rearrangement of the clay platelet groups towards a more parallel orientation.
3. The particle intensity rose diagram reveals a random particle arrangement and association ($\bar{L} < 0.15$), and a low anisotropy with preferential oriented clay platelets at the end of consolidation ($0.15 < \bar{L} < 0.21$).
4. Anisotropy ratio exhibits variability below σ_p' for overconsolidation state, and a narrower range of variation for normally consolidated state beyond it. This response is attributable to the initial random fabric anisotropy which ends in a preferential alignment of clay platelets at high consolidation stress. The observed variation suggests that V_s values of this clay soil are relatively independent of the directional feature effect under high-stress levels.
5. Empirical anisotropic correlation was proposed in function of normalized V_s considering stress components, σ_v' and σ_m', providing a comprehensive representation of the stress conditions in the plane of wave propagation and particle polarization, allowing for more accurate estimations of V_s through normalization with σ_m' stress.

This research highlights the efficacy of the employed methodology to provide insights into the sensitive marine clay anisotropy which is crucial for anisotropic empirical V_s correlations and its usage. The consistency of observation with previous studies attests to the reliability of the

experimental approach and its potential for application in future studies on clay fabric anisotropy to be considered for geotechnical engineering.

CHAPTER 5

INFLUENCE OF SEM IMAGING PARAMETERS ON CLAY FABRIC ANISOTROPY

A. Torabipour [a], Y. Ethier [b], M. Karray [c], François Duhaime [d]

[a, b, d] Department of Construction Engineering, École de technologie supérieure, 1100 Notre-Dame West, Montreal, Québec, Canada H3C 1K3
[c] Department of Civil Engineering and Building Engineering, Université de Sherbrooke, Sherbrooke, Québec, Canada

Paper submitted for publication, *Journal of Testing and Evaluation*, February 2025

Abstract

The article presents a detailed analysis of soil fabric anisotropy using scanning electron microscopy imaging, employing two quantification methods, FOCM-I and II. Two clay specimens from a block sample were analyzed through vertical and horizontal cuts, and a MATLAB-based algorithm was developed to assess anisotropy and porosity indices via threshold analysis. The results obtained with both methods were compared with available data in the literature, demonstrating a strong agreement. Key parameters affecting SEM imaging, such as accelerating voltage (10 kV to 30 kV) and magnification (1000 to 7000 times), were thoroughly examined, revealing that variations in these parameters could influence fabric anisotropy calculations by up to 100%. The study introduces a new approach to assess soil anisotropy, utilizing full-view images at 1500 magnification and grid-view images at 3000 magnifications from similar zones. Additionally, the research involved random capturing and analysis of images from peripheral areas of both full-view and grid-view zones. Comparing the results of the anisotropy in various conditions reveals that using the average results significantly minimize the difference between the indices obtained for different voltages, magnifications, and samples. It emphasizes that analyzing a greater number of particles and pores on a larger surface area could potentially yield higher accuracy. The proposed imaging technique and analytical procedure improve the accuracy of fabric orientation calculations, contributing valuable insights into soil fabric analysis and its implications for understanding soil behavior.

Keywords

Scanning Electron Microscopy; Marine Clay; Threshold Analysis; Fabric Orientation; Imaging Technique; Parametric Study.

5.1 Introduction

Clays pose challenges in engineering practice due to their unique formation process and layering characteristics. Soil formation produces fabric or inherent anisotropy, which should be considered when measuring soil properties. Inherent anisotropy refers to the intrinsic variation of soil properties, reflected by shear wave propagation (Jamiolkowski et al. 1995; Pennington et al. 1997; Gasparre et al. 2011; Nishimura, 2014; Torabi Pour et al. 2024) using piezoelectric transducers (Lee and Santamarina, 2005; Karray et al. 2015), shear strength through triaxial apparatus (Nishimura et al. 2011; Brosse et al. 2017), and permeability (Leroueil et al. 1990; Clennell et al. 1999), depending on the plane of measurement. This phenomenon can be studied utilizing both macro- and microscopic experimental procedures. The macroscopic perspective considers anisotropy in terms of the layering characteristic and stress history of the soil, while the microscopic perspective focuses on particle position and mineral composition. At the macroscale, the anisotropy ratio, indicating directional dependency of the soil properties, is commonly measured based on the two principal planes: vertical-horizontal (vh), and horizontal-horizontal (hh). This ratio is proposed in different forms including $\frac{G_{\max\,(hh)}}{G_{\max\,(vh)}}$ (maximum shear modulus ratio through measured anisotropic shear wave velocity), $\frac{S_{\mathrm{u}\,(hh)}}{S_{\mathrm{u}\,(vh)}}$ (shear strength ratio) and $\frac{K_{(hh)}}{K_{(vh)}}$ (hydraulic conductivity ratio) based on the utilized laboratory approach.

The microscopic characterization of anisotropy is more challenging due to the complex fabric outlined by individual pores and particles (Mitchell, 1972; Sasanian and Newson, 2013; Yuan et al. 2019). Delage and Lefebvre (1984), Sasanian and Newson (2013), and Yuan et al. (2019) used mercury intrusion porosimetry (MIP) to understand the pore response to applied stresses and water content changes. Delage and Lefebvre (1984) showed that the compressibility of Eastern Canadian clays is governed by the progressive destruction of the inter-aggregate pore structure during consolidation. Zheng et al. (2022) utilized MIP to analyze the porosity and the collapse of pores during compression and consolidation of illite-dominant clay. Their findings confirmed an ordered arrangement under high compression stress levels and categorized pore

spaces as inter-aggregate (between clay clusters) and intra-aggregate (within clay clusters). As the clay structure undergoes gradual compression, there is a sequential change of pore spaces, commencing with the larger pores and progressively affecting the smaller ones. Along with pore collapse, there is a tendency for the particles to flatten preferentially in the direction perpendicular to the applied load, suggesting the effect of consolidation stress on anisotropy of the consolidated clay. In previous studies, MIP was supported by the qualitative usage of scanning electron microscopy (SEM) to observe the pore distribution in Eastern Canadian clays (Delage and Lefebvre, 1984; Delage, 2010) and clays of other regions (Wang and Xu, 2007; Zeng et al. 2017; Zheng et al. 2022).

The SEM technique (Delage, 2010; Mitaritonna et al. 2014; Ural, 2021; Guglielmi et al. 2022; Zheng et al. 2022), and X-ray diffraction (Srodon et al. 2001; Bunaciu et al. 2015) allow the arrangement of particles and pores within the soil matrix to be examined. SEM is an effective method to capture high quality images from the surface of the sample to examine the rearrangement and alteration of clay aggregates and inter-aggregate pores. Digital image processing, along with optical and electronic microscopes, has made it feasible to quantitatively analyze the overall orientation of the clay fabric.

The quantitative study of soil microfabric orientation is primarily conducted through two approaches: the elliptical aspect ratio method and the normalized vector summation method. The elliptical aspect ratio method was applied in various studies (Tovey 1973; Tovey et al. 1989; Tovey and Krinsley 1992). Shi et al. (1998) expanded this method by incorporating probability entropy and frequency distribution functions to assess fabric orientation under different moisture contents and consolidation stresses. Li et al. (2020) utilized this approach to investigate the influence of particle roundness on anisotropy, while Zheng et al. (2022) employed it to evaluate pore directionality and shapes in illite-dominant clay samples. The normalized vector summation approach, formulated by Davis (1986) and utilized by Martínez-Nistal et al. (1999), has found significant application in different soil types. It has been particularly useful in studies related to soft marine clays, as demonstrated by the work of Mitaritonna et al. (2014), Cotecchia et al. (2016), and Guglielmi et al. (2022). Additionally,

Wang et al. (2022) applied this method in their research on granite residual soil. Both methodologies were utilized in assessing fine-grained soil fabric and pore orientation. The key difference between these two methods lies in their mathematical approach:

The vector-based method calculates orientation by summing and normalizing individual vector measurements, while the aspect ratio method determines orientation by measuring the elongation of a fitted ellipse shape.

The application of these fabric orientation analysis methods has provided valuable insights into soil behavior under various loading conditions. Studies of anisotropic stress paths in triaxial testing have revealed pronounced alignment of particles and voids in the horizontal direction with increasing consolidation stress (Mitaritonna et al. 2014). Similarly, Wang et al. (2022) applied these orientation calculations to compare microfabric evolution during 1D consolidation between intact and remolded specimens, demonstrating how compressibility affects particle and pore arrangements. Their findings, through polar graphs representing clay particle orientation, illustrated significant alterations in microfabric when the vertical effective stress exceeds the preconsolidation pressure.

This research aims to enhance the accuracy and reliability of SEM image processing in geotechnical characterization. To the authors' best knowledge, all previous works on soil fabric orientation analysis from SEM images have been confined to the usage of a single calculation method for fabric orientation (e.g. either vector-based method or aspect-ratio method) and a single set of SEM parameters (e.g. magnification and accelerating voltage). To advance our understanding, it is desirable to compare different methods for anisotropy calculations and to conduct parametric studies of SEM imaging parameters to quantify their influence on the calculated anisotropy. To achieve this purpose, a MATLAB script for soil microstructure analyses was developed and validated. The script determines fabric orientation and porosity. It compares two calculation methods to assess fabric orientation. The script was verified by comparing results with available SEM images and anisotropy data reported in the literature. A parametric study was conducted to verify the influence of accelerating voltage and

magnification on porosity and anisotropy. In addition, a "puzzle-like" imaging technique is introduced to address the challenges of particle and pore scattering in SEM images, aiming for a more reliable anisotropy determination. In this regard, random images from different areas of the sample surface are captured and the results of the anisotropy index in various conditions, including average results, are compared. The proposed imaging technique increases the accuracy of anisotropy determination through image processing. The study also assesses the impact of consolidation on the microstructural properties of Champlain clay, including changes in anisotropy and porosity.

5.2 Sample preparation and image acquisition

Champlain marine clay is recognized for its high plasticity, fine-grained nature, and high sensitivity, making it a material of interest in the field of geotechnical engineering. Champlain clays are predominantly found in Eastern Canada, particularly in the Province of Québec. To meet the objective of this study, an undisturbed clay block was collected in Saint-Étienne-de-Beauharnois, Canada using the Laval University sampler (La Rochelle et al. 1981).

Table 5.1 Characteristics of Champlain clay specimen

Soil Properties	**Sample**
	S3 & S7
Sampling depth (m)	6 - 7
Natural water content (ω_0%)	80
plasticity index (I_p%)	40
liquid limit (LL%)	62
OCR	2.2
Clay content (CC %) < 2μm	74
Maximum applied effective vertical stress, σ_v' (kPa)	1014
USCS soil class	CH

Beauharnois clay and Champlain clays in general consist of illite, mica, calcite, quartz, and feldspar (Locat et al. 1984, Skempton and Northey, 1952). Table 5.1 summarizes the primary

characteristics of two clay subsamples (named S3 and S7) that were cut from the same clay block and that were used for SEM imaging.

Atterberg limits tests were conducted based on the ASTM D4318 standard. The average values of the tested samples liquid limit (*LL*) and plastic limit (*PL*) are 62% and 22%, respectively. The results obtained in this study are consistent with the findings reported by Leroueil (1999), who reported *LL* values of Eastern Canadian clays below 80% and *PL* ranging between 17% and 35%. Particle size analyses were conducted following the ASTM D7928 standard. Based on the particle size distribution curve in Figure 5.1, the clay-sized fraction in this Champlain clay specimen, corresponding to a particle size (< 2 μm), is 72% of the total dry mass. Based on the unified soil classification system (USCS), the studied soil is categorized as highly plastic clay (CH). A one-dimensional consolidation test was conducted following the ASTM D2435 standard. Based on the classification provided by Chen and Kulhawy (1993), the soil can be described as lightly overconsolidated with an overconsolidation ratio (OCR) of 2.2.

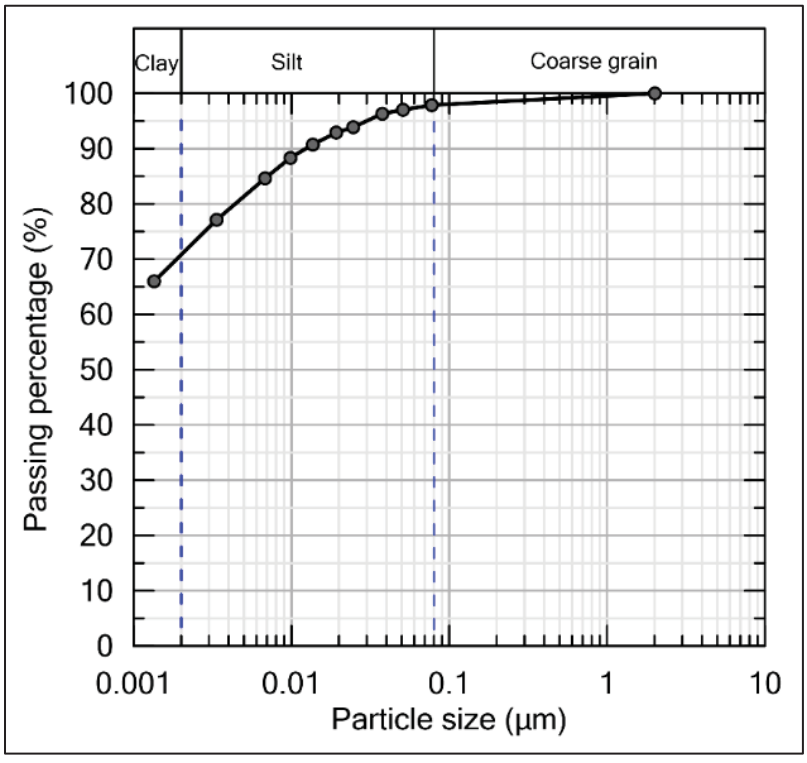

Figure 5.1 Particle size gradation of Champlain clay soil
using the sedimentation (hydrometer) analysis (ASTM D7928)

Clay subsamples with dimensions of 1 × 1 × 0.2 cm (width × length × thickness) were cut in the humid chamber with a high-precision knife. The freeze-drying method was employed to prepare the fractures for the SEM imaging. The clay was immersed in liquid nitrogen with a boiling temperature of -196 °C to be pre-frozen for the freeze-drying procedure. The frozen material was installed in the chamber of a commercial freeze-drying device manufactured by Labconco Inc. Sublimination was conducted under vacuum (pressure < 0.2 mbar) to dry the soil samples for the imaging. The imaging was performed with a Hitachi S-3600N scanning electron microscope. In SEM device, a high-energy electron beam scans the surface of the sample, generating signals as secondary electrons and backscattered electrons. These signals are detected and processed to produce an image with reasonable clarity and depth of field. This apparatus offers magnification levels ranging from 30x to over 500,000x, enabling visualization of the soil structure at the nanoscale. The imaging operation was done in high-vacuum mode (< 1 Pa) on the SEM machine. Before using SEM, electrically insulating samples, like soils, must be coated with a thin layer of conducting material (e.g., carbon or gold). The coating procedure was performed by means of a gold sputter coating K550X apparatus in order to increase the efficiency of high-resolution imaging. These steps are illustrated in Figure 5.2. The imaging of the clay sample surfaces was conducted with the lens positioned perpendicular to the surface (i.e., at a tilting angle of zero degrees). This approach eliminates the need for any adjustments to compensate for tilting or shadow effects during image processing (Luo et al. 1998).

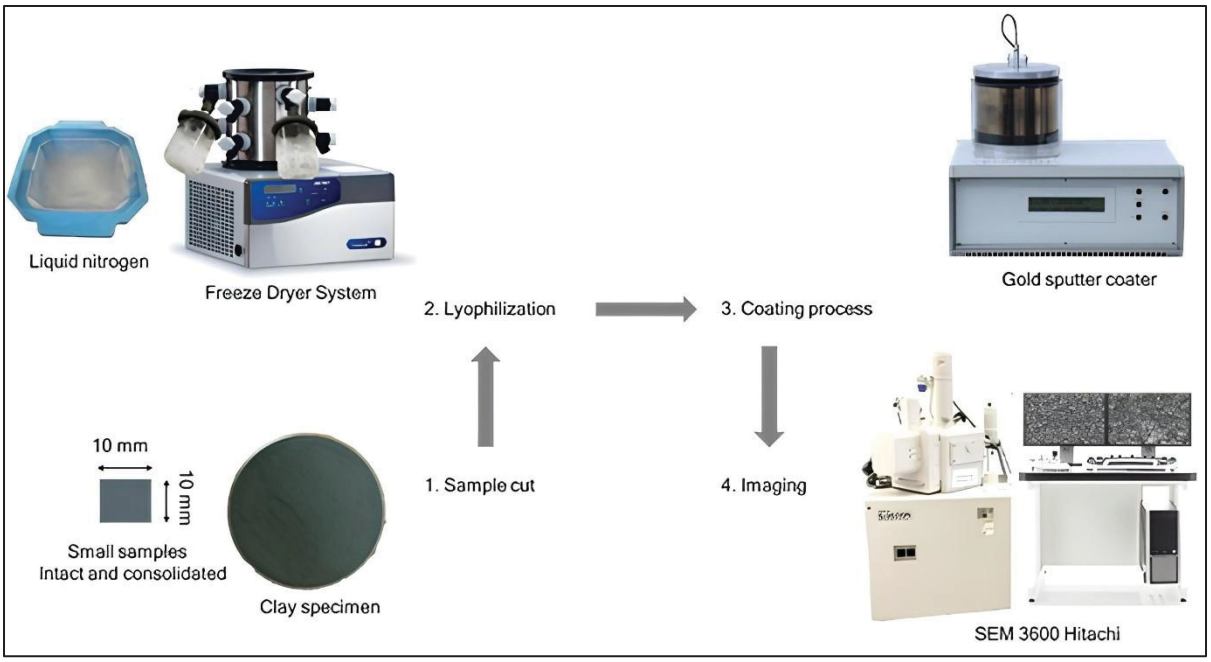

Figure 5.2 A visual representation of the sample preparation procedures employed for digital imaging

Figure 5.3 shows SEM images of the Champlain clay sample with lower gray levels (darker pixels) for pores and higher gray levels (lighter pixels) for the solid phase as the individual and group of clay particles. SEM imaging was conducted across a range of operating conditions. The accelerating voltages were varied between 10 and 30 kV, while magnification levels were adjusted from 1000× to 7000×. Multiple images were captured at different combinations of these parameters to enable a parametric study examining how these variables affect image analysis outcomes.

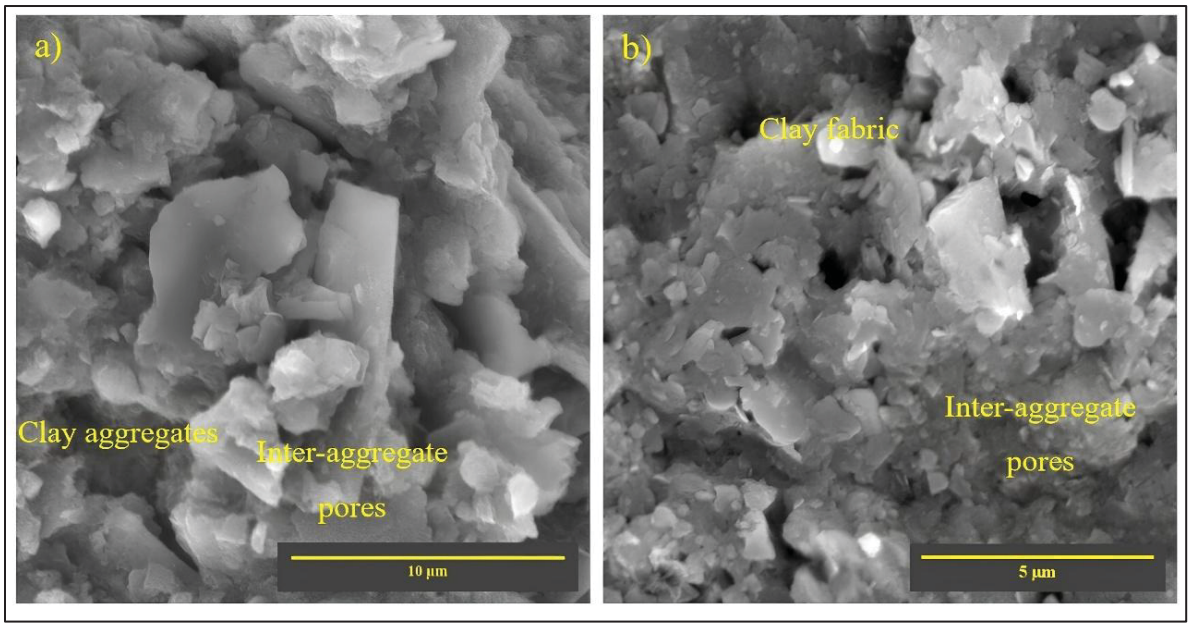

Figure 5.3 SEM images of the Champlain marine clay microstructure, a) magnitude of 4000×; b) magnitude of 7000×

5.3 Image processing

The image processing was done with a MATLAB script. The images had a resolution of 1280 x 866 pixels. Segmentation was conducted based on Otsu's method in order to identify distinct regions on the clay sample surface and to segment the pores and clay particles. After the segmentation, two fabric orientation calculation methods (FOCM-I and FOCM-II) were applied. The accuracy and reliability of the fabric orientation calculation process were validated through comparison with anisotropy results of previously published SEM images from the literature.

5.4 Segmentation and porosity calculation

The multi thresholding function *multitresh* in MATLAB was used to delineate regions with similar gray levels in the images to distinguish the clay structural features. The determination of the appropriate threshold number and values depends highly on the geological origin of the soil sample. The optimal number of thresholds (T) was obtained by varying T from 1 to 6 for

several images and by inspecting the segmented images. Figures 5.4 and 5.5 show an SEM image and examples of segmentation results for T values from 3 to 5, respectively. The segmentation procedure begins with image preprocessing to enhance contrast between pore and particle regions. The lowest threshold for each T value was used to distinguish large pores and particles on the clay surface. The segmented pores and particles for each T value are presented in the left and right panel, respectively. The color legend represents the cumulative number of identified pores (column a) and particles (column b). As shown in Figure 5.5, higher threshold numbers ($T \geq 5$) can result in very low pore surfaces and single particles that are segmented as a large number of smaller particles. This multi-threshold approach enables the evaluation of segmentation sensitivity and the identification of optimal threshold values to distinguish between pores and particles. As a result, the reasonable distinguish was obtained by considering $T = 4$. Based on this threshold limit, a multi gray scale leveling was used for all images of samples S3 and S7 ($T = 60.13; 98.96; 122.87; 157.29$). These levels correspond to the average values that were obtained for 400 SEM images. Porosity was calculated as the number of pixels with gray levels below the first threshold divided by the total pixel count.

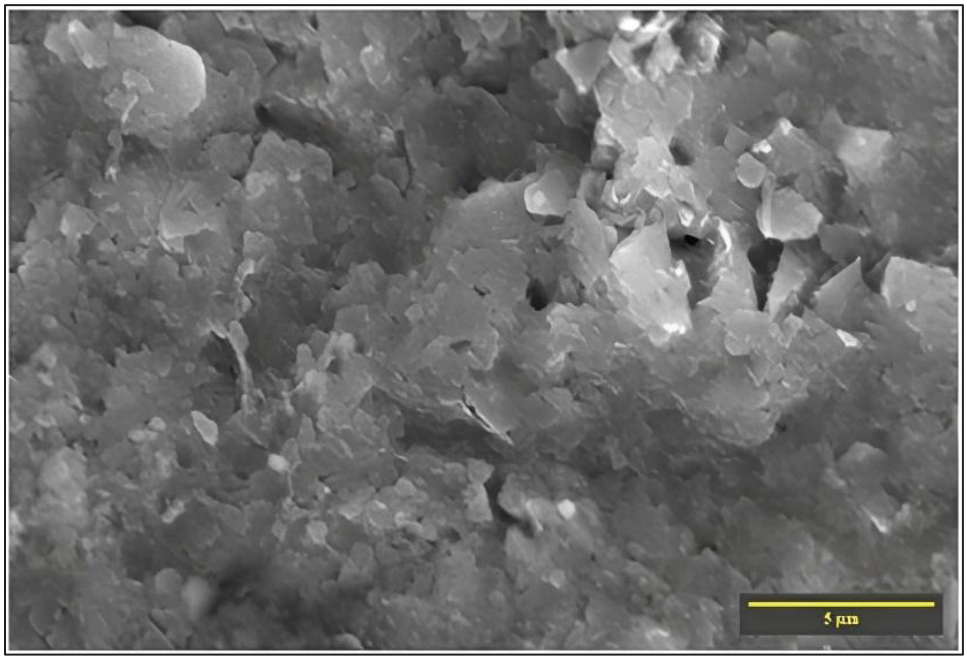

Figure 5.4 Original SEM image utilized for the threshold analysis representation (magnification at 5000 ×)

These microscale porosity values (P) do not correspond to the total clay porosity that can be calculated from the clay water content. This parameter only includes the larger inter-aggregate pores. Promising research efforts to link microscale porosity (P) and macroscopic engineering properties (n) are comprehensively reviewed by Romero and Simms (2008).

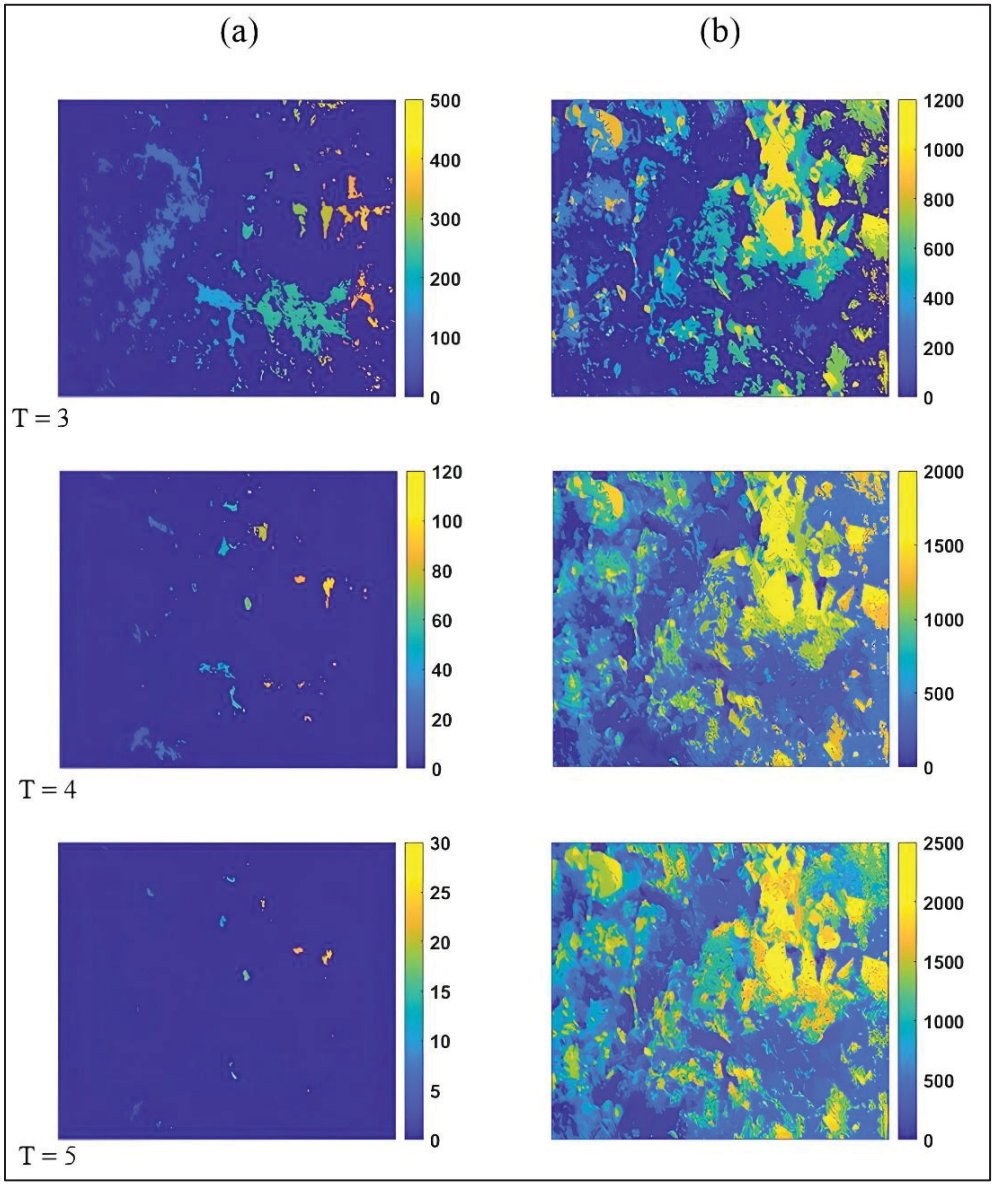

Figure 5.5 Three different applied threshold levels (T = 3 to T = 5)
for distinguishing particles zone from pore spaces,
a) contours of segmented pores; b) contours of segmented particles

5.4.1 First fabric orientation calculation method (FOCM-I)

The first method, to quantify the anisotropy, FOCM-I, was formulated by Davis (1986), and utilized by Martínez-Nistal et al. (1999). Based on this vector-based method, the overall anisotropy index ($\bar{L}$) and the mean fabric orientation (θ) are calculated based on the length of the major axes of the solid phase regions segmented (Martínez-Nistal et al. 1999):

$$\theta = tan^{-1}\left[\frac{\sum_{i=0}^{n} D_{i,major} \times sin\theta_i}{\sum_{i=0}^{n} D_{i,major} \times cos\theta_i}\right] \quad (5.1)$$

$$\bar{L} = \frac{\sqrt{\left(\sum_{i=0}^{n} D_{i,major} \times sin\theta_i\right)^2 + \left(\sum_{i=0}^{n} D_{i,major} \times cos\theta_i\right)^2}}{\sum_{i=0}^{n} D_{i,major}} \quad (5.2)$$

where $D_{i,major}$ and θ_i are respectively the major axis length and orientation for segmented region *i*, and *n* refers to the total number of segmented regions. The $D_{i,major}$ and θ_i values are obtained through the MATLAB function *regionprops*. Figure 5.6 shows a schematic view of a particle, its minor and major axes, and the angle with respect to the horizontal axis.

The anisotropy index $\bar{L}$ ranges from 0 to 1. Based on $\bar{L}$, the fabric orientation is classified into various categories to describe the uniformity of particle alignment within the clay fabric:

$\bar{L}$ =1	maximum degree of iso-orientation
0.21 < $\bar{L}$ < 1	highly oriented fabric
0.15 < $\bar{L}$ < 0.21	weakly oriented fabric
$\bar{L}$ < 0.15	randomly oriented fabric

5.4.2 Second fabric orientation calculation method (FOCM-II)

The second method to quantify anisotropy, FOCM-II, was proposed by Tovey et al. (1989) and utilized by Tovey and Krinsley (1990) and Sokolov and O'Brien (1990). It is based on the polar graph of the segmented region orientation obtained through the MATLAB function *regionprops*.

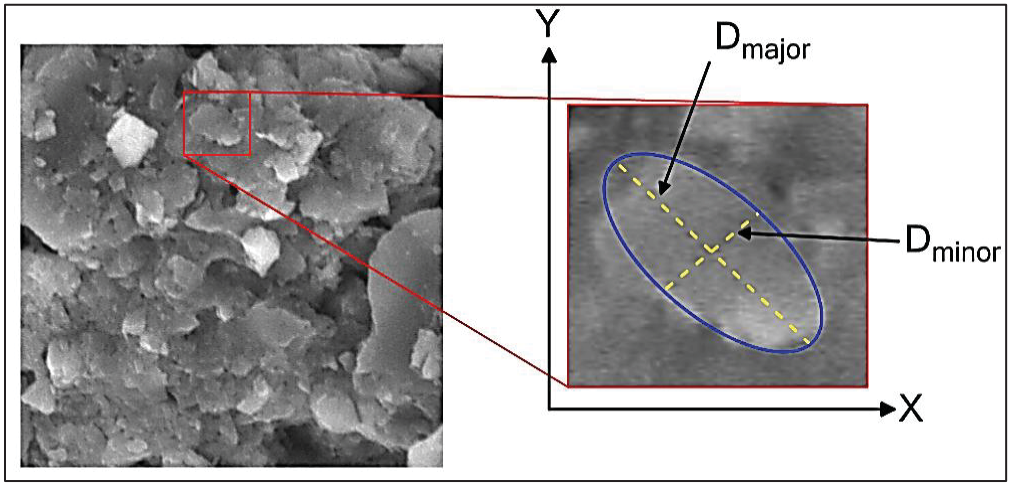

Figure 5.6 Schematic view of fitting ellipse for the identified particles

An example of a polar graph is shown in Figure 5.7. Each bar denotes the number of segmented regions corresponding to an orientation bin of 10°. The radial axis indicates the number of segmented regions for each bin. Additionally, a 360° rose diagram can be drawn from the polar graph to illustrate the distribution of particle alignments. The rose diagram is obtained by duplicating the bins presented in the first two quadrants of the polar graph (Fig. 5.7a) in the other two quadrants in the rose diagram (Fig. 5.7b). With FOCM-II, the anisotropy is described by fitting an ellipse to the rose diagram of segmented region orientations.

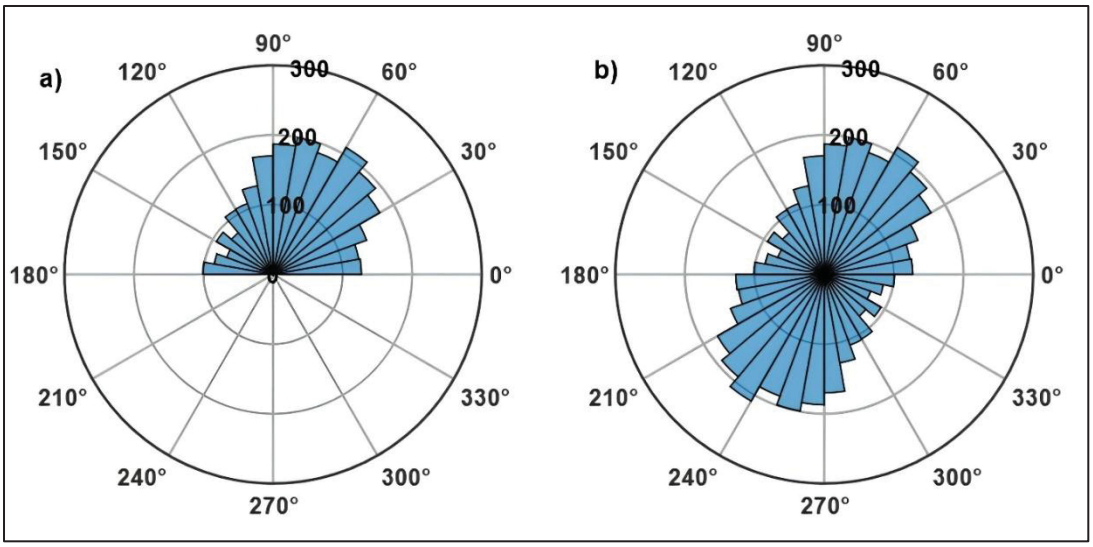

Figure 5.7 Illustration of directionality of the clay particles based on the original SEM image, a) Polar graph; b) Rose diagram

Figure 5.8 summarizes the method applied to define the fabric orientation based on the best-fit ellipse. The polar data (i.e. the number of segmented regions r corresponding to orientation θ) is first converted to Cartesian coordinates (x, y) using $x = r\cos(\theta)$ and $y = r\sin(\theta)$ (Fig. 5.8a). Subsequently, the least squares algorithm of Gal, (2024) is used to fit the conic representation of an ellipse on the data (Fig. 5.8b). This enables the extraction of the ellipse major and minor axes (a, b). The orientation index (I_o) is based on a and b (Tovey et al., 1989 and Shi 1998):

$$I_o = 1 - \frac{b}{a} \tag{5.3}$$

In this method, I_o varies from zero for a truly random orientation to unity for a perfectly aligned fabric.

Equation 5.3 can also be directly applied to the identified particles in segmented regions with minor and major axes (D_{major} and D_{minor} in Fig. 5.6) instead of the ellipse fitted to the rose diagram representing the number of segmented regions corresponding to each orientation bin. In this case, the orientation index is calculated using two average computation methods.

FOCM-II-Avg-I involves calculating the mean aspect ratio of the segmented regions. The orientation index I_{o_I} based on this method is given by the following relationship:

$$I_{o\_I} = 1 - \frac{\sum_{i=1}^{N} \frac{D_{i,minor}}{D_{i,major}}}{N} \tag{5.4}$$

Alternatively, FOCM-II-Avg-II considers the meaning of the major and minor axes individually ($\overline{D}_{major}$, $\overline{D}_{minor}$):

$$\overline{D}_{major} = \frac{\sum_{i=1}^{N} D_{i,major}}{N} \tag{5.5}$$

$$\overline{D}_{minor} = \frac{\sum_{i=1}^{N} D_{i,minor}}{N} \tag{5.6}$$

$$I_{o\_II} = 1 - \frac{\overline{D}_{minor}}{\overline{D}_{major}} \tag{5.7}$$

where I_{o_I} is the orientation index for method FOCM-II-Avg-II. Both orientation indexes, I_{o_I} and I_{o_II} are measures of the overall anisotropy of the segmented regions. Both indices increase from 0 for random orientation to 1.0 for perfectly orientated microfabric.

Both indices, I_o and $\overline{L}$, range from 0 to 1, but $\overline{L}$ has explicitly defined classification ranges ($\overline{L}$ < 0.15 for random, 0.15-0.21 for weakly oriented, > 0.21 for highly oriented, and 1 for maximum orientation), while I_o is simply interpreted on a continuous scale with no specified classification ranges.

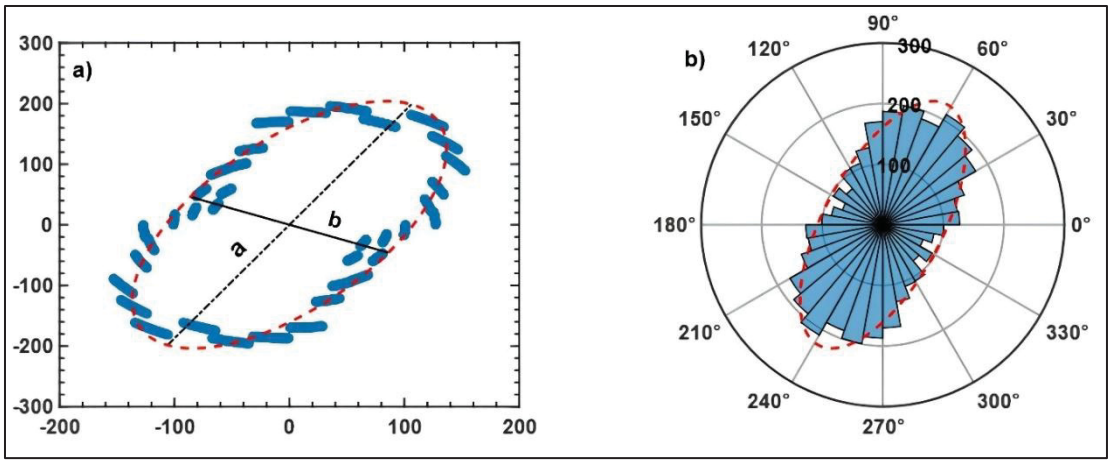

Figure 5.8 Schematic representation of directionality analysis of the original SEM image with the ellipse-fitting method, a) Ellipse fitting in cartesian coordinates; b) Ellipse fitting for rose diagram of identified particles

5.5 Numerical results and discussion

Investigations were carried out to study the effects of the accelerating voltage and magnification on anisotropy for Champlain clay samples, S3 and S7. This section presents the script validation and results for parametric study, which evaluates the influence of SEM imaging parameters on microstructural characterization. The analysis reveals key sensitivities between operating conditions and measured fabric properties, demonstrating how variations in voltage and magnification can substantially alter the interpretation of clay microstructure, especially anisotropy. Special attention is given to the response of sensitive clay samples to different imaging conditions, as they show unique challenges in microscopic analysis due to their complex particle arrangements and distinctive pore networks.

5.5.1 Script validation

Three comparisons were conducted to validate the MATLAB script for SEM image analyses. In the first step, the anisotropy index was obtained with FOCM-I for the SEM images shown in Fig. 5.9 (a) and (b). The $\bar{L}$ values obtained with the MATLAB script are compared in Table 5.2 with the results presented by Martinez-Nistal et al. (1999) and Mitaritonna et al. (2014). In the second step, the image by Tovey and Dadey (2002) shown in Fig. 5.9 (c) was used to

validate the FOCM-II method. Table 5.2 compares the I_0 value presented by Tovey and Dadey (2002) with the value obtained using the MATLAB script. It reveals a good agreement for both methods with a maximum difference of 7.8 %.

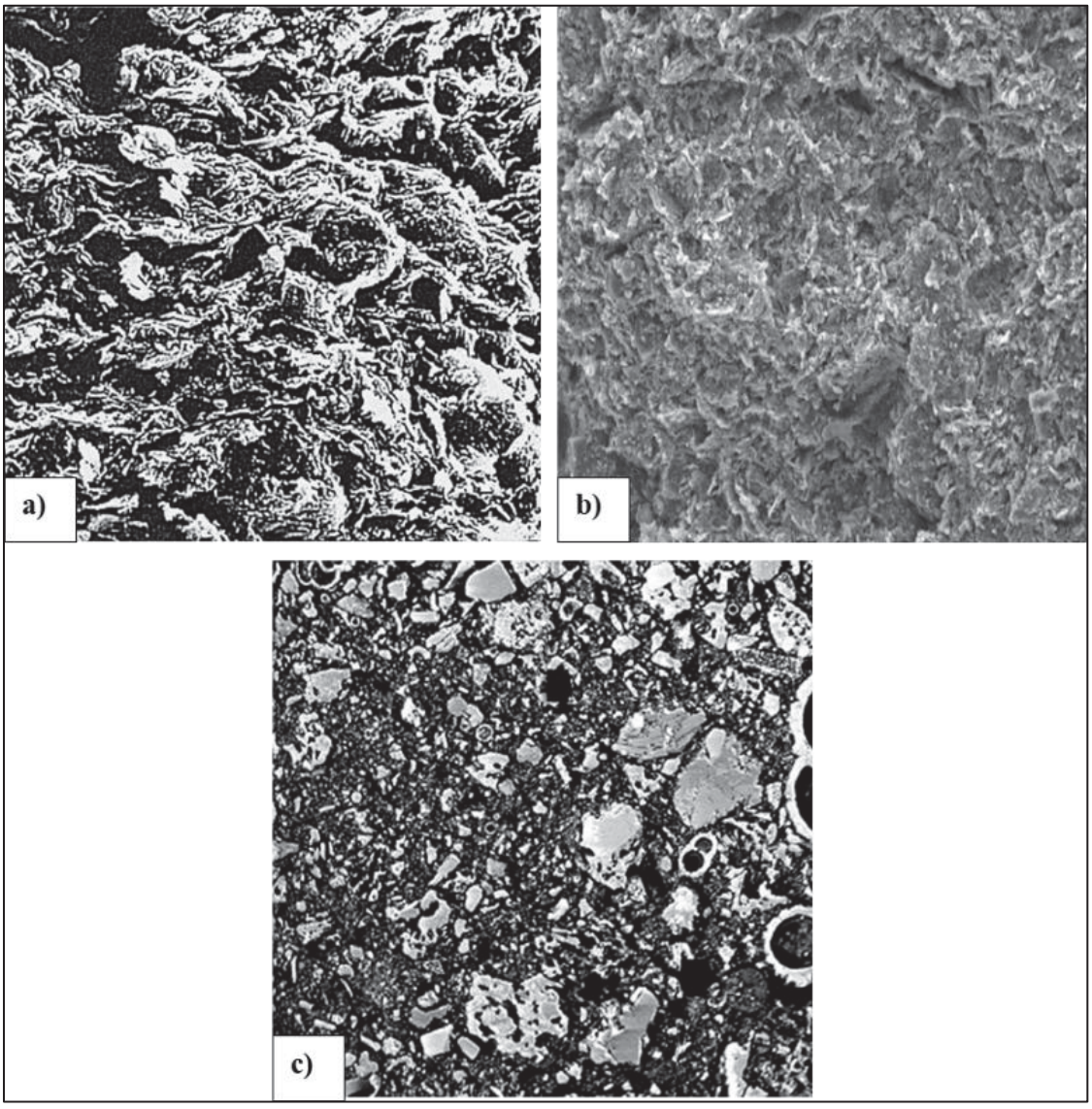

Figure 5.9 SEM images from previous studies for verifying the fabric orientation calculation procedure. a and b) FOCM-I by Martinez-Nistal et al. (1999) and Mitaritonna et al. (2014), respectively; c) FOCM-II by Tovey and Dadey (2002)

Table 5.2 Comparison of anisotropy index of the SEM image according to different methods

Method	Image	Study	Anisotropy Index	Difference %
FOCM-I	a	Current	0.256	7.8
		Martinez-Nistal et al. (1999)	0.277	
	b	Current	0.132	1.2
		Mitaritonna et al. (2014)	0.130	
FOCM-II	c	Current	0.110	0.8
		Tovey and Dadey (2002)	0.109	

5.5.2 Parametric studies

This section is dedicated to parametric studies conducted to investigate the influence of applied voltage and magnification on the anisotropy and orientation indices obtained through various methods. All results presented in this section pertain to intact samples before consolidation unless otherwise stated.

Figure 5.10 examines the effects of applied voltage on FOCM-I results for samples S3 and S7, using magnifications of 1000×-4000× and 1500×-4500×, respectively, to show two different magnification steps. For any magnification, changing the voltage applied to sample S3 surface can cause the anisotropy index to correspond to three different classifications (randomly, weakly, and highly oriented fabrics). The $\bar{L}$ range for sample S7 spans randomly to weakly oriented fabric classification. Analysis of voltage across these two samples indicates that within the considered magnification range, a voltage of 20 kV yields the maximum anisotropy index in most cases.

The influence of the applied voltage on the orientation index obtained with ellipse-fitting methods for different magnifications for samples S3 and S7 is illustrated in Figs. 5.11 and 5.12. Regardless of the sample and magnification, increasing the voltage has an insignificant effect on FOCM-II-Avg-I and FOCM-II-Avg-II, resulting in an almost constant orientation index.

However, voltage changes impacted FOCM-II and led to differences up to 100% in the orientation index results, which ranged from 0.06 to 0.72 and 0.02 to 0.65 for samples S3 and S7, respectively. It is evident from Figs. 5.11 and 5.12 that for both samples and most of the investigated magnifications, the lowest index is obtained using FOCM-II and a voltage of 15 kV. Additionally, the highest orientation index for S3 and S7 occurred respectively at voltages of 25 kV and 20 kV for most images, respectively.

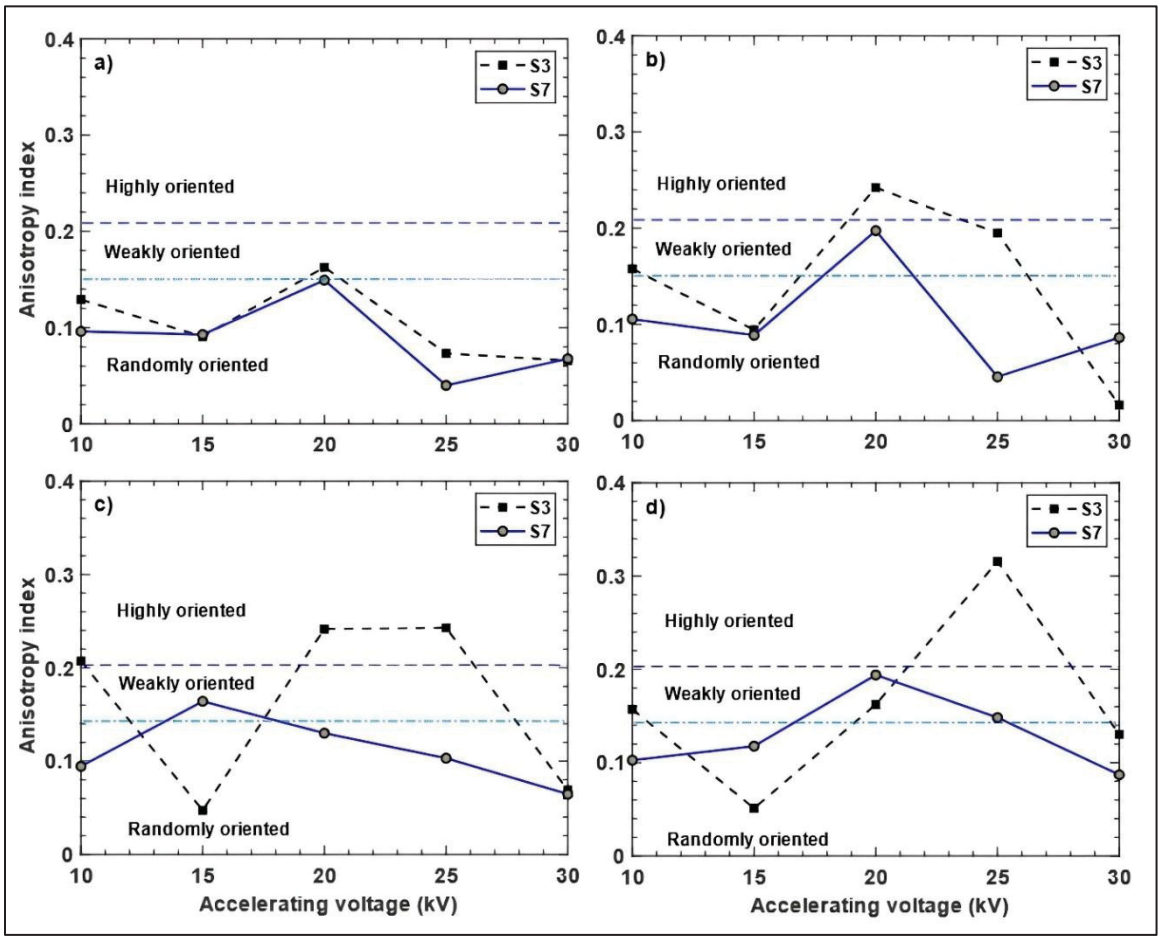

Figure 5.10 Effect of voltage on SEM imaging of the intact samples of S3 and S7 based FOCM-I approach; a) 1000×; b) 2000×, c) 3000×, d) 4000×

FOCM-II-Avg methods are robust in quantifying clay fabric anisotropy due to their focus on particle elongation rather than absolute orientation. These methods recognize that particle shape, specifically deviation from circularity, is a primary indicator of potential fabric

anisotropy. FOCM-II-Avg-I captures the inherent tendency of particles to create anisotropic structures. This method's independence from absolute orientation is advantageous as it measures an intrinsic property of the particle assembly shape elongation. The method's stability across voltage variations demonstrates its ability to capture fundamental particle characteristics despite variations in imaging conditions. FOCM-II-Avg-II, a different mathematical approach, also provides a comparable characterization of shape-based anisotropy. The consistency between these methods further validates their theoretical foundation. The relationship between these indices and the original FOCM-II method provides a framework for fabric analysis, capturing the combined effects of particle shape and orientation distribution.

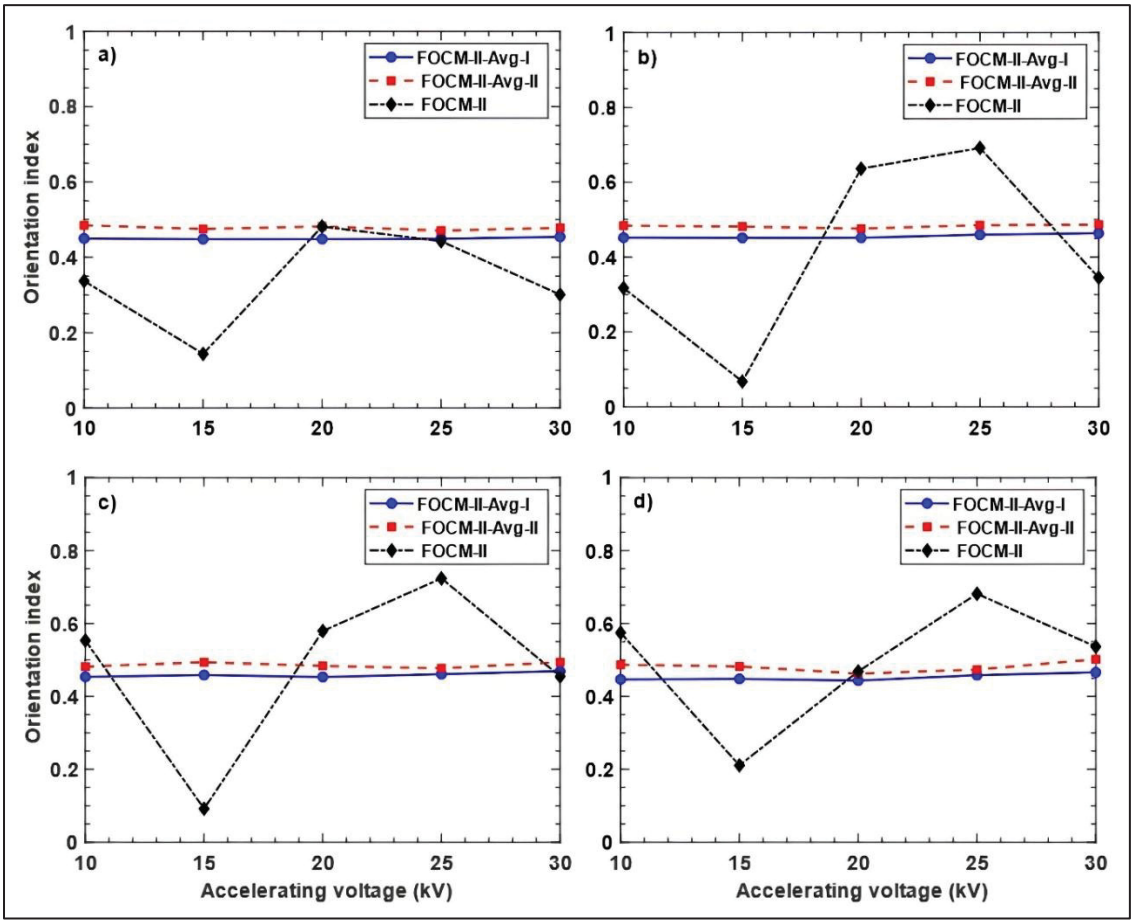

Figure 5.11 Effect of applied voltage on SEM imaging of the intact sample S3 based on ellipse-fitting method considering four different magnifications: a) 1000×; b) 2000×, c) 3000×, d) 4000×

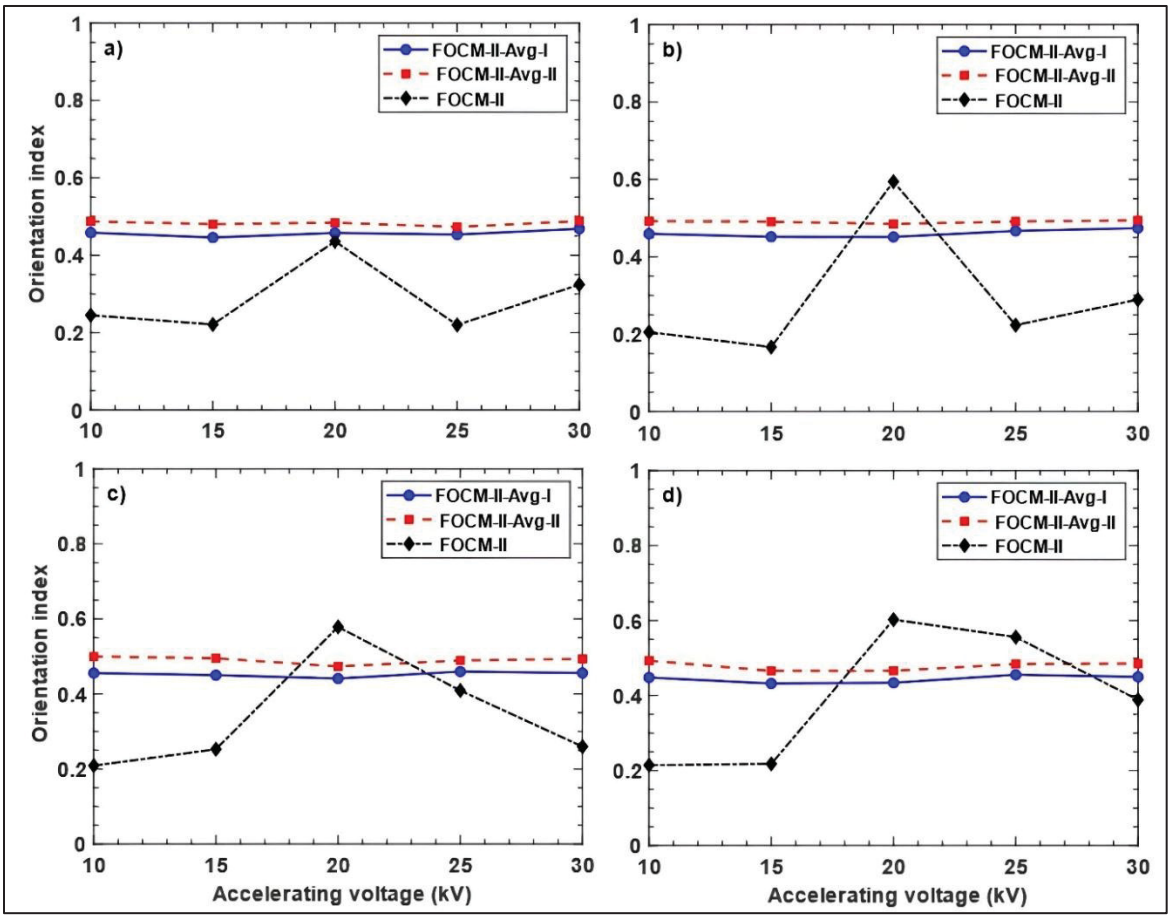

Figure 5.12 Effect of applied voltage on SEM imaging of the intact sample S7 based on ellipse-fitting method considering four different magnifications: a) 1000×; b) 2000×, c) 3000×, d) 4000×

The effect of magnification on the variation of $\bar{L}$ at different voltages is investigated for samples S3 and S7 in Fig. 5.13. For both samples, the anisotropy index varies with magnification. Depending on the voltage and the sample, a magnification increase can lead to a higher or lower anisotropy index. As it was noted in Fig. 5.10, for most magnification values, a voltage of 20 kV leads to a higher $\bar{L}$. The results for both samples indicate that voltages of 10 kV and 15 kV are less affected by magnification compared to higher voltages.

Figures 5.14 and 5.15 show the influence of magnification on the orientation index calculated with the ellipse fitting methods for samples S3 and S7, respectively. As with the voltage in Figs. 5.11 and 5.12, it can be observed that the magnification has an insignificant influence on

the orientation indices for the two average computation methods, namely FOCM-II-Avg-I and FOCM-II-Avg-II.

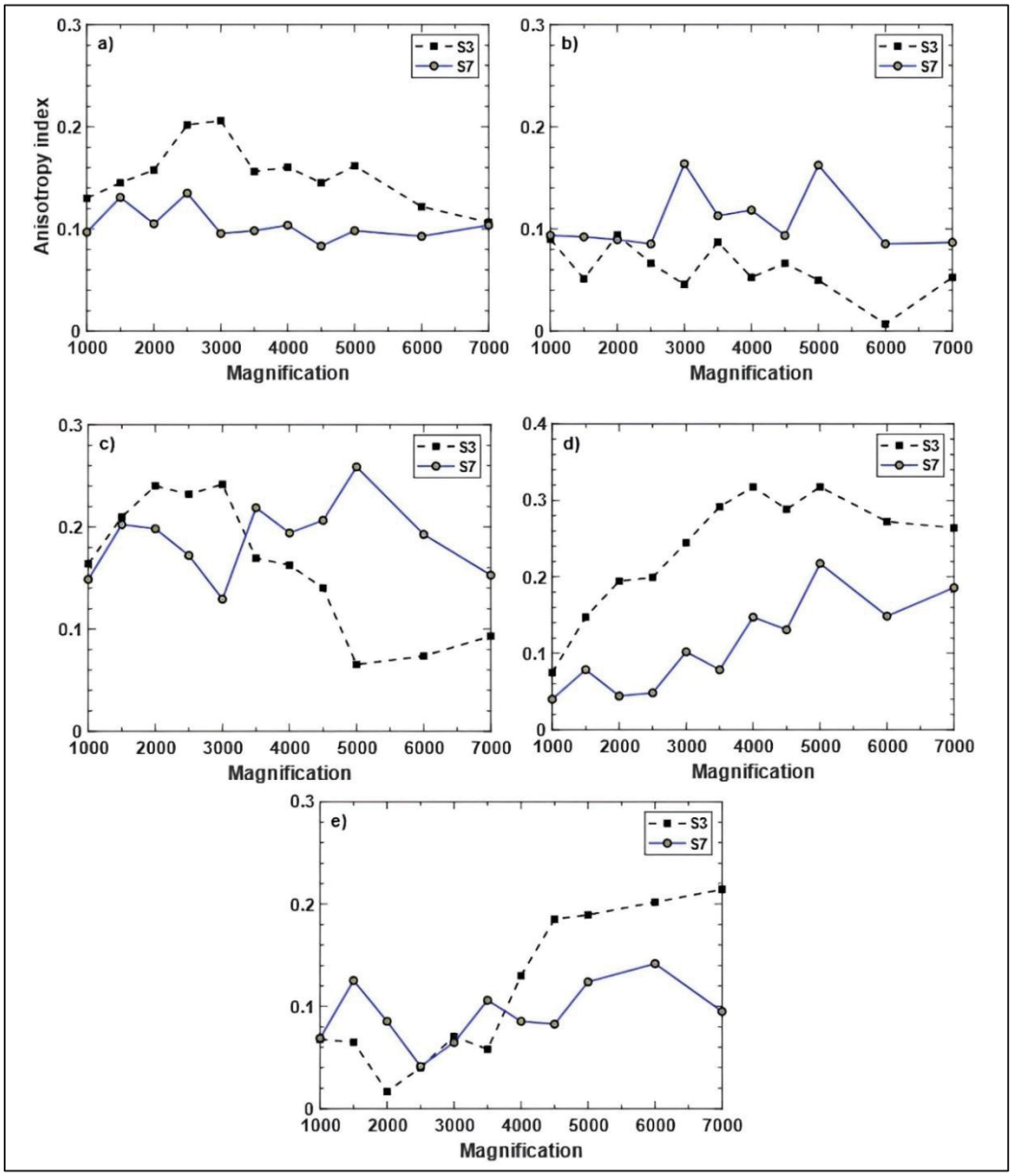

Figure 5.13 Magnification analysis of the intact sample S3 and S7 by FOCM-I method, through usage of different voltage, a) 10 kV, b) 15 kV, c) 20 kV, d) 25 kV, e) 30 kV

The indices obtained with the FOCM-II method are more variable, especially for a voltage above 15 kV. At voltage 10 kV, anisotropy index approaching approximately 0.6 and 0.2 for

samples 3 and 7, respectively, while at other voltages, the index changes by 95% in S3 ranging between 0.02 and 0.63, and 91% ranging between 0.02 and 0.71 in S7. The maximum differences occur at V = 25 kV and V = 10 kV for S3 and S7, respectively.

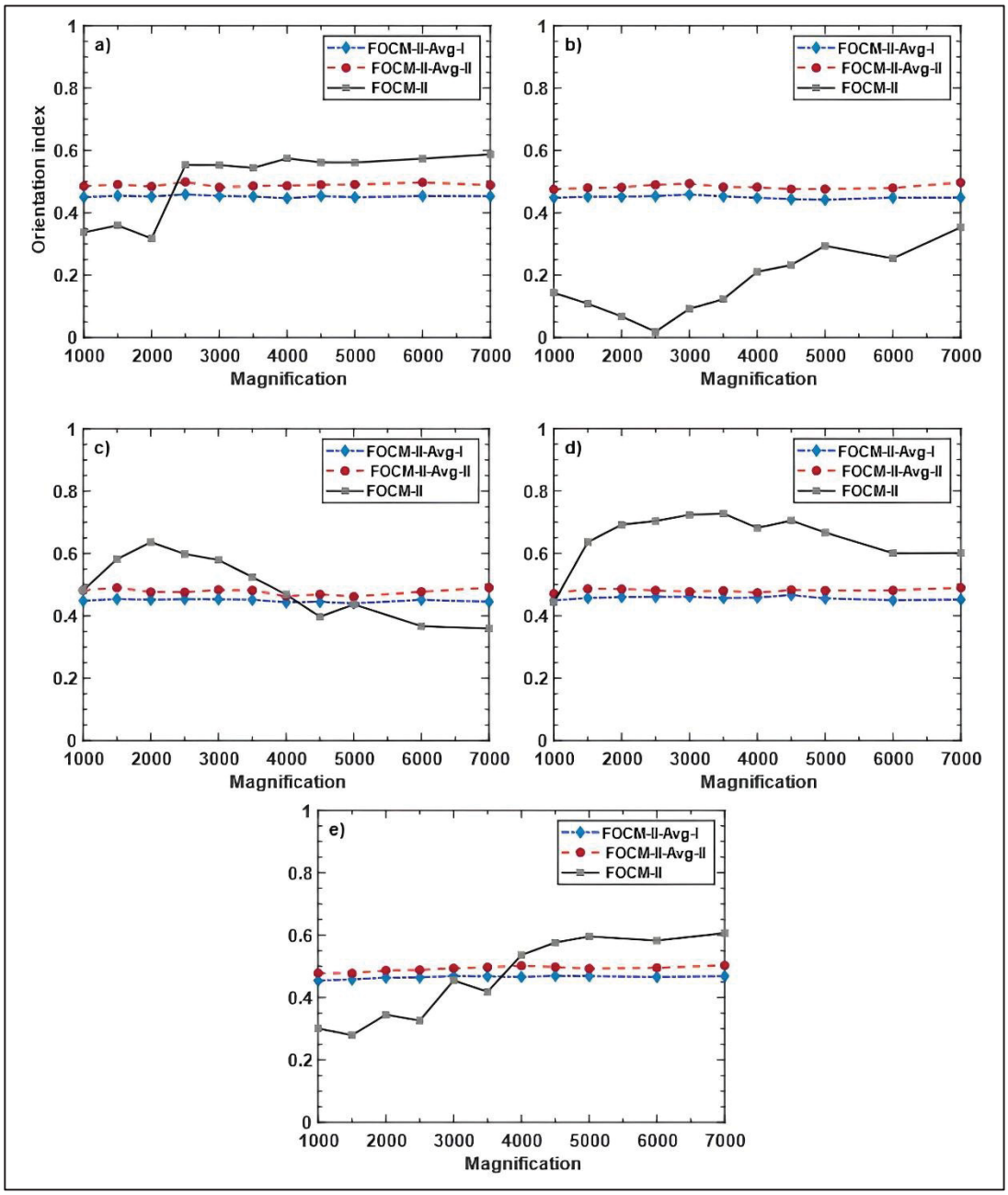

Figure 5.14 Influence of magnification with ellipse-fitting methods and different voltages for intact sample S3, a) 10 kV, b) 15 kV, c) 20 kV, d) 25 kV, e) 30 kV

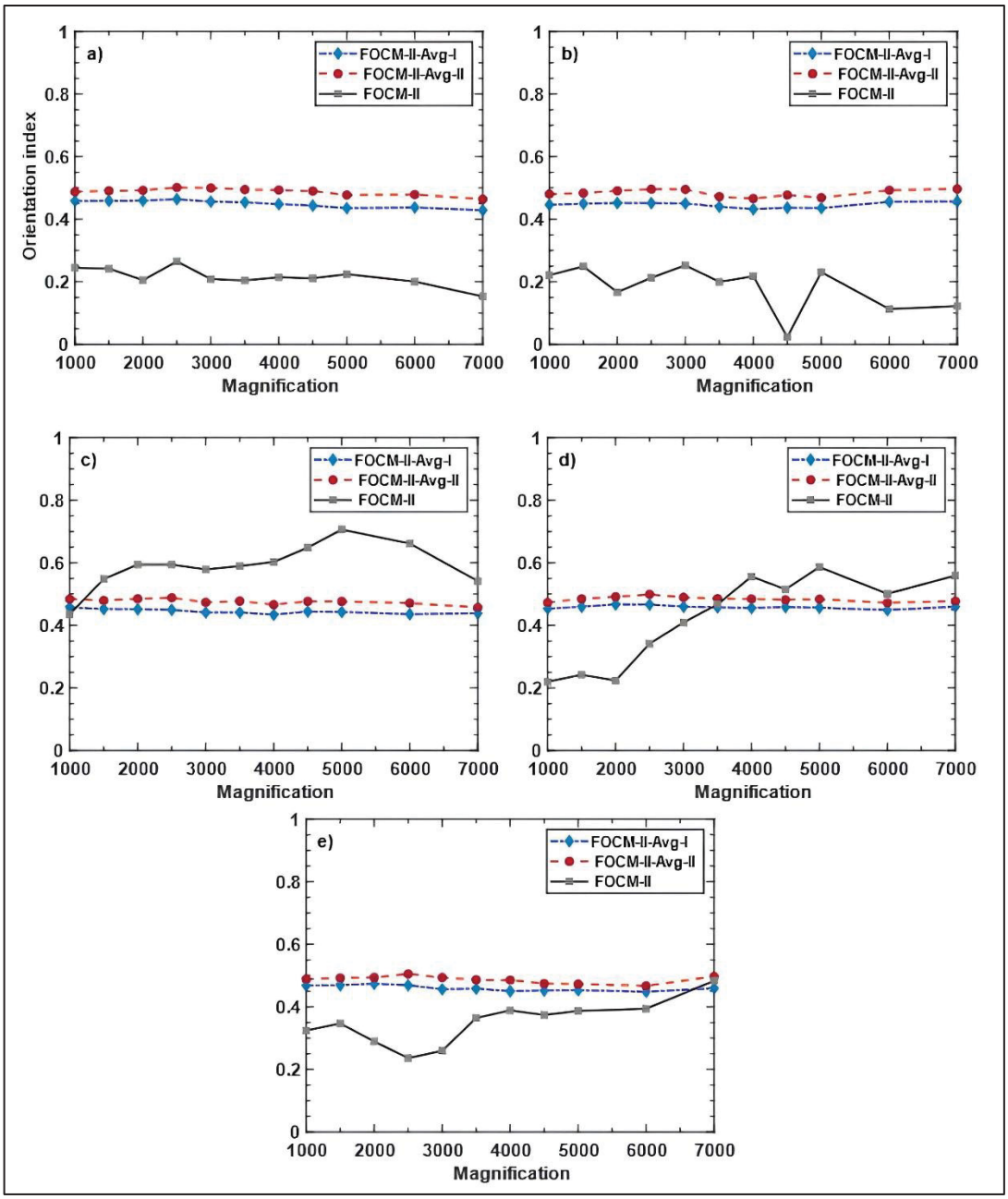

Figure 5.15 Influence of magnification with ellipse-fitting methods and different voltages for intact sample S7, a) 10 kV, b) 15 kV, c) 20 kV, d) 25 kV, e) 30 kV

The effects of voltage variations on the anisotropy and orientation indices obtained with methods FOCM-I and FOCM-II for sample S3 after consolidation are depicted in Figs. 5.16 and 5.17, respectively. As seen in Fig. 5.16, the results for FOCM-I indicate that sample 3 is mostly located in the weakly oriented range after consolidation. Figure 5.17 shows that the

sample consolidation caused the orientation indices of FOCM-II, FOCM-II-Avg-I and FOCM-II-Avg-II to approach each other more closely than for the intact samples before consolidation. Magnifications of 1000× and 2000× show closer results. The maximum difference between fitted ellipse methods is 41% at 3000×.

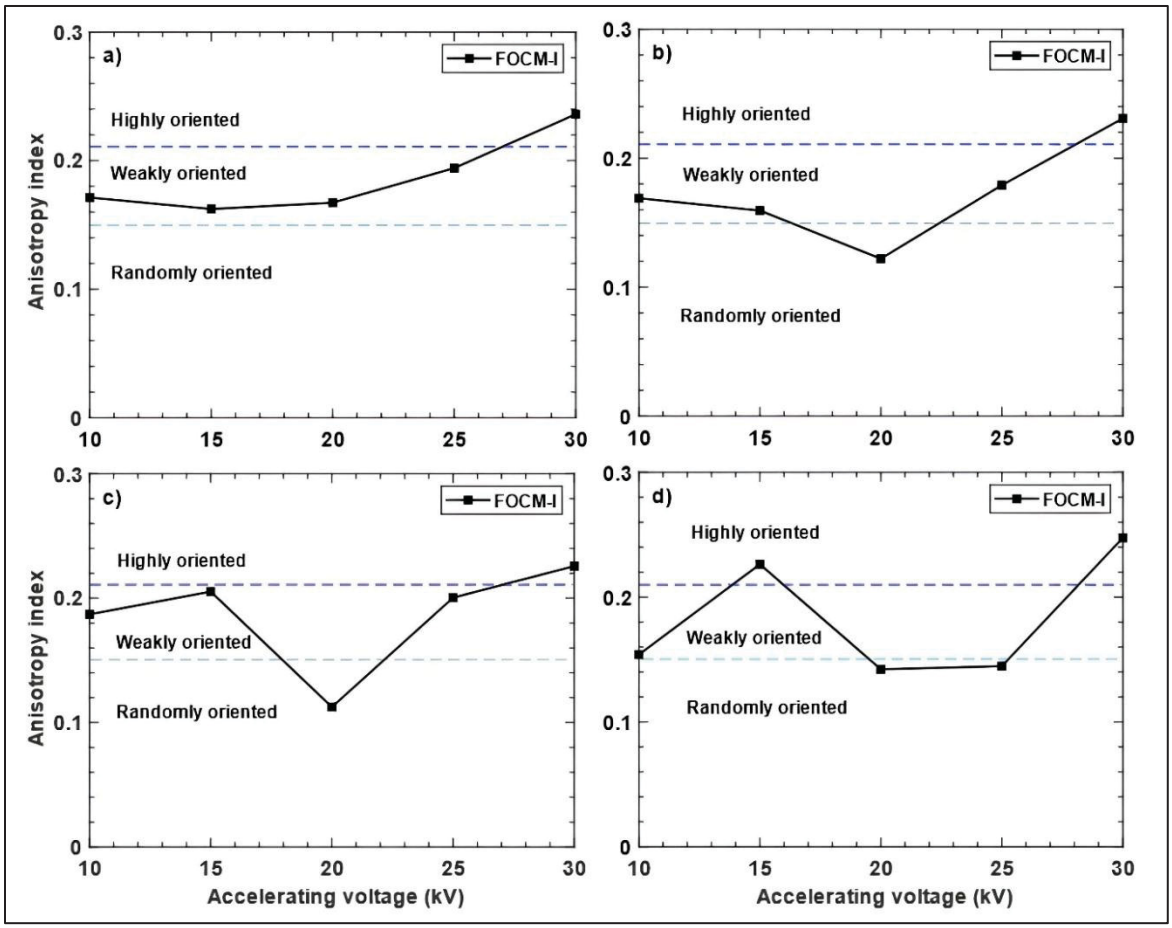

Figure 5.16 Analysis of the effect of applied voltage on SEM imaging of the consolidated sample S3 based on FOCM-I considering four different magnifications: a) 1000×; b) 2000×, c) 3000×, d) 4000×

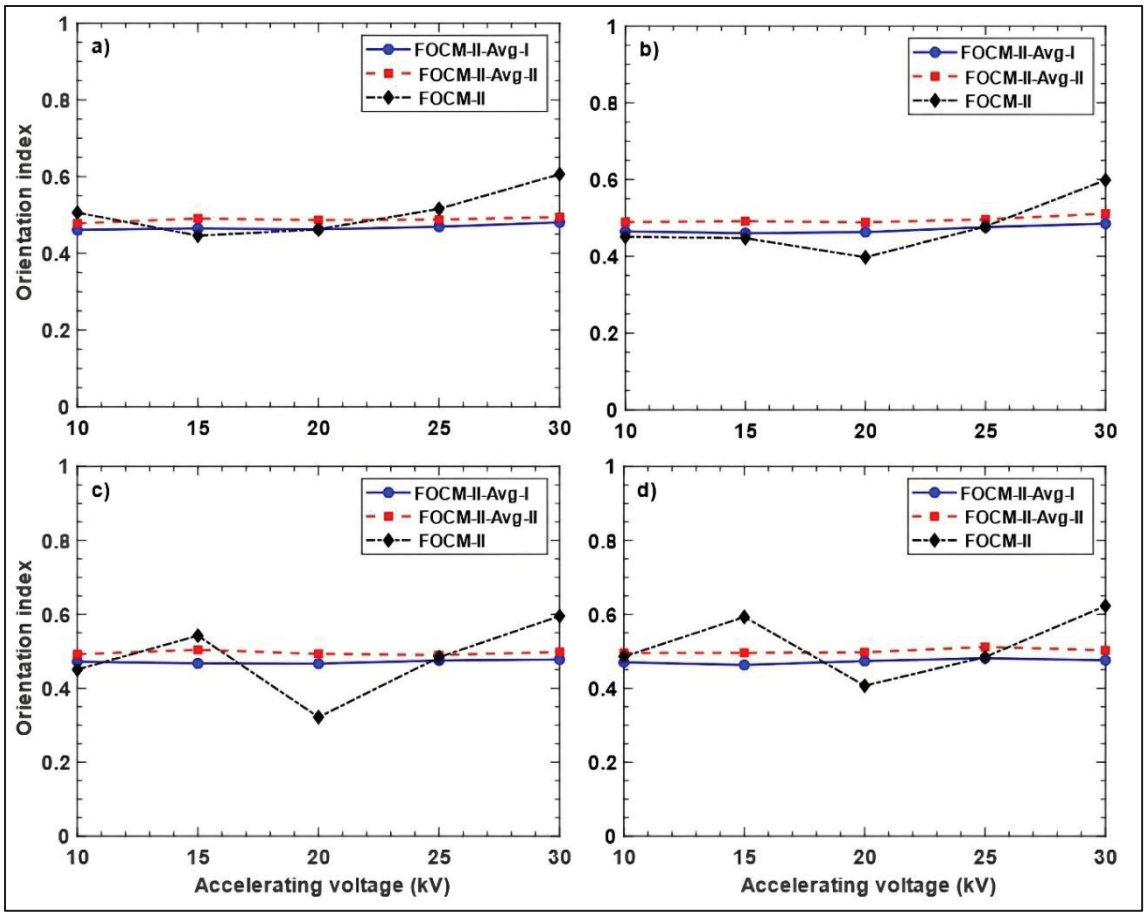

Figure 5.17 Analysis of the effect of applied voltage on SEM imaging of the consolidated sample S3 based on ellipse-fitting method considering four different magnifications: a) 1000×; b) 2000×, c) 3000×, d) 4000×

Figures 5.18 and 5.19 show the influence of magnification on FOCM-I and FOCM-II results for different voltages for sample S3 after consolidation. According to Fig. 5.18, regardless of the voltage, increasing magnification leads to a change in $\bar{L}$ for FOCM-I. Results for voltages of 10 kV and 25 kV correspond to a weakly oriented fabric, while voltages of 15 kV and 30 kV fall close to the boundary between weakly and strongly oriented fabric. The maximum difference between results for different magnification levels is 48% ranging between 0.13 and 0.25 for a voltage of 30 kV (Fig. 5.18e). For ellipse-fitting methods (Fig. 5.19), the anisotropy index obtained for sample S3 after consolidation is almost constant with the magnification level.

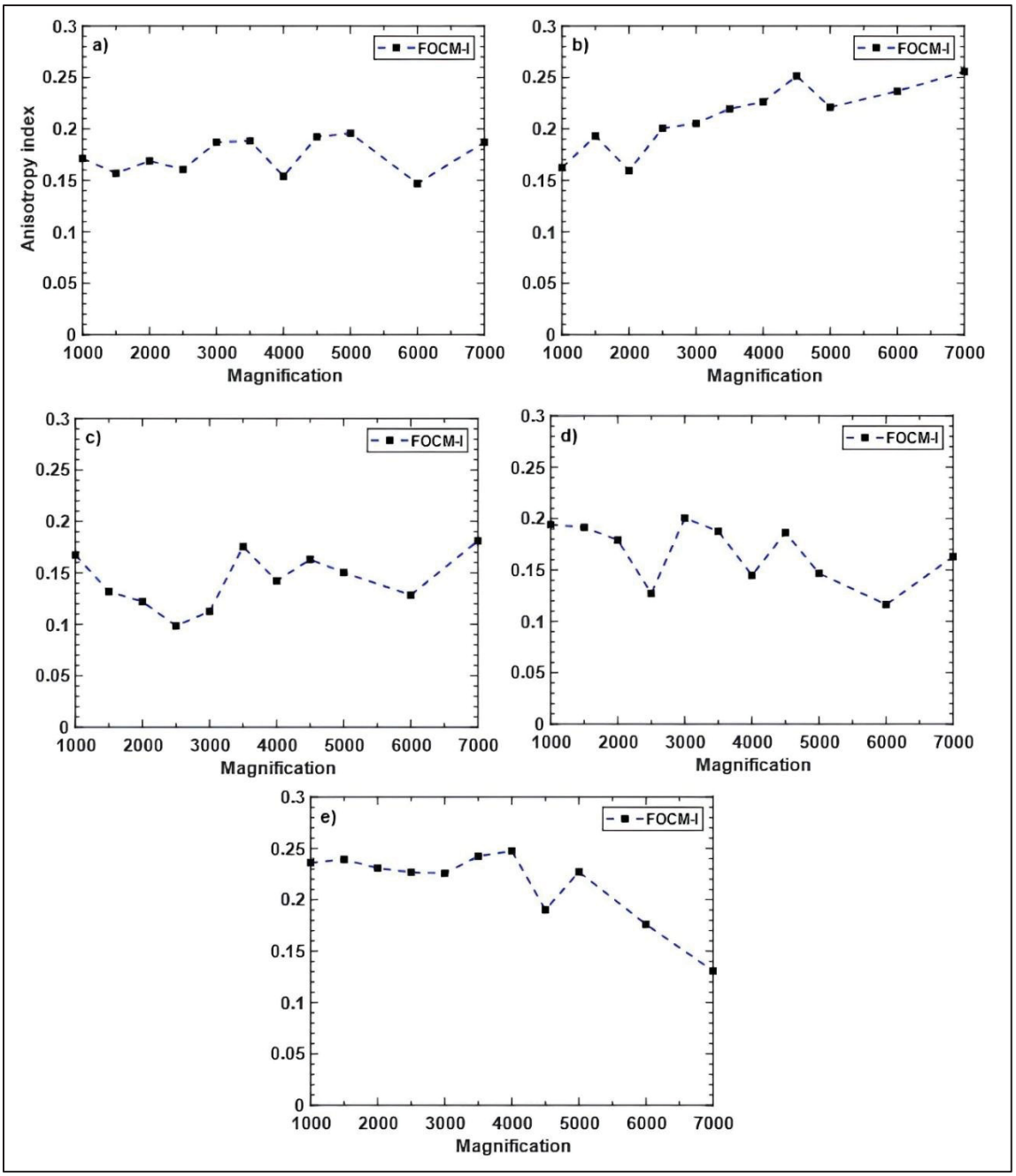

Figure 5.18 Magnification analysis of the consolidated sample S3 by FOCM-I method, through usage of different voltage, a) 10 kV, b) 15 kV, c) 20 kV, d) 25 kV, e) 30 kV

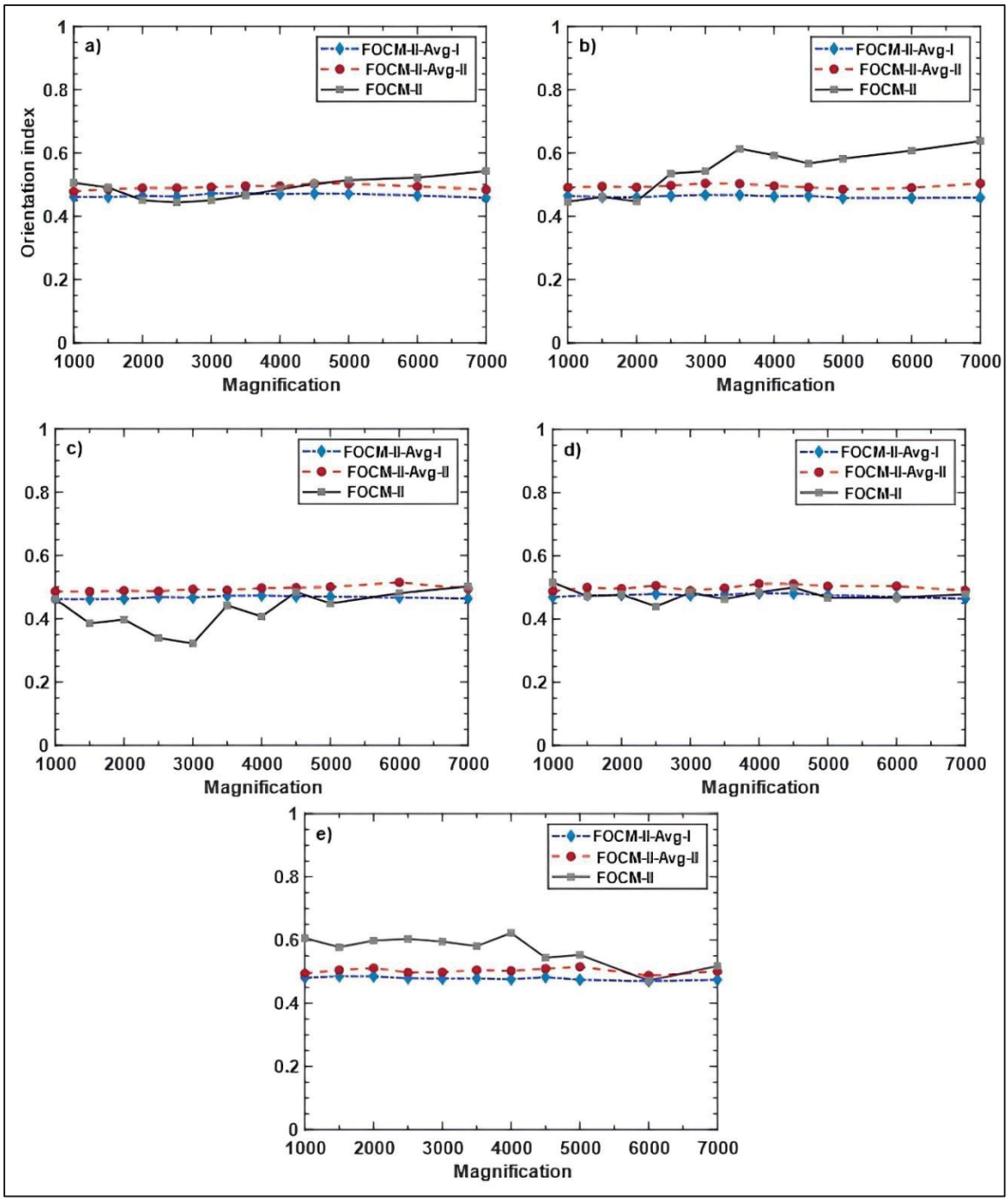

Figure 5.19 Magnification analysis of the consolidated sample S3 by ellipse-fitting method, through usage of different voltage, a) 10 kV, b) 15 kV, c) 20 kV, d) 25 kV, e) 30 kV

Similar values are obtained with the three ellipse-fitting methods. The three orientation indices at voltages of 10 kV and 25 kV approximately coincide. For other voltages, the maximum difference is 36% ranging between 0.32 and 0.5.

The results that have been presented clearly show the influence of voltages and magnifications on FOCM-I and FOCM-II results. It can be concluded that the various methods for calculating the anisotropy and orientation indices are highly sensitive to changes in imaging parameters. In many cases, the influence of imaging parameters on indices does not appear to be systematic and predictable. Results can vary by almost 100%. Consequently, in order to trust and compare the anisotropy and orientation indices extracted from SEM images from different studies, careful attention should be paid to imaging parameters. These observations motivate us to investigate the reasons for the differences between the values of the indices.

A comparison of the anisotropy and orientation indices for several SEM images from the same sample shows that long-range heterogeneity can affect the results. The influence of heterogeneity can be studied by combining the analysis of several images from the same sample. As a first step, four contiguous regions of samples S3 and S7, each region resembling a piece from a 2×2 square puzzle, were captured using SEM at a magnification of 3000× and voltages of 15 kV and 25 kV. This puzzle-like arrangement is depicted for sample S3 in Fig. 5.20a.

Table 5.3 Anisotropy indices of the intact samples S3 and S7 using two different accelerating voltage values

Sample	kV	(FOCM-I)						
		Q1[1]	Q2	Q3	Q4	Avg-Q[2]	Grid-View[3]	Full-View[4]
S3	15	0.039	0.071	0.050	0.012	0.043	0.053	0.021
	25	0.257	0.231	0.334	0.364	0.296	0.309	0.157
S7	15	0.090	0.064	0.030	0.067	0.063	0.087	0.116
	25	0.256	0.361	0.350	0.329	0.324	0.351	0.246

[1]Image quarters at 3000x magnification. [2]The average of quarters. [3]A combination of four quarters of taken image. [4]An overall view image taken at 1500x magnification

Table 5.4 Percent difference between anisotropy analysis results based on FOCM-I approach for different SEM image formations

Sample	kV	Percent Difference %				
		Q1 to Q4	Q & GV	Q & FV	GV & FV	GV & Avg-Q
S3	15	83	78	71	61	19
	25	37	25	57	49	4
S7	15	67	65	74	25	28
	25	29	27	32	30	8

The anisotropy indices obtained by FOCM-I for the four subimages (Q1 to Q4) are reported in Table 5.3 for samples S3 and S7, respectively. As shown in table 5.4, although the four regions or quarters are situated in close proximity to each other, their results exhibit significant discrepancies. For instance, in sample S3 at a voltage of 15 kV, the percentage difference reaches 83%. Next, the four images were merged to form a single grid image at a magnification of 3000× (Fig. 5.20b). Consequently, at a given magnification, a larger surface area of the sample is examined, incorporating more particles and pores into the calculations. Table 5.3 also presents the results for the grid-view SEM images. Irrespective of the sample type, there is a discrepancy between the anisotropy values of grid-view and quarter images of up to 77%. Through analysis, it can be inferred that besides the location of an image of the sample, the

surface area is crucial and can influence the results significantly. Consequently, the larger the surface area, the more particles and pores are analyzed, potentially leading to more accurate results. Finally, as illustrated in Fig. 5.20c, a zone on the same level as the grid-view image with a magnification of 1500 was captured using SEM. These images are referred to as full-view images. The corresponding anisotropy indices are also reported in Table 5.3. A closer examination of the results in both samples reveal a substantial difference between the results, even between the grid-view and full-view images captured from the same surface. Such differences between the two views can be attributed to the difference in pixel numbers of the images. Considering that the grid-view image, created from the combination of four images, has more pixels, it appears that more data is involved in the calculations, potentially leading to improved results.

For a more precise study, a comparison between the anisotropy results of the average of quarters and the grid-view and full-view images is conducted and presented in Table 5.4. It is observed that the difference between the results of the average and grid-view is noticeably reduced compared to previous cases. Hence, it can be inferred that averaging the results of SEM analyses can be an ideal alternative idea instead of combining images into a single one to investigate soil behavior. Accordingly, random images of the sample surface from areas surrounding the grid-view and full-view zones associated with a magnification of 3000× and 1500×, respectively, were captured. Some examples are displayed on Fig. 5.21.

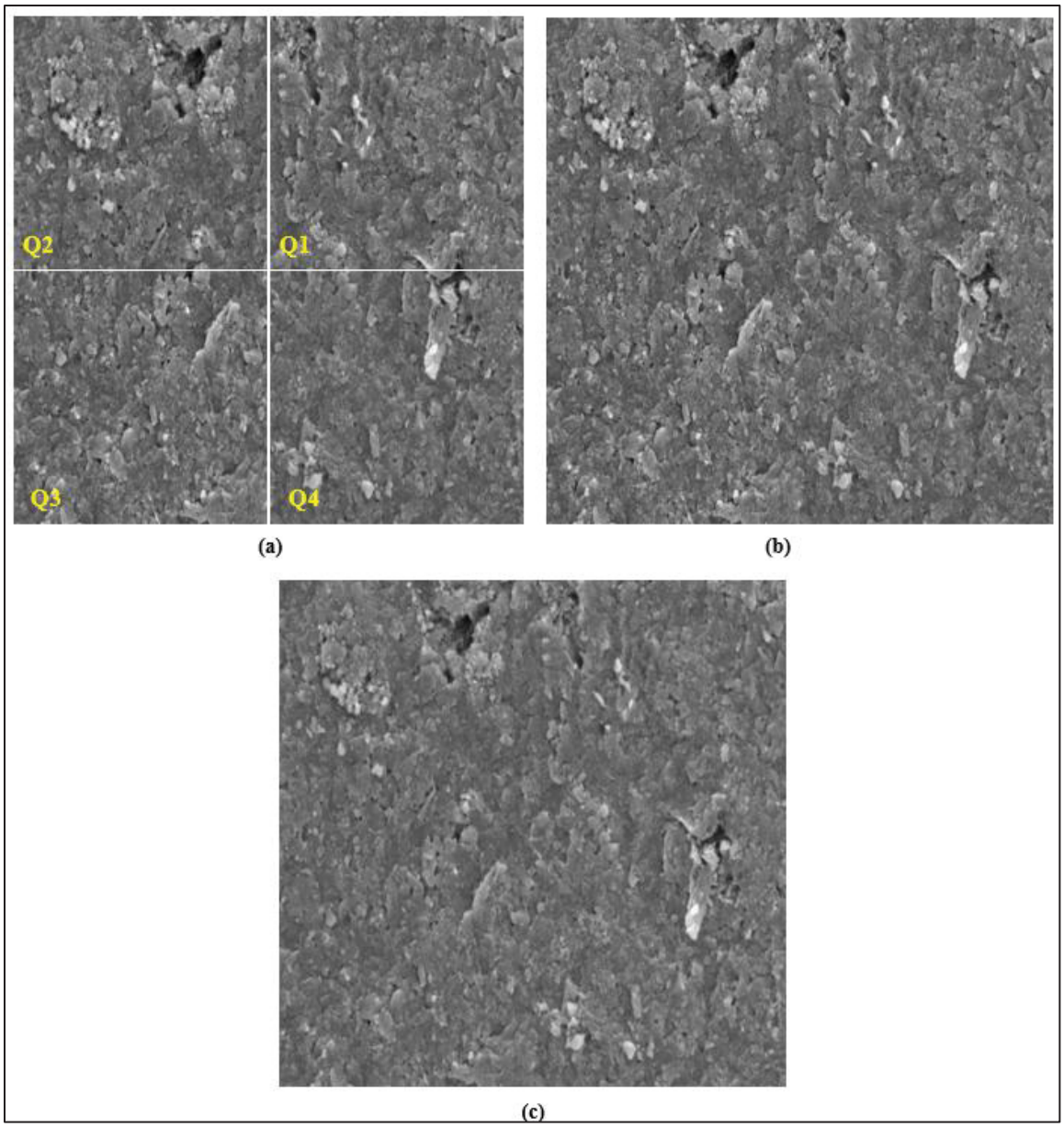

Figure 5.20 Grid view and full view of SEM images for intact sample S3 with voltage of 15 kV; a) quarter images at magnification of 3000×; b) Grid-view image at magnification of 3000×; c) Full-view image at magnification of 1500×

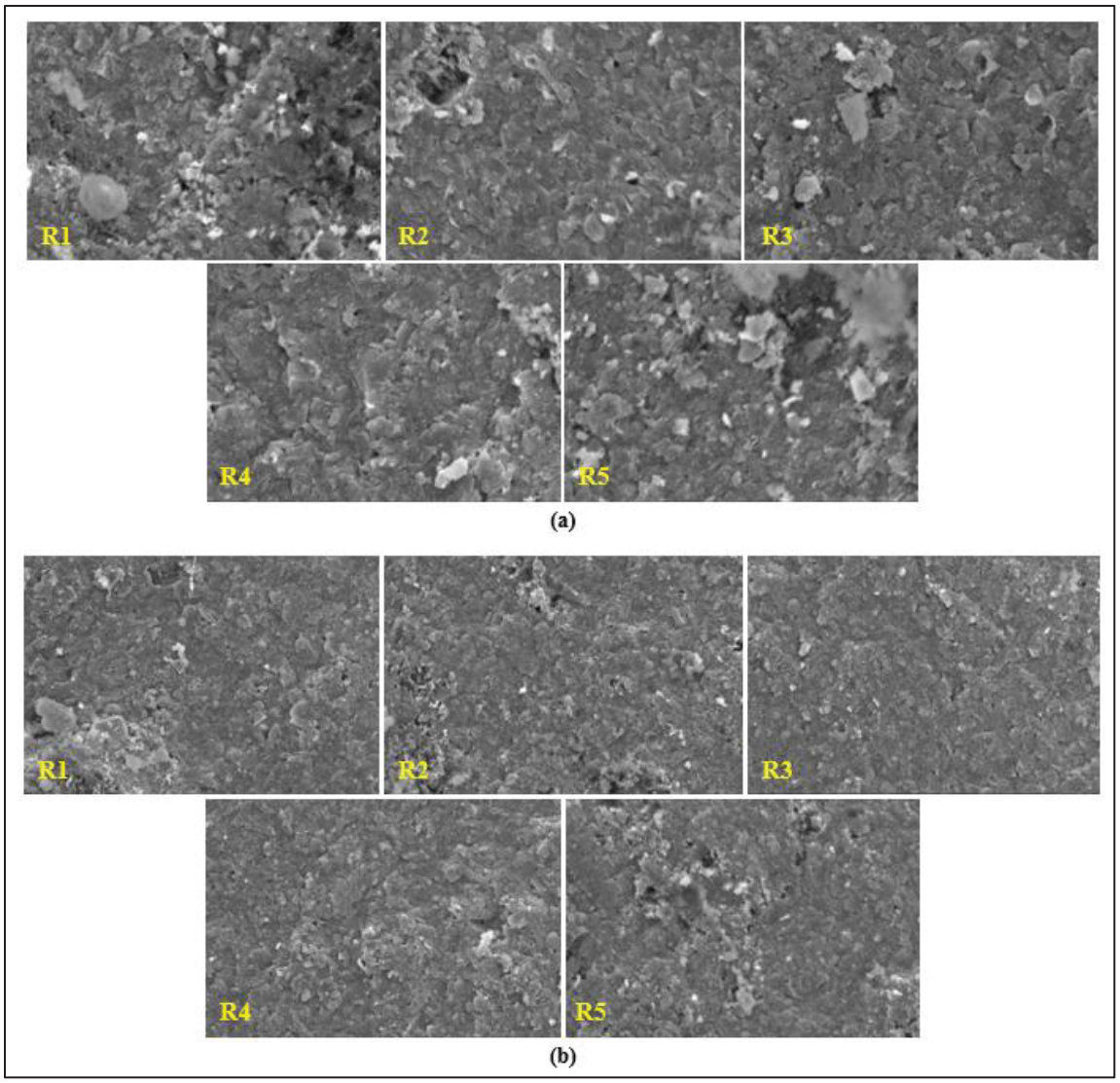

Figure 5.21 Random images (R1 to R5) of the surface of the S3 sample with voltage of 15 kV, from surrounding areas of a) Grid-view zone at magnification of 3000×; and b) Full-view zone at magnification of 1500×

The images were captured to be representative of various zones of the sample surface presenting different types of particles and pores, or different image textures. The anisotropy indices of the random images for samples S3 and S7 along with data from the grid and full-view images at magnifications of 3000× and 1500×, are provided in Tables 5.5 and 5.6. As evidenced in these tables, the average FOCM-I value at two voltages and even for two different samples is the same, both in the grid and full-view zooms. This consistency in the anisotropy

index for two soil samples from the same region confirms the robustness of the analysis and process. Moreover, a comparison between Tables 5.5 and 5.6 reveals that, compared to previous discussions, the difference between the results of grid- and full-view images is reduced. Perhaps, by incorporating more random images in the averaging process, it is possible to achieve similar results between the two different magnifications. Based on the aforementioned analysis, it can be concluded that the best approach to attain an accurate and representative anisotropy index for soil from various regions is to capture SEM images of soil surfaces in different types of zones and utilize the average results.

Table 5.5 Anisotropy analysis based on the grid-view image and randomly taken images from the surrounding area (magnification 3000×)

Sample	kV	Anisotropy index (FOCM-I)						
		Avg-Q	*R-1	R-2	R-3	R-4	R-5	Total Average
S3	15	0.043	0.124	0.256	0.185	0.136	0.269	0.169
	25	0.296	0.222	0.205	0.070	0.120	0.153	0.178
S7	15	0.063	0.140	0.201	0.169	0.227	0.244	0.174
	25	0.324	0.163	0.112	0.138	0.130	0.194	0.177
*R: Randomly taken image.								

Table 5.6 Anisotropy analysis based on the full-view image and randomly taken images from the surrounding area (magnification 3000×)

Sample	kV	Anisotropy index (FOCM-I)						
		Full-View	R-1	R-2	R-3	R-4	R-5	Total Average
S3	15	0.021	0.130	0.091	0.158	0.201	0.272	0.145
	25	0.157	0.094	0.161	0.085	0.185	0.174	0.143
S7	15	0.116	0.173	0.193	0.143	0.158	0.092	0.146
	25	0.246	0.200	0.197	0.070	0.101	0.062	0.146

According to the previous analysis, anisotropy index ranges around 0.145 and 0.17 have been obtained for the intact Champlain clay samples. This range through microscopic SEM analysis

of Champlain clay aligns well with the macroscopic anisotropy behavior reported by Leroueil et al. (1990) and Torabipour et al. (2024) through macroscale anisotropy ratios of $\frac{K_{(hh)}}{K_{(vh)}}$ and $\frac{G_{\max\,(hh)}}{G_{\max\,(vh)}}$, respectively. These studies indicated that the anisotropy ratio for Champlain clay samples from different sites generally remained between 1.1 and 1.5, indicating relatively weak to moderate anisotropy. This consistency between microscopic fabric measurements and macroscopic behavior suggests that Champlain clay maintains modest levels of anisotropy across different scales of observation.

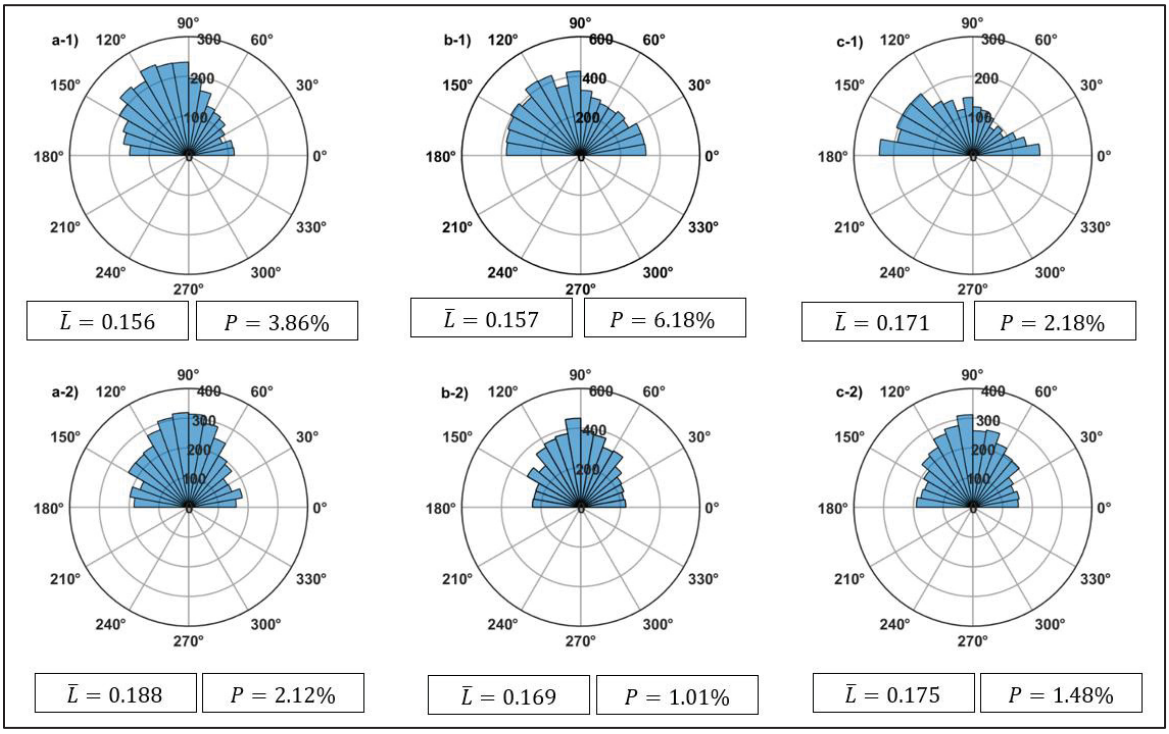

Figure 5.22 Anisotropy illustration through polar graphs for intact (a-1 to c-1) and consolidated (a-2 to c-2) sample of S3: a) 10 kV-3500×, b) 10 kV-2000× and c) 20 kV-3500×

In the final part of this section, the geotechnical properties of samples falling within this range are examined. Comparative studies are conducted to analyze particle orientation based on anisotropy representation through polar graphs for both intact and consolidated samples, as illustrated in Figs. 5.22 and 5.23, corresponding to samples S3 and S7, respectively. Polar diagrams, depicting the number of particles as a function of orientation, are plotted to quantify

orientation characteristics observed in SEM images. In this study, the polar diagrams are divided into 18 bins, each spanning 10° intervals, to provide a detailed analysis of orientation characteristics.

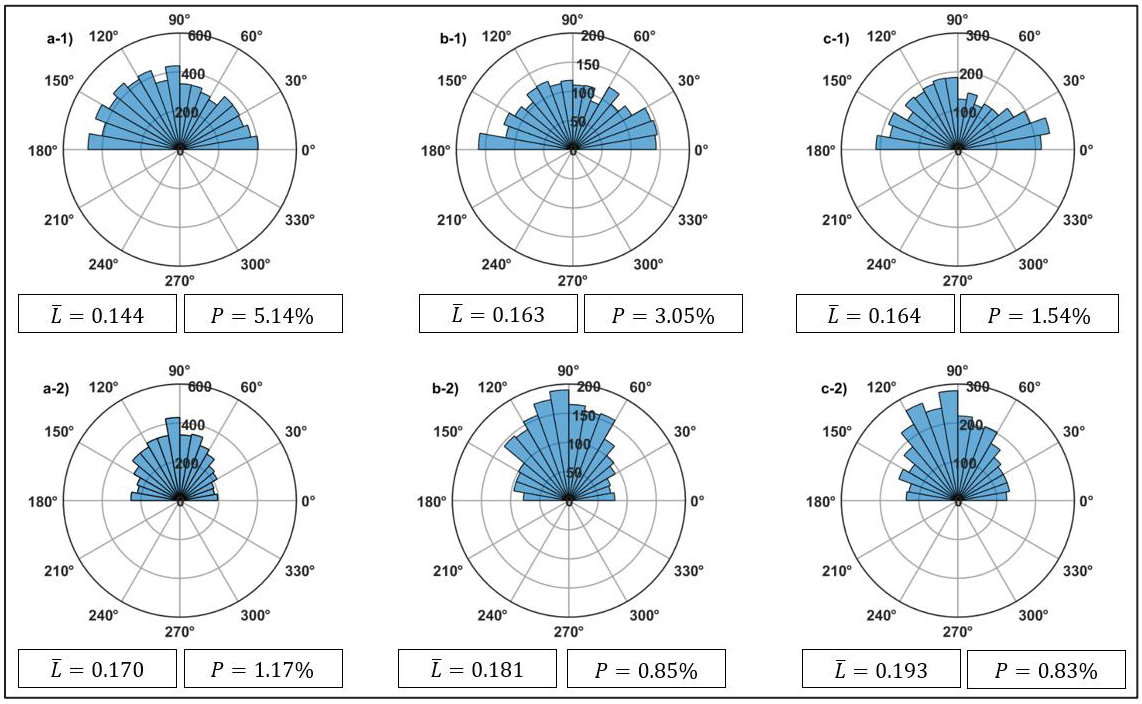

Figure 5.23 Anisotropy illustration through polar graphs for intact (a-1 to c-1) and consolidated (a-2 to c-2) sample of S7: a) 10 kV-2500×, b) 15 kV-5000×, c) 15 kV-3000×

The figures indicate that in both intact samples, particles are distributed across almost all angles, while in consolidated samples, particles oriented between 60° and 120° are notably prominent. Furthermore, alongside these visual representations, the relevant evaluation parameters, including the anisotropy index and microscopic porosity percentage, are depicted in Figs. 5.22 and 5.23. It can be observed that as intact samples are consolidated, the anisotropy index ($\bar{L}$) increases. Additionally, it is obvious from these figures that a decrease in porosity percentage during the consolidation process occurs, indicating that pores transform from large to smaller ones due to the applied compression pressure during consolidation process.

5.6 Conclusion remarks

This study investigated the soil fabric through different quantification methods using captured SEM images and a reliable image processing for two clay samples. The validity of analytical simulations was assessed by comparing the results with available literature. To calculate the anisotropy and porosity indices of the soil structure, an investigation was first conducted on different threshold numbers and values to specify the appropriate threshold level for the utilized clay samples. It was found that lower threshold numbers caused the established limit to align more closely with the peak of the gray scale curve, while higher thresholds could underestimate clay pores segmentation. Therefore, prior to image processing, a reasonable segmentation threshold level must be identified for different soil types. Parametric studies were conducted to study the effect of accelerating voltage and magnification level on the calculated anisotropy index through employed fabric orientation calculation methods. Increasing the voltage shows an insignificant effect on FOCM-II-Avg-I and FOCM-II-Avg-II, resulting in an almost constant anisotropy index. Based on the FOCM-I method, analysis indicates that V = 20 kV yields the maximum anisotropy index in most cases. The lowest value of anisotropy index is obtained using FOCM-II at V=15 kV, and the highest one in S3 and S7 occurs at V = 25 kV and V = 20 kV, respectively. Magnification analysis was carried out on samples S3 and S7 ranging from 1000 to 7000 magnitudes. Anisotropy index varies within the random-oriented region and shifts between two regions of randomness and low-oriented. Voltages including 10 kV, and 15 kV are less affected by magnification compared to other accelerating voltages.

In consolidated samples, the consolidation process causes the resulting index of the utilized methods to appear more closely aligned compared to intact samples. The study across different applied voltages for a consolidated sample showed a constant trend as magnification increased. The analysis of intact clay samples presents a significant challenge due to the considerable variability in results, underscoring the critical importance of thorough evaluation when determining the anisotropy index. This index is particularly sensitive to the complex microstructure of intact clay samples. Unlike remolded or restructured samples, intact samples

retain their natural fabric, including the original arrangement of particles, pore spaces, and inherent structural features developed over geological time.

Employing a new approach associated with incorporating more particles and pores into the calculations, a larger surface area was analyzed. Based on the acquired insight, it was determined that analyzing random images captured from different areas of samples, which consist of various particle forms, and calculating the average of the results, enhances the anisotropy evaluation. This approach effectively minimizes the disparity in indices by up to approximately 80%, which results from variations in both the SEM imaging parameters and the sample characteristics. The proposed imaging technique attains a representative anisotropy index for intact Champlain clay samples. Therefore, it can be considered a reliable approach to imaging for anisotropy determination through image processing.

CHAPTER 6

BEDDING LAYER INCLINATION EFFECTS ON CHAMPLAIN CLAY ANISOTROPY

A. Torabipour [a], Y. Ethier [b], M. Karray [c], François Duhaime [d]

[a, b, d] Department of Construction Engineering, École de technologie supérieure, 1100 Notre-Dame West, Montreal, Québec, Canada H3C 1K3
[c] Department of Civil Engineering and Building Engineering, Université de Sherbrooke, Sherbrooke, Québec, Canada

Paper submitted for publication, *Journal of Geotechnical and Geoenvironmental Engineering*, September 2025

Abstract

This study explores the anisotropic behavior of Champlain soft marine clay through shear wave velocity measurements and microstructural analysis. The influence of bedding layer orientation on stiffness anisotropy is revealed through analysis of specimens cut at different angles (0°, 30°, 45°, 60°, and 90°) relative to the horizontal plane. The investigation employs piezoelectric ring actuator technique for shear wave velocity measurements, demonstrating a consistent change where values at intermediate angles bridges the gap between principal directions. Additionally, the consolidation characteristic, compression index, shows a decrease from 1.53 to 1.12 as orientation shifts from the angle of 90° to 0° degree. Complementing these findings, scanning electron microscopy of Champlain marine clay from two sites (current study and literature) revealed clay fabric evolution under increasing consolidation stresses, showing initially random particle orientations in intact clay progressively aligning perpendicular to applied stress direction. Comparison of lightly overconsolidated Champlain clay with heavily overconsolidated clays from other regions highlights stress history's effect on anisotropic behavior. This integrated macro-micro measurement approach provides valuable insights into constitutive model development.

Keywords

Bedding layers; Angular Trimming Path; Anisotropy; Shear Wave Measurements; P-RAT; Champlain Clay

6.1 Introduction

During the deposition and sedimentation of fine soils, platy particles are arranged to secure their structural stability (Quigley 1980). Platelets are rearranged to transmit the additional surcharge impacts. Their predominant planes tend to align perpendicular to the loading direction (Locat et al. 1984; Chandler 2010). Fine soils such as glacial and marine clay exhibit an evident internal arrangement marked by the presence of multiple bedding planes due to sedimentation and natural progressive consolidation. This inherent anisotropy causes the stress-strain response to be influenced by the alignment of the principal stresses with respect to the direction of sedimentation. Rotation of principal stresses with respect to the direction of sedimentation occurs frequently in a variety of geotechnical applications, including slopes, tunnels, and excavations (Grammatikopoulou, et al. 2008; Gonzalez et al. 2012; Teng et al. 2018). This might occur due to either an inclined loading or an alteration in the direction of the bedding plane from the horizontal alignment.

The significant impact of anisotropy on soil behaviour has been demonstrated through experiments (Ling et al. 2000; Hicher et al. 2000) and simulations (Rowe and Booker, 1981; Simpson et al. 1996; Zentar et al. 2002; Teng et al. 2014, Teng et al. 2018). Rowe and Booker (1981) found that neglecting anisotropy causes ground movement estimation errors from 16% underestimation to 45% overestimation. Simpson et al. (1996) demonstrated improved tunnel model accuracy when incorporating appropriate anisotropy ratios, highlighting the importance of directional property dependence. Anisotropy assumptions enhance geo-structure design including foundation bearing capacity in clays (Siva and Srinivasan, 1970; Davis and Christian, 1971) and granular soils (Azami et al. 2010; Veiskarami et al. 2017), and shear strength of embankment (Zdravković et al. 2002; Karstunen et al. 2005).

Anisotropy relevance extends to Eastern Canada's sensitive marine clays, where understanding anisotropic behavior is crucial for stability assessment during excavation or natural landslide risk (Eden and Mitchell, 1973), as shown in landslide studies at St. Vallier de Bellechasse (1968, 1969), St. Louis de Bonsecours (1968), St. Jude (2010) (Locat et al. 2017), and St. Luc-

de-Vincennes (2016) (Tremblay-Auger et al. 2021). Champlain marine clays exhibit high sensitivity due to strength loss upon disturbance, attributed to their flocculated, card-house structure with weak electrostatic bonds (Quigley and Ogunbade, 1972; Quigley, 1980; Philibert, 1984). Their anisotropic nature stems from marine deposition, affecting responses to stresses based on orientation relative to clay fabric. Studies from St-Louis and St-Vallier sites confirm bedding angles significantly influence strength and failure behavior (Lo and Morin, 1972; Lefebvre and Rochelle, 1974; Yong and Silvestri, 1979). Specimen orientation relative to in-situ vertical direction affects observed strength, with unequal strengths in vertical (90°) and horizontal (0°) directions, and minimum strength at approximately 50°. Lefebvre and Rochelle (1974) found high anisotropy in shear strength due to particle arrangement and cementation bonds, with peak strength higher in vertical specimens than inclined ones. St-Vallier clay showed decreasing drained strength as the angle between major principal stress and vertical direction increased from 0° to 90°, while St-Louis clay exhibited minimum strength at 45° to 60° before slightly increasing at 90°. The necessity of considering strength parameters at inclination angle varying between 0 to 60° is recommended by Lefebvre and Rochelle, (1974) to assume a conservative estimation for further analysis.

This characteristic can be studied experimentally by different geotechnical devices. Hollow cylinder torsional (HCT) apparatus allows complex stress states and varied stress paths (Hight et al. 1983; Brosse et al. 2017). Brosse et al. (2017) found slight stiffness variations in London and Gault clays when rotating the principal stress axis (0°-90°). Despite advantages, HCT faces challenges: difficult specimen preparation causing non-uniform stress-strain (Saada, 1988; Sayao and Vaid, 1991) and limited small-strain measurement capability, yielding lower initial stiffness than piezoelectric methods (Brosse et al. 2017).

Anisotropy in soils can be evaluated using triaxial testing or shear wave velocity measurements. V_S measurements are performed at small strain levels (<0.001%). Conversely, anisotropy derived from triaxial testing whether in terms of undrained shear strength or stiffness captures behavior at large strains (typically >0.1%) where plastic deformation is

significant. During shearing, the soil fabric may progressively degrade or rearrange as yielding and pore pressure changes occur.

Additionally, the two tests operate under different stress conditions. Triaxial testing applies an axisymmetric loading condition ($\sigma_1 \neq \sigma_3$), altering the stress path and promoting fabric disturbance. In contrast, V_s measurements evaluate the soil under the current in-situ effective stress conditions without modifying the stress regime. Owing to these differences in strain level, behavioral domain (elastic vs. plastic), soil structure disturbance, and stress path, anisotropy values derived from triaxial shear cannot be expected to match those obtained from Vs measurements during consolidation.

Because shear wave propagation and polarization are sensitive to the orientation of clay bedding, shear wave velocity (V_s) measurements are a valuable tool for investigating and quantifying the effects of bedding on clay behavior. Piezoelectric techniques have been frequently utilized in geotechnical testing to study dynamic characteristics of clays, focusing on maximum shear modulus (G_{max}) under inherent and stress-induced conditions (Pennington et al. 1997; Hicher et al. 2000; Gasparre et al. 2011; Nishimura, 2014). Cross-anisotropy characterization primarily measures G_{max} on two principal planes: vertical-horizontal (90°) and horizontal-horizontal (0°), and the stiffness anisotropy degree (α) is determined by comparing the stiffness of two principal directions ($\alpha = \frac{G_{(0°)}}{G_{(90°)}}$). Literature reports the lowest G_{max} occurs when principal stress is perpendicular to the bedding plane orientation (vh). For overconsolidated clays, α values range from just above 1 to 2.2 (Jamiolkowski et al. 1995; Pennington et al. 1997; Jovičić and Coop, 1998).

Although previous studies have examined horizontal and vertical wave propagation through soils, the effect of intermediate wave travel path inclinations remains understudied. These intermediate angles potentially reveal anisotropic behavior not fully captured by conventional measurements. It states the importance of testing at multiple orientations beyond just the primary directions (typically parallel and perpendicular to bedding planes).

This study examines the influence of bedding layer orientation on the anisotropic response of Champlain clay, particularly its V_s and G_{max} Undisturbed specimens were taken from two block samples at different angles relative to the deposition direction. Using a conventional oedometer with vertically mounted piezoelectric sensors, Piezoelectric Ring Actuator Technique (P-RAT) (Ethier, 2009; Karray et al. 2015; Hussien and Karray, 2021), was employed to generate and detect high-quality shear waves during 1D-consolidation testing. Laboratory testing examined specimens at specific angles (0°, 30°, 45°, 60°, and 90°) defined relative to the horizontal direction. Results showed consistent patterns in shear wave velocity, with values at intermediate angles bridging the gap between both major planes. Consolidation testing and compression index (C_c) analyses, complemented by scanning electron microscopy, confirmed this anisotropic behavior through consistent C_c trends and anisotropic microstructure across vertical and horizontal direction.

To develop understanding of anisotropic stiffness, findings of this study are compared with previous studies on various clay types, especially marine and glacial ones, based on geological history, stress state, and microstructure influence anisotropic properties across different depositional environments. The microscopic aspect of bedding layers is quantitatively analyzed in slightly overconsolidated clays and highly overconsolidated clays from current study and the literature.

6.2 Material and testing procedure

Champlain marine clays were deposited during the late Quaternary in Eastern Canada's former Champlain Sea (Yong and Silvestri, 1979; Quigley 1980). The block samples were obtained from Beauharnois region using Laval University sampler at depths of 6 to 7 meters (La Rochelle et al. 1981). Index properties clay samples showed high plasticity (liquid limit, LL = 65%; plastic limit, PL = 23%; plasticity index, I_p = 42%), 78% natural water content (liquidity index, LI=1.3), and 70% clay fraction (< 2 μm). Standard 1D-consolidation specimens (63.5×19 mm) were prepared in a humidity-controlled chamber following ASTM D2435-11 protocols to preserve natural moisture and structure. As shown in Figure 6.1, an experimental

setup was developed by integrating P-RAT and high-precision strain gauges with a conventional oedometer setup, enabling simultaneous measurement of shear wave velocity and lateral strains during 1D-consolidation testing (Torabipour et al. 2024). Scanning electron imaging (SEM) was also performed in intact and consolidated specimens extracted from B-I and B-II.

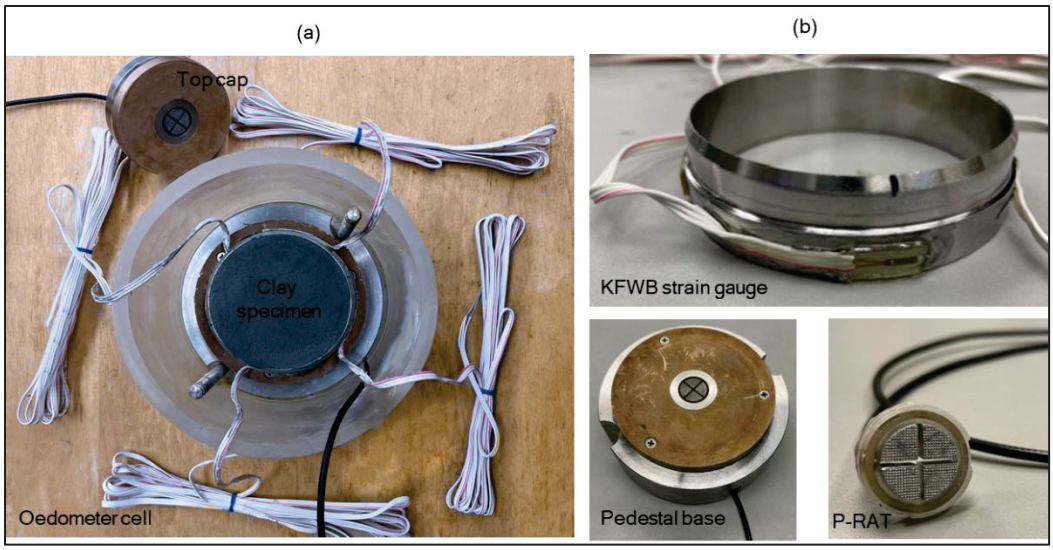

Figure 6.1 (a) Assembled instrumented oedometer setup with clay specimen. (b) Components: lateral strain gauge, pedestal base equipped with P-RAT, and fabricated sensor

6.2.1 Directional V_s testing with P-RAT

This transducer system consists of an emitter and receiver, each containing a piezoelectric ring covered with conductive layers on both inner and outer faces, connected to shielded wires that transfer voltage pulses. These components are installed in the top and bottom heads of an oedometer cell (Figure 6.1a), with inner parts making direct contact with the specimen surfaces. When voltage pulses are sent to the emitter, they create radial deformation in the piezoelectric ring, which generates a shear wave that propagates through the sample. Upon reaching the receiver, this wave creates another transverse deformation that induces electric voltage in the receiver's electrodes through the inverse piezoelectric effect. The mounted P-RAT on oedometer cell setup was utilized for determination of directional shear wave velocity, $V_{s\theta}$, regarding bedding layer orientation (Figure 6.2). The utilized P-RAT system includes two key features: inner parts divided into four alloys to minimize longitudinal displacement and

compression wave generation, and encapsulation of sensors in stainless steel to absorb longitudinal expansion of the piezoelectric ring.

The signal interpretation follows a developed approach (Karray et al. 2015) involving three main steps. First, the time domain signals are projected into the frequency domain to identify the energy-containing frequency range. Next, the phase shift between transmitted and received signals is corrected within this range. Finally, the theoretical phase shift curve (transfer function) obtained from face-to-face calibration tests is applied (Fig. 6.3).

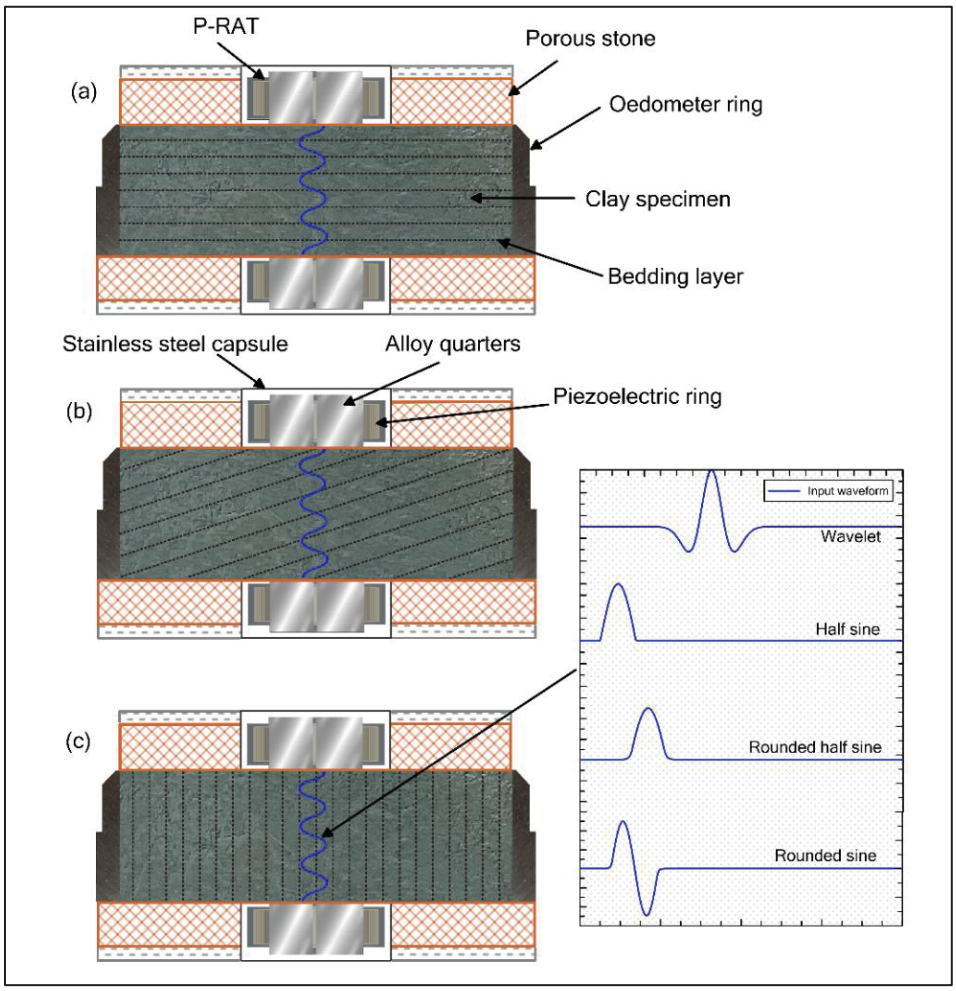

Figure 6.2 Specimen and transducer setup for shear wave velocity tests at (a) vertical, (b) inclined, and (c) horizontal bedding orientations

The transmitter-receiver system experiences a phase shift due to soil properties and sensor characteristics. Phase shift correction is based on a single degree of freedom system modeling with specific resonant frequency and damping ratio. The resonance frequency and damping ratio of the piezoelectric system are 35 kHz and 8%, respectively. The transfer function (Eq. 6.1) determines output signals based on input characteristics.

$$\varphi_i = tan^{-1} \frac{2D(\frac{f}{f_0})}{1-(\frac{f}{f_0})^2} \tag{6.1}$$

where φ_i is the system phase shift created by the emitter or the receiver; D (%) is the damping ratio of the transducer system; f is the frequency; and f_0 is the fundamental frequency of the system.

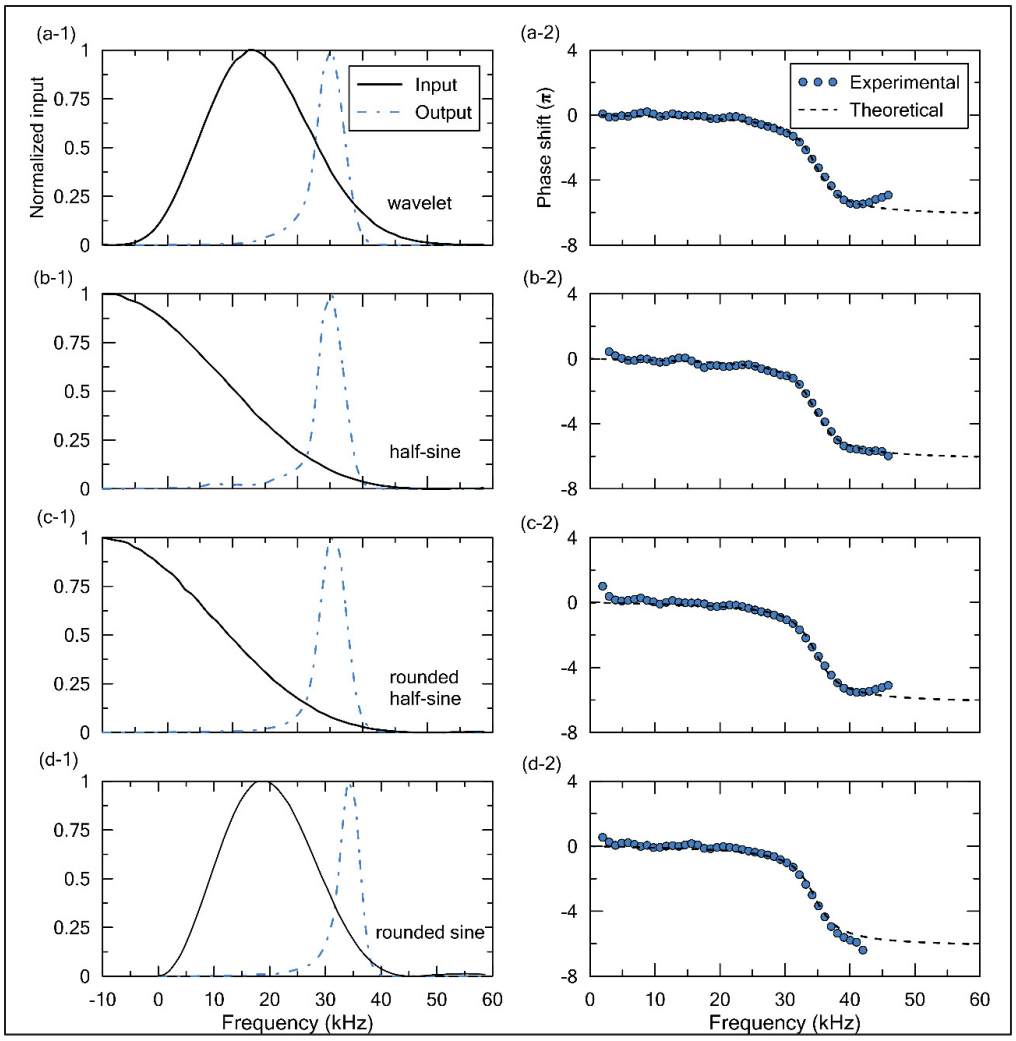

Figure 6.3 Frequency and phase response of the P-RAT
determined from face-to-face tests using different input waveforms

This interpretation method (Hussien and Karray, 2021), provides consistent V_s values independent of wave shape and frequency content. Calibration through face-to-face tests allows the determination of Eq. (6.1) under different applied stresses, which represents the advantage of this technique. The resulting $V_{s\theta}$ measurements are validated by ensuring they remain constant regardless of transmitted signal characteristics.

The $V_{s\theta}$ determination were conducted during 1D-consolidation tests with specimens cut at various orientations (θ = 0°, 30°, 45°, 60°, 90°), leading to investigating anisotropic

consolidation characteristics. The wave propagation paths are oriented relative to the horizontal axis, allowing for the anisotropic assessment. The propagated shear waves were assessed along principal and intermediate inclined paths within the soil medium. By maintaining a constant source and receiver position while varying the wave propagation direction with respect to the bedding layers, the conventional test setup of an oedometer enables the evaluation of the soil's directional dependence on V_s (Fig. 6.2b).

During consolidation tests, twelve incremental effective vertical stress levels (from 2 kPa to a maximum of over 1000 kPa) were applied. This incremental loading procedure established consolidation characteristics while enabling the assessment using P-RAT at various effective stress levels, providing insights into V_s (or G_{max}) evolution with consideration of particle characteristics.

The obtained V_s values were normalized using the relationship $V_{s1} = V_s(100/\sigma_v')^{1/4} OCR^{k/2}$, where σ_v' represents the effective vertical stress in kPa, OCR is the overconsolidation ratio, and $k/2$ is an empirical coefficient that determines the influence of OCR. This normalization standardizes measurements across varying stress conditions and reveals important aspects of soil rigidity that conventional deformation parameters often overlook, particularly the significant influence of loading history on soil structure. By incorporating both σ_v' and OCR ratio, the normalized shear wave velocity V_{s1} enables more meaningful comparisons of soil properties across different depths and stress states. Utilizing this V_s method along 1D-consolidation testing, the effect of bedding plane orientation can be studied through V_s-consolidation characteristics.

The V_s is also fundamentally linked to the G_{max} through the relationship $G_{max} = \rho V_s^2$, where ρ the soil particle density is. The directional maximum shear modulus ($G_{max(ij)}$) can be calculated from directional V_s. Hardin and Black (1968) established that $G_{max(ij)}$ correlates with void ratio (e), mean effective stress (σ'_m), and OCR through the empirical relationship $\left(\frac{G_{max(ij)}}{P_a}\right) = S_{(ij)} F(e) OCR^K \left(\frac{\sigma'_m}{P_a}\right)^n$, where P_a is atmospheric pressure (~100 kPa), while S, K,

n are clay soil constants determined through laboratory testing. This direct relationship between V_s and G_{max} allows for anisotropy characterization of small-strain soil stiffness from both wave propagation and modulus perspectives. The anisotropy ratio is calculated based on the stiffness ratio between different directional measurements, typically expressed as the ratio of horizontal to vertical shear moduli.

1D consolidation requires determination of lateral pressure to respect the characterization of clay anisotropy theory where the plane of propagation-polarization of shear wave is dependant on stress planes. The measurement of consolidation stress was conducted using high-precision lateral strain gauges (Figure 6.1b). Lateral stress measurements allow the stress condition in the plane of wave propagation and particles movement to be known. The relationship between σ_v' and $K_0(=\frac{\sigma_h'}{\sigma_v'})$, the coefficient of lateral earth pressure at rest, changes as effective vertical stress increases, reflecting the soil's stress history and consolidation state.

As reported by Torabipour et al. (2024), K_0 decreases with the effective stress from a value of 1 in the overconsolidated range to a plateau at K_0 = 0.6 at σ_v' above 600 kPa. Mean effective stress (σ_m') is recommended for empirical correlations of directional G_{max} in clays (Jamiolkowski et al. 1995; Gasparre et al. 2011; Yimsiri et al. 2011), providing more consistent results than individual stress components or assuming K_0 conditions (Ku and Mayne, 2015). To accurately interpret the V_s-consolidation response and assess anisotropy, the stress conditions during 1D consolidation must be considered.

6.3 Result and discussion

6.3.1 Bedding layer characteristics

The consolidation characteristics of clays can be influenced by structural heterogeneity and stress state. The effect of the orientation of clay particles or bedding planes on consolidation behavior can be observed in Fig. 6.4. This Figure illustrates a set of consolidation graphs for different orientations, to study the anisotropic behavior of the tested clay.

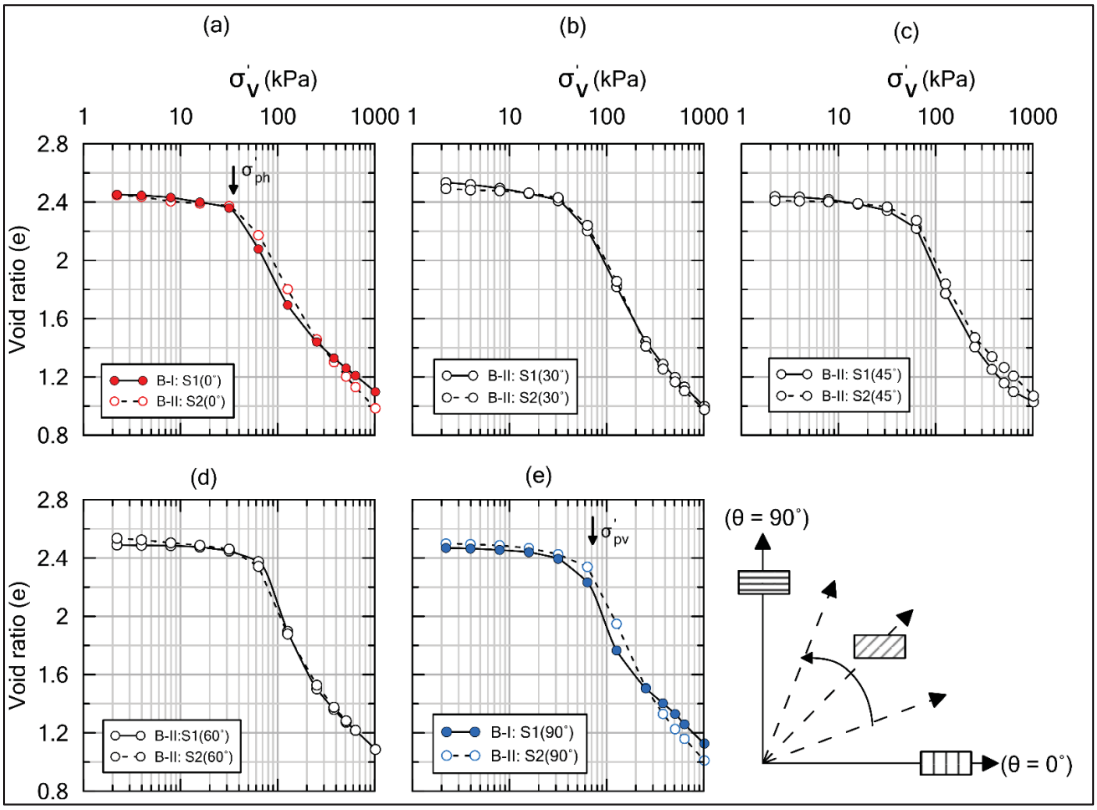

Figure 6.4 Void ratio versus vertical effective stress relationship for 1D consolidation of Beauharnois clay specimens at different bedding plane orientations; (a) θ = 0°, (b) 30°, (c) 45°, (d) 60°, and (e) 90°

Figs. 6.4a-e show 1D-consolidation curves for specimens at 0°- 90° orientations, depicting void ratio (e) versus σ_v' relationships for different specimens from both block sample sets, B-I and B-II. A gradual transition in compression behavior occurs as inclination changes from 90° to 0°, with inclined ones (60°, 45°, 30°) showing intermediate consolidation behavior between principal orientations.

Table 6.1 Compression index values of the conducted 1D-consolidation tests

Block clay sample	**Average C_c**				
Beauharnois	(θ = 90°)	(θ = 60°)	(θ = 45°)	(θ = 30°)	(θ = 0°)
B-I & II	1.53	1.40	1.34	1.22	1.12

The consolidation curve at an angle of 90° exhibit more pronounced curvature near the preconsolidation pressure (σ'_{pv}), while at an angle of 0° show a more gradual transition around σ'_{ph}. As shown in Fig. 6.4, the consolidated specimens have σ'_p of 71 kPa and 35 kPa in the vertical and horizontal plane, respectively. Consolidation curves of different inclinations exhibit a similar variation of void-ratio range, however with potential differences in compressibility as shown in Table 6.1. This table shows consistent C_c changes with specimen orientation, showing a structured relationship between bedding plane inclination and particle compressibility (O'Kelly, 2006). The horizontal-to-vertical C_c ratio is less than 1, indicating higher vertical compressibility and greater horizontal stiffness in the normally consolidated state. It is also noted that the plasticity index (PI) values of these specimens are relatively similar, as they were obtained from the same block sample. Otherwise, such comparisons should be interpreted carefully by considering possible variations in PI and their relationship with specimen disturbance.

The C_c index varies with inclination angle, using the slope method from the $e\text{-}log\sigma'_v$ relationship of the virgin compression lines (normal consolidation line). Intermediate inclinations (60°, 45°, and 30°) show a gradual variation in C_c, with values of 1.40 to 1.22, progressively decreasing as the angle shifts from 90° to 0°. At the angle of 90° orientation shows the steepest slope with the highest average value of C_c (1.53), while 0° degree exhibit the gradual slope with the lowest average value (1.12). The vertical compression index values

obtained in this study are consistent with the range reported by Leroueil et al. (1983) and Dion Gagnier (2019) for the clay from the same site.

While compression index reflects the static compressibility of the clay structure, the dynamic response captured through V_s provides the possibility of investigating fabric anisotropy under different loading stages. To study this, frequency-domain analysis was performed on specimens subjected to shear wave testing during consolidation.

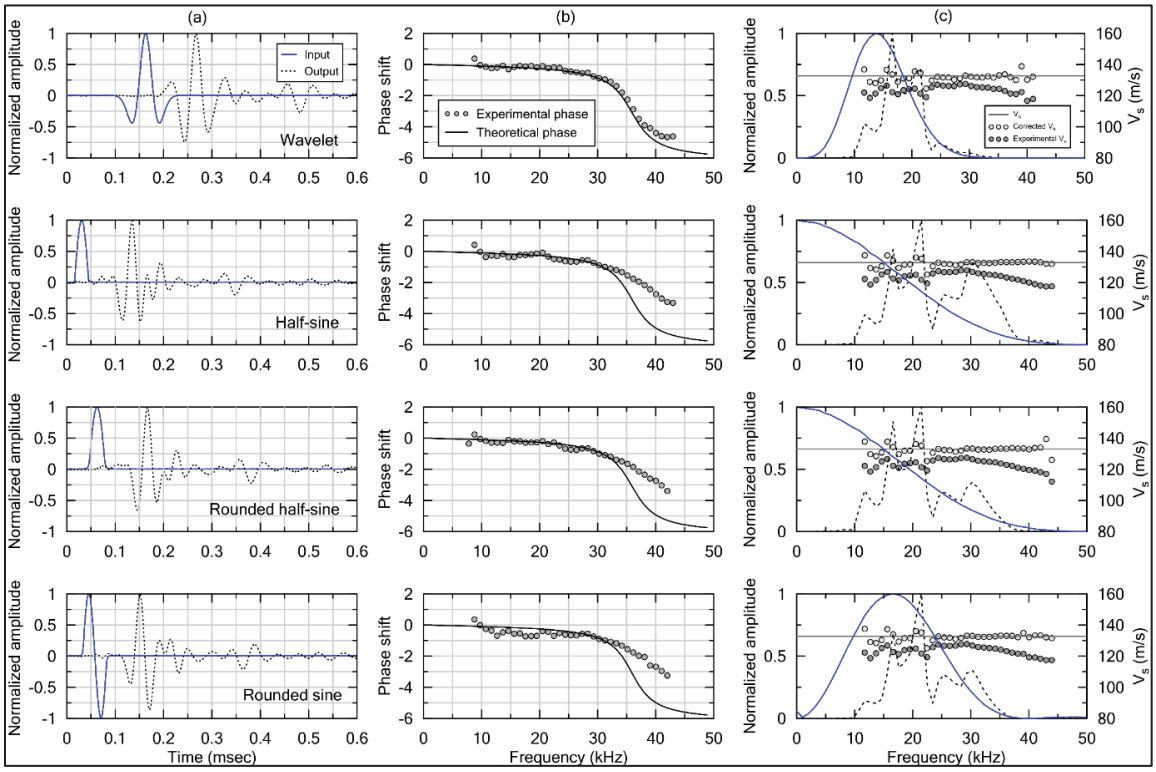

Figure 6.5 Shear wave, $V_s(\theta h)$, measurements at 45° under 253 kPa vertical stress using four input signals: a) time-domain waveforms, b) frequency-dependent phase shifts, and c) amplitude response and phase velocity

Fig. 6.5 illustrates frequency domain using different frequency contents for measured V_s at an effective vertical stress of 253 kPa and an angle of 45° degrees. In this figure, the four sets of graphs correspond to four different input signals. Figure. 6.5a shows the temporal traces of the normalized amplitude of inputs and outputs. Figure. 6.5b illustrates the comparison between experimental phase shift error against the theoretical curve based on the phase shift analysis.

For all four employed input signals, a reasonable agreement is observed between experimental and theoretical phases at frequencies below the resonance frequency of 35 kHz. The measured V_s values for all input forms ranges approximately from 130 to 135 m/s (Fig. 6.5c). A mean V_s value was determined based on the four signal forms in each loading stage during 1D-consolidation testing.

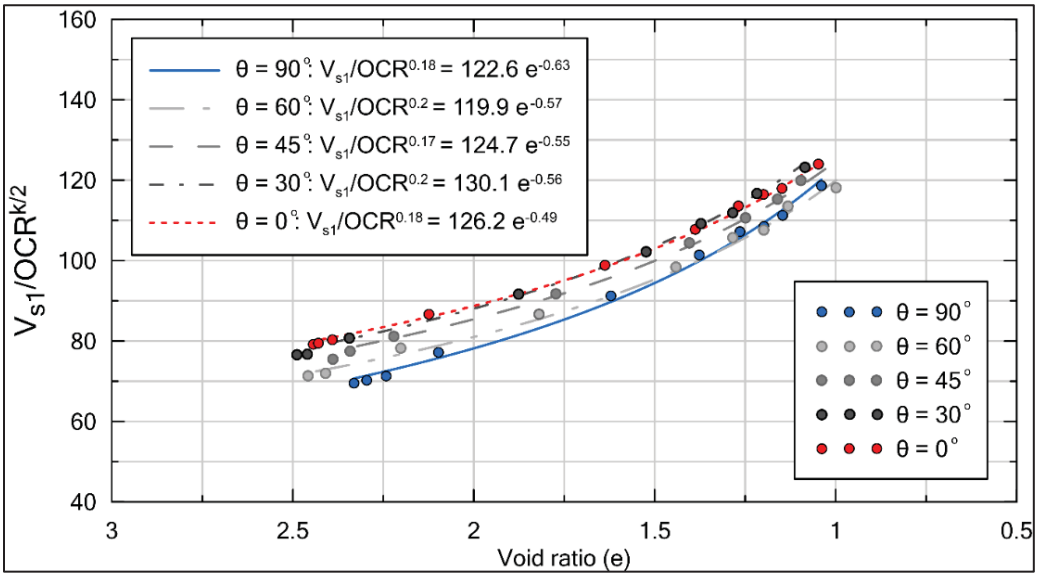

Figure 6.6 Empirical correlations of normalized V_s, over void ratio for different bedding plane orientations

The anisotropic behavior becomes particularly evident when examining the directional characteristics of normalized shear wave velocity. As shown in Figure 6.6 indicates the anisotropic nature of the Beauharnois clay through $V_{s1} - e$ relationship across different bedding layer orientations. Peak velocities consistently occur at bedding layer angles near 0° and 90°, indicating that wave propagation is most efficient when aligned parallel or perpendicular to the bedding planes. This directional dependency persists throughout the entire consolidation range, confirming the existing of anisotropy effect. At θ = 0°, where shear waves propagate parallel to bedding planes, the high sensitivity to void ratio suggests that inter-particle contact efficiency within individual layers dominates wave transmission. The bedding layers in this direction act as continuous transmission paths, making the propagation more sensitive to changes clay structure.

6.3.2 Stress history effects

The stress-dependent anisotropy indicates that consolidation stress not only increases absolute velocity magnitudes but also amplifies directional preferences. Figure 6.7 demonstrates the anisotropy of the tested specimens through V_{s1} normalized to OCR across various bedding layer orientations and stress conditions. As 1D consolidation gradually progress (16-32 kPa), the velocity peaks at 0° and 90° indicate that random distribution of bedding layers effect on dynamic response as evident in V_{s1} values. Gradual increase of the stress allowing stress redistribution that minimizes directional contrasts. Notably, while normalized velocities increase with higher effective stress for all orientations, the relative difference between horizontal and vertical directions appears more pronounced at lower stress levels, suggesting that higher stresses albeit enhance the preferential directionality due to layers become mechanically locked, creating distinct load-bearing networks, but more compacted specimen show less anisotropy degree anisotropy. In lower stress levels, the anisotropy is preliminary a result of the inherent bedding plane orientation within the clay soil, which tends to align particles in a preferential horizontal arrangement during the progressive consolidation process regardless of trimming direction.

Based on Fig. 6.7, the close agreement between measured data and theoretical predictions based on Equation 6.2 validates the applicability of elasticity-based models for describing velocity anisotropy in consolidated clays. The harmonic mean formulation, originally proposed by Zeng and Ni (1999), successfully captured the non-linear transition between principal orientations across all stress levels tested. This finding suggests that the fundamental assumptions of elastic wave propagation remain valid even under significant consolidation stress, despite the complex microstructural changes occurring within the clay matrix.

$$V_{s1(\theta)} = \frac{V_{s1(vh)}V_{s1(hh)}}{V_{s1(hh)}sin^2\theta + V_{s1(vh)}cos^2\theta} \tag{6.2}$$

The equation's structure ensures that $V_{s1(\theta)}$ equals $V_{s1(vh)}$ when θ is 90° (perpendicular to the bedding plane) and $V_{s1(hh)}$ when θ is 0° (parallel to the bedding plane), with a non-linear transition between these two principal directions.

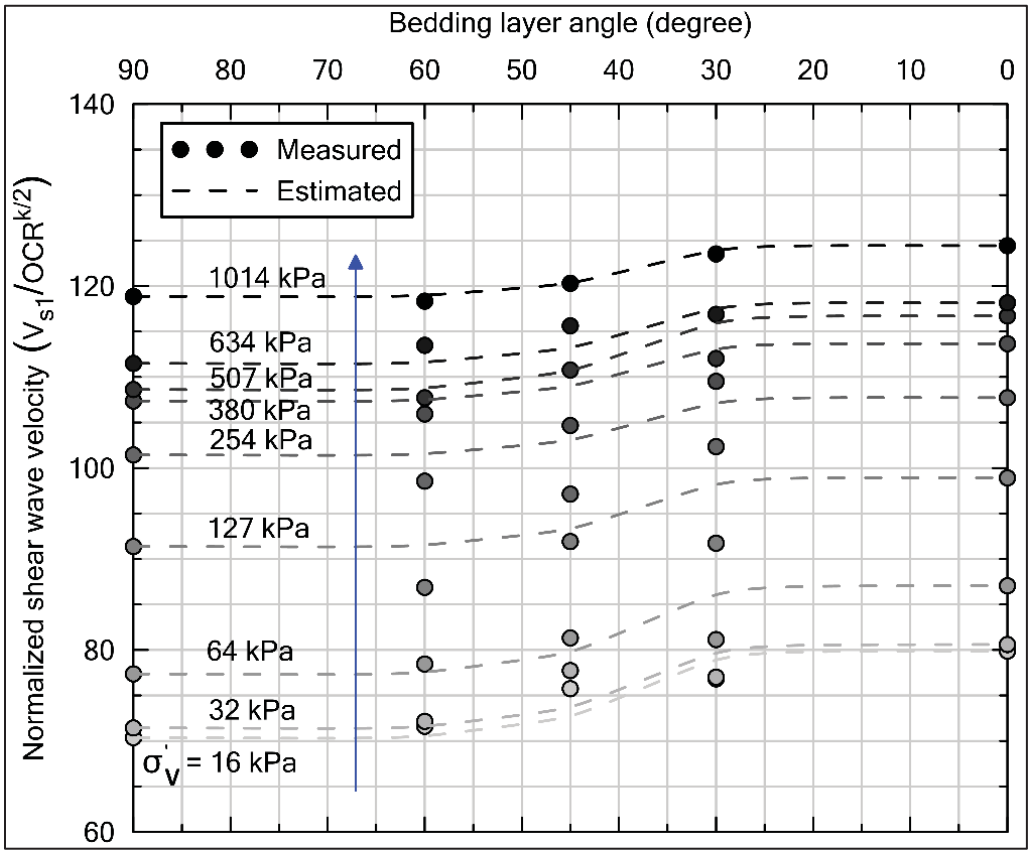

Figure 6.7 Normalized shear wave velocity versus bedding layer angle at various stress levels

The results presented in Fig. 6.8 provide crucial insights into how anisotropy show across different measurement orientations. The highest anisotropy ratios observed at 0° orientation (1.15-1.25) indicate maximum anisotropy when wave propagation occurs parallel to bedding planes. The higher stiffness in the horizontal direction suggests that the clay particles are preferentially aligned along the bedding planes, resulting in a stronger resistance to shear deformation in this orientation. This finding aligns with the conceptual model of layered soil behavior, where horizontal particle arrangements create preferential pathways for stress transmission.

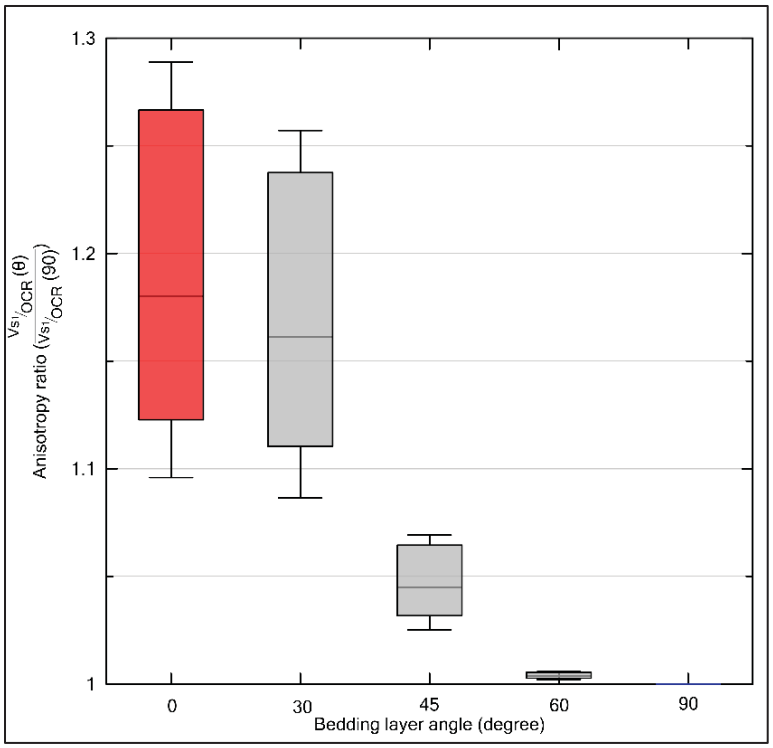

Figure 6.8 Variation in anisotropy ratio as a function of bedding layer inclination angle under increasing consolidation stress

At 30° orientation, the anisotropy ratio ranges approximately 1.10-1.20, which represents a moderate level of directional dependency. At this angle, the measurement direction is still relatively close to the bedding plane orientation (0°), so the wave propagation partially follows the preferential horizontal fabric arrangement. At 45°, the anisotropy ratio decreases to approximately 1.05-1.10, representing the transitional zone where directional effects are most balanced. This angle is geometrically significant because it represents equal contributions from both horizontal (parallel to bedding) and vertical (perpendicular to bedding) components. The reduced anisotropy at 45° suggests that the combination of both directional influences tends to average out the extreme directional preferences, creating more isotropic-like behavior.

At 60°, the anisotropy ratio drops to 1.03–1.07, as wave propagation becomes more perpendicular to the bedding planes. The progressive reduction in anisotropy ratio toward 90° orientation show that perpendicular measurements encounter more uniform resistance, as wave propagation crosses rather than follows the bedding structure.

To assess whether the observed anisotropic behavior, between principal directions, is consistent across different geological settings and stress histories, a compilation of clay from different regions was conducted.

Table. 6.2 represents a thorough view of the mechanical properties of several clays from different origins including North America (Cho and Finno, 2010; Kim and Finno, 2012), Asia (Nishimura, 2014; Teachavorasinskun and Lukkanaprasit, 2008; Li et al. 2012) and Europe (Jamiolkowski et al. 1995; Pennington et al. 1997; Jovičić and Coop, 1998; Ling, 2000; Yimsiri and Soga. 2011; Gasparre et al. 2007; Brosse et al. 2017). It encompasses a wide spectrum of clay types, ranging from glacial deposits to marine sediments, each with its unique stress history and compositional characteristics. The data provided in table 2 show the prevalence of high plasticity indices among most clay soils, except for Chicago glacial clays. This high plasticity is particularly significant as it correlates with a more pronounced influence of overconsolidation ratio (OCR) on clay behavior, as previously noted by Dobry and Vucetic (1987) and Viggiani and Atkinson (1995). Figures 6.9a and b illustrate the variation of normalized G_{vh} and G_{hh}versus σ'_m for both lightly and heavily overconsolidated clays, respectively. The consistent trend observed across different clay types as consolidation stress increases shows the stress-dependent stiffness response, despite variations in clay origin and stress history. A significant observation from these figures is the markedly higher rigidity exhibited by London and Gault clays in both vertical and horizontal orientations compared to Champlain clay. This heightened stiffness can be attributed to their glacial origin and subsequent geological history, resulting in moderate to high overconsolidation (OCR ≈ 6.5 to 40). The medium to high plasticity of these UK clays, deposited in marine environments during the Eocene and Cretaceous epochs, further contributes to their distinct mechanical behavior (Gasparre et al. 2007; Yimsiri and Soga. 2011).

Table 6.2 Different clays utilized in stiffness anisotropy studies from various sites

Region	Research	Clay	W (%)	PI (%)	Depth (m)	CC (%)	OCR	Stress ratio	Device	$\alpha = \frac{G_{hh}}{G_{vh}}$
North America	Cho and Finno (2010)	Chicago Glacial	25	15	8.3	-	1.7	0.6	TRX*+ BE*	1-1.14
	Kim and Finno (2012)	Chicago glacial	26	15.8	5.5	-	1.3	anisotropic	TRX+BE	1-1.14
		Chicago glacial	24.4	16.7	12	-	1.1	anisotropic	TRX+BE	1-1.2
Asia	Nishimura (2014)	Ma11	44	52	95	32	NC**	1	TRX+BE	1.32-1.37
		Ma12	41	35	60	54	NC	1	TRX+BE	1.66
		Ma13	68	41	14	49	NC	1	TRX+BE	1.1-1.13
		Ur	78	27	35	34	NC	1	TRX+BE	1.16-1.26
		Mo	60	26	13	31	NC	1	TRX+BE	1.03-1.07
		Iz	35	26	2	25	22.5	1	TRX+BE	1.73
	Teachavorasinskun & Lukkanaprasit (2008)	Bangkok	44.26	27.14	7-8	-	NC	0.54	Sq oed*+BE	1.13-1.23
		Bangkok	60-67	55-57	13-14	-	NC	0.64	Sq oed+BE	1.12-1.25
	Li et al. (2012)	Shanghai	47	25	8.5	33	1.2	1	TRX+BE	1.08-1.39
Europe	Jamiolkowski et al. (1995)	Pisa-S1	60	41	12.9	30-70	1.5-2	0.55-251	Sq oed+BE	1.72-1.21
		Pisa-S2	60	23-46	13	30-70	1.5-2	K_0	Sq oed+BE	1.21-1.34
		Panigaglia-S1	-	44	15.2	40	1-1.1	0.55-285	Sq oed+BE	2-1.31
		Panigaglia-S2	-	44	19.3	40	1-1.1	K_0	Sq oed+BE	1.88-1.36
	Jovičić and Coop (1998)	London	-	40	6	-	HOC**	1	TRX+BE	1.48-2.26
	Pennington et al. (1997)	Gault	29-31	26-32	7-8	-	30	1-2.1	TRX+BE	2.28-2.84
	Ling (2000)	Gault	29-31	26-32	6-8	-	45	2	TRX+BE	2.25
	Yimsiri & Soga. (2011)	London	20	30-40	12-23	-	6.5	1	TRX+BE	1.2
		Gault	30	43	14-16	-	40	1	TRX+BE	1.68

Table 6.2 Different clays utilized in stiffness anisotropy studies from various site (continued)

Region	Research	Clay	W (%)	PI (%)	Depth (m)	CC (%)	OCR	Stress ratio	Device	$\alpha = \frac{G_{hh}}{G_{vh}}$
Europe	Gasparre et al. (2007)	London -C	23-26	37-50	0-5	49-62	HOC	anisotropic	TRX+ BE	1.83-2.2
		London -B2(c)	23-26	37	5-8	41-50	HOC	anisotropic	TRX+ BE	1.84-2
		London -B2(b)	24-28	38-47	8-16	54-63	HOC	anisotropic	TRX+ BE	1.8-2.1
		London -B2(a)	22-29	40-48	16-26	55-62	HOC	anisotropic	TRX+ BE	1.89-2.2
		London -$A3_{(2)}$	21-25	33-62	26-40	51-54	HOC	anisotropic	TRX+ BE	2.1
	Brosse et al. (2017)	Oxford	30	32	10	45	HOC	1.75	TRX+ BE	2.31
		Kimmeridge	20-35	26	10	50	HOC	1.7-1.8	TRX+ BE	1.73
		Gault	35	46	10	47	HOC	1.8	TRX+ BE	1.93
		London -B2(c)	25	37	1-2.6	57	HOC	1.9	TRX+ BE	1.92

Figure 6.9c and d illustrate the relationship between anisotropy ratio and consolidation stress, revealing distinct patterns for clays under different overconsolidation conditions. The lightly overconsolidated clays (Fig. 6.9c) demonstrate α ranging from 1.15 to 1.55, indicating a low to moderate degree of anisotropic behavior. In contrast, heavily overconsolidated clays (Fig. 10d) exhibit significantly higher α value, spanning from 1.7 to 2.0. This marked increase in anisotropy ratio for heavily overconsolidated clays highlight the profound effect of stress history on the development of directional stiffness properties. Heavily overconsolidated clays have experienced higher stress levels in their geological past, leading to a more pronounced particle reorientation and fabric development. Additionally, the increased inter-particle bonding and cementation that often occur in overconsolidated clays may contribute to the enhanced stiffness anisotropy. Given the observed differences in stiffness and anisotropy across various clays, further insight can be gained by examining their microstructural characteristics through SEM-based morphological analysis, particularly focusing on lightly overconsolidated clays such as Champlain clay and heavily overconsolidated clays like London clay.

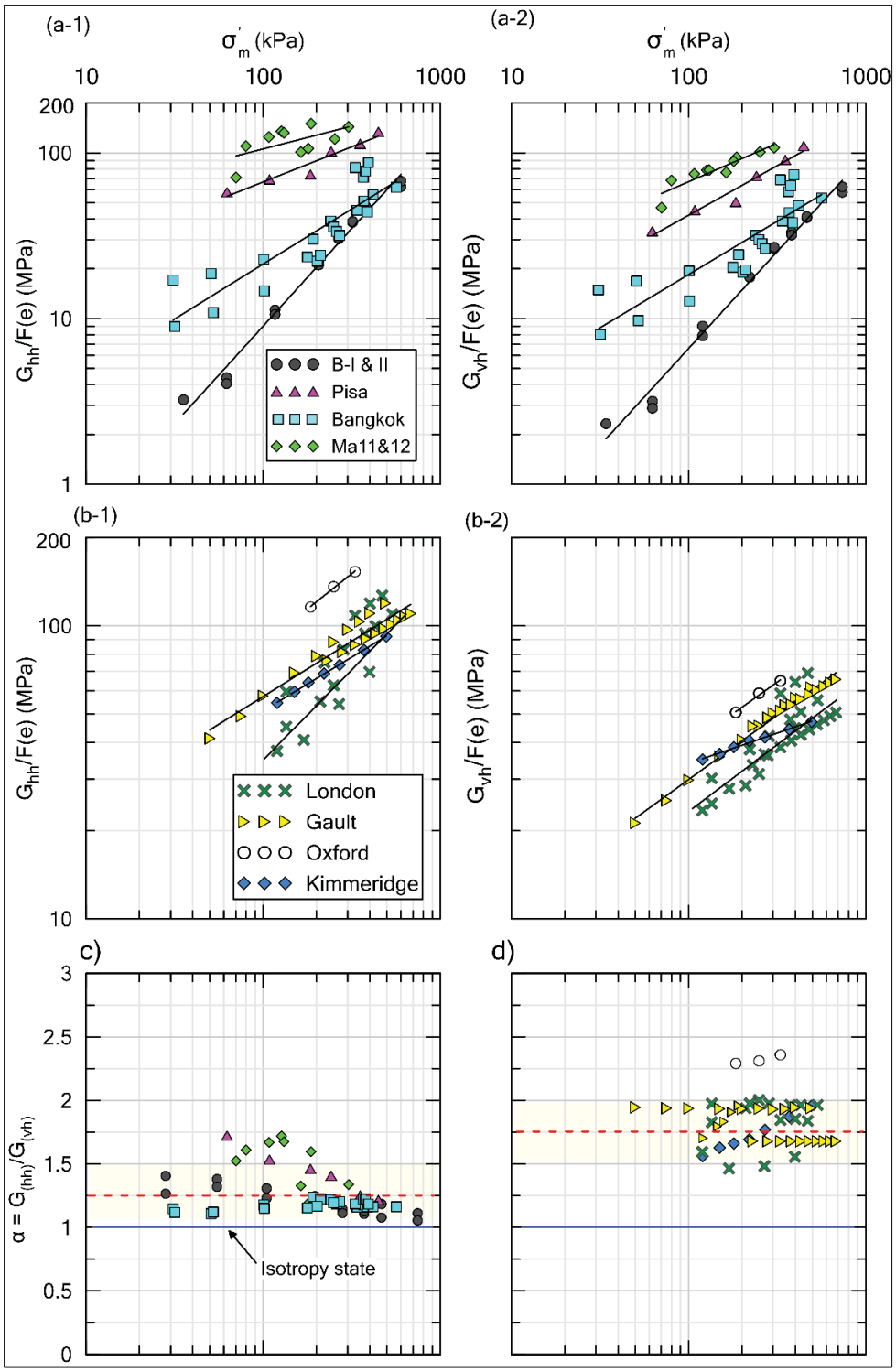

Figure 6.9 Normalized G_θ for various clay deposits: (a) Lightly OCR, (b) Heavily OCR; stiffness anisotropy degree: (c) OCR and (d) Heavily OCR

6.3.3 Clay morphology

Recent advances in SEM have transformed quantitative analysis of clay fabrics from subjective visual assessment to rigorous automated methodologies. The quantitative approach offers several possibilities including the ability to reasonably measure and compare structural features across different clay types, identify delicate variations in particle orientations and distributions, and quantify the degree of anisotropy in different clay fabrics.

Tested SEM specimens oriented in vertical and horizontal directions (Fig. 6.10) were compared with published data from Champlain clay at the St Marcel site (Fig. 6.11) and London clays with high OCR (Fig. 6.12). Clay fabric morphology was analyzed across varying overconsolidation states using soft marine clays and stiff glacial clays. In Champlain clays, digital image analysis was conducted at multiple stress levels and magnification ranges to characterize microstructural variations.

A MATLAB script was developed to quantify fabric orientation parameters from SEM micrographs of clay specimens. SEM images taken from previous studies were preprocessed using digital filtering techniques to enhance contrast and eliminate noise artifacts prior to automated particle detection. Threshold values were determined using Otsu's method combined with iterative optimization to ensure accurate segmentation of particle boundaries and minimize detection errors. Otsu's method (MathWorks, 2024) finds the optimal grayscale intensity threshold (ranging from 0 to 255, where 0 is pure black and 255 is pure white) by evaluating how well it separates clay particles from pores. At each potential threshold value within this 0-255 range, the algorithm calculates four key factors: (1) the proportion of darker pixels (pores) below the threshold, (2) the proportion of brighter pixels (particles) above the threshold, (3) the average darkness of pixels classified as pores, and (4) the average brightness of pixels classified as particles. The optimal threshold is the one that simultaneously minimizes the mixing of the two groups within themselves while maximizing the difference in average intensity between the particle and pore classes—essentially finding the grayscale value where the separation between dark and bright regions is sharpest with the least overlap. This objective

ensures that pores and particles are reliably distinguished, enabling accurate fabric orientation calculations from SEM images.

To assess the fabric orientation, anisotropy index (I_a), the calculation process utilized by Martínez-Nistal et al. (1999) is adopted in this study. Based on Eq. (6.3), I_a was calculated based on the length and orientation of the major axes of the segmented and identified particles:

$$I_a = \frac{\sqrt{\left(\sum_{i=0}^{n} D_{i,major} \times sin\theta_i\right)^2 + \left(\sum_{i=0}^{n} D_{i,major} \times cos\theta_i\right)^2}}{\sum_{i=0}^{n} D_{i,major}} \quad (6.3)$$

where $D_{i,major}$ and θ_i are respectively the major axis length and orientation for segmented region *i*, and *n* refers to the total number of segmented regions. Accordingly, the overall fabric alignment, ranging from randomly oriented fabric (I_a < 0.15) to the maximum degree of iso-orientation (I_a =1): highly oriented fabric corresponds to 0.21 < I_a < 1, while weakly oriented fabric is 0.15 < I_a< 0.21.

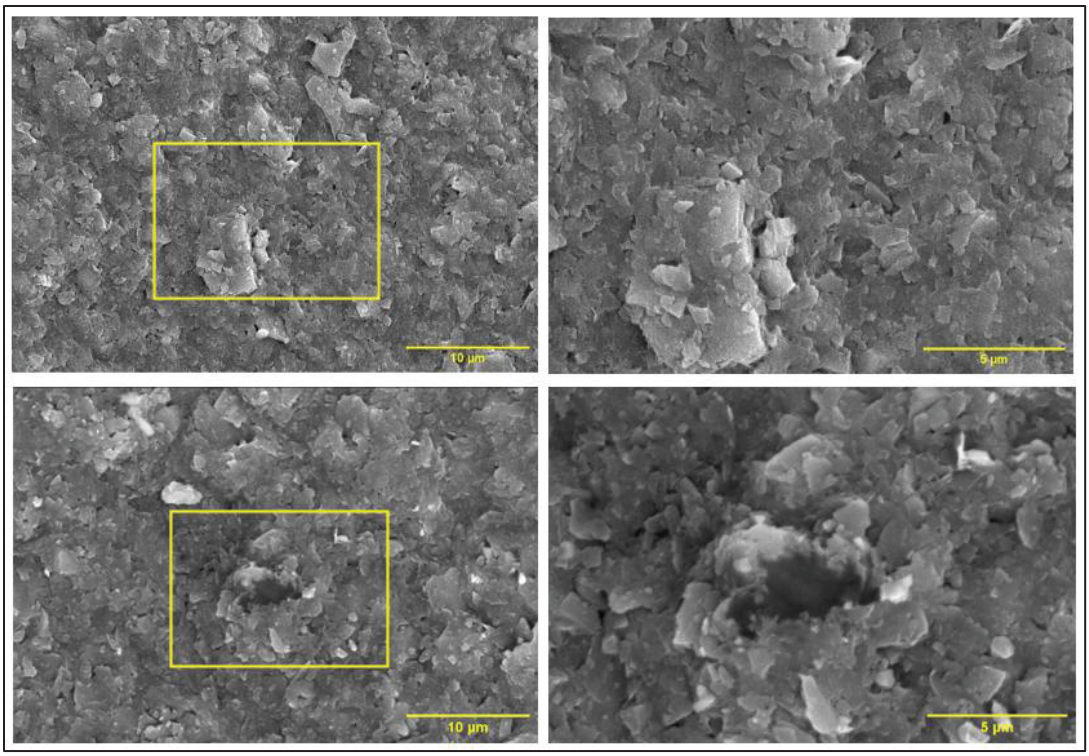

Figure 6.10 Intact structure of Beauharnois clay at magnifications of 3000× and 7000×

Figure 6.10 presents SEM images of the intact clay fabric at two magnification levels: 3000× and 7000×. At 3000× magnification, the broader arrangement of clay platelets and pore structures is evident, offering a general overview of the soil matrix. In contrast, the higher magnification of 7000× enables a more detailed visualization of individual clay platelets, providing insight into inter-particle contact mechanisms and microstructural alignment. This dual-scale imaging approach allows a microstructural interpretation, bridging the particle-level interactions with the larger-scale structural fabric. I_a was quantified for both vertical and horizontal SEM specimens in their intact state and after consolidation to stress levels exceeding 1000 kPa, comparing fabric evolution under different loading conditions.

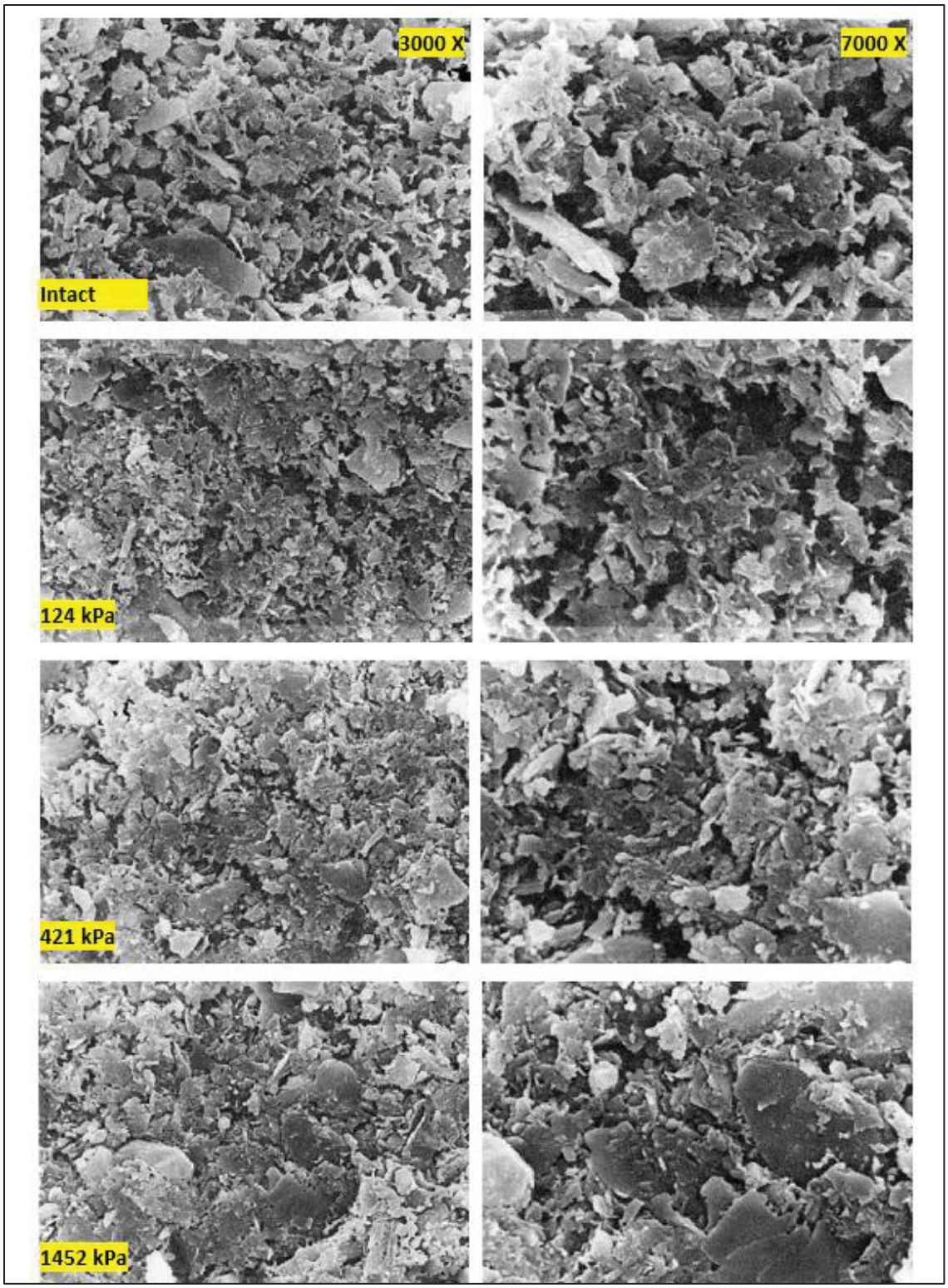

Figure 6.11 SEM images from different stages of 1D-consolidation test of clay from St Marcel site at orientation of 90 degree (Delage and Lefebvre, 1984)

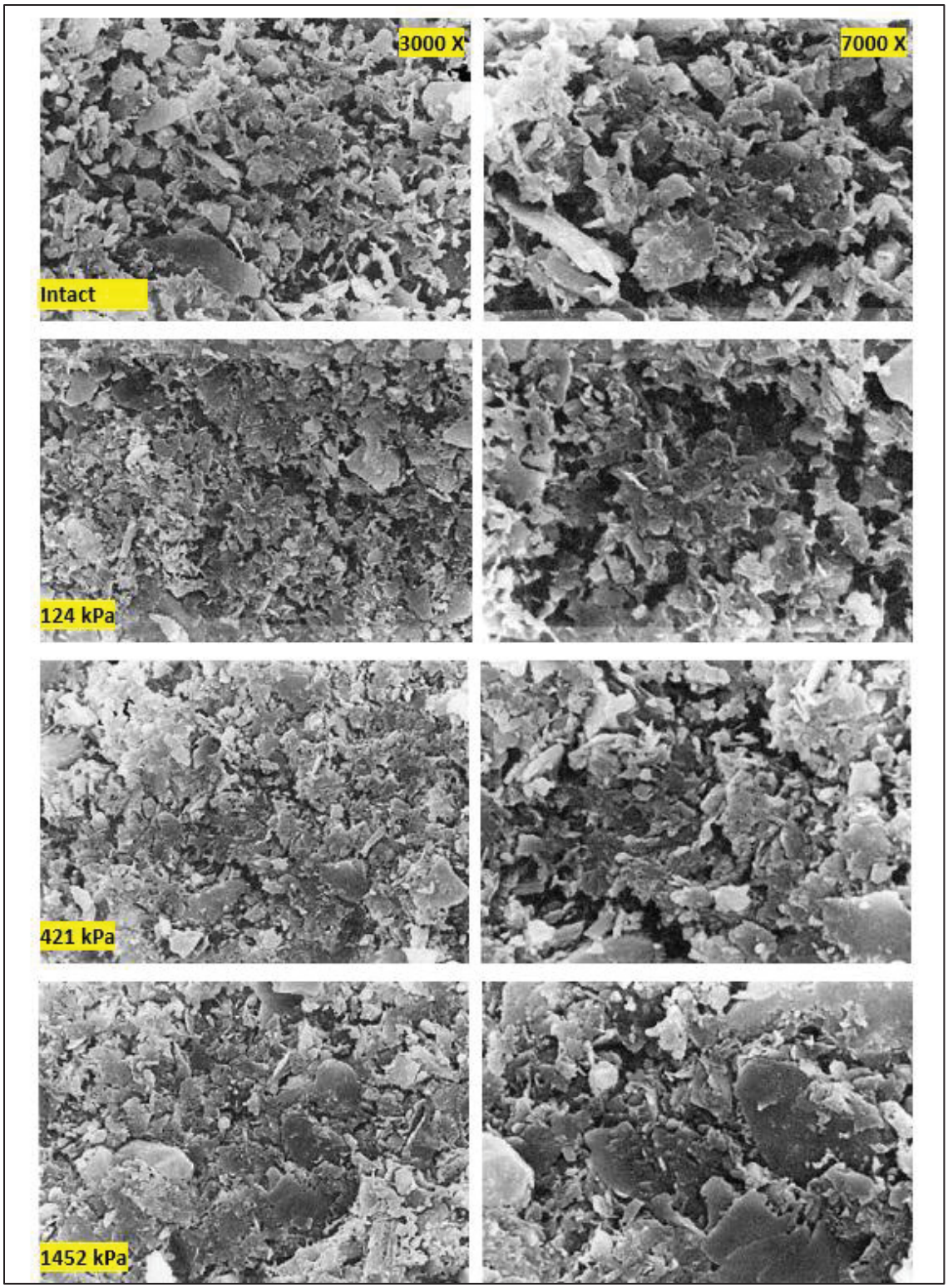

Figure 6.12 SEM images from different stages of 1D-consolidation test of clay from St Marcel site at orientation of zero degree (Delage and Lefebvre, 1984)

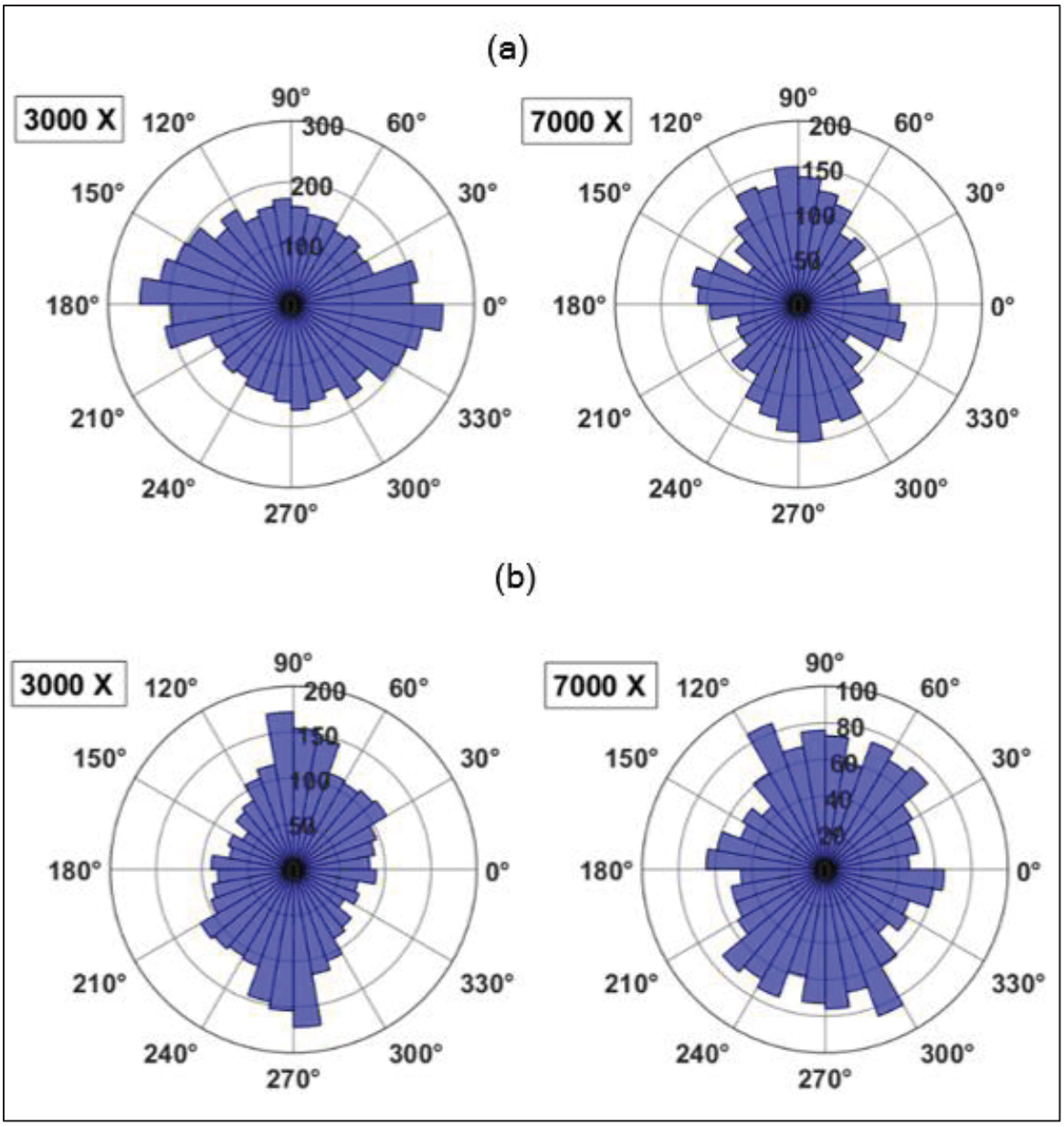

Figure 6.13 Rose diagram of fabric orientation analysis of SEM specimens at 90 degrees (a) intact and (b) consolidated at 1014 kPa

The rose diagrams in Figures 6.13 and 6.14 illustrate fabric orientation analysis of SEM specimens of clays from Beauharnois sites, comparing intact clay with specimens consolidated under 1014 kPa vertical effective stress at two different magnifications (3000× and 7000×). Figure 6.13 presents the results at 90 degrees orientation while Figure 6.14 is at 0 degrees orientation. In these diagrams, the radial distance from the center represents the frequency or

intensity of particle orientations in each angular direction, providing insight into the preferred alignment of clay particles. The intact clay specimens shown in both figures demonstrate relatively uniform, near-isotropic fabric orientation patterns across all angular directions. The bars extending from the center display relatively even distribution around the circumference, indicating that clay particles maintain a largely random orientation with no significant preferential alignment. This random fabric arrangement is characteristic of undisturbed clay before experiencing significant external stresses, reflecting the natural depositional processes and minimal stress history.

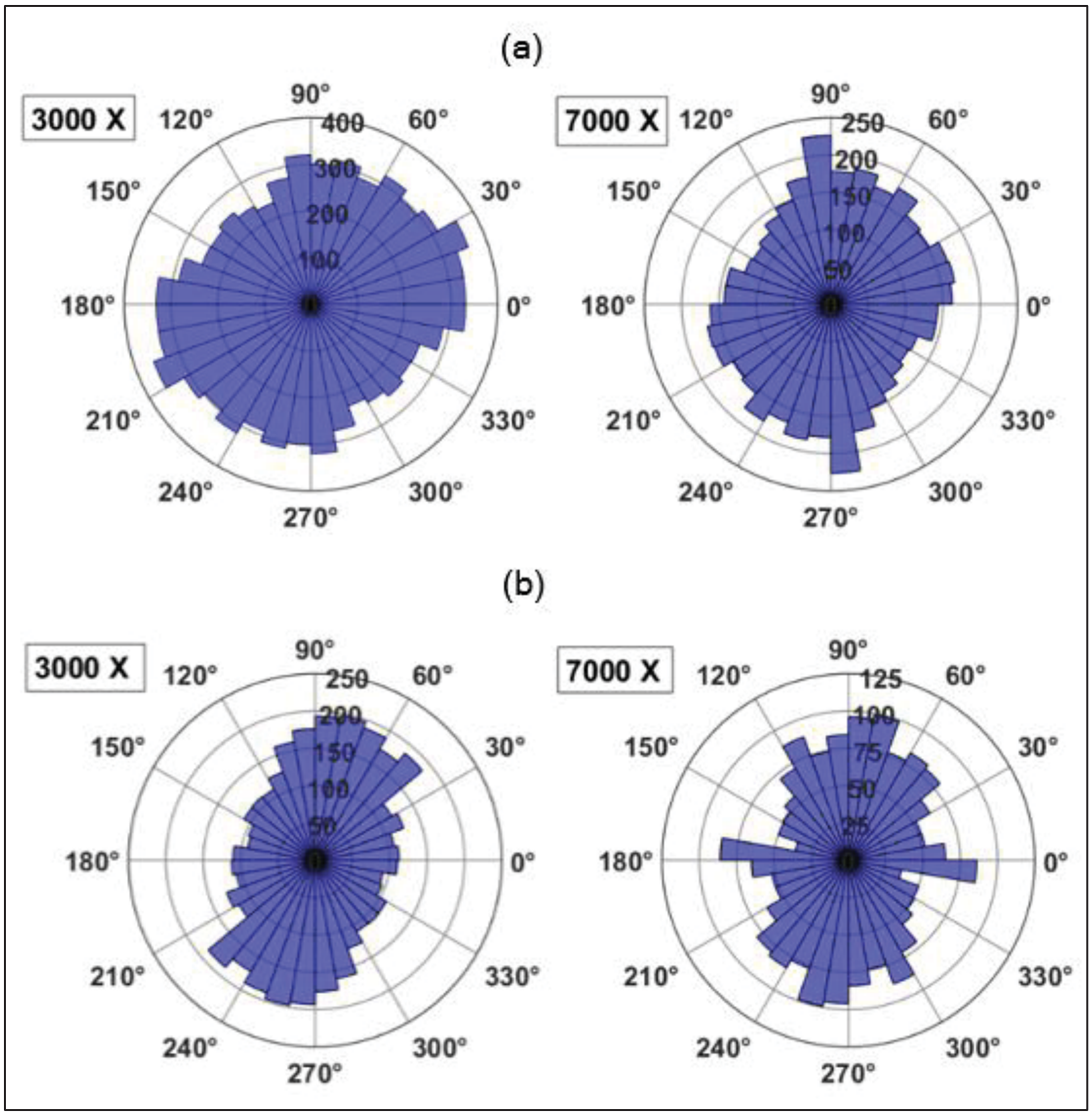

Figure 6.14 Rose diagram of fabric orientation analysis of SEM specimens at 0 degree (a) intact and (b) consolidated at 1014 kPa

Table 6.3 summarizes the average anisotropy indices for both undisturbed and consolidated specimens, quantifying the degree of fabric orientation changes. The progression from intact specimens with random orientation to consolidated specimens confirming preferential alignment demonstrates the clay's systematic response to applied stress through particle reorientation and fabric evolution.

Table 6.3 Anisotropy assessment of SEM specimens of Beauharnois clay

Stress (kPa)	Magnification	Average Anisotropy index	
		Horizontal Plane	Vertical Plane
0	3000	0.15	0.16
	7000	0.12	0.12
1014	3000	0.22	0.2
	7000	0.18	0.16

Figures 6.15 and 6.16 demonstrate the quantification of fabric anisotropy in Champlain clay from St Marcel site (Delage and Lefebvre, 1984) subjected to different 1D-consolidation stresses under vertical and horizontal conditions, respectively. The rose diagrams show patterns of particle reorientation as a function of applied stress magnitude and direction, with quantitative validation provided through anisotropy index calculations (Table 6.4).

Table 6.4 Comparison of anisotropy index of the SEM images of St- Marcel clay

Stress (kPa)	Magnification	Anisotropy Index	
		Horizontal Plane	Vertical Plane
0	3000	0.11	0.17
	7000	0.19	0.17
124	3000	0.15	0.27
	7000	0.14	0.27
421	3000	0.08	0.36
	7000	0.13	0.37
1452	3000	0.07	0.42
	7000	0.13	0.40

Under vertical consolidation (Figure 6.15), the intact clay indicates relatively isotropic fabric orientation with random particle alignment, confirmed by low anisotropy indices in the horizontal plane ($I_a \approx 0.11$-0.19) and vertical plane ($I_a = 0.17$).

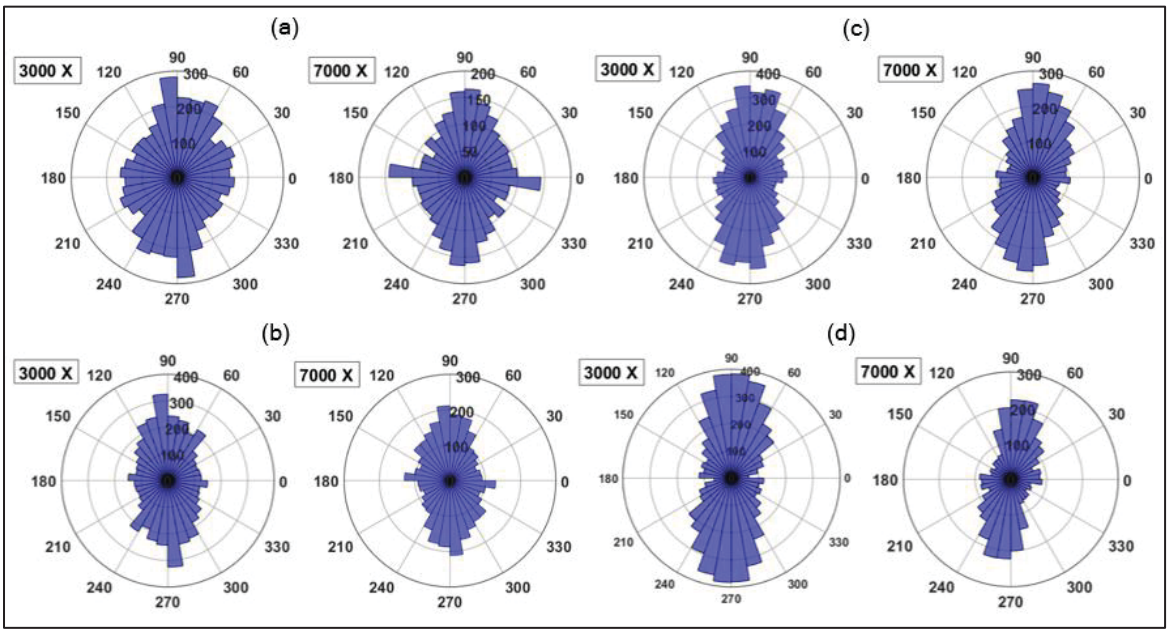

Figure 6.15 Quantification of fabric anisotropy of vertically trimmed St Marcel clay under different 1D-consolidation stresses; (a) Intact, (b) 124 kPa, (c) 421 kPa and (d) 1452 kPa

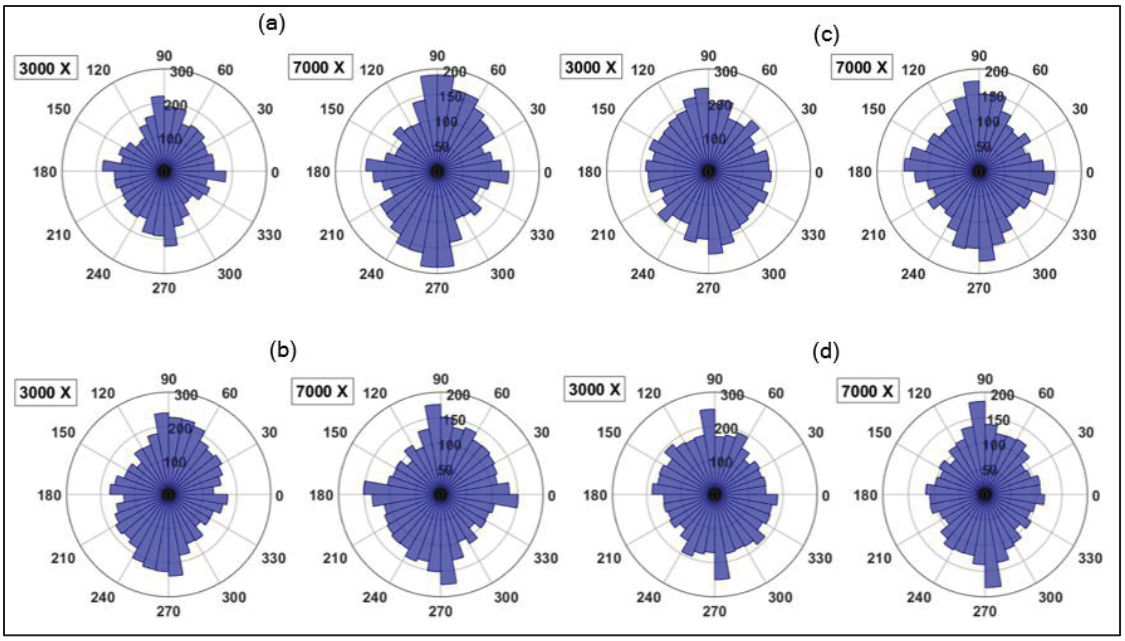

Figure 6.16 Quantification of fabric anisotropy of horizontally trimmed St Marcel clay under different 1D-consolidation stresses; (a) Intact, (b) 124 kPa, (c) 421 kPa and (d) 1452 kPa

As consolidation stress increases progressively from 124 kPa (Fig. 6.13b) to 1452 kPa (Fig. 6.15d), particles develop preferential orientation in the horizontal directions (0° and 180°), perpendicular to the applied effective vertical stress. This reorientation is quantified by the vertical plane anisotropy index increasing from $I_a = 0.27$ at 124 kPa to $I_a = 0.40$ at 1452 kPa, progressing from weakly oriented to highly oriented fabric according to the classification criteria (weakly oriented 0.15-0.21, highly oriented > 0.21). Simultaneously, the horizontal plane anisotropy index decreases from $I_a = 0.15$ at 124 kPa to $I_a \approx 0.07$-0.13 at 1452 kPa, indicating reduced randomness in particle orientation.

Conversely, horizontal consolidation (Figure 6.16) demonstrates the same concept with particles aligning perpendicular to the applied stress, resulting in vertical orientation (90° and 270°). However, the stress-induced fabric changes are less pronounced compared to vertical consolidation. The horizontal plane anisotropy indices show more modest variations, progressing from $I_a = 0.15$ at 124 kPa (Fig. 15b) to $I_a \approx$ 0.07-0.13 at 1452 kPa (Fig. 16d), indicating a more gradual fabric evolution under horizontal conditions.

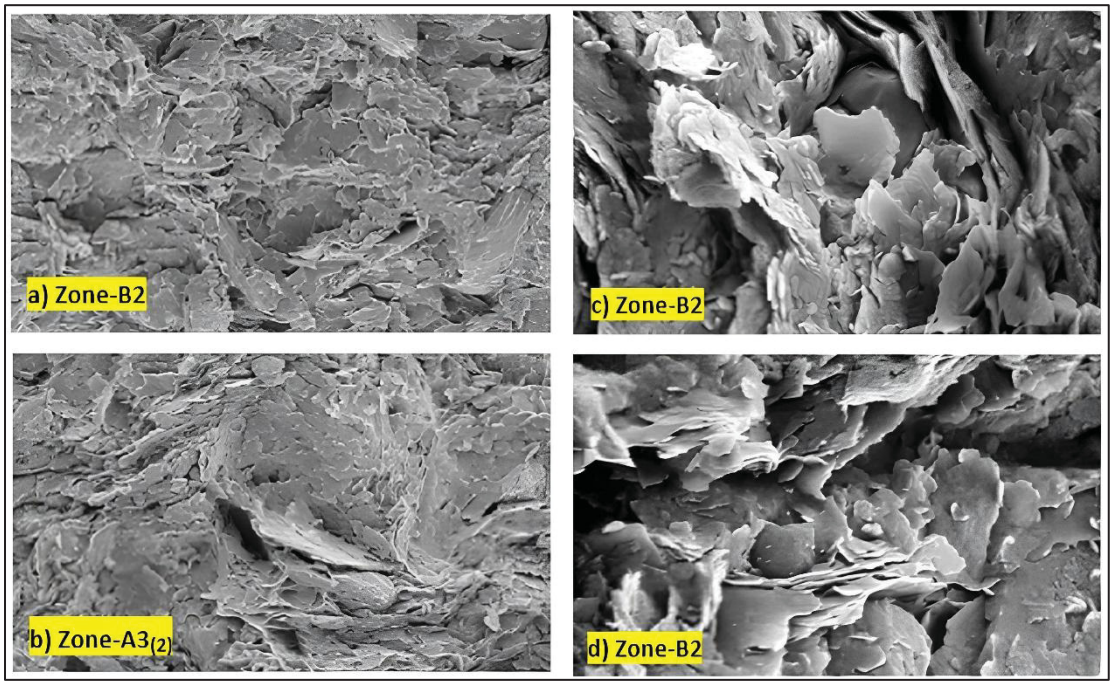

Figure 6.17 SEM images of heavily overconsolidated London clay captured by Gasparre et al. (2011) (Zones: C, B2 and A3) and Hight et al. (2003) (Zones: B2)

The rose diagrams in Figure 6.18 and quantitative indices in Table 6.5 represent significant fabric anisotropy in intact, heavily overconsolidated London clay specimens from different depths and studies.

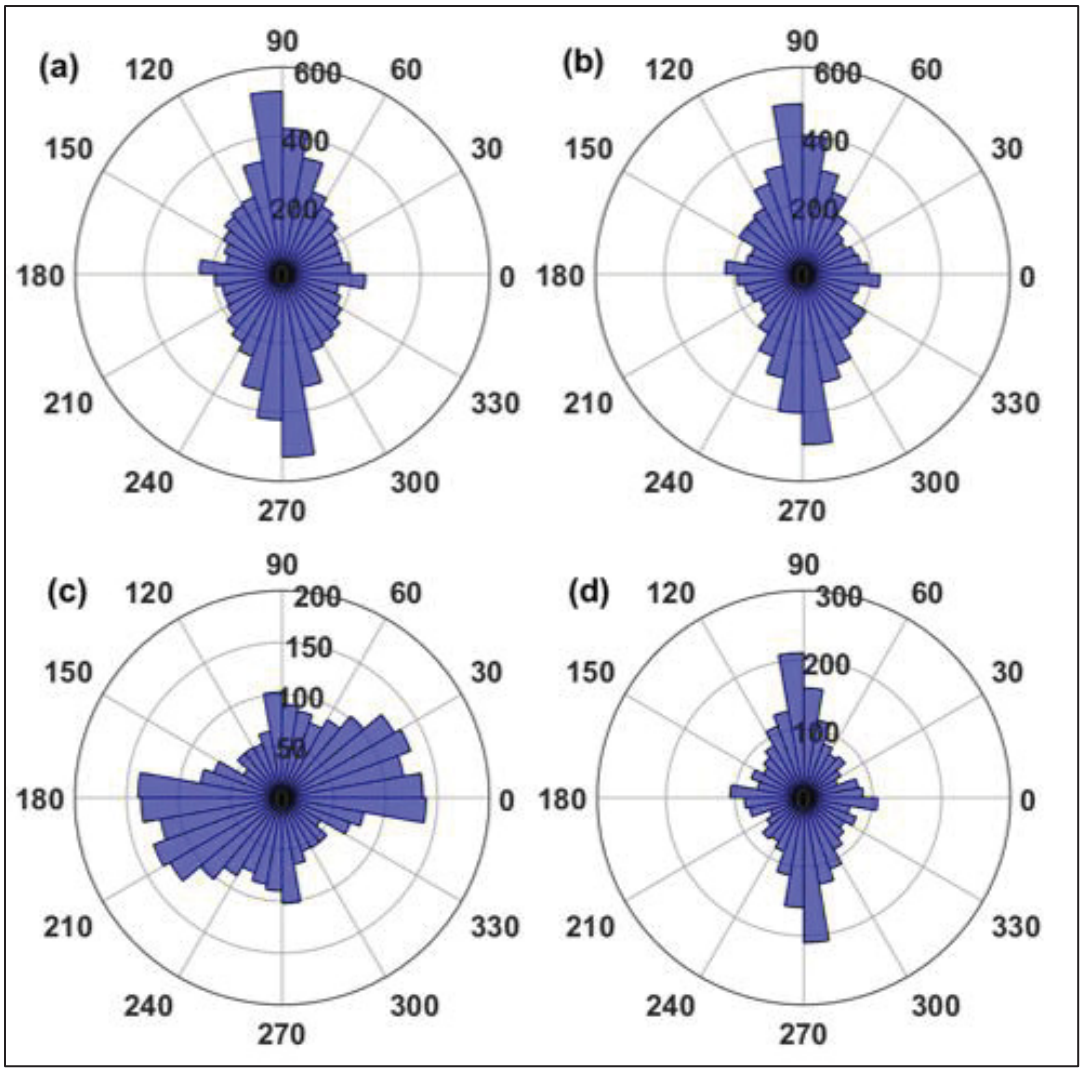

Figure 6.18 Intact London clay (a) and (b), SEM images by Gasparre et al. (2011) (c) and (d), SEM images by Hight et al. (2003)

Table 6.5 Anisotropy assessment of SEM images of London clay

Intact sample	Reference	Depth (m)	Anisotropy Index
(a) London-B2	Gasparre et al. (2011)	21	0.27
(b) London-A3$_{(2)}$	Gasparre et al. (2011)	33	0.25
(c) London- B2	Hight et al. (2003)	19.5	0.19
(d) London- B2	Hight et al. (2003)	9.5	0.28

The anisotropy indices range from 0.19 to 0.28, with most values exceeding, $I_a > 0.21$. The consistently high anisotropy indices (0.25-0.28 at greater depths, 0.19-0.28 at shallower depths) demonstrate that fabric anisotropy is an inherent characteristic of this heavily overconsolidated clay, developed through natural geological processes rather than external forces. Reported anisotropy degrees in Table 2 also confirm the higher variation of anisotropy through laboratory measurements.

The comparison between Champlain and London clays reveals two distinct pathways for fabric anisotropy development: stress-induced evolution versus geological inheritance. Champlain clay, being lightly overconsolidated, shows initially random to low fabric orientation in its intact state (anisotropy indices 0.11-0.19), making it interesting for studying under controlled laboratory conditions. London clay as a heavily overconsolidated deposit displays inherently high fabric anisotropy in its natural intact state (anisotropy indices 0.19-0.28), reflecting its complex geological history of deposition, consolidation, and subsequent unloading. The difference between these clay types demonstrates that OCR is an influential parameter in initial fabric state, with lightly overconsolidated clays retaining more random orientations while heavily overconsolidated clays preserve strong directional preferences.

6.4 Conclusion

The study of intermediate inclinations shares insights into the fabric evolution of clays based on bedding layer characteristics. The gradual changes in shear wave velocity and consolidation properties across intermediate angles reflect the progressive reorientation of clay particles and the development of preferential fabric alignments. The investigation of soft marine specimens trimmed at angles 30°, 45°, and 60° demonstrates a gradual transition in consolidation behavior between the principal orientations (0° and 90°). This transition is particularly evident in the C_c values, which vary with inclination angle, ranging from 1.53 to 1.12, decreasing as inclination shifts from 90° to 0°. The structured relationship between bedding plane orientation and soil compressibility, highlighting the inherent anisotropy in the tested clay.

V_{s1} measurements using P-RAT demonstrated a distinctive angular dependency pattern, where V_{s1} at intermediate angles (30°, 45°, 60°) systematically transitions between the principal directions $V_{s1\,(vh)}$ and $V_{s1\,(hh)}$. The V_s normalization was done to show consistent anisotropic behavior across varying stress levels (Fig. 6.7), with the angular variation following the harmonic mean formulation (Eq. 6.2). For lightly overconsolidated clays like Champlain clay, the combined evidence from V_s measurements and SEM analysis also report a stress-induced anisotropy development mechanism. The anisotropy ratios range from 1.03 to 1.25 depending on orientation angle, while microscale analysis confirms the evolution from initially random particle orientations in intact clay to progressively aligned fabric under increasing consolidation stress. The observed anisotropic behavior, especially at intermediate inclinations, suggests that conventional isotropic models may not adequately capture the stress-strain relationships in these soils, namely if overconsolidation is important.

CONCLUSION

This research investigated the anisotropic characteristics of Champlain marine clay through a multi-faceted experimental approach combining macro and microscale analyses. The study employed innovative laboratory techniques including P-RAT, high-precision strain gauges, and SEM to examine clay fabric anisotropy effects. It represents an important contribution in this field for Champlain clays, as prior assessments of directional properties were predominantly confined to conventional mechanical testing protocols, such as permeability and triaxial testing characteristics. The current work extends beyond the conventional methods of studying anisotropic response based on soil dynamic characteristics, directional V_s ($V_{s(vh)}$; $V_{s(hh)}$; $V_{s(\theta h)}$).

The pioneer of the P-RAT represents a reliable evolution in shear wave velocity measurement through laboratory methodology. A substantial focus of this research was devoted to the advancement and implementation of P-RAT methodology at ÉTS laboratory, which proved instrumental in facilitating the experimental investigations presented herein. The current work builds upon this foundation by fabricating a capsulated P-RAT design using stainless-steel (SS grade 304) encapsulation. This enhancement improved the system's performance by ensuring uniform stress distribution and reducing unwanted boundary effects between the piezoelectric components and the soil specimen. This setup facilitates the application of effective vertical stress magnitudes up to 1000 kPa, ensuring optimal sensor performance and data acquisition integrity under substantial consolidation conditions. The encapsulated design, operating with a resonant frequency range of 34-36 kHz and 6-9% damping ratio range, demonstrated high signal quality and measurement reliability compared to previous iterations. The system's ability to effectively transmit and receive multiple waveforms while minimizing compression wave interference represents an important development in fabrication process at ÉTS laboratory.

To preserve experimental simplicity and cost-effectiveness, rotation technique proposed by Roesler (1979) was implemented for directional V_s determination within the conventional oedometer framework. This approach eliminated the need for specialized equipment

modifications while maintaining testing protocol integrity. Specimens were trimmed along multiple orientations, enabling comprehensive investigation of anisotropic responses through the standard consolidation testing sequence. The methodology's integration with routine 1D-consolidation procedures offered an advantage by allowing simultaneous acquisition of both standard consolidation parameters and directional stiffness characteristics.

To capture the propagation-polarization characteristics of shear waves within the specimen body, four high-precision strain gauges (manufactured by Kyowa Inc.) were installed to the outer surface of a standard oedometer ring (63.5 × 19 mm), enabling measurement of lateral strain at the micron scale. This instrumentation developed the standard oedometer's capabilities by facilitating the conversion of tangential (hoop) strains to lateral stress components, a necessary parameter for anisotropy characterization. The instrumented oedometer apparatus thus overcame the inherent limitations, which measures only effective vertical stress.

The experimental results contribute to understanding how bedding layer orientation, consolidation stress, and microstructural evolution influence the clay's anisotropic behavior. Results of anisotropy study of Champlain clay samples are presented in the format of three chapters 4, 5 and 6. The key conclusions drawn from each chapter are summarized below:

Chapter 4:

Initially, a reliable experimental methodology was introduced to reinforce a conventional oedometer apparatus for the purpose of anisotropic characterization through employing P-RAT for V_s measurements and lateral strain gauges for subsequent purpose of the lateral pressure monitoring during constrained 1D-consolidation testing. The surface digital imaging as SEM technique was also proposed as an approach to progress fabric orientation calculation based on microstructure of the soil matrix.

- The integrated methodological approach implemented within the conventional oedometer effectively characterized clay anisotropy throughout consolidation testing,

demonstrating robust repeatability and yielding consistent results across multiple experimental iterations.

- The consolidation process induced changes in the clay microstructure, with clay particles progressively realigning towards a more parallel orientation under increasing stress. This was evidenced by both shear wave measurements and SEM imaging.
- The preconsolidation pressure values obtained in vertical and horizontal directions indicate higher rigidity in the horizontal direction compared to the vertical orientation.
- P-RAT testing showed that $V_{s(vh)}$ and $V_{s(hh)}$ increased proportionally with consolidation stress across all studied samples, conforming to the velocity-stress power law relationship.
- Standard oedometer apparatus fundamentally captures both types of anisotropy during 1D-consolidation: inherent anisotropy predominating in the initial consolidation phase (pre-σ_p') and stress-induced anisotropy manifesting primarily in the subsequent primary consolidation phase.
- The anisotropy ratio (α) showed variability in the overconsolidated state but exhibited a narrower range in the normally consolidated state (virgin compression), suggesting that high consolidation stresses tend to produce more uniform fabric alignment.
- Estimated α values ranging less than 1.30 indicate cross-anisotropic behavior in the Champlain clay specimens, with greater stiffness in the horizontal than vertical direction. These findings align with the literature on Champlain clays characterized through alternative laboratory methodologies.
- Fabric qualification and quantification through SEM imaging illustrate an initial random particle arrangement evolved into preferentially oriented structures after consolidation, indicating moderate development of stress-induced anisotropy.
- Empirical correlations were proposed in function of normalized V_s, void-ratio and σ_m' providing a representation of more realistic stress condition in the plane of wave propagation and particle polarization.

Chapter 5:

This chapter developed and validated a comprehensive methodological approach to analyzing microstructure of Champlain clay using SEM imaging. Two different fabric orientation calculations methods (FOCM-I and FOCM-II) were employed, and a parametric study examined the effects of key SEM parameters on directionality quantification. The experimental work proposed a new imaging technique that improved the reliability of anisotropy calculation based on microstructure of soils. An algorithm was developed in MATLAB to quantify clay fabric orientation characteristics. The image processing was calibrated through comprehensive analysis of four hundred images captured across multiple magnification scales and electron beam voltage settings. This extensive dataset enabled the identification and implementation of an optimal multi-level threshold that remained consistent across microstructural study.

- Determination of the optimal image processing threshold value proved critical for precise particle and pore delineation within the microstructural analysis. For utilized Champlain clay samples, a threshold value of T = 4 yielded superior segmentation outcomes, enabling clear differentiation between soil matrix and void spaces.
- For Champlain clay samples, a threshold value of T = 4 yielded superior segmentation outcomes with multi-level threshold values (T = 60.13; 98.96; 122.87; 157.29) representing average values obtained for 400 SEM images.
- A thorough analysis of SEM imaging parameters indicated that variations in accelerating voltage (10 kV to 30 kV) and magnification (1000× to 7000×) can significantly affect fabric anisotropy calculation, with differences of up to 100% between maximum and minimum anisotropy indices.
- The proposed imaging protocol-incorporating full-view and grid-view methodologies with randomized sampling from the peripheral regions- improved measurement precision by reducing quantification disparities by approximately 80%. This advancement enabled substantially more reliable characterization of fabric anisotropy through comprehensive and unbiased visual assessment of the Champlain clay structure.

- According to anisotropy classification of FOCM-I, intact Champlain clay samples show randomly oriented and low-oriented association (ranges around 0.145 and 0.17).
- For FOCM-I analysis, a voltage of 20 kV yields the maximum anisotropy index in most cases, while the lowest anisotropy index is obtained using FOCM-II at 15 kV.
- Voltages of 10 kV and 15 kV are less affected by magnification compared to other accelerating voltages (Figure 5.13 and 5.15 analysis). This makes the 1000×-3000× range most suitable when using lower voltages, ensuring measurement reproducibility regardless of magnification changes.
- Consolidated samples showed more consistent results across both methods compared to intact samples, suggesting that stress-induced fabric alignment minimize the influence of imaging parameters.
- The optimized SEM settings for reliable fabric anisotropy calculation are 15 kV accelerating voltage combined with 3000× magnification (grid-view) supplemented by 1500× magnification (full-view)

Chapter 6:

This chapter explored how the orientation of bedding layers affects the anisotropic behavior of Champlain clay. Using specimens cut at various angles (0°, 30°, 45°, 60°, and 90°) relative to the depositional direction, provided insights into the continuous nature of anisotropic behavior and its relationship with stress history. The research included comparative illustration and detailed microstructural investigation with other clay types.

- The study represents variations in C_c with specimen orientation, decreasing from 1.53 to 1.12 as inclination shifted from 90° to 0°, demonstrating bedding plane effects on compressibility of Chaplain clay during 1D-consolidation testing.
- Shear wave velocities at intermediate angles (30°, 45°, 60°) showed a transition trend between principal directions, following theoretical predictions and confirming the continuous nature of anisotropic behavior.
- Based on relationship between bedding layer inclination and α under increasing consolidation stress, the progressive reduction in α values from 1.1-1.25 at 30°

inclination to 1.05-1.15 at 45° and further decreasing to 1.0-1.1 at 60° demonstrates the continuous directional properties within the clay fabric.

- Comparison with other clay types revealed that Champlain clay from Beauharnois exhibits moderate anisotropy (ranging 1.15-1.55) compared to heavily overconsolidated clays like London Clay (ratios 1.7-2.0), reflecting differences in stress history and depositional environment.
- The microstructural analysis of Champlain clays of two different sites confirmed that particle reorientation under consolidation stress occurs gradually, with initial random association of clay platelets evolving into preferentially oriented structures aligned perpendicular to the applied stress.
- Multi-scale investigations of lightly overconsolidated Champlain clay showed consistent anisotropic behavior across both microscopic and macroscopic domains. Quantitative assessments indicated a low degree of anisotropy, with remarkable correspondence between fabric-derived measurements at the microstructural level and mechanical property evaluations at the specimen scale.
- The observed anisotropy aligns with the geological formation history of Champlain clay deposits, reflecting their post-depositional stress conditions based on the literature regarding the marine and glacial formations.

RECOMMENDATIONS

The methodology's applicability extends to projects involving tunneling, deep excavations, and foundation design in regions where Champlain marine clay deposits are prevalent particularly in Eastern Canada where these sensitive clays pose geotechnical challenges. Since the technique maintains compatibility with standard oedometer apparatus through specimen rotation, P-RAT and lateral strain gauge instrumentation, implementation requires minimal budget while providing substantial improvements in characterizing directional stiffness properties. The empirical correlations for normalized shear wave velocity developed from this research can be incorporated into result from neglecting anisotropy in design calculations.

This framework bridges laboratory investigation with field application, providing engineers with evidence-based tools to recognize and account for directional soil properties that fundamentally govern deformation, stability, and long-term performance of infrastructure in anisotropic clay deposits. Concerning the future directions of this research, the experimental methodology will enable the investigation of the following key aspects:

- To strengthen the understanding of regional variability and improve geotechnical design frameworks, it is recommended to expand the experimental database by testing Champlain clay specimens from multiple sites across Québec. Conducting anisotropy measurements on specimens obtained from different geological zones help capture variations in depositional environment, mineralogy, and stress history within the Champlain marine deposits. Such comparative testing enables the development of site-specific empirical correlations, obtaining the range of anisotropy ratio for Champlain clays and eventually others.
- Investigate the relationship between plasticity index and cross-anisotropic behavior in low-to-moderate I_p clays (I_p < 20), as these clays are most frequently involved in landslide failures yet remain underrepresented in anisotropy literature. Using the integrated methodology established in this research, conduct studies on clay samples

with I_p ranging from 5 to 40 to quantify how I_p influences: (1) the magnitude of anisotropy ratios (G_{hh}/G_{vh}), (2) fabric anisotropy evolution during 1D-consolidation.

- To complement the laboratory findings on stiffness anisotropy, field validation through in-situ geophysical works such as Modal Analysis of Surface Waves (MASW) and seismic cone penetration (SCPTu) testing is recommended. These techniques enable in-situ measurement of shear wave velocity profiles and can capture directional variations in stiffness related to bedding orientation and depositional structure at larger scales. By conducting those approaches along multiple azimuths relative to the known bedding direction, it becomes feasible to assess field-scale anisotropy and support and possibly improve the correlations established in laboratory P-RAT measurements.
- It is also recommended to further investigate the link between microstructural and macro anisotropy through coordinated laboratory testing. While the anisotropy index derived from SEM imaging provides valuable insight into the particle-scale fabric orientation, it does not directly correspond to the macroscopic stiffness anisotropy ratio obtained from shear wave velocity or shear modulus measurements. To establish a more robust relationship, future studies should perform parallel SEM and directional stiffness tests on identical specimens under controlled consolidation conditions like triaxial testing with isotropic stress states (to investigate the effect of clay fabric on anisotropy). Such an approach allows for the development of scaling or correlation models that bridge the micro- and macro-scale behaviors of Champlain clays.

ANNEX I

LABORATORY MEASUREMENT APPROACH FOR ANISOTROPY IN CHAMPLAIN CLAYS

A. Torabipour [a], Y. Ethier [b] and M. Karray [c],

[a, b] Department of Construction Engineering, École de technologie supérieure,
1100 Notre-Dame West, Montreal, Québec, Canada H3C 1K3
[c] Department of Civil Engineering and Building Engineering, Université de Sherbrooke,
Sherbrooke, Québec, Canada

Paper published in GeoManitoba conference, July 2025

Abstract

Soil anisotropy in natural clay deposits is a consideration in several geotechnical applications, including the design of foundations, slopes, and excavations. The Champlain clays of Eastern Canada, formed through marine sedimentation 10,000–12,000 years ago, exhibit distinct bedding characteristics that make them susceptible to anisotropy. This behavior can originate from either the microstructure of the clay fabric or the stress history. A series of laboratory methods used to assess anisotropy is reviewed. Wave-based approaches highlight some practical advantages in terms of simplicity and testing duration. This study employs an advanced laboratory setup using piezoelectric ring actuators integrated into an oedometer apparatus to quantify the anisotropic behavior through shear wave velocity. The measurements were conducted during 1D consolidation testing, allowing for simultaneous evaluation of stress-induced changes in anisotropy. The shear wave velocities were measured in both vertical and horizontal directions (V_{vh} and V_{hh}) under varying applied stress levels. Through wave propagation measurements in these two directions, the inherent and stress-induced components of anisotropy were inferred. The tested soft marine clay specimens demonstrated relatively low to moderate directional dependency, reflecting the effect of both their depositional fabric and stress history. These findings provide valuable insights into the mechanical behavior of Champlain clays and contribute to the understanding of anisotropy for geotechnical analyses.

Introduction

Champlain marine clays, which are widespread across Eastern Canada, exhibit anisotropic behavior that influences their geotechnical properties and engineering performance. These sensitive fine-grained soils owe their unique characteristics to a combination of depositional environment, post-depositional processes, and the formation of strong interparticle cementation bonds (Silvestri and Morgavi, 1982).

Anisotropy in Champlain clays manifests as directional variations in key mechanical properties such as strength, stiffness, deformation response, and hydraulic conductivity. These directional dependencies are observed when testing is conducted along principal directions, vertical versus horizontal orientations. The anisotropic fabric may be attributed to the open, flocculated microstructure of clay particles and the cementation bonds that developed during sedimentation and early diagenesis.

Understanding the degree of anisotropy in Champlain clays is of importance for engineering applications, namely in regions where construction of tunnels, deep excavations, foundations, and underground infrastructure is common. Such activities impose multidirectional stress states that interact with the soil's inherent directional properties, affecting its mechanical response and long-term performance.

In this study, a small-strain ($\gamma \leq 10^{-3}\%$) laboratory approach was employed to investigate the anisotropic behavior of Champlain clays using shear wave velocity (V_s) measurements. A review of previous utilized laboratory methodologies reported in the literature is presented to contextualize this investigation. This paper specifically characterized the anisotropic response using the Piezoelectric Ring Actuator Technique (PRAT), which enables directional V_s measurements under controlled loading conditions. The anisotropy index ($\alpha = G_h/G_v$) was quantified to evaluate the variation in stiffness between different orientations. Experimental results highlight the respective roles of inherent anisotropy, linked to the natural fabric and cementation, and stress-induced anisotropy, which evolves during loading. Because the P-RAT

method captures wave response at very small strain levels, it allows for a refined understanding of anisotropic stiffness properties that may be overlooked in conventional mechanical testing. The technique used provides for an interesting alternative to assess the initial and evolution of anisotropy in Champlain clays at strain levels far smaller than those reached by conventional testing methods.

Review of laboratory methods

The investigation of anisotropic behavior in Champlain marine clays has been approached across limited studies. The literature reports static experimental methods of anisotropy determination on this clay from various regions. Table A I.1 represents the laboratory methodologies employed to analyze anisotropic properties in vertical and rotated clay specimens.

Table A I.1 Common laboratory experimental programs utilized for Champlain clay anisotropy

Test method	Key parameter	Reference
Triaxial testing	Shear strength, Young's modulus (E_{hh}/E_{vh})	Mitchell 1970; Lo et al. 1971; Yong and Silvestri, 1979; Silvestri and Morgavi, 1982.
Anisotropic Oedometer	Preconsolidation pressure (σ_p')	Silvestri and Morgavi, 1982; Philibert, 1984.
Radial & Vertical permeability	Hydraulic conductivity ($r_k = k_h/k_v$)	Tavenas et al. 1983a, 1983b; Leroueil et al. 1990; Benabdallah, 2006.
Modulus anisotropy ratio: E_{hh}/E_{vh}; Permeability anisotropy ratio: $r_k = k_h/k_v$.		

Mitchell (1970) established anisotropic yield curves using fully drained triaxial tests, including both constant stress ratio ($\eta = q/p$) and constant mean normal stress (p) tests, on Champlain/Leda specimens trimmed horizontally and vertically from a block sample collected

at depths of 7.3-11.6 m. The study demonstrated that the yield curve for this marine clay deviated significantly from that expected for isotropic conditions.

Lo et al. (1971) examined anisotropy in stiff marine clays through unconsolidated-undrained triaxial tests on specimens oriented at angles of 0°, 30°, 45°, 60°, and 90° to the vertical axis or natural depositional direction. The tested clay was sampled from different depths while anisotropy tests specifically conducted on specimens from the 6.1 m level. The clay soil featured a random system of vertical and horizontal fissures. The degree of anisotropy, modulus ratio (E_{hh}/E_{vh}), was determined to be approximately 1.4 showing slight anisotropy effects as reported to reduce computed settlements by about 10% compared to isotropic conditions.

Yong and Silvestri (1979) also employed triaxial compression tests under both conventional axisymmetric and true-triaxial stress states on soft clay specimens from St-Louis, Quebec, collected from a test pit at depths of 13.7-19 m below a landslide crater. They conducted strain-controlled tests and stress-controlled tests with constant η and constant p paths, through preparing specimens at various orientations (β = 0°, 45°, 60°, 90°) to quantify directional strength properties.

Silvestri and Morgavi (1982) conducted anisotropic testing by means of triaxial and oedometer instrumented with lateral strain gauges on stiff Champlain clay specimens recovered from block samples at depths of 3.7-4.5 m in Rigaud region.

The laboratory data revealed mechanical anisotropy with vertical/horizontal strength ratios of 1.41, and $\frac{E_{hh}}{E_{vh}}$ of 1.60, for St-Louis clay (Yong and Silvestri, 1979), and Rigaud clay showed anisotropic modulus ratio of 1.54 (Silvestri and Morgavi, 1982).

This anisotropy appears most pronounced in the intermediate stress region where cementation bonding governs behavior, suggesting it may result from both depositional history and

cementation processes rather than particle orientation alone (Mitchell, 1970; Yong and Silvestri 1979).

From the hydraulic conductivity perspective, Triaxial and oedometer devices enable measurement of directional permeability in soils through controlled hydraulic gradients (Chapuis, 2012). In triaxial setups, vertical permeability (k_v) can be accessed via longitudinal flow, while radial permeability requires central drains creating inward flow paths. Modified oedometers with permeable rings permit horizontal flow assessment alongside vertical measurements. Under cross-anisotropy assumptions, radial permeability directly corresponds to horizontal permeability (k_h), as this framework treats the horizontal plane as isotropic.

Tavenas et al. (1983a, 1983b) developed specialized triaxial cells for constant head permeability tests on specimens of different sizes, testing both vertical and horizontal specimens cut from the same large block sample (from Saint-Zotique; 2-17m depth, Fort Lennox; 6.1m, Saint-Hilaire; 9.5m, Mascouche; 3.8m, Louiseville; 2.9-26m, Batiscan; 5.5-20.5m, Saint-Thuribe; 6.9m, and Saint-Alban; 1.9-7.8m). They also conducted falling head permeability tests in modified oedometer cells on specimens cut in both major orientations. Building on this work, Leroueil et al. (1990) developed a radial-flow permeameter specifically designed to measure horizontal permeability in specimens (from Louiseville; 9.2m depth, Saint-Esprit; 3.4m, 5.9m, 9.2m, and Saint-Alban; 2.5m) with a central injection hole, where flow was directed radially from center to circumference.

The testing protocol involved compressing specimens to various strain levels and measuring permeability at each stage to track changes in anisotropy. This methodical approach provided insights into how permeability anisotropy evolves during consolidation.

Permeability anisotropy, expressed as the ratio ($r_k = k_h/k_v$), varied in soft marine clays of different regions, generally exhibited low anisotropy with average r_k values between 1.0-1.2, ranging from 0.81 to 1.42 across different tests. The Louiseville clay showed slightly higher anisotropy (r_k = 1.35) compared to other marine clays.

Benabdallah (2006) also reported that the more stressed the soil is, the smaller the hydraulic conductivity and it is expected lower r_k after preconsolidation. The anisotropy degree of Lachenaie clay (from 2.3 m to 5.87 m) was investigated to be in range of 0.6 to 1.13.

Importantly, in marine clays, r_k remained relatively constant with compression up to 25% strain (Leroueil et al. 1990). All studies consistently show Champlain marine clays exhibit anisotropic elasto-plastic behavior at stresses below preconsolidation pressure. Cementation bonds dominate this behavior, influencing both deformation and strength characteristics, as well as soil particle arrangement affecting hydraulic conductivity.

While reviewed conventional laboratory methods shared important data into the mechanical behavior of Champlain clays, they are limited in their ability to fully capture anisotropic characteristics particularly at small strain levels. In contrast, advanced techniques that focus on small-strain stiffness offer a unique image of anisotropy. The shear wave velocity (V_s), as an elastic parameter, provides valuable insight into anisotropy of clay. Researchers have investigated glacial and marine clays from various regions using this approach in conjunction with geotechnical laboratory apparatus such as triaxial and oedometer tests (Pennington et al., 1997; Gasparre et al., 2011).

Different studies have examined stiffness anisotropy by evaluating the ratio of horizontal to vertical shear moduli (G_{hh}/G_{vh}), using the relationship between the small strain stiffness or maximum shear modulus (G_{max}) and V_s, as expressed in $G_{\max\,(ij)} = \rho V_{s(ij)}^2$ where ρ is the soil mass density, and $V_{s(ij)}$ is the shear wave velocity measured in a specific plane ij. To enhance the characterization of cross-anisotropic behavior in fine soils, alternative laboratory techniques utilizing shear wave measurements with piezoelectric transducers offer enhanced capability for characterizing cross-anisotropic behavior in soils.

This laboratory method provides multi-directional wave propagation data, enabling a comprehensive assessment of the soil's directional stiffness properties. By measuring V_s along

different planes and directions, it is possible to quantify G_{hh}/G_{vh}, evaluate fabric evolution under varying stress paths, and aid to establish a robust constitutive relationship. The non-destructive nature of piezoelectric techniques allows for continuous monitoring throughout loading sequences, monitoring the evolution of anisotropy during consolidation and shearing phases that conventional methods intrinsically cannot capture.

Directional V_s using P-RAT

This study utilized Piezoelectric Ring Actuator Technique (P-RAT) sensors installed vertically in both the cap and base of a modified oedometer cell (As shown in Figure A I.1). The feasibility of anisotropy investigation was accomplished through directional trimming, with specimens obtained in both vertical and horizontal orientations relative to their in-situ depositional direction. The trimming approach is important as it allows for a direct comparison of soil properties along different axes of the naturally deposited clay structure.

The experimental work focused on two block samples 22 × 15 cm (D × H) of Champlain clay extracted from the Beauharnois region of Quebec, Canada using the Laval Sampler (La Rochelle et al. 1981). Champlain clay was selected due to its distinctive depositional history and structural characteristics, making it particularly relevant for anisotropy investigation. The block samples were extracted from the depth of 6 to 7 meters, consisting of approximately 70% clay content and exhibiting a high natural water content of 80%. The fine soil is classified as a highly plastic marine clay, with a Liquid Limit (LL) of 65% and a Plasticity Index (I_p) of 42%. The P-RAT sensors employed in this study were custom-fabricated to meet the specific requirements of the investigation, offering several advantages over conventional bender elements, including enhanced signal quality, reduced near-field effects, and improved coupling with the soil specimen (Karray et al. 2015).

The testing procedure consisted of conducting 1D consolidation in the modified oedometer cell equipped with P-RAT sensors. Identification of influential planar stresses are essential for directional shear waves. This requirement was addressed by installing four strain gauges on the outer surface of a stainless steel oedometer ring (Figure A I.1).

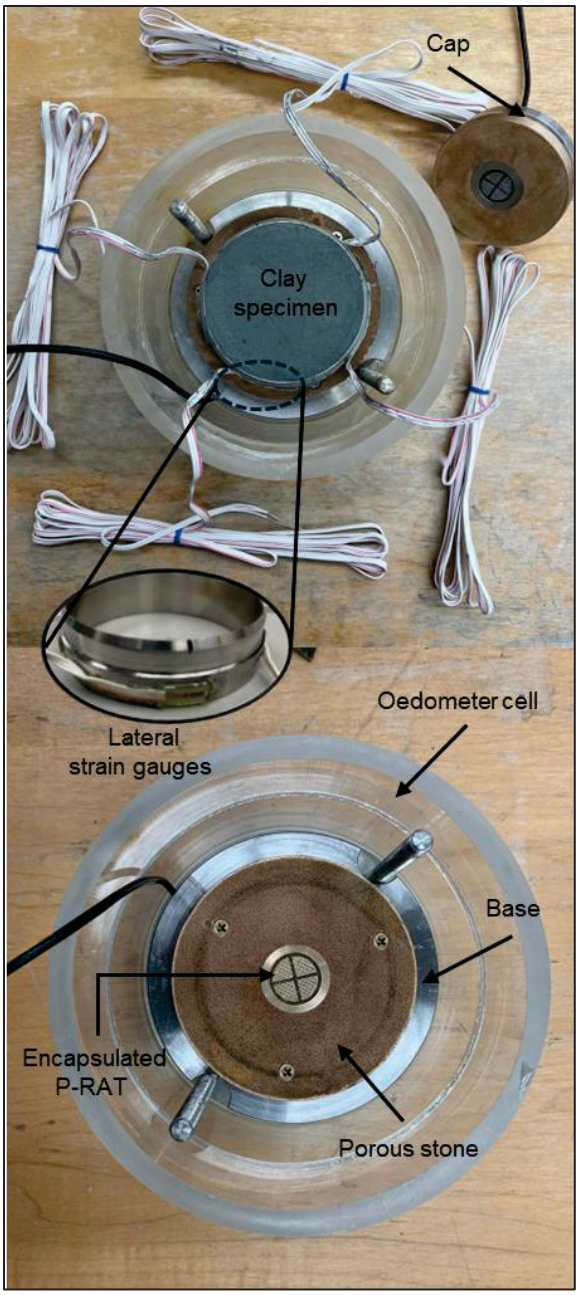

Figure A I.1 Modified oedometer for the purpose of stiffness anisotropy identification

While the triaxial stress state is known in standard test procedures, the oedometer configuration requires determination of lateral stress components, which can be measured using this strain gauge arrangement. This methodology is further explained and documented by Torabipour et al. (2024). This testing regime allowed simultaneously monitoring both the consolidation

behavior and the very small strain properties of the clay specimens under incrementally increasing vertical effective stress.

Throughout the consolidation process, the signal processing methodology encompassed wave generation from P-RAT transmitter in the base of the oedometer cell, signal reception by P-RAT receiver in the cap, and data acquisition during each loading stage of the consolidation process. The timing of shear wave measurements was carefully planned to capture the evolution of anisotropic properties throughout the consolidation process. Prior to reaching the preconsolidation pressure, measurements were conducted only after ensuring complete consolidation at each loading stage, as verified using the Taylor method. After exceeding the preconsolidation pressure, measurements were performed at regular 24-hour intervals, enabling the assessment of time-dependent changes in anisotropic behavior during both primary and secondary consolidation phases. This methodological approach offers advantages for investigating the evolution of anisotropic properties in clay soils under consolidation. By obtaining measurements throughout the consolidation process, the study provides the relationship between stress history and anisotropic behavior in clayey soils, the evolution of directional stiffness properties during consolidation, and allow correlation with consolidation parameters.

The acquired signals can be analyzed using approaches either in time or frequency domains. Time domain analysis involves direct assessment of wave arrival times and amplitude characteristics to determine shear wave velocity based on temporal traces. Frequency domain analysis allows for the evaluation of frequency-dependent behaviors to extract additional information about the soil-system's dynamic response.

The interpretation methodology followed an established protocol detailed in the works of Karray et al. (2015) and Hussein and Karray (2021), which provide comprehensive frameworks for extracting reliable shear wave velocity data from P-RAT measurements.

During 1D consolidation testing, two distinct series of directional shear wave velocities can be measured to characterize the cross-anisotropic behavior of clay specimens. The vertical-horizontal shear wave velocity (Vs_{vh}) represents wave propagation in the vertical direction with particle motion in the horizontal plane, while the horizontal-horizontal shear wave velocity (Vs_{hh}) corresponds to horizontally propagating waves and horizontal particle motions.

The measurement of both $V_{s(vh)}$ and $V_{s(hh)}$ enables quantification of the cross-anisotropic nature of Champlain clays, where the horizontal plane exhibits isotropic properties while the vertical axis maintains distinct characteristics. This directional stiffness identification reveals how the clay fabric responds differently to loading in various orientations, particularly during K_0 consolidation where lateral strains are constrained. By continuously monitoring V_s throughout the consolidation, the evolution of G_{hh}/G_{vh} can be considered as a function of stress state and loading history. The directional Vs measured during consolidation reveal a distinct behavioral transition: structural-dominated response at lower stress levels transitioning to predominantly stress-dependent behavior as higher stress levels are applied.

Discussion

The mechanical behavior of Champlain clays has been characterized by previous studies through various testing methodologies, showing the trace of anisotropic properties. The following results aim to expand on this foundational work by quantifying anisotropy through V_s measurements during 1D-consolidation, providing an insight into directional stiffness that complements the existing literature on anisotropic mechanical properties of this marine clay.

The consolidation curves in Figure A I.2 represent distinct differences between vertically and horizontally trimmed specimens, providing direct evidence of cross-anisotropic behavior in the tested Champlain clay. This directional dependency in consolidation characteristics aligns with the inherent fabric anisotropy reported by Yong and Silvestri (1979) and Philibert (1984), who reported different preconsolidation pressure (σ_p') for vertically and horizontally trimmed specimens of Champlain clay. For the specimen tested, the values of σ_p' are 71 and 35 kPa in vertical (usual) and horizontal orientation, respectively. The difference in compressibility

between orthogonal directions underscores the effect of depositional characteristics that causes preferential mechanical response in Champlain clays which is confirmed with hydraulic conductivity during compression (Tavenas et al. 1983 b) and Triaxial testing (Lo et al. 1971).

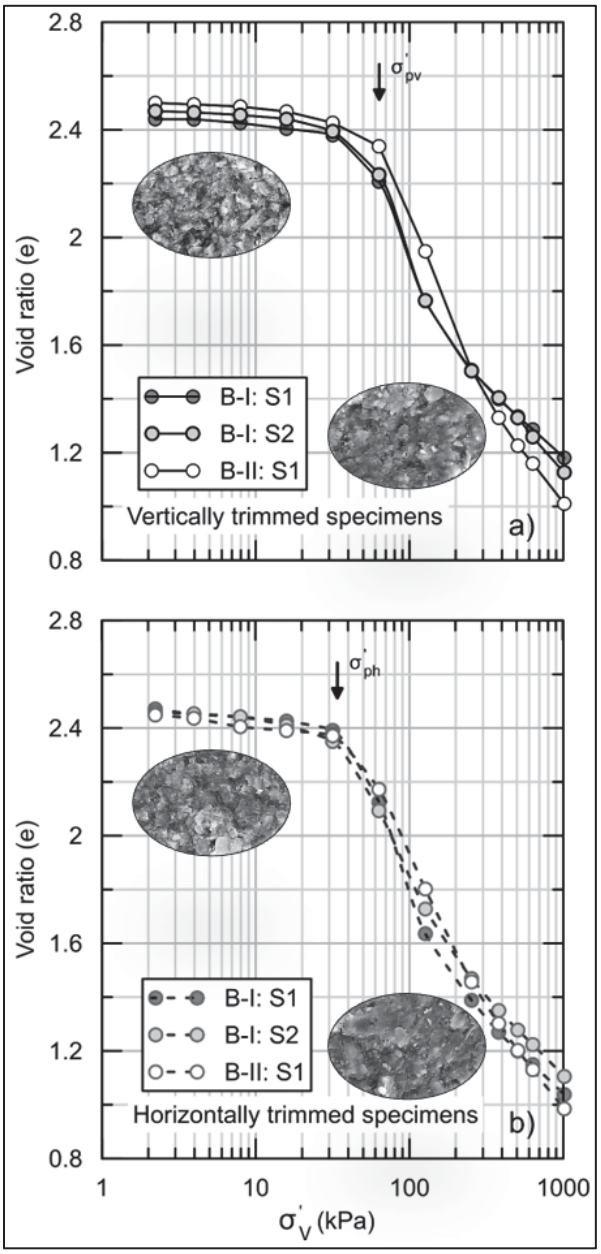

Figure A I.2 Consolidation curve of vertically and horizontally trimmed specimens

Figure A I.3 shows the interpretation of directional wave signals, vh and hh, in frequency domain. The recorded wave signatures reveal fundamental differences in how shear waves propagate through the clay fabric depending on both propagation and polarization directions. These variations are indicative of cross-anisotropic behavior, where the alignment of microstructural features such as particle orientation and bedding planes combined with the applied stress state, results in direction-dependent stiffness and wave velocity. The arrivals of these waveforms demonstrate that the dynamic response of the clay is not uniform in all directions, confirming the presence of inherent structural anisotropy that persists even at the small strains associated with elastic wave propagation. The directional shear wave signals at a specific loading stage shown in Figure A I.3 further quantify the degree of anisotropy through wave propagation characteristics and small strain stiffness. The temporal trace of waves shows an apparent difference between $V_{s(vh)}$ and $V_{s(hh)}$ where vertically versus horizontally propagating shear waves demonstrate that the small-strain stiffness properties of the clay exhibit directional dependency. This observation supports Mitchell's (1970) findings that Champlain clay exhibits anisotropic yield behavior that deviates from that expected for isotropic soils.

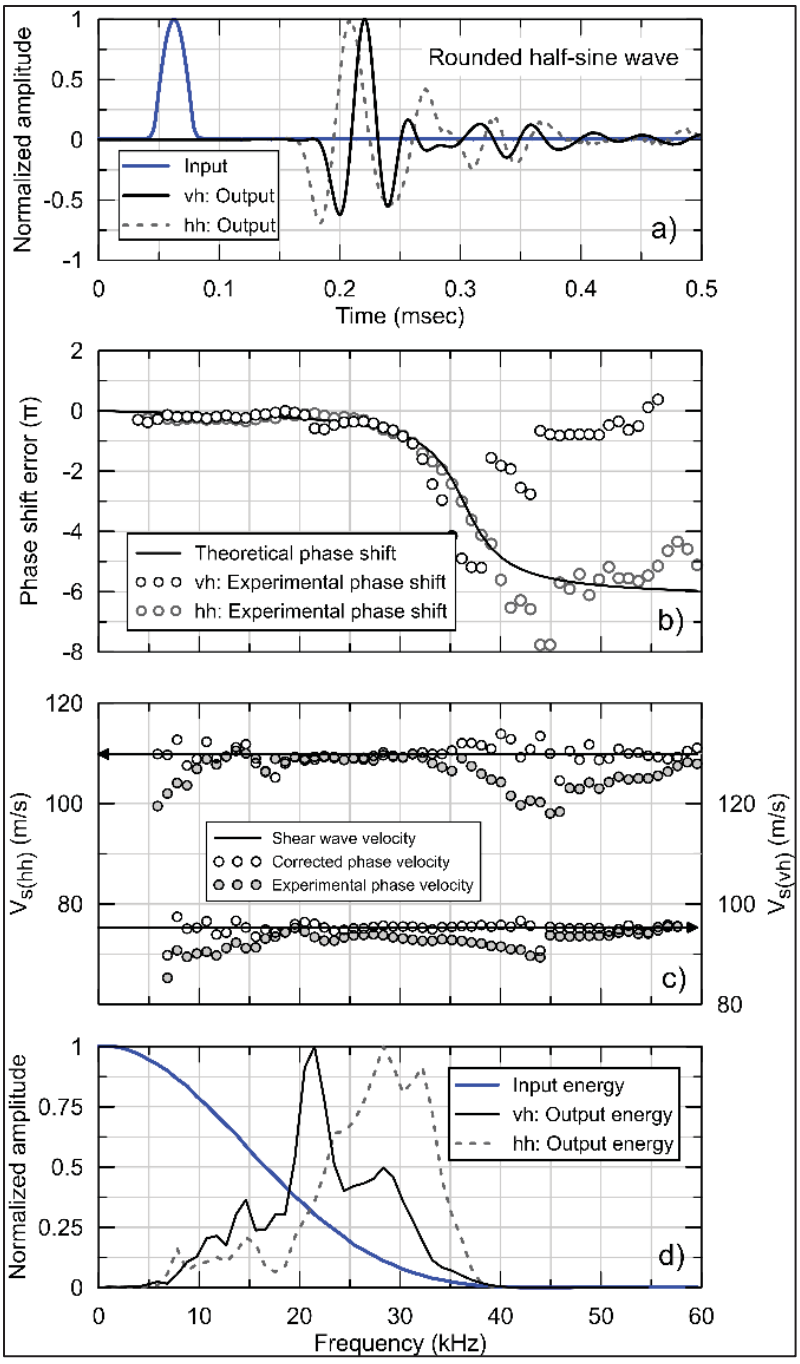

Figure A I.3 Interpretation of shear wave signals captured at 127 kPa vertical effective stress during consolidation

The influence of bedding layers is a primary factor contributing to anisotropy, as they affect shear wave transmission depending on their orientation relative to the direction of polarization. This behavior, combined with the evolving stress state during consolidation, governs the

directional variation in shear wave velocity. A series of wave signal interpretations was carried out at each loading stage of the 1D-consolidation test to determine the directional V_s. The stress level shown (127 kPa) exceeds the pre-yield stress (beginning of destruction), representing a transition zone where particles begin to rearrange. This observation aligns with Mitchell's (1970) findings that stress history influences the anisotropic yield response of Leda clays, with cementation effects being most pronounced at intermediate stress levels. Frequency domain analysis of the waveforms enabled estimation of the G_{max} in both vh and hh planes, capturing the directional stiffness characteristics. As illustrated in Figure A I.4a, the evolution of normalized cross-anisotropic stiffness in Champlain clay is plotted against the applied consolidation stress. The mean effective stress at each vertical loading level was calculated under K_o condition obtained from strain gauges utilized in the oedometer cell (Figure A I.1). It allows for realistic stress path simulation and accurate evaluation of anisotropic stiffness parameters (e.g., G_{vh} and G_{hh}) as a function of stress state and fabric orientation (Figure A I.4b). The relationship between K_o and the anisotropic G_{max} is primarily introduced by Jamiolkowski et al. (1995). The ratio of stiffness, $\alpha = (G_{hh}/G_{vh})$ follows a power law relationship with K_o, expressed as $G_{hh}/G_{vh} = (S_{hh}/S_{vh})K_0^n$, where S_{hh}/S_{vh} represents the fabric anisotropy.

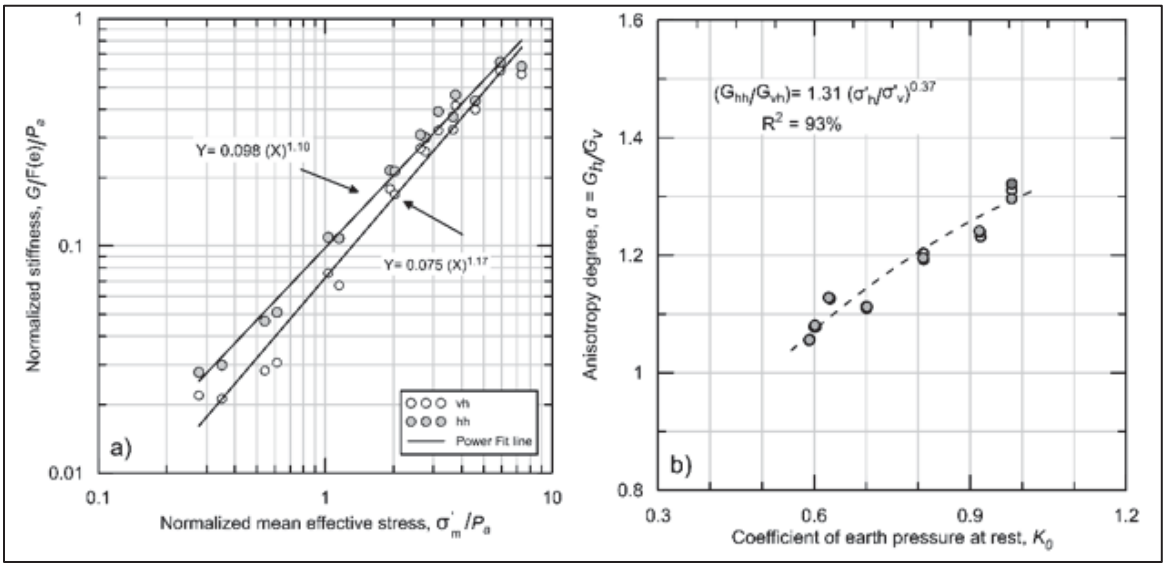

Figure A I.4 Vertical and horizontal G_{max} of tested specimens versus mean effective stress

The approximate consistency of α throughout the tested stress range suggests that the structural features causing anisotropy remained stable during compression. This supports Tavenas et al. (1983b) assertion that fabric anisotropy of marine clays maintains relatively consistent because compression affects their aggregate structure similarly in all directions. Unlike varved clays that exhibit drastic changes in anisotropy with stress level due to their strongly layered structure, the Champlain clay shows a more moderate and stable anisotropic response, reflecting its more homogeneous yet directionally oriented microstructure.

Table A I.2 Anisotropy ratio of Champlain marine clays

Study	Ratio
Mitchell 1970	$\frac{E_h}{E_v} = 1.4$
Lo et al. 1971	$\frac{E_h}{E_v} = 1.4$
Yong and Silvestri, 1979	$\frac{E_h}{E_v} = 0.63$
Silvestri and Morgavi, 1982	$\frac{E_h}{E_v} = 1.54$
Tavenas et al. 1983a, b	$\frac{k_h}{k_{v_{(Oed)}}} = 0.91 \sim 1.42$ $\frac{k_h}{k_{v_{(Trx)}}} = 0.81 \sim 1.16$
Leroueil et al. 1990	$\frac{k_h}{k_v} = 1.0 \sim 1.35$
Benabdallah, 2006	$\frac{k_h}{k_v} = 0.6 \sim 1.13$
Current study	$\frac{G_h}{G_v} = 1.31$

Table A I.2 offers a comparison of anisotropy ratios for Champlain marine clays across multiple decades of research, revealing important patterns in how directional properties have been quantified through different methodologies. The compilation of these ratios provides a unique opportunity to evaluate the consistency of anisotropic behavior across different

properties and testing approaches. The current study's G_h/G_v ratio of 1.31 falls within the broad range established by previous researchers but utilizes small-strain measurements that capture the clay's behavior before significant destructuration occurs. This approach offers an important advantage over other methods, as it characterizes inherent anisotropy with minimal disturbance to the clay's natural structure. The alignment between this G_{max}-derived anisotropy ratio and those obtained through different testing methodologies suggests a fundamental consistency in the directional nature of Champlain clays, despite variations in testing techniques, specific sampling locations and depth.

The relatively moderate magnitude of these ratios supports Tavenas et al.'s (1983) and Benabdallah (2006) assertion that anisotropy, while measurable, may not be a dominant parameter controlling the overall behavior of marine clays in most engineering applications. This finding has important practical implications, suggesting that while anisotropy should be acknowledged in detailed analyses and in applications where directionality plays a critical role, simplified isotropic approaches may provide reasonable approximations for preliminary design scenarios where directionality is not a primary concern.

Conclusion

Studies of Champlain marine clays reveal differences between horizontal and vertical properties in k, E, and G_{max}, indicating these clays exhibit low to moderate anisotropy. This behavior supports the assumption of transverse isotropy or cross-anisotropy, which is applied in geotechnical analyses of natural clayey deposits.

Experimental results from the present study, based on V_s measurements using the P-RAT technique, indicate that α decreases gradually during consolidation from approximately 1.31 in the natural state to lower values, reaching to 1.10 under normally consolidated condition (Figure A I.4). This minor reduction in stiffness anisotropy ratio suggests that consolidation-induced fabric reorientation slightly reduces inherent anisotropy but does not eliminate it.

Our observed α values fall within the r_k range (1.0-1.5) that Olson and Daniel (1981) reported for marine clays, including Champlain deposits. These values indicate that soil anisotropy remains relatively low throughout the entire consolidation process.

APPENDIX A

STRAIN GAUGES FUNDAMENTAL

Strain gauge installation and measurement

High-precision strain gauges typically used for oedometer rings have a resolution in the range of 1 micro strain (1×10^{-6}). The gauges must be installed circumferentially on the outer surface of the ring to capture the hoop strain directly. Their measurement represents a localized reading at a specific point on the circumference of the ring. Multiple gauges are often installed at different circumferential positions to account for any non-uniform deformation. The average of these readings provides a more representative measurement of the overall hoop strain. The strain gauge model was used in this study, KFWB uniaxial gauges. The KFWB uniaxial strain gauge is a waterproof foil strain gauge designed for specialized measurements in challenging environments. This strain gauge is particularly notable for its waterproof structure, making it suitable for underwater or high-moisture environments. It can operate within a temperature range of -10 to +80°C, as indicated in the operating temperature specifications. An important feature is that these gauges use a special waterproof covering resin that can withstand approximately 10 MPa of underwater pressure and shows virtually no deterioration even after 100 hours of underwater use, making them highly reliable for long-term underwater strain measurements.

Thin-walled cylinder criteria

Before applying this methodology, it is essential to verify that the cylinder meets the thin-walled criteria. A cylinder is considered thin walled when:

$$\frac{S}{d_i} \leq \frac{1}{20} \; or \; (0.05) \qquad \text{(A A.1)}$$

Where:

S = wall thickness of the oedometer ring

d_i = internal diameter

Stress components

In a thin-walled cylinder under internal pressure, three principal stresses exist. Figure A A.1 indicates a) a small element of a cylindrical section along its length dz, and b) small element along the axial plane:

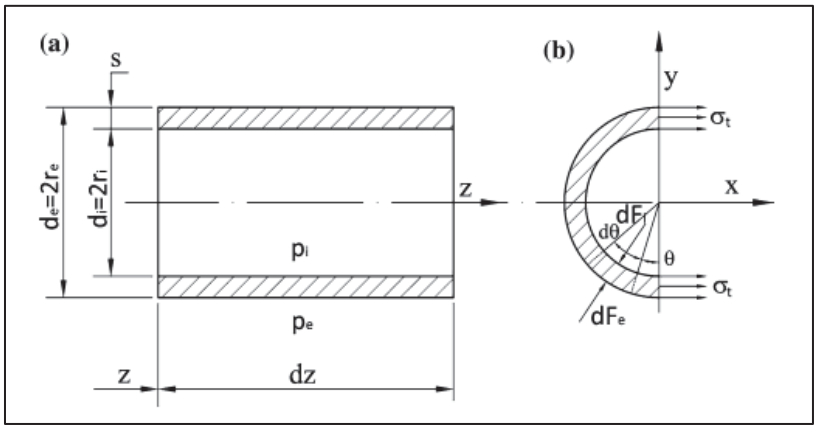

Figure A A.1 Stress state in thin-walled circular cylinders
Taken from Vullo (2014, p. 5)

- Hoop stress (σ_t)

The primary stress of interest, acting tangentially to the cylinder's circumference. This stress tends to split the cylinder along its longitudinal axis. As shown in Figure A A.1(b), the hoop stress acts perpendicular to the radial plane and is distributed along the wall thickness. For thin-walled cylinders, this distribution is approximated as uniform through the thickness.

- Longitudinal stress (σ_z)

Acts parallel to the cylinder's axis, as depicted in Figure A A.1. For closed-end cylinders, this stress is approximately half the magnitude of the hoop stress. The longitudinal stress arises from the pressure acting on the end closures of the cylinder. The relationship between hoop and longitudinal stress can be expressed as:

$$\sigma_z \cong \frac{\sigma_t}{2} \quad \text{(A A.2)}$$

For thin-walled circular cylinders, axial stress depends on whether the ends are closed (with real or virtual closures) or open. In the case of open or free ends, where the pressure is not acting on any end closures, σ_z is indeed zero.

- Radial stress (σ_r)

This stress component varies from $-P_i$ at the inner surface to 0 at the outer surface. The variation follows a logarithmic pattern, but for thin-walled cylinders, it can be approximated by taking the average value:

$$\sigma_r = -(\frac{P_i}{2}) \quad \text{(A A.3)}$$

In thin-walled cylinders with $\frac{S}{d_i} \leq \frac{1}{20}$, the absolute value of radial stress is less than 1/20 of the hoop stress.

The detailed process for calculating hoop stress follows these steps:
Through equilibrium analysis:

$$2 \times \sigma_t \times S \times dz = \int (dF_i - dF_e) sin\theta \quad \text{(A A.4)}$$

Where:

$$dF_i = P_i r_i d\theta \, dz \quad \text{(A A.5)}$$

$$dF_e = P_e(r_i + S) d\theta \, dz \quad \text{(A A.6)}$$

After integration and simplification, for internal pressure only ($P_e = 0$), the equation becomes:

$$\sigma_t = \left(\frac{P_i d_i}{2S}\right) \quad \text{(A A.7)}$$

While the methodology assumes uniform stress distribution, it's important to understand the actual stress variation through the wall thickness. The experimental analysis of hoop stress reveals that the traditional assumption of uniform stress distribution through wall thickness requires significant refinement. The following approaches provide more accurate representations of actual stress states as an equivalent stress (σ_e) in thin-walled cylinders. This experimentally verified equation shows that the ratio of outer to inner radius follows an exponential relationship with the pressure-to-stress ratio, rather than the linear relationship assumed in basic theory. This finding is based on the reported number of experimentally conducted research (Vullo 2014).

$$\frac{r_e}{r_i} = e^{\frac{P_i}{\sigma_{ei}}} \quad \text{(A A.8)}$$

Strain state

The strain state in thin-walled cylinders can be analyzed using the thermoelastic stress-strain relations, also known as Hooke's relations. For the oedometer ring, we can specifically examine the hoop strain condition.

According to Hooke's relationships, the hoop (circumferential) strain, ε_t, is given by:

$$\varepsilon_t = \left(\frac{1}{E}\right)[\sigma_t - v(\sigma_z + \sigma_r)] + \alpha T \quad \text{(A A.9)}$$

σ_z is zero since the ring has free ends. The σ_r is relatively small compared to the hoop stress and can be neglected. Additionally, since we are considering ambient temperature conditions in the laboratory, thermal expansion term αT can be omitted. Therefore, the final format of the equation is as follows:

$$\varepsilon_t = (\frac{1}{E})\sigma_t \qquad \text{(A A.10)}$$

Figure A A.2 presents the specifications of the KFWB Series Waterproof Strain Gauges, which were selected for their moisture resistance and reliability in varying environmental conditions. The waterproof resin covering provides protection while remaining flexible enough to accurately transfer strain from the measured surface.

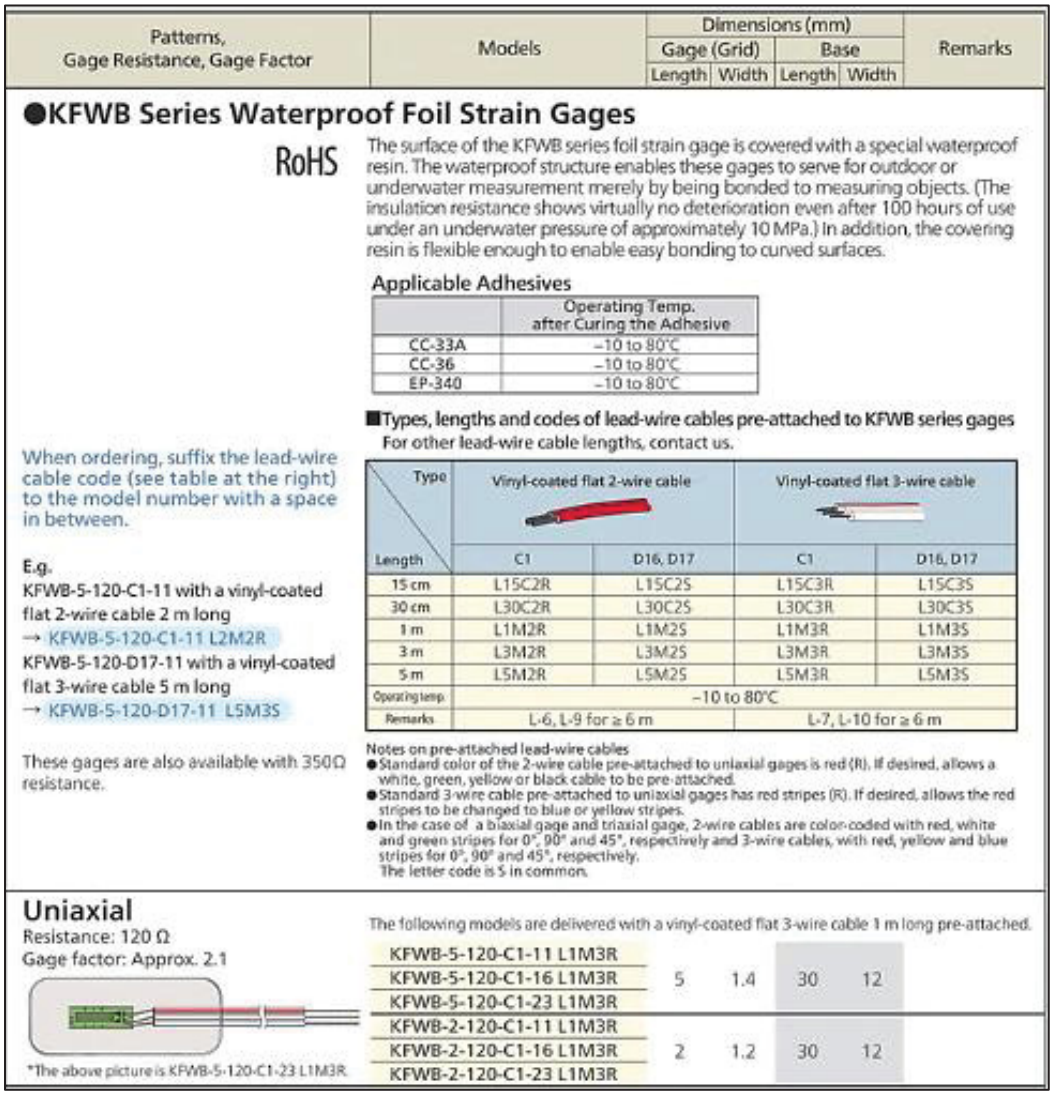

Patterns, Gage Resistance, Gage Factor	Models	Dimensions (mm) Gage (Grid) Length	Gage (Grid) Width	Base Length	Base Width	Remarks

●KFWB Series Waterproof Foil Strain Gages

RoHS

The surface of the KFWB series foil strain gage is covered with a special waterproof resin. The waterproof structure enables these gages to serve for outdoor or underwater measurement merely by being bonded to measuring objects. (The insulation resistance shows virtually no deterioration even after 100 hours of use under an underwater pressure of approximately 10 MPa.) In addition, the covering resin is flexible enough to enable easy bonding to curved surfaces.

Applicable Adhesives

	Operating Temp. after Curing the Adhesive
CC-33A	–10 to 80°C
CC-36	–10 to 80°C
EP-340	–10 to 80°C

■Types, lengths and codes of lead-wire cables pre-attached to KFWB series gages

For other lead-wire cable lengths, contact us.

When ordering, suffix the lead-wire cable code (see table at the right) to the model number with a space in between.

E.g.
KFWB-5-120-C1-11 with a vinyl-coated flat 2-wire cable 2 m long
→ KFWB-5-120-C1-11 L2M2R
KFWB-5-120-D17-11 with a vinyl-coated flat 3-wire cable 5 m long
→ KFWB-5-120-D17-11 L5M3S

These gages are also available with 350Ω resistance.

Type / Length	Vinyl-coated flat 2-wire cable C1	Vinyl-coated flat 2-wire cable D16, D17	Vinyl-coated flat 3-wire cable C1	Vinyl-coated flat 3-wire cable D16, D17
15 cm	L15C2R	L15C2S	L15C3R	L15C3S
30 cm	L30C2R	L30C2S	L30C3R	L30C3S
1 m	L1M2R	L1M2S	L1M3R	L1M3S
3 m	L3M2R	L3M2S	L3M3R	L3M3S
5 m	L5M2R	L5M2S	L5M3R	L5M3S
Operating temp.	–10 to 80°C			
Remarks	L-6, L-9 for ≥ 6 m		L-7, L-10 for ≥ 6 m	

Notes on pre-attached lead-wire cables
- Standard color of the 2-wire cable pre-attached to uniaxial gages is red (R). If desired, allows a white, green, yellow or black cable to be pre-attached.
- Standard 3-wire cable pre-attached to uniaxial gages has red stripes (R). If desired, allows the red stripes to be changed to blue or yellow stripes.
- In the case of a biaxial gage and triaxial gage, 2-wire cables are color-coded with red, white and green stripes for 0°, 90° and 45°, respectively and 3-wire cables, with red, yellow and blue stripes for 0°, 90° and 45°, respectively.
  The letter code is S in common.

Uniaxial

Resistance: 120 Ω
Gage factor: Approx. 2.1

*The above picture is KFWB-5-120-C1-23 L1M3R

The following models are delivered with a vinyl-coated flat 3-wire cable 1 m long pre-attached.

KFWB-5-120-C1-11 L1M3R	5	1.4	30	12
KFWB-5-120-C1-16 L1M3R				
KFWB-5-120-C1-23 L1M3R				
KFWB-2-120-C1-11 L1M3R	2	1.2	30	12
KFWB-2-120-C1-16 L1M3R				
KFWB-2-120-C1-23 L1M3R				

Figure A A.2 Waterproof strain gauge (KFWB) specifications
Taken from KYOWA measuring equipment general catalog (p. 35)

Figure A A.3 illustrates the complete strain gauge bonding procedure, detailing the critical eight-step process that ensures proper installation and optimal measurement accuracy. This standardized procedure was followed meticulously for all specimens to maintain consistency in the experimental results.

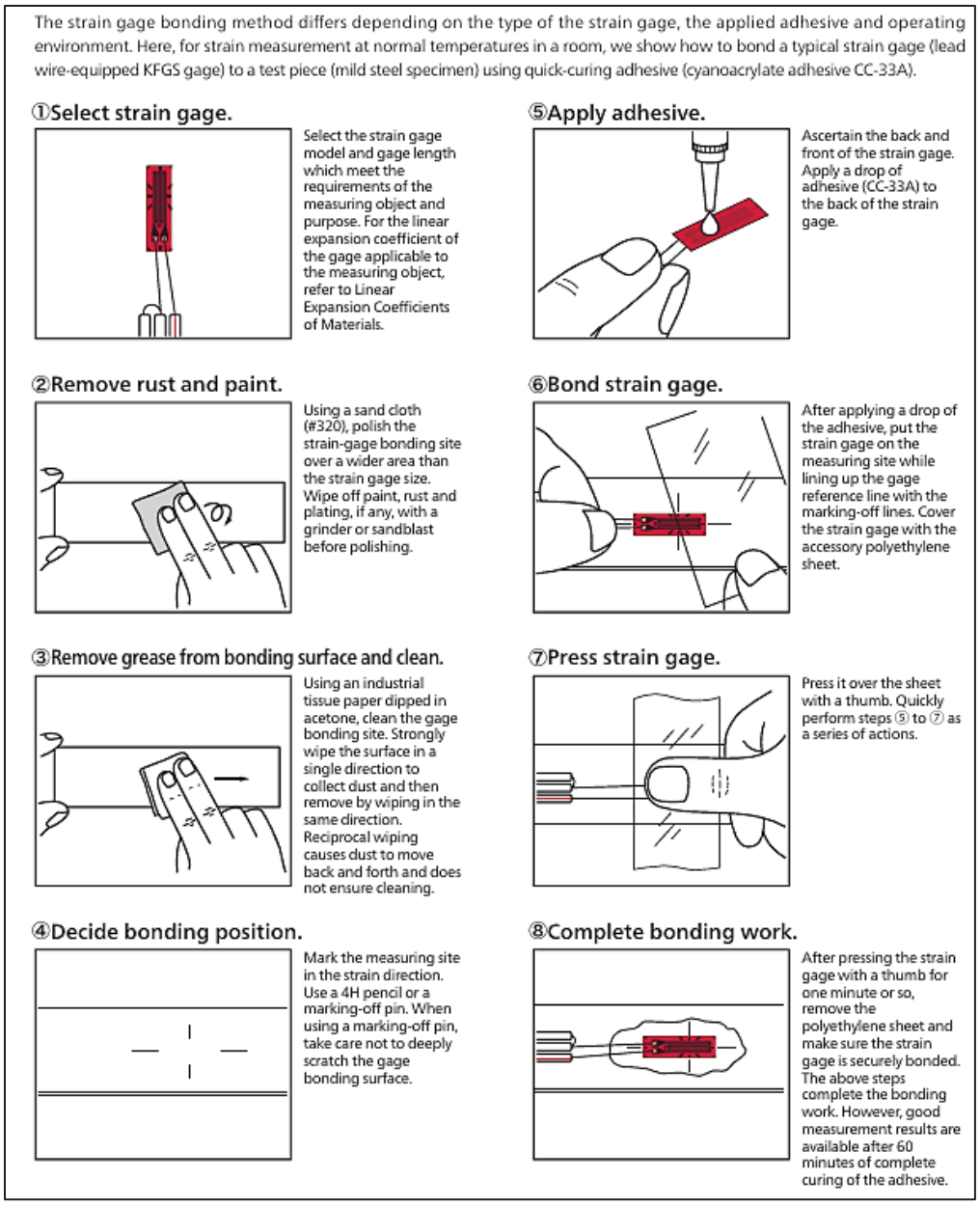

Figure A A.3 Strain gauge bonding procedure
Taken from KYOWA measuring equipment general catalog- Technical memo (p. 9)

Figure A A.4 outlines the fundamental principles governing strain gauge measurements, including the mathematical relationships between resistance change and mechanical strain.

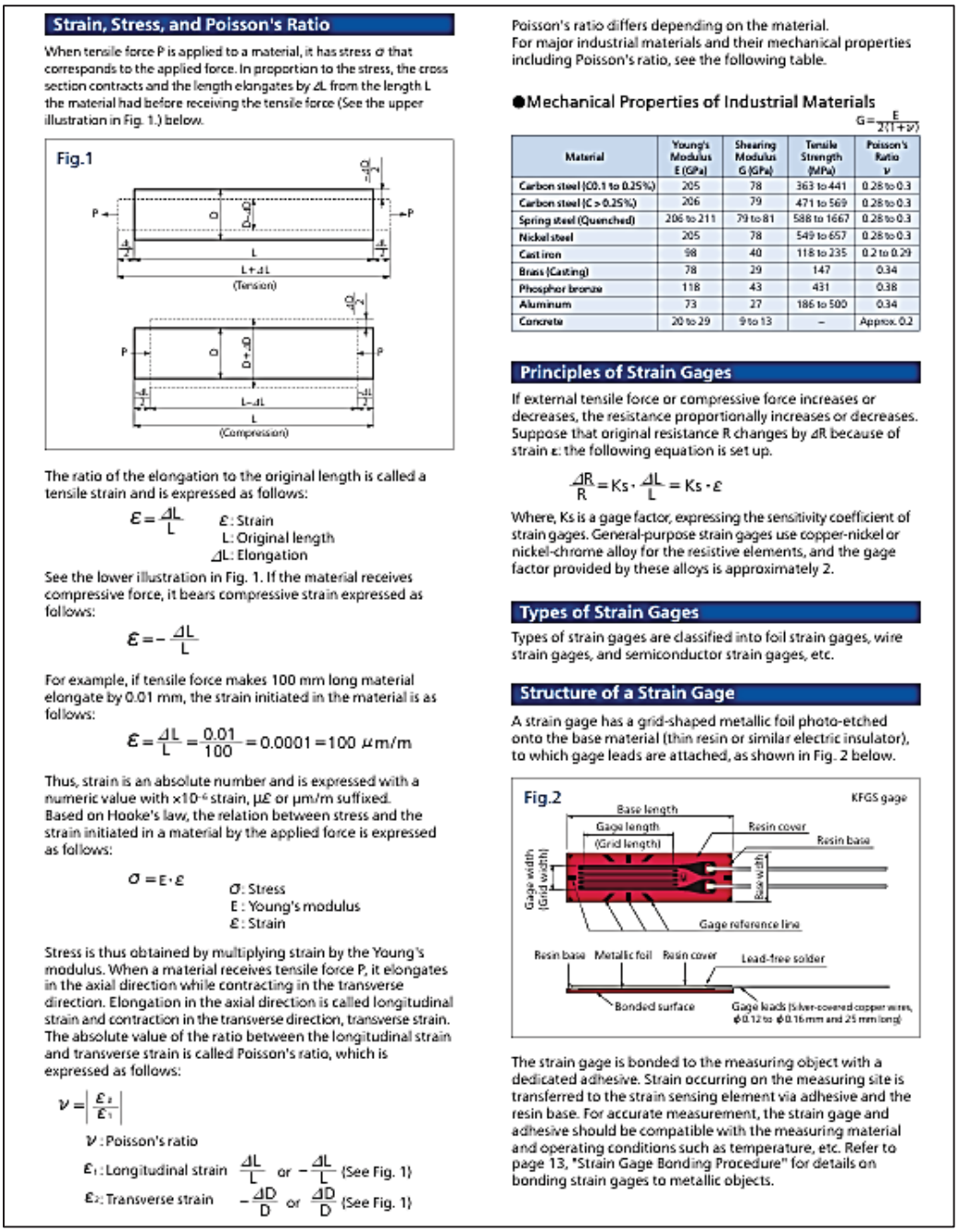

Strain, Stress, and Poisson's Ratio

When tensile force P is applied to a material, it has stress σ that corresponds to the applied force. In proportion to the stress, the cross section contracts and the length elongates by ΔL from the length L the material had before receiving the tensile force (See the upper illustration in Fig. 1.) below.

Fig.1

The ratio of the elongation to the original length is called a tensile strain and is expressed as follows:

$$\varepsilon = \frac{\Delta L}{L}$$

ε: Strain
L: Original length
ΔL: Elongation

See the lower illustration in Fig. 1. If the material receives compressive force, it bears compressive strain expressed as follows:

$$\varepsilon = -\frac{\Delta L}{L}$$

For example, if tensile force makes 100 mm long material elongate by 0.01 mm, the strain initiated in the material is as follows:

$$\varepsilon = \frac{\Delta L}{L} = \frac{0.01}{100} = 0.0001 = 100\ \mu m/m$$

Thus, strain is an absolute number and is expressed with a numeric value with $\times 10^{-6}$ strain, με or μm/m suffixed.
Based on Hooke's law, the relation between stress and the strain initiated in a material by the applied force is expressed as follows:

$$\sigma = E \cdot \varepsilon$$

σ: Stress
E: Young's modulus
ε: Strain

Stress is thus obtained by multiplying strain by the Young's modulus. When a material receives tensile force P, it elongates in the axial direction while contracting in the transverse direction. Elongation in the axial direction is called longitudinal strain and contraction in the transverse direction, transverse strain. The absolute value of the ratio between the longitudinal strain and transverse strain is called Poisson's ratio, which is expressed as follows:

$$\nu = \left| \frac{\varepsilon_2}{\varepsilon_1} \right|$$

ν: Poisson's ratio
ε_1: Longitudinal strain $\frac{\Delta L}{L}$ or $-\frac{\Delta L}{L}$ (See Fig. 1)
ε_2: Transverse strain $-\frac{\Delta D}{D}$ or $\frac{\Delta D}{D}$ (See Fig. 1)

Poisson's ratio differs depending on the material.
For major industrial materials and their mechanical properties including Poisson's ratio, see the following table.

●Mechanical Properties of Industrial Materials

$$G = \frac{E}{2(1+\nu)}$$

Material	Young's Modulus E (GPa)	Shearing Modulus G (GPa)	Tensile Strength (MPa)	Poisson's Ratio ν
Carbon steel (C0.1 to 0.25%)	205	78	363 to 441	0.28 to 0.3
Carbon steel (C > 0.25%)	206	79	471 to 569	0.28 to 0.3
Spring steel (Quenched)	206 to 211	79 to 81	588 to 1667	0.28 to 0.3
Nickel steel	205	78	549 to 657	0.28 to 0.3
Cast iron	98	40	118 to 235	0.2 to 0.29
Brass (Casting)	78	29	147	0.34
Phosphor bronze	118	43	431	0.38
Aluminum	73	27	186 to 500	0.34
Concrete	20 to 29	9 to 13	–	Approx. 0.2

Principles of Strain Gages

If external tensile force or compressive force increases or decreases, the resistance proportionally increases or decreases. Suppose that original resistance R changes by ΔR because of strain ε: the following equation is set up.

$$\frac{\Delta R}{R} = Ks \cdot \frac{\Delta L}{L} = Ks \cdot \varepsilon$$

Where, Ks is a gage factor, expressing the sensitivity coefficient of strain gages. General-purpose strain gages use copper-nickel or nickel-chrome alloy for the resistive elements, and the gage factor provided by these alloys is approximately 2.

Types of Strain Gages

Types of strain gages are classified into foil strain gages, wire strain gages, and semiconductor strain gages, etc.

Structure of a Strain Gage

A strain gage has a grid-shaped metallic foil photo-etched onto the base material (thin resin or similar electric insulator), to which gage leads are attached, as shown in Fig. 2 below.

Fig.2 KFGS gage

The strain gage is bonded to the measuring object with a dedicated adhesive. Strain occurring on the measuring site is transferred to the strain sensing element via adhesive and the resin base. For accurate measurement, the strain gage and adhesive should be compatible with the measuring material and operating conditions such as temperature, etc. Refer to page 13, "Strain Gage Bonding Procedure" for details on bonding strain gages to metallic objects.

Figure A A.4 Principles of strain gauges measurements
Taken from KYOWA measuring equipment general catalog (p. 1 & 2)

Also, Table A A.1 reports the uniform air-pressure pump testing details over strain gauges applicability.

Table A A.1 Calibration of installed strain gauges with air pressure

Air pressure (kPa)	**Gauge #1**	**Gauge #2**	**Gauge #3**	**Gauge #4**	**Average strain (10^{-6})**	**Lateral stress (kPa)**
57	2.8739	2.8738	2.8831	2.8928	2.88	56
113	5.7479	5.7976	5.7703	5.7856	5.78	112
175	8.6219	9.1005	8.8554	9.1606	8.93	173
240	11.4959	12.9323	11.0547	12.5357	12.00	233
307	15.3279	16.2852	14.9449	16.3228	15.72	305
361	18.2019	19.6354	15.8684	19.7679	18.37	356
411	20.5079	22.0330	17.7918	22.6608	20.75	403
483	22.9920	27.7809	20.1065	27.4840	24.59	477
555	25.3871	32.5709	22.6005	31.3041	27.97	543
601	27.7821	34.9659	25.0049	34.7149	30.62	594

APPENDIX B

SEM IMAGES OF PARAMETRIC STUDY- CHAPTER 5

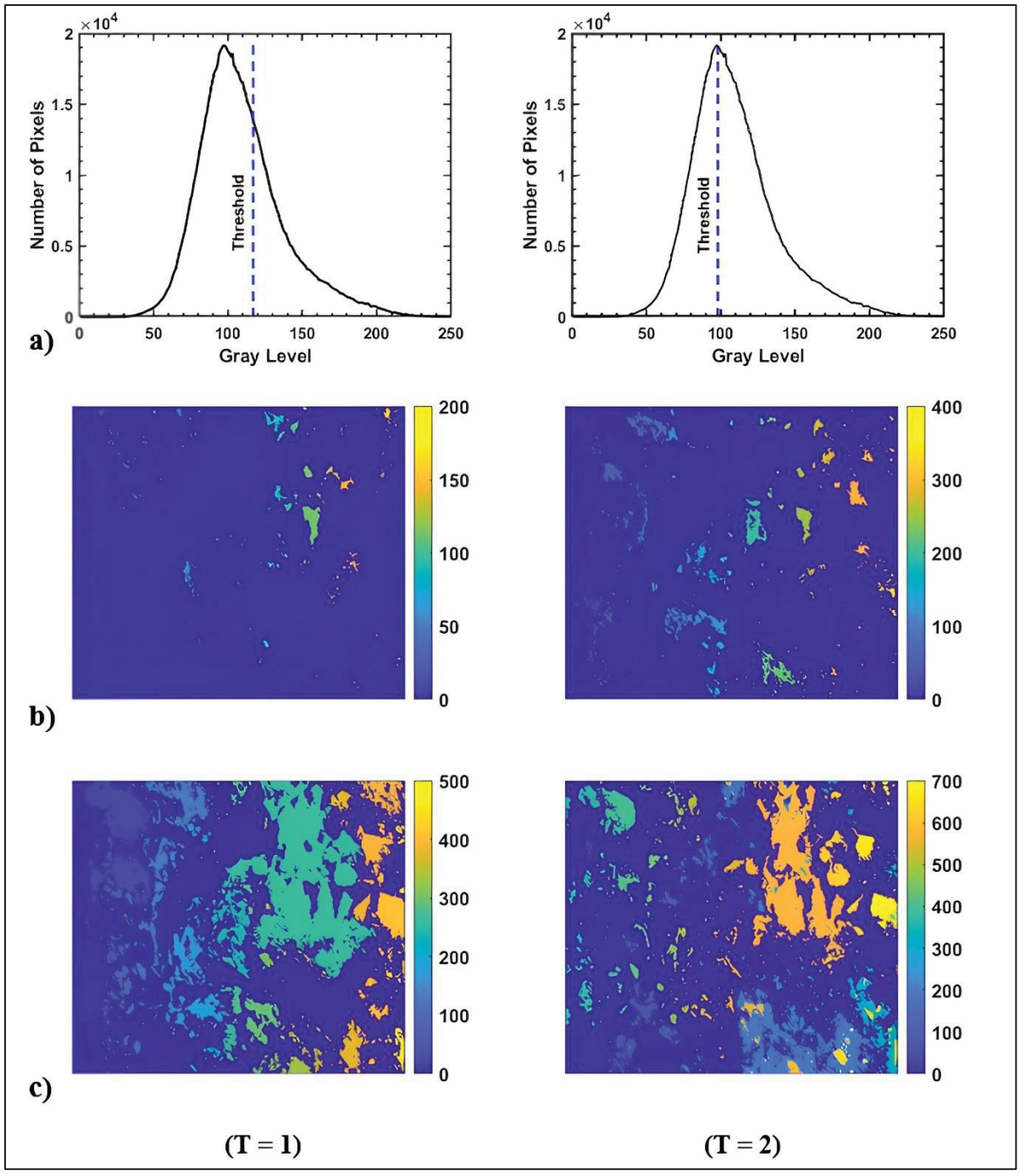

Figure A B.1 Different applied threshold levels (T = 1 and T = 2) for distinguishing of particles zone from pore spaces, a) gray scale level and the determined limit; b) segmented pores; c) segmented particles

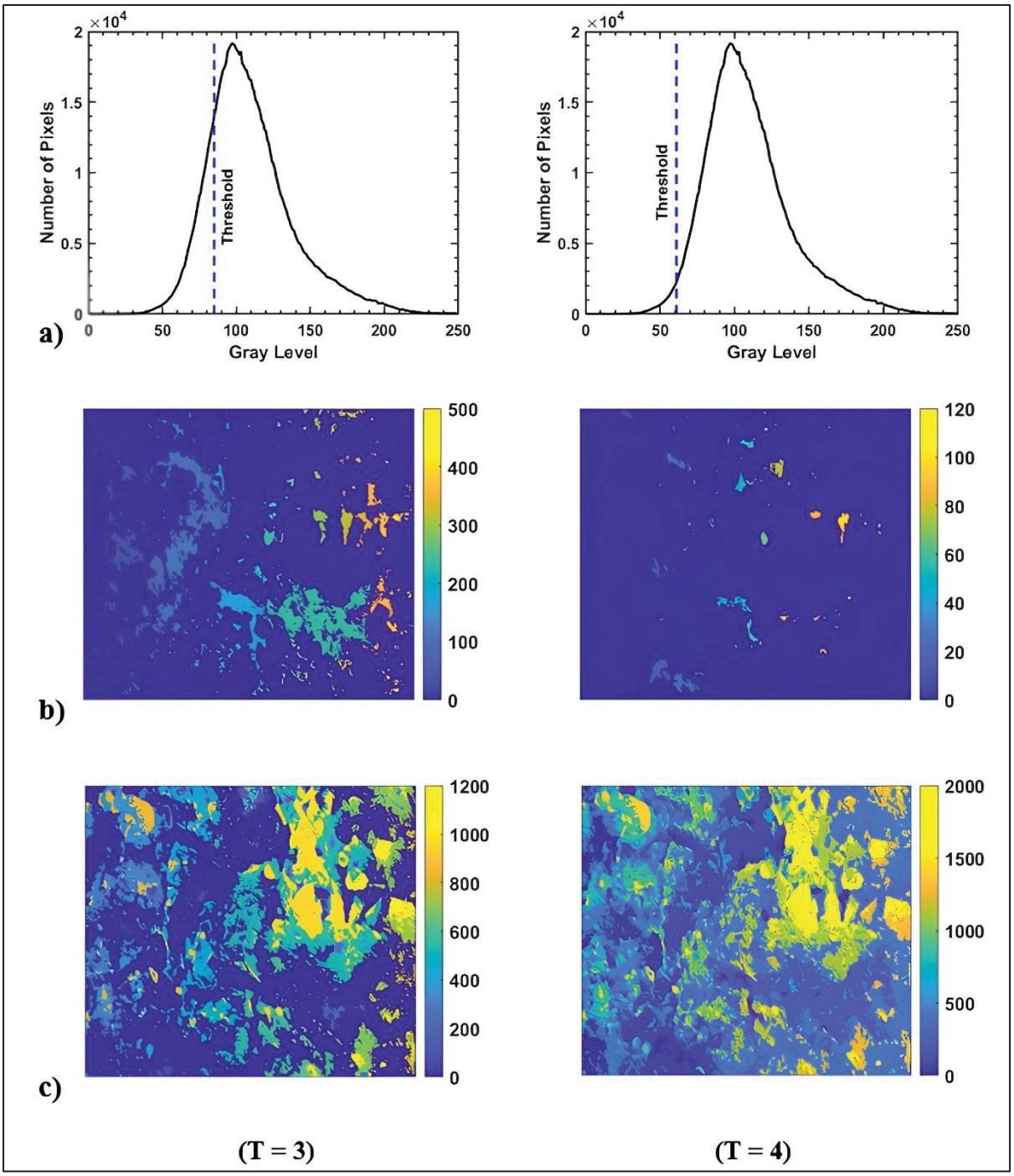

Figure A B.2 Different applied threshold levels (T = 3 and T = 4) for distinguishing of particles zone from pore spaces, a) gray scale level and the determined limit; b) segmented pores; c) segmented particles

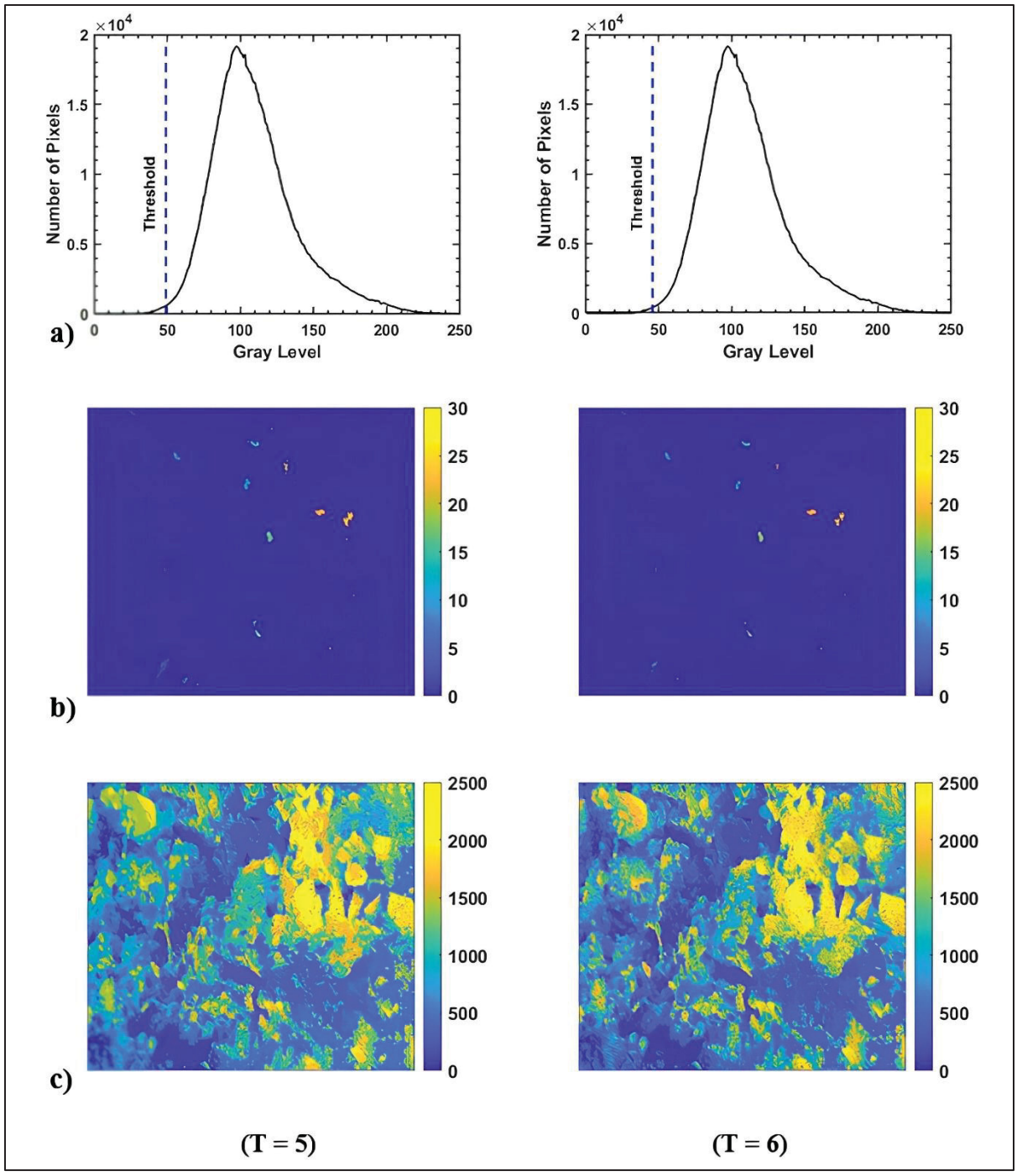

Figure A B.3 Different applied threshold levels (T = 5 and T = 6) for distinguishing of particles zone from pore spaces, a) gray scale level and the determined limit; b) segmented pores; c) segmented particles

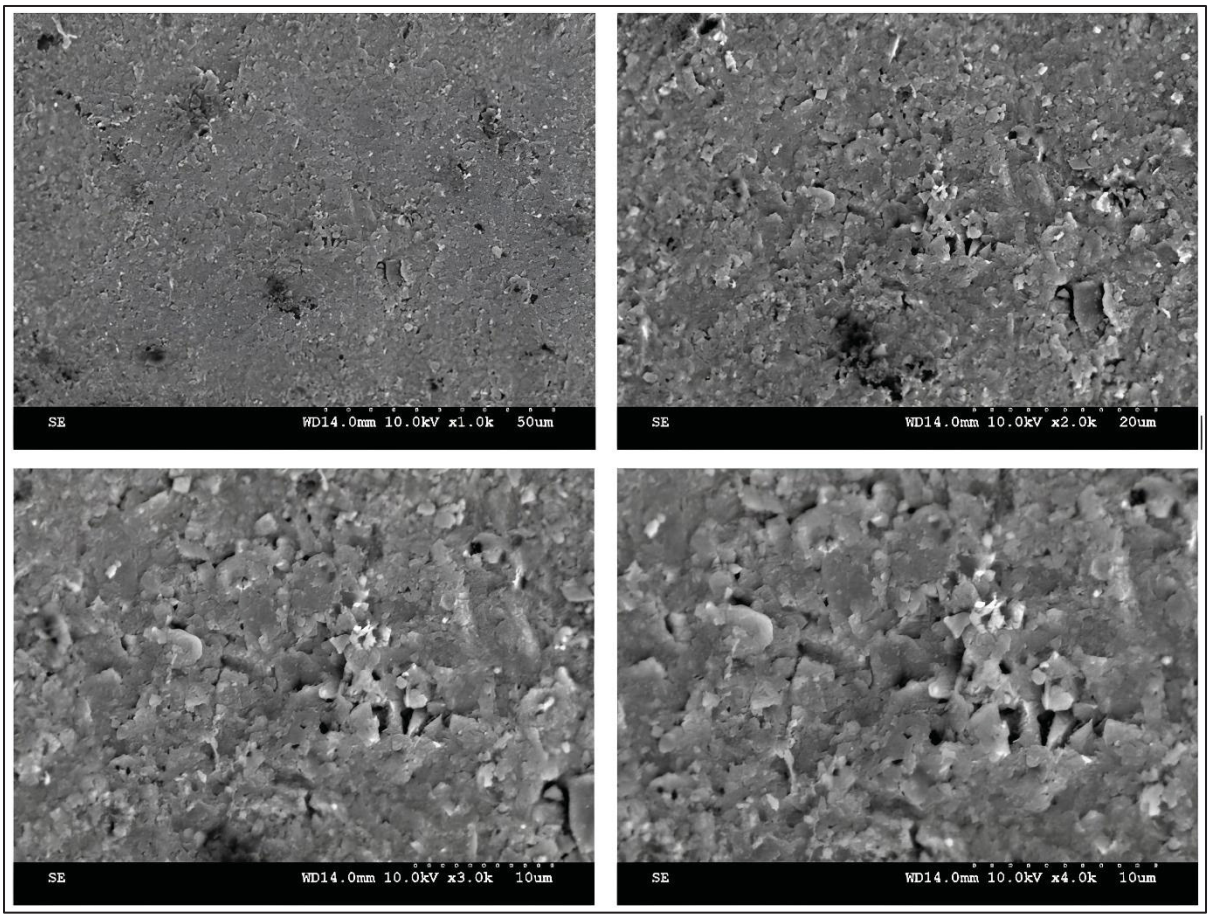

Figure A B.4 SEM images of the intact S3 sample at 10 kV

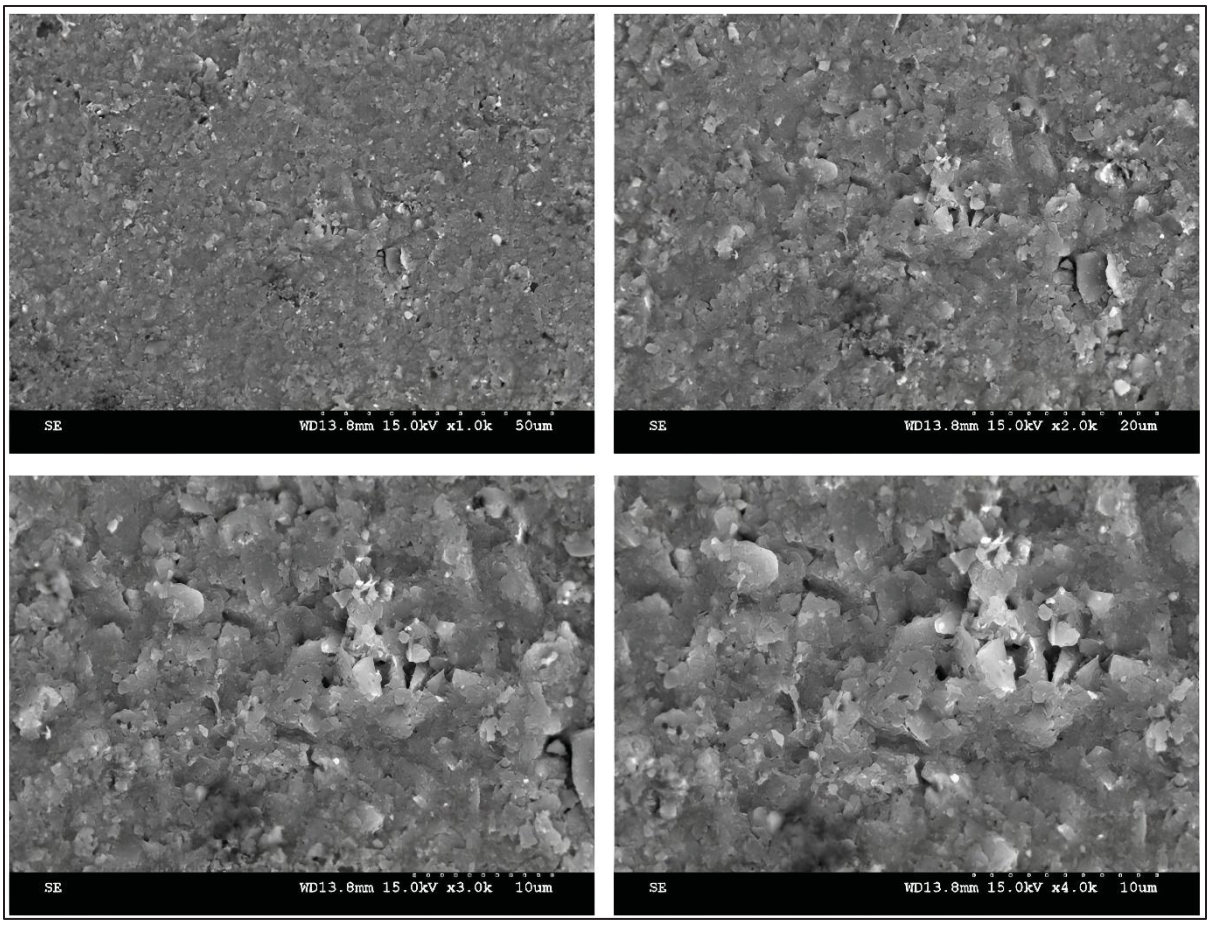

Figure A B.5 SEM images of the intact S3 sample at 15 kV

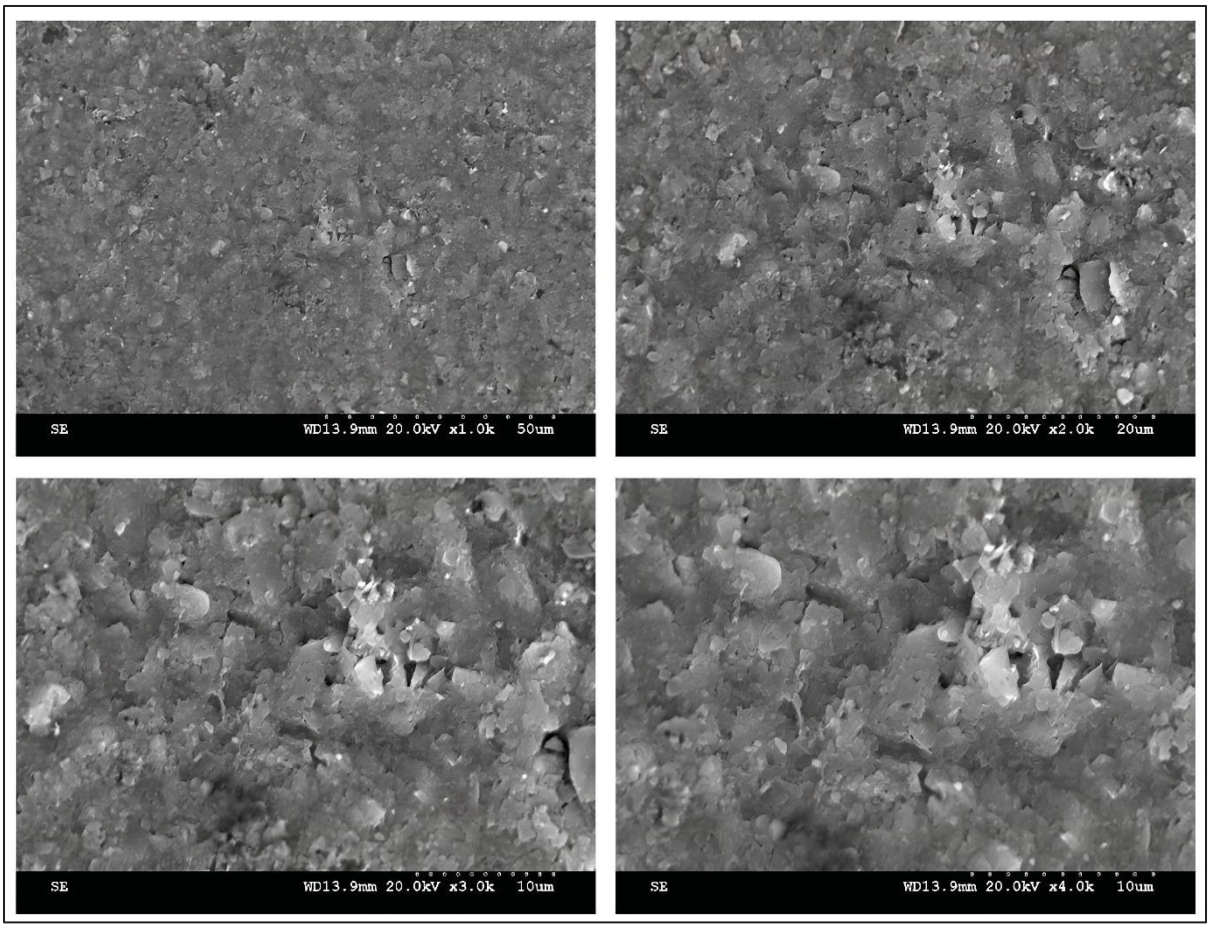

Figure A B.6 SEM images of the intact S3 sample at 20 kV

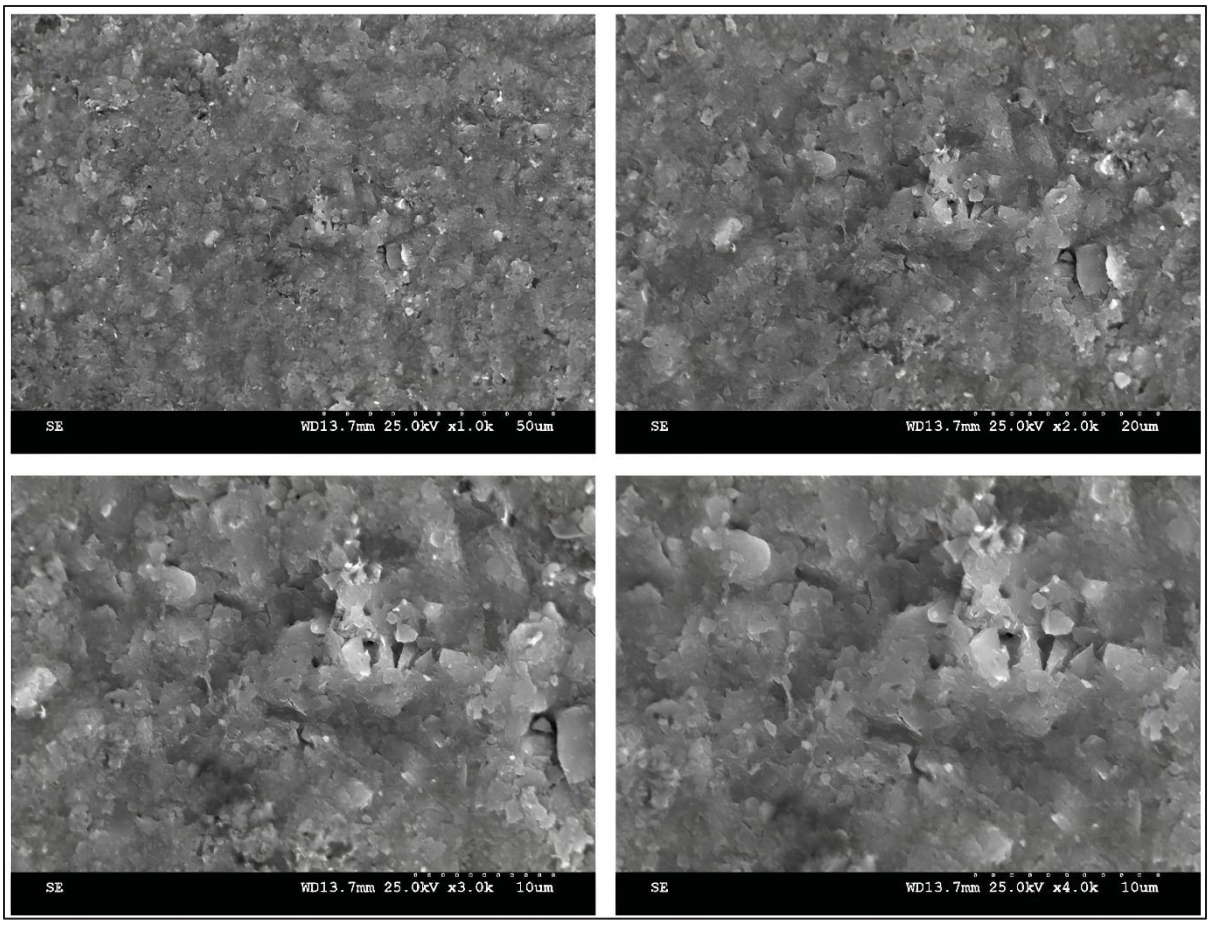

Figure A B.7 SEM images of the intact S3 sample at 25 kV

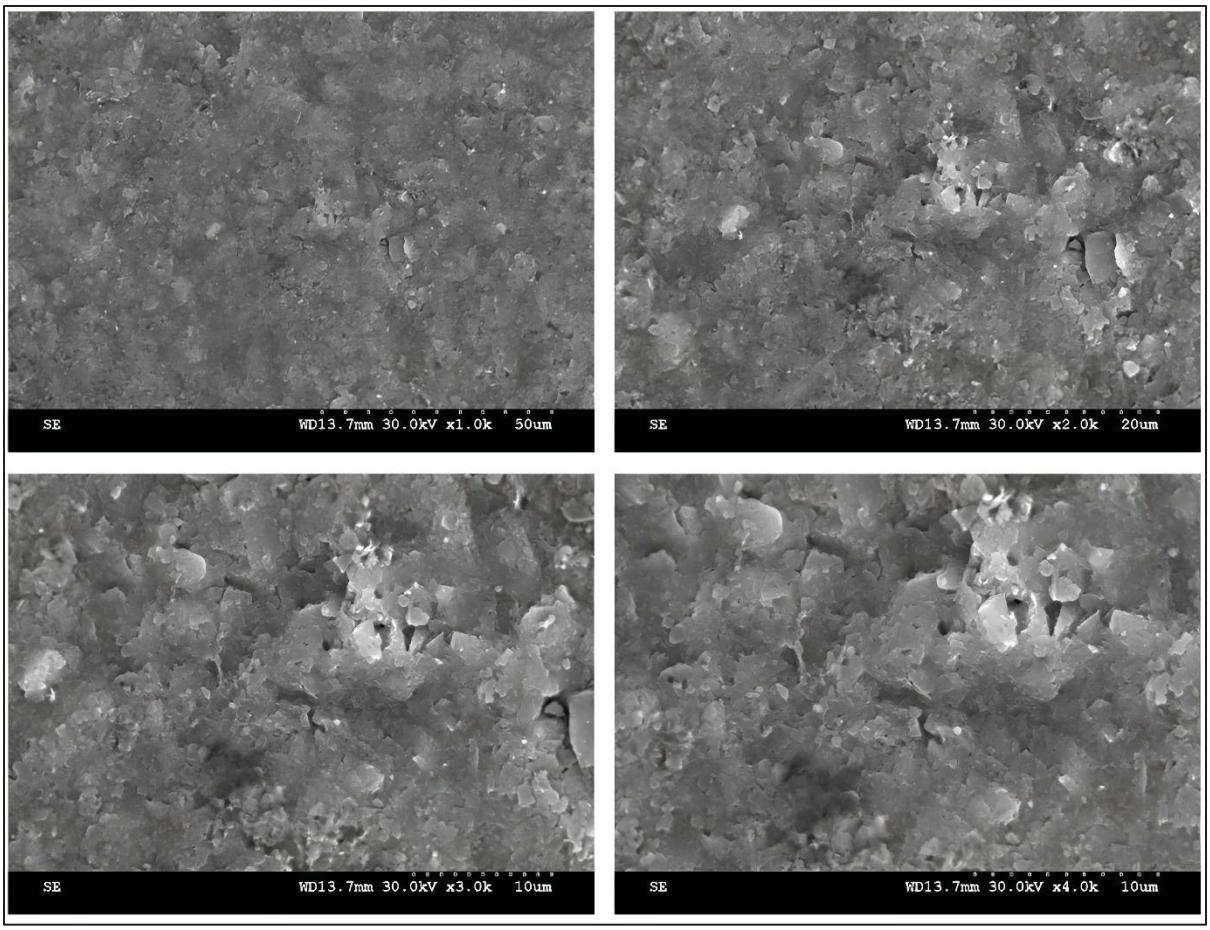

Figure A B.8 SEM images of the intact S3 sample at 30 kV

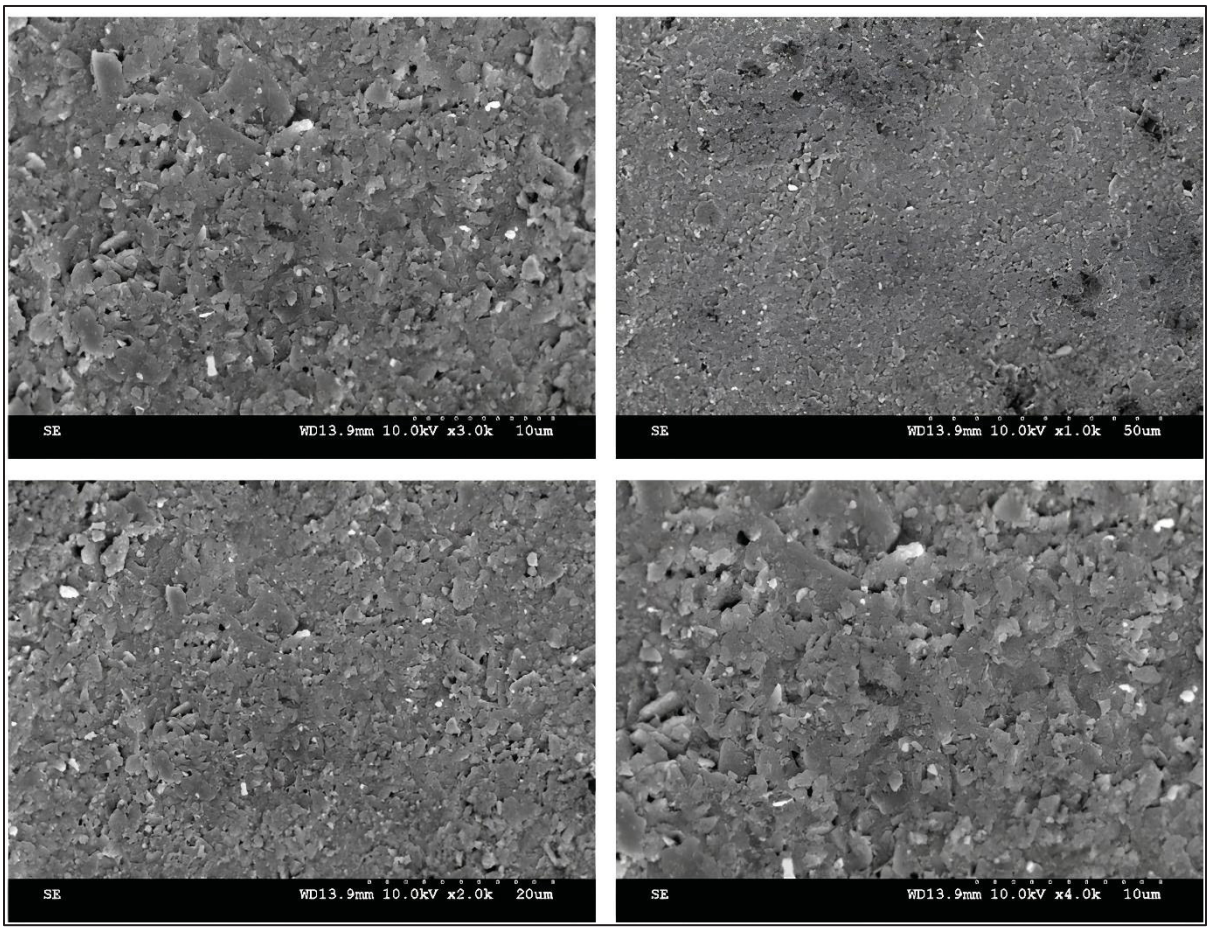

Figure A B.9 SEM images of the intact S7 sample at 10 kV

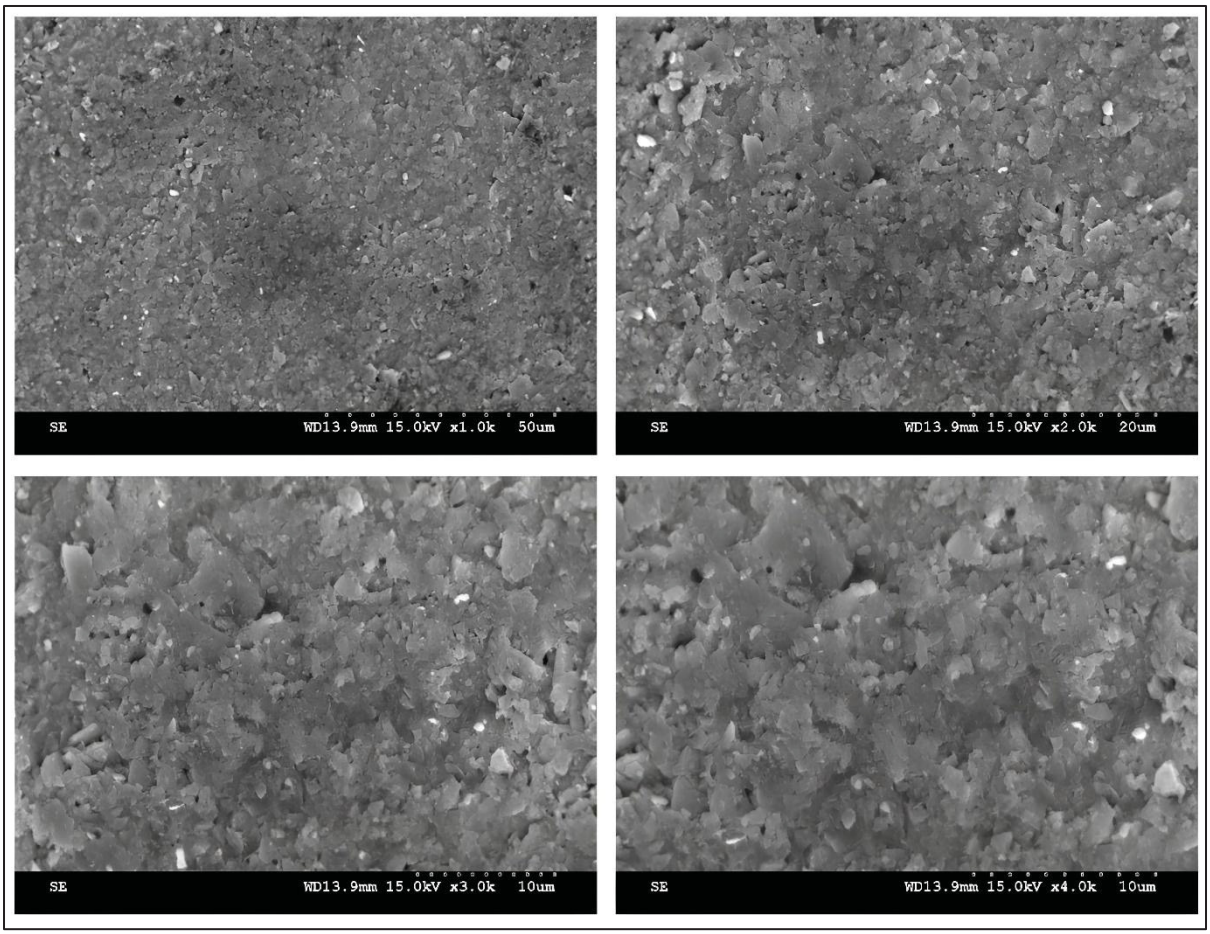

Figure A B.10 SEM images of the intact S7 sample at 15 kV

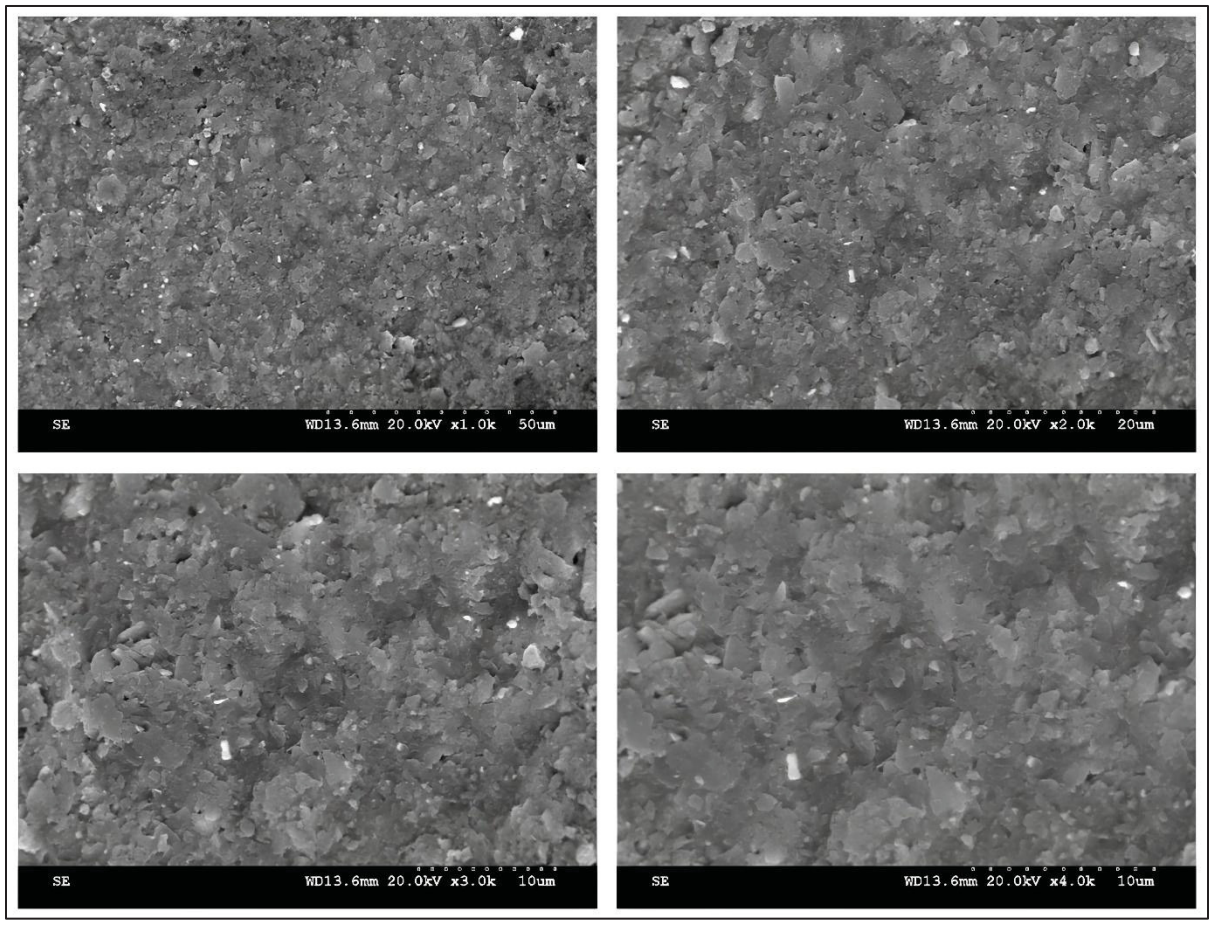

Figure A B.11 SEM images of the intact S7 sample at 20 kV

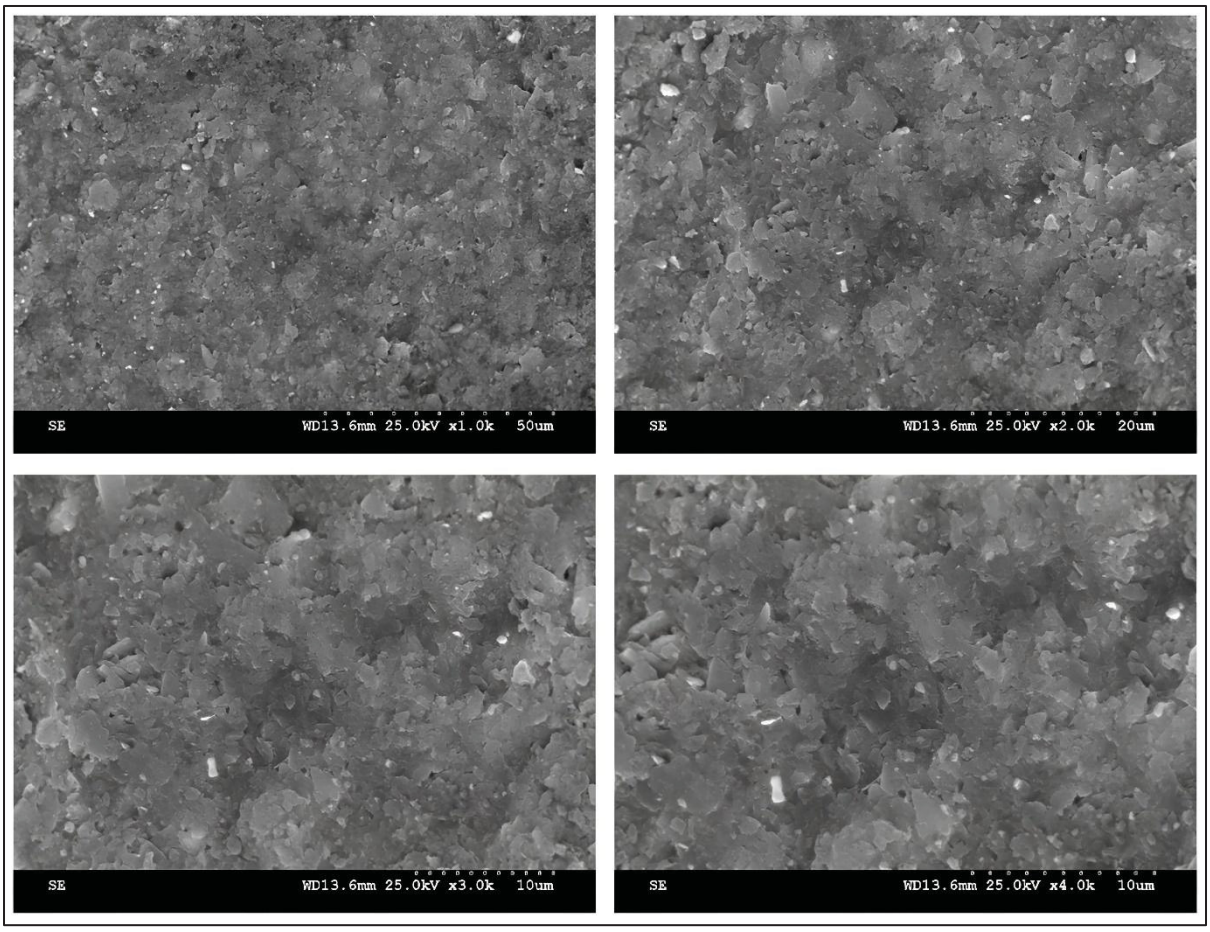

Figure A B.12 SEM images of the intact S7 sample at 25 kV

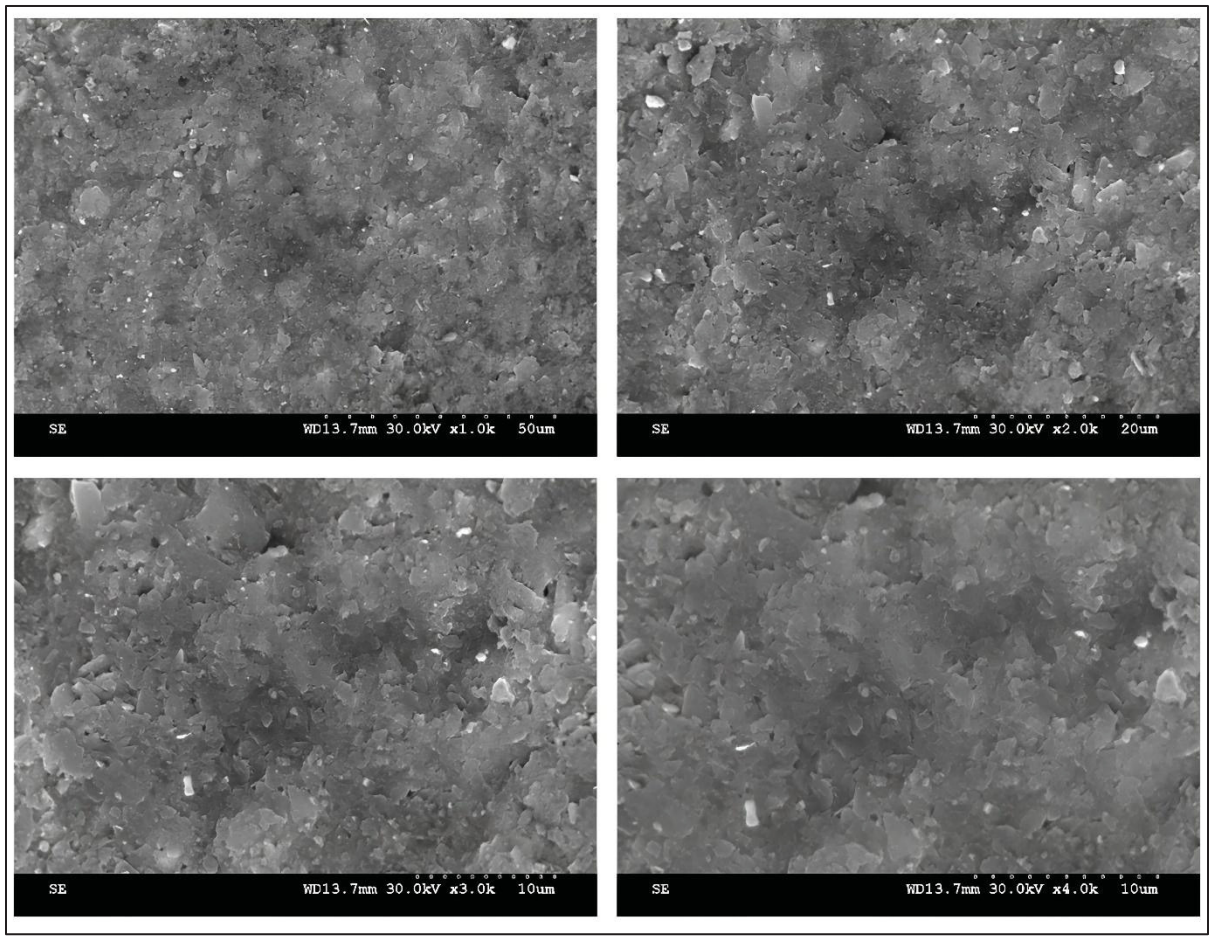

Figure A B.13 SEM images of the intact S7 sample at 30 kV

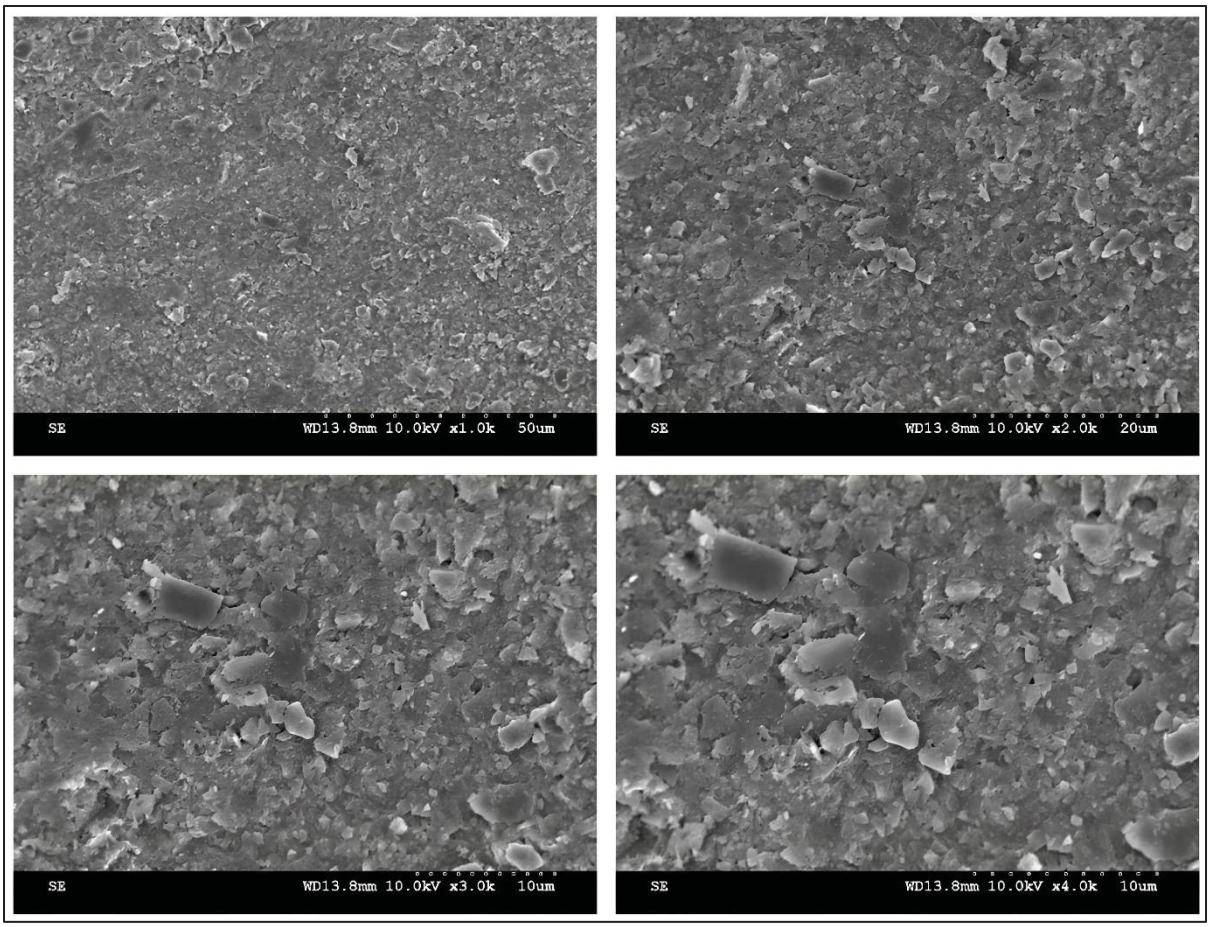

Figure A B.14 SEM images of the consolidated S3 sample at 10 kV

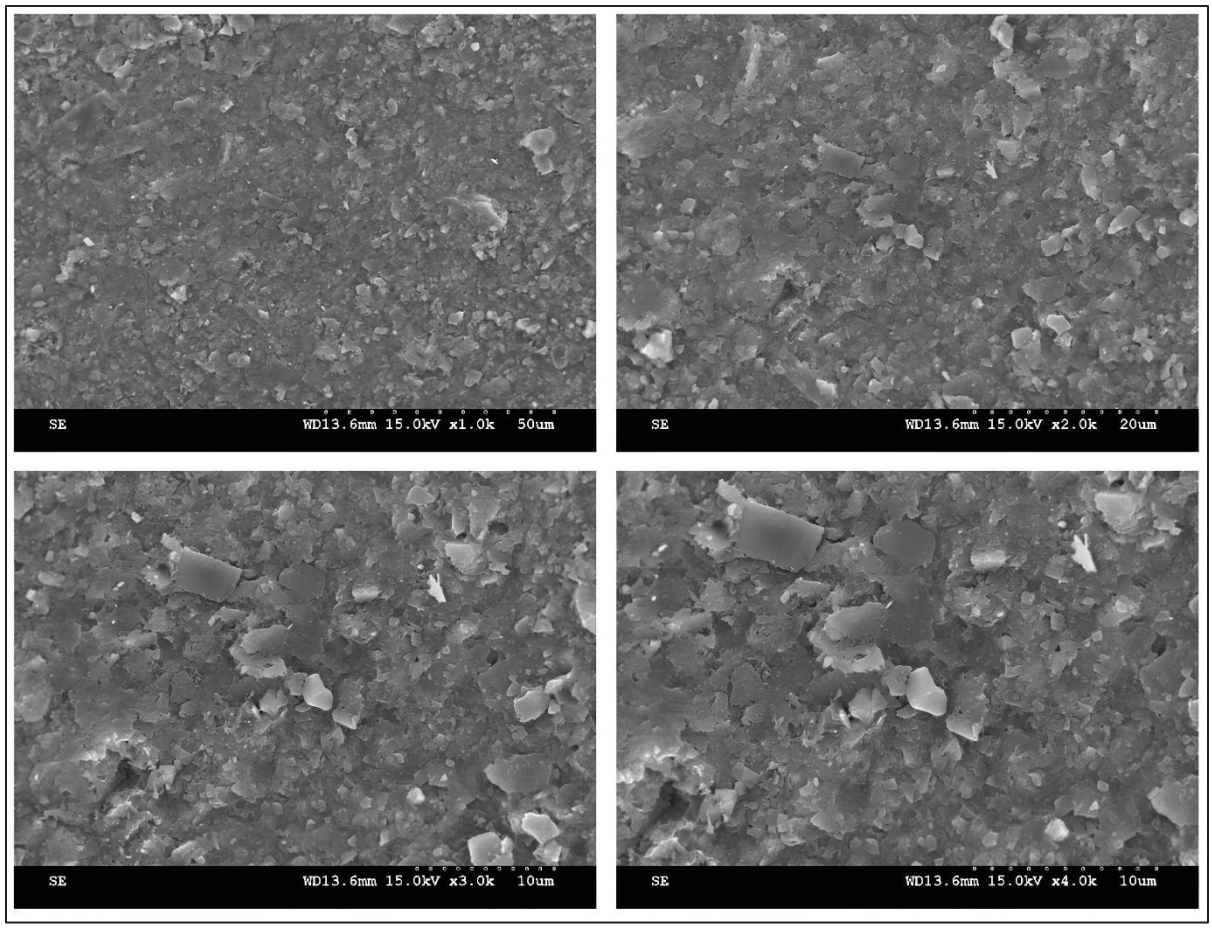

Figure A B.15 SEM images of the consolidated S3 sample at 15 kV

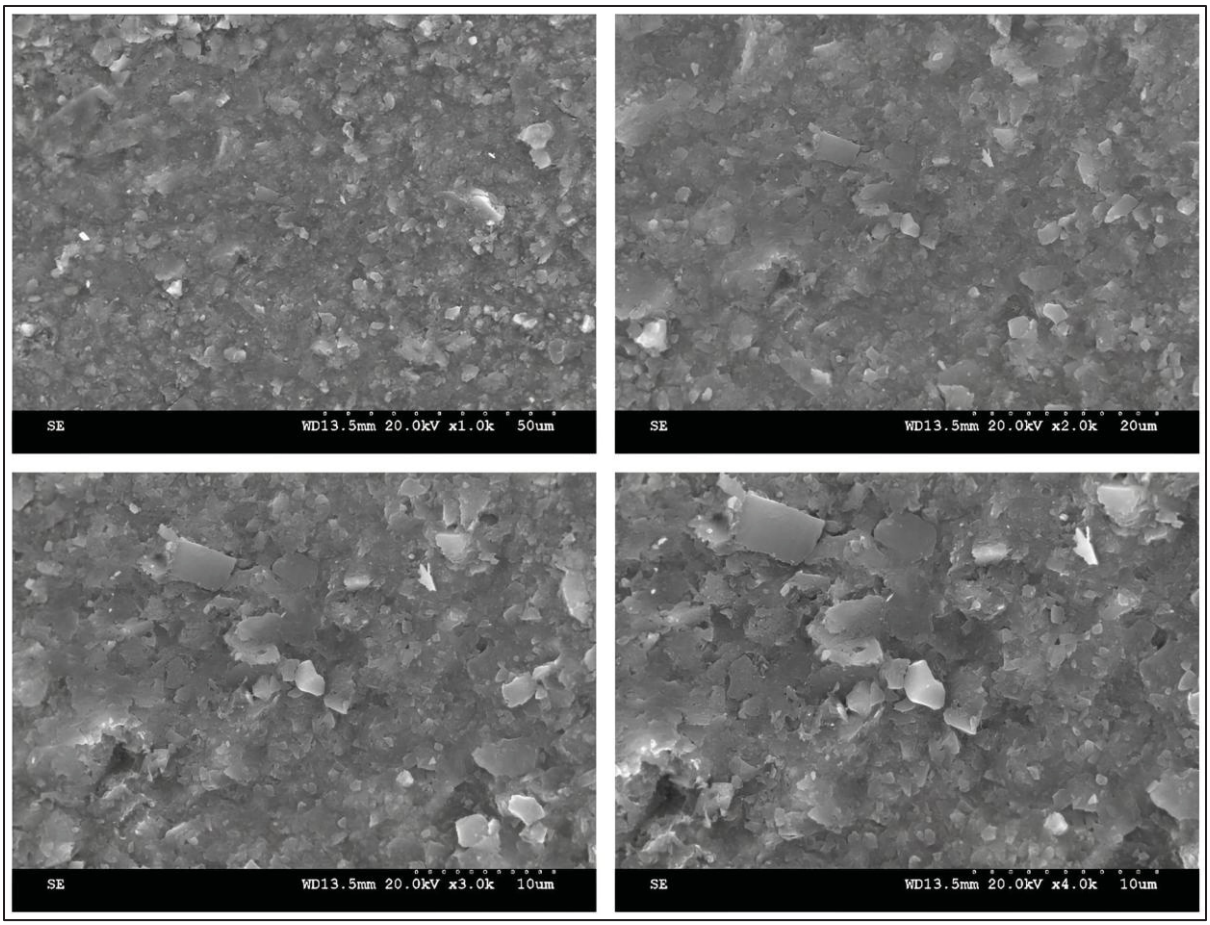

Figure A B.16 SEM images of the consolidated S3 sample at 20 kV

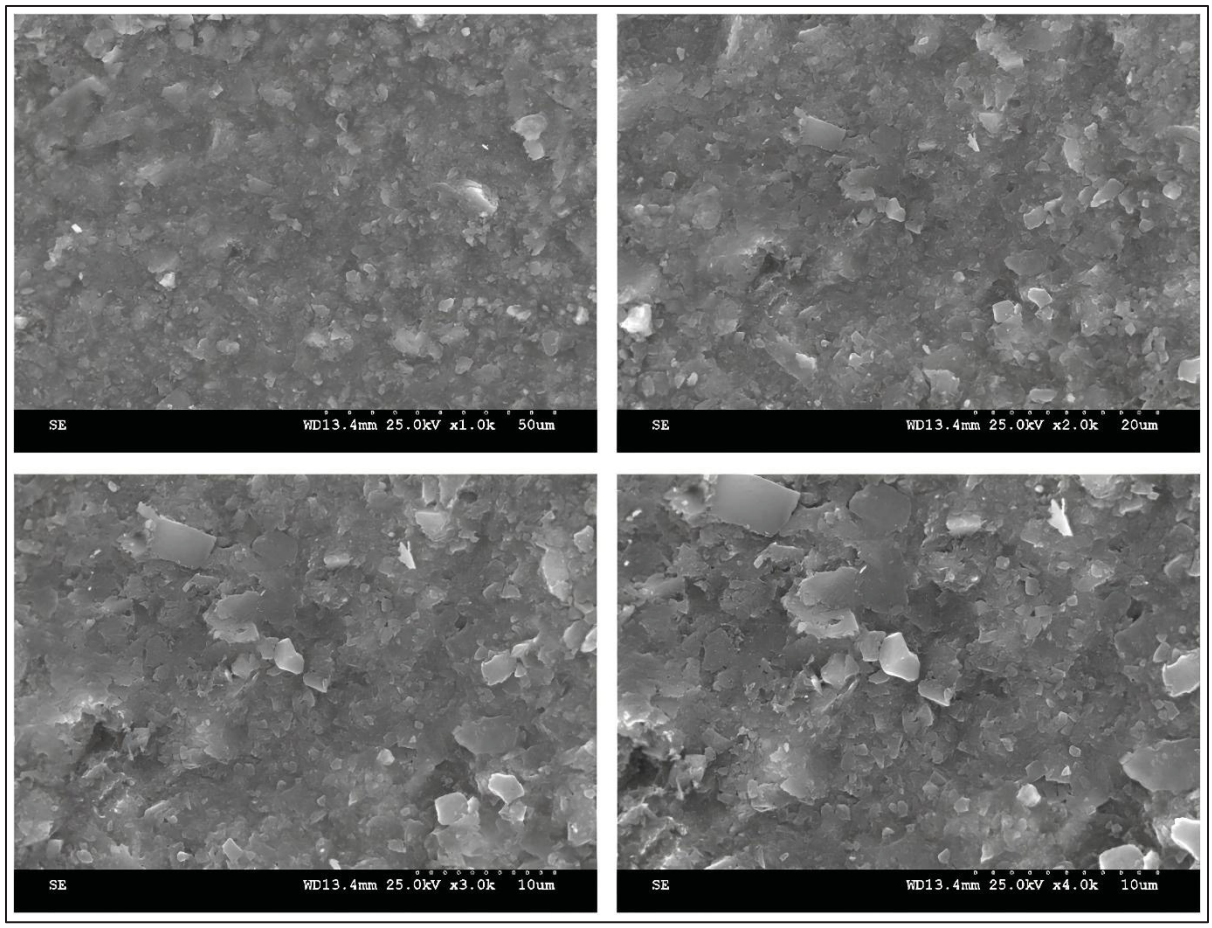

Figure A B.17 SEM images of the consolidated S3 sample at 25 kV

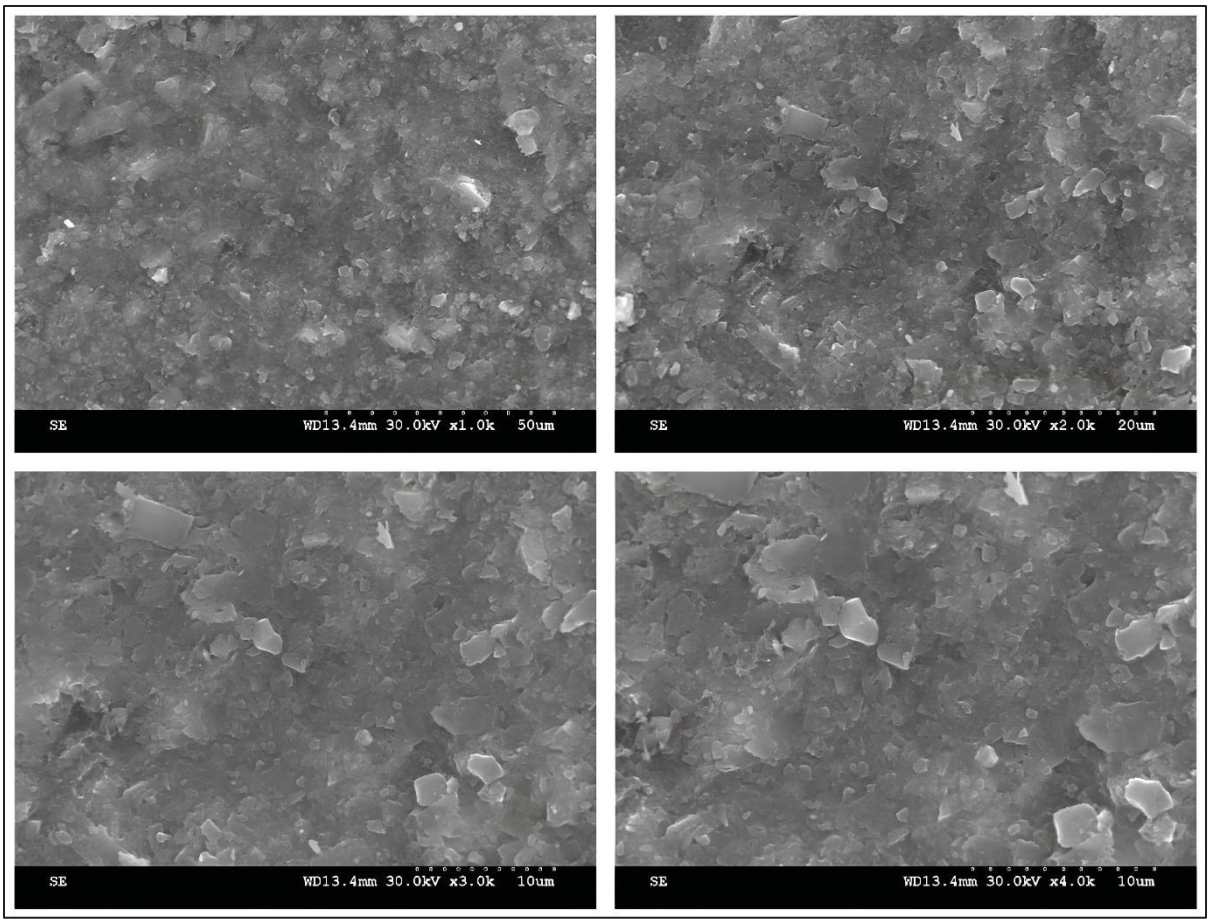

Figure A B.18 SEM images of the consolidated S3 sample at 30 kV

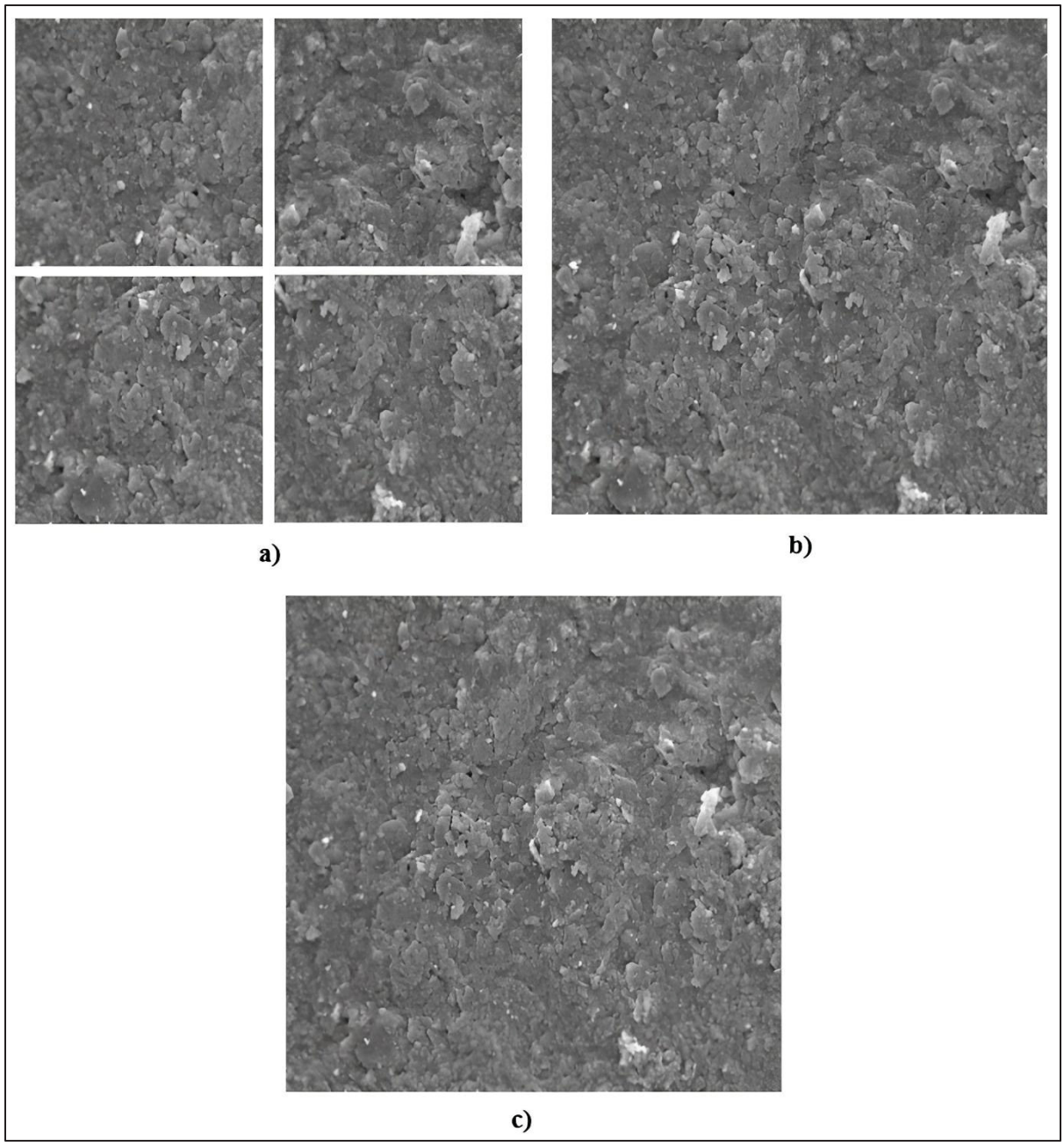

Figure A B.19 Grid view and full view of SEM images for intact S7 with voltage of 15 kV; a) quarter images at magnification of 3000×; b) Grid-view image at magnification of 3000×; c) Full-view image at magnification of 1500×

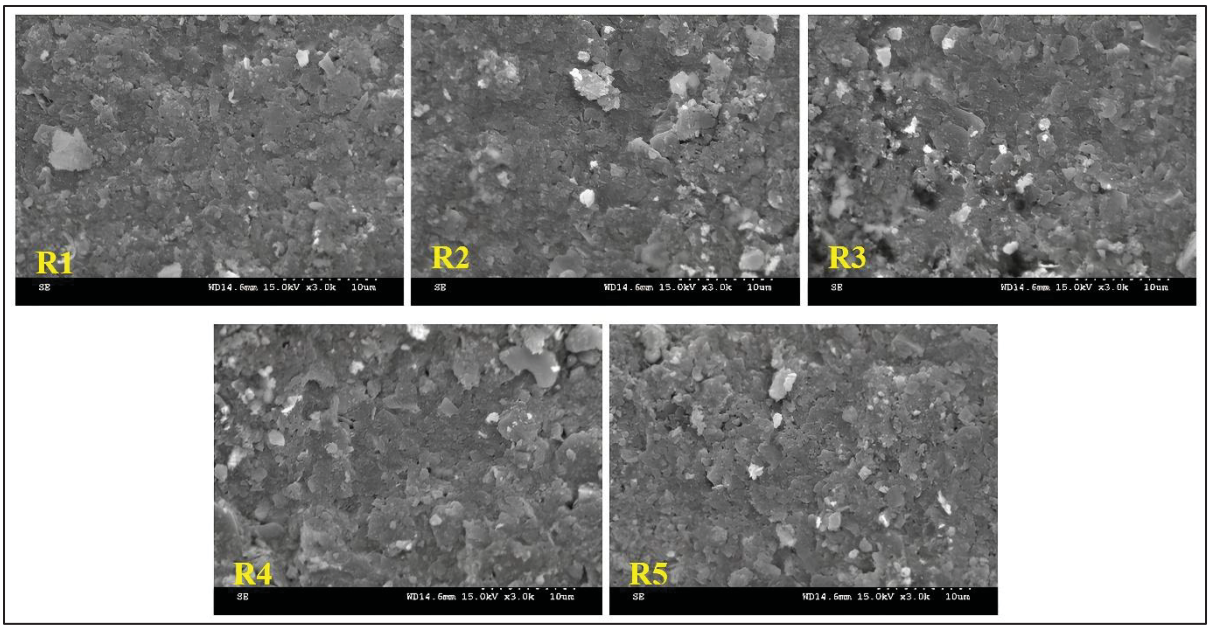

Figure A B.20 Random images (R1 to R5) of the surface of intact S7 sample with voltage of 15 kV, from surrounding areas, Grid-view zone at magnification of 3000×

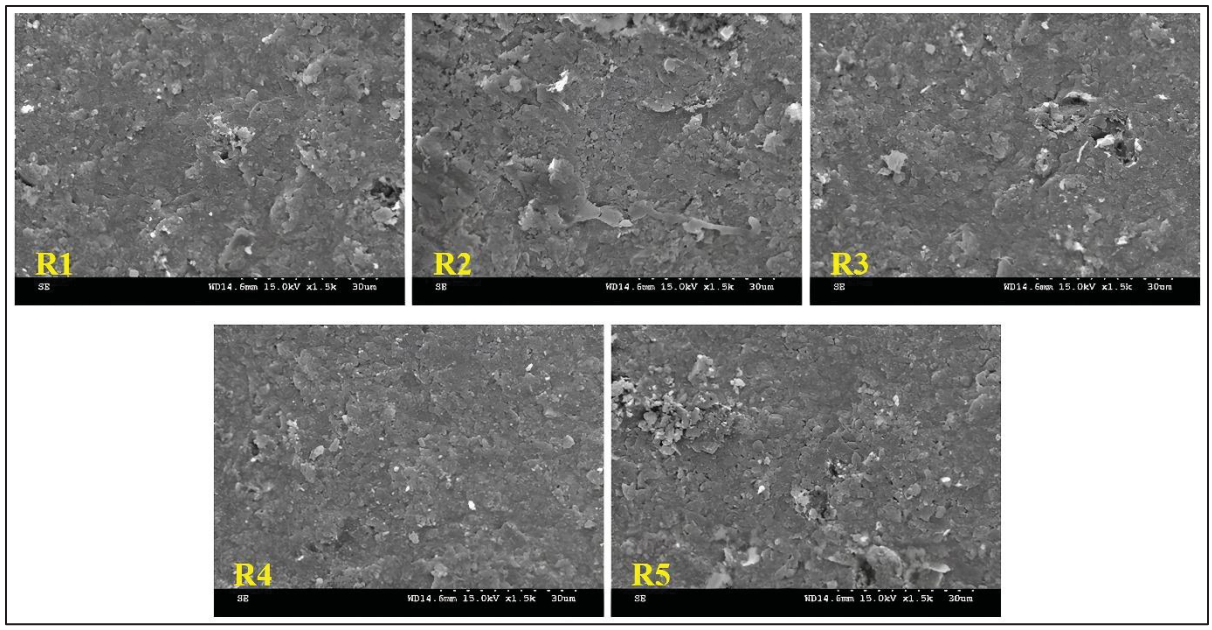

Figure A B.21 Random images (R1 to R5) of the surface of intact S7 sample with voltage of 15 kV, from surrounding areas, Full-view zone at magnification of 1500×

LIST OF BIBLIOGRAPHICAL REFERENCES

Addo, K. O., and Robertson, P. K. (1992). "Shear wave velocity measurement of soils using Rayleigh waves." Can. Geotech. J., 29, 558-568.

Anandarajah, A., Kuganenthira, N., and Zhao, D. (1996). "Variation of fabric anisotropy of kaolinite in triaxial loading." J. Geotech. Eng., 122(8), 633-640.

Arroyo, M., Muir Wood, D., and Greening, P. D. (2003). "Source near-field effects and pulse tests in soil samples." Géotechnique, 53(3), 337-345.

Arulanandan, K. (1991). "Dielectric method for prediction of porosity of saturated soil." J. Geotech. Eng., 117(2), 319-330.

Arulnathan, R., Boulanger, R. W., Kutter, B. L., and Sluis, W. K. (2000). "New tool for shear wave velocity measurements in model tests." Geotech. Test. J., 23(4), 444-453.

Arulnathan, R., Boulanger, R. W., and Riemer, M. F. (1998). "Analysis of bender element tests." Geotech. Test. J., 21(2), 120-131.

ASTM. (2017). "Standard test methods for liquid limit, plastic limit, and plasticity index of soils." D4318-17e1, ASTM International, West Conshohocken, PA.

ASTM. (2019). "Standard test methods for laboratory determination of water (moisture) content of soil and rock by mass." D2216-19, ASTM International, West Conshohocken, PA.

ASTM. (2020). "Standard test methods for one-dimensional consolidation properties of soils using incremental loading." D2435M-11, ASTM International, West Conshohocken, PA.

ASTM. (2021a). "Standard test method for particle-size distribution (gradation) of fine-grained soils using the sedimentation (hydrometer) analysis." D7928-21e1, ASTM International, West Conshohocken, PA.

ASTM. (2021b). "Standard test methods for modulus and damping of soils by the resonant-column method." D4015-21, ASTM International, West Conshohocken, PA.

ASTM. (2025a). "Standard practice for classification of soils for engineering purposes (Unified Soil Classification System)." D2487-17R25, ASTM International, West Conshohocken, PA.

ASTM. (2025b). "Standard test methods for cross hole seismic testing." D4428/D4428M-25, ASTM International, West Conshohocken, PA.

ASTM. (2025c). "Standard test methods for downhole seismic testing (Revision of D7400/D7400M-19)." WK90017, ASTM International, West Conshohocken, PA.

Atkinson, J. H. (1975). "Anisotropic elastic deformations in laboratory tests on undisturbed London Clay." Géotechnique, 2, 357-374.

Atkinson, J. H. (2000). "Nonlinear soil stiffness in routine design." Géotechnique, 50(5), 487-508.

Aylmore, L. A. G., and Quirk, J. P. (1960). "Domain or turbostratic clay structure." Nature, 187(4742), 1046-1048.

Ballard Jr, R. F. (1976). "Method for cross hole seismic testing." J. Geotech. Eng. Div., 102(12), 1261-1273.

Barden, L., and Sides, G. (1971). "Sample disturbance in the investigation of clay structure." Géotechnique, 21(3), 211-222.

Benabdallah, E. M. (2006). "Caractérisation de la perméabilité d'une argile sensible de Lachenaie." M.Sc. thesis, École Polytechnique de Montréal, Montreal, QC, Canada.

Bennett, R. H. (1976). "Clay fabric and geotechnical properties of selected submarine sediment cores from the Mississippi delta." Texas A and M University, College Station, TX.

Blewett, I., Blewett, I. J., and Woodward, P. K. (1999). "Measurement of shear-wave velocity using phase-sensitive detection techniques." Can. Geotech. J., 36(5), 934-939.

Brandenberg, S. J., Kutter, B. L., and Wilson, D. W. (2008). "Fast stacking and phase corrections of shear wave signals in a noisy environment." J. Geotech. Geoenviron. Eng., 134(8), 1154-1165.

Brignoli, E. G. M., Gotti, M., and Stokoe, K. H. (1996). "Measurement of shear waves in laboratory specimens by means of piezoelectric transducers." Geotech. Test. J., 19(4), 384-397.

Brooks, G. R. (2014). "Prehistoric sensitive clay landslides and paleoseismicity in the Ottawa Valley, Canada." Landslides in sensitive clays: From geosciences to risk management, 119-131.

Brosse, A. M., Jardine, R. J., and Nishimura, S. (2017). "The undrained shear strength anisotropy of four Jurassic to Eocene stiff clays." Géotechnique, 67(8), 653-671.

Brosse, A., Hosseini Kamal, R., Jardine, R. J., and Coop, M. R. (2017). "The shear stiffness characteristics of four Eocene-to-Jurassic UK stiff clays." Géotechnique, 67(3), 242-259.

Bryson, L. S., and Bathe, A. (2009). "Determination of selected geotechnical properties of soil using electrical conductivity testing." Geotech. Test. J., 32(3), 252-261.

Bunaciu, A. A., UdriŞTioiu, E. G., and Aboul-Enein, H. Y. (2015). "X-ray diffraction: instrumentation and applications." Crit. Rev. Anal. Chem., 45(4), 289-299.

Butler, D. K., and Curro Jr, J. R. (1981). "Cross hole seismic testing-Procedures and pitfalls." Geophysics, 46(1), 23-29.

Campanella, R. G. (1994). "Field methods for dynamic geotechnical testing: an overview of capabilities and needs." ASTM Spec. Tech. Publ., 1213, 3-3.

Campanella, R. G., Robertson, P. K., Gillespie, D., Laing, N., and Kurfurst, P. J. (1987). "Seismic cone penetration testing near offshore of the Mackenzie Delta." Can. Geotech. J., 24(1), 154-159.

Canadian Geotechnical Society, 2023. Canadian Foundation Engineering Manual. 5th ed. Ottawa: Canadian Science Publishing.

Cascante, G., Santamarina, C., and Yassir, N. (1998). "Flexural excitation in a standard torsional-resonant column device." Can. Geotech. J., 35, 478-490.

Chandler, R. (2010). "Stiff sedimentary clays: geological origins and engineering properties." Géotechnique, 60(12), 891-902.

Chapuis, R. P. (2012). "Predicting the saturated hydraulic conductivity of soils: a review." Bull. Eng. Geol. Environ., 71, 401-434.

Chen, Y. J., and Kulhawy, F. H. (1993). "Undrained strength interrelationships among CIUC, UU, and UC tests." J. Geotech. Eng., 119(11), 1732-1750.

Cho, W., and Finno, R. J. (2010). "Stress-strain responses of block samples of compressible Chicago glacial clays." J. Geotech. Geoenviron. Eng., 136(1), 178-188.

Chow, J. K., Li, Z., and Wang, Y. H. (2019). "Comprehensive microstructural characterizations of 1-D consolidated kaolinite samples with fabric tensors and pore elongation factors." Eng. Geol., 248, 22-33.

Chung, R. M., Yokel, F. Y., and Drnevich, V. P. (1984). "Evaluation of dynamic properties of sands by resonant column testing." Geotech. Test. J., 7(2), 60-69.

Clayton, C. R. I. (2011). "Stiffness at small strain: research and practice." Géotechnique, 61(1), 5-37.

Clayton, C. R. I., Theron, M., and Best, I. (2004). "The measurement of vertical shear-wave velocity using side-mounted bender elements in the triaxial apparatus." Géotechnique, 54(7), 495-498.

Clennell, M. B., Dewhurst, D. N., Brown, K. M., and Westbrook, G. K. (1999). "Permeability anisotropy of consolidated clays." Geol. Soc. London Spec. Publ., 158(1), 79-96.

Cotecchia, F., Cafaro, F., and Guglielmi, S. (2016). "Microstructural changes in clays generated by compression explored by means of SEM and image processing." Procedia Eng., 158, 57-62.

Crampin, S. (1977). "A review of the effects of anisotropic layering on the propagation of seismic waves." Geophys. J. Int., 49(1), 9-27.

Crampin, S. (1981). "A review of wave motion in anisotropic and cracked elastic-media." Wave Motion, 3(4), 343-391.

Crawford, C. B. (1961). "Engineering studies of Leda clay." Soils in Canada, Vol. 3, University of Toronto Press, Toronto, ON, Canada, 200-217.

Da Fonseca, A. V., Ferreira, C., and Fahey, M. (2009). "A framework interpreting bender element tests, combining time-domain and frequency-domain methods." Geotech. Test. J., 32(2), 91-107.

Dai, C. X., Zhang, Q. F., He, S. H., Zhang, A., Shan, H. F., and Xia, T. D. (2021). "Variation in micro-pores during dynamic consolidation and compression of soft marine soil." J. Mar. Sci. Eng., 9(7), 750.

Dao, L. Q., Delage, P., Tang, A. M., Cui, Y. J., Pereira, J. M., Li, X. L., and Sillen, X. (2014). "Anisotropic thermal conductivity of natural Boom Clay." Appl. Clay Sci., 101, 282-287.

Das, B. M., and Sobhan, K. (1990). Principles of geotechnical engineering. PWS-Kent Publishing Co., Boston, MA.

Delage, P. (2010). "A microstructure approach to the sensitivity and compressibility of some Eastern Canada sensitive clays." Géotechnique, 60(5), 353-368.

Delage, P., and Lefebvre, G. (1984). "Study of the structure of a sensitive Champlain clay and of its evolution during consolidation." Can. Geotech. J., 21(1), 21-35.

Delage, P., and Pellerin, F. M. (1984). "Influence de la lyophilisation sur la structure d'une argile sensible du Québec." Clay Miner., 19(2), 151-160.

Delage, P., Tessier, D., and Marcel-Audiguier, M. (1982). "Use of the Cryoscan apparatus for observation of freeze-fractured planes of a sensitive Quebec clay in scanning electron microscopy." Can. Geotech. J., 19(1), 111-114.

Demers, D., Robitaille, D., Locat, P., and Potvin, J. (2014). "Inventory of large landslides in sensitive clay in the province of Québec, Canada: preliminary analysis." Landslides in sensitive clays: from geosciences to risk management, 77-89.

Dion Gagnier, G. (2019). "Analyse de la méthode P-RAT et caractérisation des argiles de la mer Champlain par la vitesse de propagation des ondes de cisaillement Vs." M.Sc. mémoire, École de Technologie Supérieure, Montreal, QC, Canada.

Dobry, R., and Vucetic, M. (1987). "Dynamic properties and seismic response of soft clay deposits." Proc., Int. Symp. on Geotechnical Engineering of Soft Soils, Mexico, 2, 51-87.

Douglass, P. M., and Voight, B. (1969). "Anisotropy of granites: a reflection of microscopic fabric." Géotechnique, 19, 376-398.

Drnevich, V. P. (1985). "Recent developments in resonant column testing." Richart commemorative lectures, ASCE, Reston, VA, 79-107.

Dyvik, R., and Madshus, C. (1985). "Laboratory measurements of Gmax using bender elements." Proc., ASCE Annual Convention: Advances in the Art of Testing Soils under Cyclic Conditions, Detroit, MI, 186-196.

Eden, W. J., and Mitchell, R. J. (1973). "Landslides in sensitive marine clay in eastern Canada." Highway Research Board Bulletin, 463, 18-27.

Edil, T. B., and Luh, G.-F. (1978). "Dynamic modulus and damping relationships for sands." Proc., Specialty Conference on Earthquake Engineering and Soil Dynamics, ASCE, Pasadena, CA, 394-409.

Elbeggo, D. (2023). "La vitesse de propagation des ondes de cisaillement dans les argiles de l'Est du Canada: mesures et corrélations." Ph.D. thesis, École de Technologie Supérieure, Montreal, QC, Canada.

Elbeggo, D., Ethier, Y., Karray, M., and Dubé, J. S. (2023). "Assessment of existing Vs-Lab correlations regarding Eastern Canadian clays." Soil Dyn. Earthquake Eng., 164, 107607.

Elbeggo, D., Hussein, M. N., Ethier, Y., and Karray, M. (2019). "Robustness of the P-RAT in the shear-wave velocity measurement of soft clays." J. Geotech. Geoenviron. Eng., 145(5), 0401-9014.

Elliot, T. R., and Heck, R. J. (2007). "A comparison of optical and X-ray CT technique for void analysis in soil thin section." Geoderma, 141(1-2), 60-70.

Ethier, Y. (2009). "La mesure en laboratoire de la vitesse de propagation des ondes de cisaillement." Ph.D. thesis, Dept. of Civil Engineering, Univ. of Sherbrooke, Sherbrooke, QC, Canada.

Ethier, Y. A., Karray, M., and Lefebvre, G. (2011). "Simulations of elastic wave propagation using FLAC to optimize the measurement of shear wave velocity in the laboratory." Proc., 2nd Int. FLAC/DEM Symp., Continuum and Distinct Element Numerical Modeling in Geomechanics, Melbourne, Australia, 519-527.

Fam, M., and Santamarina, C. (1995). "Study of geoprocesses with complementary mechanical and electromagnetic wave measurements in an oedometer." Geotech. Test. J., 18(3), 307-314.

Franzius, J. N., Potts, D. M., and Burland, J. B. (2005). "The influence of soil anisotropy and K0 on ground surface movements resulting from tunnel excavation." Géotechnique, 55(3), 189-199.

Fulton, R. J., and Richard, S. H., (1987). "Chronology of late Quaternary events in the Ottawa Region in Quaternary geology of the Ottawa Region, Ontario and Quebec." *Geological Survey of Canada*, 86(23), 24-30.

Gamal El Dean, D. (2007). "Development of a new piezoelectric pulse testing device and soil characterization using shear waves." Ph.D. thesis, Dept. of Civil Engineering, Univ. of Sherbrooke, Sherbrooke, QC, Canada.

Gasparre, A., Nishimura, S., Coop, M. R., and Jardine, R. J. (2011). "The influence of structure on the behavior of London Clay." Stiff Sedimentary Clays: Genesis and Engineering Behavior: Géotechnique Symposium in Print 2007, Thomas Telford Ltd., London, UK, 67-79.

Gazetas, G. (1981a). "Dynamic compliance matrix of rigid strip footing bonded to a viscoelastic cross anisotropic half space." Int. J. Mech. Sci., 23(9), 547-559.

Gazetas, G. (1981b). "Strip foundations on a cross-anisotropic soil layer subjected to dynamic loading." Géotechnique, 31(2), 161-179.

Gazetas, G. (1982). "Stresses and displacements in cross-anisotropic soils." J. Geotech. Eng. Div., 108(4), 532-553.

Gillot, J. E. (1970). "Fabric of Leda clay investigated by optical, electron-optical and x-ray diffraction methods." Eng. Geol., 4, 133-153.

Gonzalez, N. A., Rouainia, M., Arroyo, M., and Gens, A. (2012). "Analysis of tunnel excavation in London Clay incorporating soil structure." Géotechnique, 62(12), 1095-1109.

Goto, S., Tatsuoka, F., Shibuya, S., and Sato, T. (1991). "A simple gauge for local strain measurements in the laboratory." Soils Found., 31(1), 169-180.

Grammatikopoulou, A., Zdravkovic, L., and Potts, D. M. (2008). "The influence of previous stress history and stress path direction on the surface settlement trough induced by tunnelling." Géotechnique, 58(4), 269-281.

Greening, P. D., and Nash, D. F. (2004). "Frequency domain determination of G using bender elements." Geotech. Test. J., 27(3), 288-294.

Guglielmi, S., Cotecchia, F., Cafaro, F., and Gens, A. (2018). "Microstructural changes underlying the macro-response of stiff clay." Micro to macro mathematical modelling in soil mechanics, Springer International Publishing, Cham, Switzerland, 89-97.

Guglielmi, S., Cotecchia, F., Cafaro, F., and Gens, A. (2022). "Analysis of the micro to macro response of clays to compression." Géotechnique, 74(2), 134-154.

Hamouche, K. K., Leroueil, S., Roy, M., and Lutenegger, A. J. (1995a). "In situ evaluation of K0 in Eastern Canada clays." Can. Geotech. J., 32, 677-688.

Hamouche, K. K., Roy, M., and Leroueil, S. (1995b). "A pressuremeter study of Louiseville sensitive clay deposit." Proc., 4th Int. Symp. on Pressuremeters, Sherbrooke, QC, Canada, 161-168.

Hardin, B. O., and Black, W. L. (1968). "Vibration modulus of normally consolidated clay." J. Soil Mech. Found. Div., 94(2), 353-369.

Hardin, B. O., and Blandford, G. E. (1989). "Elasticity of particulate materials." J. Geotech. Eng., 115(6), 788-805.

Hardin, B. O., and Drnevich, V. P. (1972). "Shear modulus and damping in soils: design equations and curves." J. Soil Mech. Found. Div., 98(7), 667-692.

Hardin, B. O., and Richart, F. E., Jr. (1963). "Elastic wave velocities in granular soils." J. Soil Mech. Found. Div., 89(1), 33-65.

Hattab, M., and Fleureau, J. M. (2010). "Experimental study of kaolin particle orientation mechanism." Géotechnique, 60(5), 323-331.

Hattab, M., Hammad, T., Fleureau, J. M., and Hicher, P. Y. (2013). "Behavior of a sensitive marine sediment: microstructural investigation." Géotechnique, 63(1), 71-84.

Hayat, T. M. (1992). "The coefficient of earth pressure at rest." Ph.D. thesis, Dept. of Civil Engineering, Univ. of Illinois, Urbana, IL.

Hicher, P. Y., Wahyudi, H., and Tessier, D. (2000). "Microstructural analysis of inherent and induced anisotropy in clay." Mech. Cohesive-Frictional Mater., 5(5), 341-371.

Hicks, M. A., and Samy, K. (2002). "Influence of heterogeneity on undrained clay slope stability." Q. J. Eng. Geol. Hydrogeol., 35(1), 41-49.

Hight, D. W., Gens, A., and Symes, M. J. (1983). "The development of a new hollow cylinder apparatus for investigating the effects of principal stress rotation in soils." Géotechnique, 33(4), 355-383.

Hight, D. W., McMillan, F., Powell, J. J. M., Jardine, R. J., and Allenou, C. P. (2003). "Some characteristics of London clay." Characterization and Engineering Properties of Natural Soils, Vol. 2, A.A. Balkema Publishers, Lisse, Netherlands, 851-907.

Holtz, R. D., Kovacs, W. D., and Sheahan, T. C. (2011). An introduction to geotechnical engineering. 2nd ed., Prentice Hall, Hoboken, NJ.

Hooper, J. A. (1975). "Elastic settlement of a circular raft in adhesive contact with a transversely isotropic medium." Géotechnique, 25(4), 691-711.

Hussien, M. N., and Karray, M. (2021). "Piezoelectric ring-actuator technique: in-depth scrutiny of interpretation method." Geotech. Test. J., 44(1), 205-215.

Isenhower, W. M. (1980). "Torsional simple shear/resonant column properties of San Francisco Bay mud." M.S. thesis, Univ. of Texas at Austin, Austin, TX.

Ishihara, K. (1996). Soil behavior in earthquake geotechnics. Oxford University Press, Oxford, UK.

Iwasaki, T., Tatsuoka, F., and Takagi, Y. (1978). "Shear moduli of sands under cyclic torsional shear loading." Soils Found., 18(1), 39-50.

Jamiolkowski, M., Lancellotta, R., and Lo Presti, D. C. F. (1995). "Remarks on the stiffness at small strains of six Italian clays." Pre-failure deformation of geomaterials, Proc., Int. Symp., Sapporo, Japan, 12-14 September 1994, 2 vols.

Jovičić, V., Coop, M. P., and Simic, M. (1996). "Objective criteria for determining Gmax from bender element test." Géotechnique, 46(2), 357-362.

Jovičić, V., and Coop, M. P. (1998). "The measurement of stiffness anisotropy in clays with bender element tests in the triaxial apparatus." Geotech. Test. J., 21(1), 3-10.

Kang, M. S., Watabe, Y., and Tsuchida, T. (2003). "Effect of drying process on the evaluation of microstructure of clays using scanning electron microscope (SEM) and mercury intrusion porosimetry (MIP)." Proc., 13th Int. Offshore and Polar Engineering Conf., OnePetro, Richardson, TX.

Kang, X., Kang, G. C., and Bate, B. (2014). "Measurement of stiffness anisotropy in kaolinite using bender element tests in a floating wall consolidometer." Geotech. Test. J., 37(5), 869-883.

Karray, M. (1999). "Utilisation de l'analyse modale des ondes de Rayleigh comme outil d'investigation géotechnique in-situ." Ph.D. thesis, Univ. of Sherbrooke, Sherbrooke, QC, Canada.

Karray, M., and Lefebvre, G. (2009). "Techniques for mode separation in Rayleigh waves testing." Soil Dyn. Earthquake Eng., 29, 607-619.

Karray, M., Ben Romdhan, M., Hussein, M. N., and Ethier, Y. (2015). "Measuring shear wave velocity of granular material using the piezoelectric ring-actuator technique (P-RAT)." Can. Geotech. J., 52(9), 1302-1317.

Karray, M., Lefebvre, G., Ethier, Y., and Bigras, A. (2011). "Influence of particle size on the correlation between shear wave velocity and cone tip resistance." Can. Geotech. J., 48(4), 599-615.

Karray, M., et al. (2019). "The piezo-electric ring actuator technique (P-RAT) – 16 years of progress." Proc., 72nd Canadian Geotechnical Conf., GeoSt.John's, St. John's, NL, Canada.

Karrow, P. F. (1961). "The Champlain Sea and its sediments." Soils in Canada: geological, pedological, and engineering studies, 97-108.

Khan, Z., El Naggar, M. H., and Cascante, G. (2011). "Frequency dependent dynamic properties from resonant column and cyclic triaxial tests." J. Franklin Inst., 348(7), 1363-1376.

Kim, T., and Finno, R. J. (2012). "Anisotropy evolution and irrecoverable deformation in triaxial stress probes." J. Geotech. Geoenviron. Eng., 138(2), 155-165.

Kim, T. C., and Novak, M. (1981). "Dynamic properties of some cohesive soils of Ontario." Can. Geotech. J., 18, 371-389.

Kirkpatrick, W. M., and Rennie, I. A. (1972). "Directional properties of consolidated kaolin." Géotechnique, 22(1), 166-169.

Klug, H. P., and Alexander, L. E. (1974). X-ray diffraction procedures. Wiley, New York.

Kokusho, T. (1980). "Cyclic triaxial test of dynamic soil properties for wide strain range." Soils Found., 20, 45-60.

Kokusho, T., Yoshida, Y., and Esashi, Y. (1982). "Dynamic properties of soft clays for wide strain range." Soils Found., 22(4), 1-18.

Kolymbas, D., and Bauer, E. (1993). "Soft oedometer—a new testing device and its application for the calibration of hypoplastic constitutive laws." Geotech. Test. J., 16(2), 263-270.

Kong, Y., Zhao, J., and Yao, Y. (2013). "A failure criterion for cross-anisotropic soils considering microstructure." Acta Geotech., 8, 665-673.

Kramer, S. L. (1996). Geotechnical earthquake engineering. Pearson Education India, New Delhi, India.

Krizek, R. J., Edil, T. B., and Ozaydin, I. K. (1975). "Preparation and identification of clay samples with controlled fabric." Eng. Geol., 9(1), 13-38.

Ku, T., and Mayne, P. W. (2015). "Directional properties of small strain shear stiffness in soils." Geomech. Geoeng., 10(1), 68-81.

Kuwano, R., and Jardine, R. J. (2002). "On the applicability of cross-anisotropic elasticity to granular materials at very small strains." Géotechnique, 52(10), 727-749.

Kyowa Inc. (2022). Measuring Equipment General Catalog 2022: Strain Gauges and Measurement Systems. Kyowa Electronic Instruments Co., Ltd., Tokyo, Japan. Retrieved from [https://product.kyowa-ei.com/en/downloads/catalogs].

La Rochelle, P., Sarrailh, J., Tavenas, F., Roy, M., and Leroueil, S. (1981). "Causes of sampling disturbance and design of a new sampler for sensitive soils." Can. Geotech. J., 18(1), 52-66.

Lambe, T. W. (1953). "The structure of inorganic soil." Proc., American Society of Civil Engineers, ASCE, Reston, VA, 79(10), 1-49.

Lambe, T. W., and Whitman, R. V. (1969). Soil mechanics. John Wiley and Sons, New York.

Lee, C., Lee, J. S., Lee, W., and Cho, T. H. (2008). "Experiment setup for shear wave and electrical resistance measurements in an oedometer." Geotech. Test. J., 31(2), 149-156.

Lee, J. S., and Santamarina, J. C. (2005). "Bender elements: performance and signal interpretation." J. Geotech. Geoenviron. Eng., 9, 1063-1070.

Lefebvre, G., Bonzozuk, K., Philibert, A., and Hornych, P. (1991). "Evaluating K0 in Champlain clays with hydraulic fracture tests." Can. Geotech. J., 28(3), 365-377.

Lefebvre, G., and Karray, M. (1998). "New development in in-situ characterization using Rayleigh waves." Proc., 51st Canadian Geotechnical Conf., GeoEdmonton, Edmonton, AB, Canada.

Lefebvre, G., and Rochelle, P. L. (1974). "The analysis of two slope failures in cemented Champlain clays." Can. Geotech. J., 11(1), 89-108.

Lefebvre, G. (1996). "Soft sensitive clays." Landslides: investigation and mitigation, 607-619.

Leroueil, S., Bouclin, G., Tavenas, F., Bergeron, L., and Rochelle, P. L. (1990). "Permeability anisotropy of natural clays as a function of strain." Can. Geotech. J., 27(5), 568-579.

Leroueil, S., Tavenas, F., and Bihan, J. P. L. (1983). "Propriétés caractéristiques des argiles de l'est du Canada." Can. Geotech. J., 20(4), 681-705.

Lessard, G., and Mitchell, J. K. (1985). "The causes and effects of aging in quick clays." Can. Geotech. J., 22(3), 335-346.

Li, X. A., Hong, B., Wang, L., Li, L., and Sun, J. (2020). "Microanisotropy and preferred orientation of grains and aggregates (POGA) of the Malan loess in Yan'an, China: a profile study." Bull. Eng. Geol. Environ., 79, 1893-1907.

Ling, M. L., Pennington, D. S., and Nash, D. F. T. (2000). "Anisotropic stiffness parameters and their measurement in a stiff natural clay." Géotechnique, 50(2), 109-125.

Lo, K. Y., Seychuk, J. L., and Adams, J. I. (1971). "A study of the deformation characteristics of a stiff fissured clay." Sampling of Soil and Rock, ASTM International, West Conshohocken, PA.

Lo, K. Y., and Morin, J. P. (1972). "Strength anisotropy and time effects of two sensitive clays." Can. Geotech. J., 9(3), 261-277.

Lo Presti, D. C. F., Jamiolkowski, M., Pallara, O., Cavallararo, A., and Pedroni, S. (1997). "Shear modulus and damping of soils." Géotechnique, 47(3), 603-617.

Lo Presti, D. C. F., Pallara, O., Lancellota, R., Armandi, M., and Maniscalco, R. (1993). "Monotonic and cyclic loading behavior of two sands at small strains." Geotech. Test. J., 16(4), 409-424.

Locat, J., Lefebvre, G., and Ballivy, G. (1984). "Mineralogy, chemistry, and physical properties interrelationships of some sensitive clays from Eastern Canada." Can. Geotech. J., 21(3), 530-540.

Locat, A., Locat, P., Demers, D., Leroueil, S., Robitaille, D., and Lefebvre, G. (2017). "The Saint-Jude landslide of 10 May 2010, Quebec, Canada: Investigation and characterization of the landslide and its failure mechanism." Can. Geotech. J., 54(10), 1357-1374.

Locat, J., Tanaka, H., and Locat, A. (2025). "A new microstructure model for clayey sediments including microfossils." In IOP Conference Series: Earth and Environmental Science., 1523(1), 012-016. IOP Publishing.

Lu, Y., Ye, W. M., Wang, Q., Zhu, Y. H., Chen, Y. G., and Chen, B. (2020). "Investigation on anisotropic thermal conductivity of compacted GMZ bentonite." Bull. Eng. Geol. Environ., 79(3), 1153-1162.

Luo, D., et al. (1998). "Recent studies in geotechnical image analysis." Imaging Technologies: Techniques and Applications in Civil Engineering, 2nd Int. Conf., Engineering Foundation; and Imaging Technologies Committee of the Technical Council on Computer Practices, ASCE, Reston, VA.

Marcuson III, W. F., and Wahls, H. E. (1972). "Time effect on dynamic shear modulus of clays." J. Soil Mech. Found. Div., 98(12), 1359-1373.

Martínez-Nistal, A., Veniale, F., Setti, M., and Cotecchia, F. (1999). "A scanning electron microscopy image processing method for quantifying fabric orientation of clay geomaterials." Appl. Clay Sci., 14(4), 235-243.

Mašín, D., and Herle, I. (2005). "Numerical analyses of a tunnel in London clay using different constitutive models." Proc., 5th Int. Symp. TC28 Geotechnical Aspects of Underground Construction in Soft Ground, Amsterdam, Netherlands, 595-600.

MathWorks. (2024). MATLAB (R2024a) [Computer software]. The MathWorks, Inc. https://www.mathworks.com.

Mesri, G., and Hayat, T. M. (1993). "The coefficient of earth pressure at rest." Can. Geotech. J., 30(4), 647-666.

Mhenni, A., Hussien, M. N., and Karray, M. (2015). "Improvement of the piezo-electric ring actuator technique (P-RAT) using 3D numerical simulations." Proc., 68th Canadian Geotechnical Conf., GeoQuebec, Quebec City, QC, Canada.

Mitaritonna, G., Amorosi, A., and Cotecchia, F. (2014). "Experimental investigation of the evolution of elastic stiffness anisotropy in a clayey soil." Géotechnique, 64(6), 463-475.

Mitchell, J. K., and Kao, T. C. (1978). "Measurement of soil thermal resistivity." J. Geotech. Eng., 104(5), 1307-1320.

Mitchell, R. J. (1972). "Some deviations from isotropy in a lightly overconsolidated clay." Géotechnique, 22, 459-467.

Moore, D. M., and Reynolds, R. C. (1989). X-ray diffraction and the identification and analysis of clay minerals. Oxford University Press, Oxford, UK.

Moyano, B., Spikes, K. T., Johansen, T. A., and Mondol, N. H. (2012). "Modeling compaction effects on the elastic properties of clay-water composites." Geophysics, 77(5), D171-D183.

Nakagawa, K., Soga, K., and Mitchell, J. K. (1996). "Pulse transmission systems for measuring wave propagation in soils." J. Geotech. Eng., 122(4), 302-308.

Nazarian, S., and Stokoe, K. H., II. (1986). "In situ determination of elastic moduli of pavements systems by special-analysis-of-surface-waves method (theoretical aspects)." Research Rep. 437-2, Center for Transportation Research, Univ. of Texas at Austin, Austin, TX.

Ng, C. W. W., and Yung, S. Y. (2008). "Determination of the anisotropic shear stiffness of an unsaturated decomposed soil." Géotechnique, 58(1), 23-35.

Nishimura, S. (2014). "Cross-anisotropic deformation characteristics of natural sedimentary clays." Géotechnique, 64(12), 981-996.

Nishimura, S., Jardine, R. J., and Minh, N. A. (2011). "Shear strength anisotropy of natural London clay." Stiff Sedimentary Clays: Genesis and Engineering Behavior: Géotechnique Symposium in Print 2007, Thomas Telford Ltd., London, UK, 97-110.

Olson, R. E., and Daniel, D. E. (1981). "Measurement of the hydraulic conductive of fine-grained soil." Permeability and Groundwater Contaminant Transport, ASTM STP 746, T. P. Zimmie and C. O. Riggs, Eds., ASTM International, West Conshohocken, PA, 18-64.

Penner, E. (1963). "Anisotropic thermal conduction in clay sediments." Proc., Int. Clay Conf., 1963, I. T. Rosenqvist and P. Graff-Petersen, Eds., Pergamon, London, UK, 1, 365-376.

Penner, E., and Burn, K. N. (1978). "Review of engineering behavior of marine clays in Eastern Canada." Can. Geotech. J., 15(2), 269-282.

Pennington, D. S., Nash, D. F. T., and Lings, M. L. (1997). "Anisotropy of G0 shear stiffness in Gault Clay." Géotechnique, 47(3), 391-398.

Pennington, D. S., Nash, D. F., and Lings, M. L. (2001). "Horizontally mounted bender elements for measuring anisotropic shear moduli in triaxial clay specimens." Geotech. Test. J., 24(2), 133-144.

Philibert, A. (1976). "Étude de la résistance au cisaillement d'une argile Champlain." M.Sc. thesis, Faculté des Sciences Appliquées, Univ. of Sherbrooke, Sherbrooke, QC, Canada.

Philibert, A. (1984). "Le champ des contraintes et son évolution sous des conditions de chargement unidimensionnel dans les dépôts d'argile structurée de l'Est du Canada." Ph.D. thesis, Univ. of Sherbrooke, Sherbrooke, QC, Canada.

Potts, D. M., and Addenbrooke, T. I. (1997). "A structure's influence on tunnelling-induced ground movements." Proc. Inst. Civ. Eng. Geotech. Eng., 125(2), 109-125.

Presti, D. C. F. Lo, and Jamiolkowski, M. (1998). "Discussion: Estimate of elastic shear modulus in Holocene soil deposits." Soils Found., 38, 263-265.

Quigley, R. M. (1980). "Geology, mineralogy and geochemistry of Canadian soft soils: a geotechnical perspective." Can. Geotech. J., 17, 261-285.

Quigley, R. M., and Ogunbadejo, T. A. (1972). "Clay layer fabric and odometer consolidation of soft vawed clay." Can. Geotech. J., 9, 165-175.

Quigley, R. M., and Thompson, C. D. (1966). "The fabric of anisotropically consolidated sensitive marine clay." Can. Geotech. J., 7(3), 61-73.

Quigley, R. M., Gwyn, Q. H. J., White, O. L., Rowe, R. K., Haynes, J. E., and Bohdanowicz, A. (1983). "Leda clay from deep boreholes at Hawkesbury, Ontario. Part I: Geology and géotechnique." Can. Geotech. J., 20(2), 288-298.

Richart, F. E. (1977). "Dynamic stress-strain relations for soils." Proc., 9th Int. Conf. on Soil Mechanics and Foundation Engineering, Tokyo, Japan, 2, 605-612.

Richart, F. E., Hall, J. R., and Woods, R. D. (1970). Vibration of soils and foundations. Prentice-Hall Inc., Englewood Cliffs, NJ.

Robertson, P. K. (2009). "Interpretation of cone penetration tests—a unified approach." Can. Geotech. J., 46(11), 1337-1355.

Robertson, P. K. (2015). "Comparing CPT and Vs liquefaction triggering methods." J. Geotech. Geoenviron. Eng., 141(9), 04015037.

Robertson, P. K., Campanella, R. G., Gillespie, D., and Rice, A. (1986). "Seismic CPT to measure in-situ shear wave velocity." J. Geotech. Eng., 112(8), 791-803.

Robertson, P. K., Woeller, D. J., and Finn, W. D. L. (1992). "Seismic cone penetration test for evaluating liquefaction potential under cyclic loading." Can. Geotech. J., 29(4), 686-695.

Rochelle, P. L., Chagnon, J. Y., and Lefebvre, G. (1970). "Regional geology and landslides in the marine clay deposits of eastern Canada." Can. Geotech. J., 7(2), 145-156.

Rochelle, P. L., Lefebvre, G., and Bilodeau, P. M. (1977). "The stabilization of a slide in Saint-Jérôme, Lac Saint-Jean." Can. Geotech. J., 14(3), 340-356.

Roesler, S. K. (1979). "Anisotropic shear modulus due to stress anisotropy." J. Geotech. Eng. Div., 105(7), 871-880.

Romero, E. (2013). "A microstructural insight into compacted clayey soils and their hydraulic properties." Eng. Geol., 165, 3-19.

Rowe, R. K., and Booker, J. R. (1980). "Finite layer analysis of non-homogeneous soils." Research Rep. GEOT-2-80, Univ. of Western Ontario, London, ON, Canada.

Rowe, R. K., and Booker, J. R. (1981). "The behavior of footings resting on a non-homogeneous soil mass with a crust. Part II. Circular footings." Can. Geotech. J., 18(2), 265-279.

Saada, A. S. (1988). "State of the art: Hollow cylinder torsional devices: their advantages and limitations." Advanced Triaxial Testing of Soil and Rock, ASTM STP 977, ASTM International, West Conshohocken, PA, 766-795.

Santamarina, J. C., Klein, A., and Fam, M. A. (2001). "Soils and waves: Particulate materials behavior, characterization and process monitoring." J. Soils Sediments, 1(2), 130-130.

Sasanian, S., and Newson, T. A. (2013). "Use of mercury intrusion porosimetry for microstructural investigation of reconstituted clays at high water contents." Eng. Geol., 158, 15-22.

Sawangsuriya, A. (2012). "Wave propagation methods for determining stiffness of geomaterials." Wave processes in classical and new solids, 44.

Sayao, A. S. F. J., and Vaid, Y. P. (1991). "A critical assessment of stress nonuniformities in hollow cylinder test specimens." Soils Found., 31(1), 60-72.

Seed, H. B., and Idriss, I. M. (1970). "Soil moduli and damping factors for dynamic response analyses." Rep. EERC 70-10, Earthquake Engineering Research Center, Univ. of California, Berkeley, CA.

Sergeyev, J., Osipov, V., and Sokolov, V. (1985). "Quantitative analysis of soil structure with the microcomputer system." Bull. Eng. Geol. Environ., 31(1), 131-136.

Shi, B., Murakami, Y., and Wu, Z. (1998). "Orientation of aggregates of fine-grained soil: quantification and application." Eng. Geol., 50(1-2), 59-70.

Shibata, T., and Soelarno, D. S. (1975). "Stress-strain characteristics of sands under cyclic loading." Proc., Japan Society of Civil Engineering, No. 239, 57-65. (in Japanese).

Shibuya, S., and Tanaka, H. (1996). "Estimate of elastic shear modulus in Holocene soil deposits." Soils Found., 36(4), 45-55.

Shibuya, S., Hwang, S. C., and Mitachi, T. (1997). "Elastic shear modulus of soft clays from shear wave velocity measurement." Géotechnique, 47(3), 593-601.

Shirley, D. J., and Hampton, L. D. (1978). "Shear-wave measurements in laboratory sediments." J. Acoust. Soc. Am., 63(2), 607-613.

Silvestri, V., and Aubertin, M. (1988). "Anisotropy and in-situ vane tests. Vane shear strength testing in soils: field and laboratory studies." ASTM STP1014, ASTM International, West Conshohocken, PA, 88-103.

Silvestri, V., and Morgavi, R. (1982). "Measurement of lateral stresses in one-dimensional tests on a sensitive clay of Eastern Canada." Proc., 19th Annual Engineering Geology and Soils Engineering Symp., Idaho State Univ., Pocatello, ID, 19, 201-216.

Simpson, B., Atkinson, J. H., and Jovicic, V. (1996). "The influence of anisotropy on calculations of ground settlements above tunnels." Geotechnical aspects of underground construction in soft ground, 591-594.

Skempton, A. W., and Northey, R. D. (1952). "The sensitivity of clays." Géotechnique, 3(1), 30-53.

Sloane, R., and Kell, T. (1966). "The fabric of mechanically compacted kaolin." Clays and clay minerals, Proc., 14th National Clay Conf., 289-296.

Smart, P. (1967). "Particle arrangements in kaolin." Clays Clay Miner., 15, 241-254.

Sokolov, V. N., and O'Brien, N. R. (1990). "A fabric classification of argillaceous rocks, sediments and soils." Appl. Clay Sci., 5, 353-360.

Srodon, J., Drits, V. A., McCarty, D. K., Hsieh, J. C., and Eberl, D. D. (2001). "Quantitative X-ray diffraction analysis of clay-bearing rocks from random preparations." Clays Clay Miner., 49(6), 514-528.

Sully, J. (1991). "Measurement of lateral stress during full-displacement penetration tests." Ph.D. thesis, Univ. of British Columbia, Vancouver, BC, Canada.

Taina, I. A., Heck, R. J., and Elliot, T. R. (2008). "Application of X-ray computed tomography to soil science: A literature review." Can. J. Soil Sci., 88(1), 1-19.

Tanaka, H., and Locat, J. (1999). "A microstructural investigation of Osaka Bay clay: the impact of microfossils on its mechanical behavior." Can. Geotech. J., 36(3), 493-508.

Tavenas, F. A., Blanchette, G., Leroueil, S., Roy, M., and La Rochelle, P. (1975). "Difficulties in the in-situ determination of K0 in soft sensitive clays." Proc., Conf.: In Situ Measurement of Soil Properties, 1, 450-476.

Tavenas, F., Jean, P., LeBlond, P., and Leroueil, S. (1983a). "The permeability of natural soft clays. Part II: Permeability characteristics." Can. Geotech. J., 20(4), 645-660.

Tavenas, F., Leblond, P., Jean, P., and Leroueil, S. (1983b). "The permeability of natural soft clays. Part I: Methods of laboratory measurement." Can. Geotech. J., 20(4), 629-644.

Tchalenko, J. S. (1967). "The influence of shear and consolidation on the microscopic structure of some clays." Ph.D. dissertation, Univ. of London, London, UK.

Teachavorasinskun, S., and Lukkanaprasit, P. (2008). "Stress induced and inherent anisotropy on elastic stiffness of soft clays." Soils Found., 48(1), 127-132.

Teng, F. C., Ou, C. Y., and Hsieh, P. G. (2014). "Measurements and numerical simulations of inherent stiffness anisotropy in soft Taipei clay." J. Geotech. Geoenviron. Eng., 140(1), 237-250.

Teng, F., Arboleda-Monsalve, L. G., and Finno, R. J. (2018). "Numerical simulation of recent stress-history effects on excavation responses in soft clays." J. Geotech. Geoenviron. Eng., 144(8), 06018005.

Terzaghi, C. (1925). "Principles of soil mechanics: V-physical differences between sand and clay." Eng. News Rec., 96, 912-915.

Tessier, D., Lajudie, A., and Petit, J. C. (1992). "Relation between the macroscopic behavior of clays and their microstructural properties." Appl. Geochem., 7, 151-161.

Torabipour, A., and Hamidi, A. (2020). "Ground response analysis of cemented alluviums using non-recursive algorithm." J. Earthquake Eng., 24(9), 1390-1416.

Torabipour, A., Ethier, Y., and Karray, M. (2024). "Use of shear wave velocity to assess Champlain marine clay fabric anisotropy." Can. Geotech. J., 62, 1-16.

Tovey, N., Smart, P., Hounslow, M., and Leng, X. L. (1989). "Practical aspects of automatic orientation analysis of micrographs." Scanning Microscopy, 3, 771-784.

Tovey, N., and Krinsley, D. (1990). "A technique for quantitatively assessing orientation patterns in sand grain surface micro textures." Bull. Int. Assoc. Eng. Geol., 41, 117-127.

Tovey, N., and Krinsley, D. (1992). "Mapping of the orientation of fine-grained minerals in soils and sediments." Bull. Eng. Geol. Environ., 46(1).

Ul-Hamid, A. (2018). A beginners' guide to scanning electron microscopy. Vol. 1, Springer International Publishing, Cham, Switzerland, 309-359.

Viggiani, G., and Atkinson, J. H. (1995). "Stiffness of fine-grained soils at very small strains." Géotechnique, 45(2), 249-265.

Vullo, V. (2014). Circular cylinders and pressure vessels. Stress analysis and design. Springer, Berlin/Heidelberg, Germany.

Wang, G., Zhang, X., Liu, X., Xu, Y., and Lu, J. (2022). "Microscopic evolution of pore characteristics and particle orientation of granite residual soil in one-dimensional compression." Geofluids.

Wang, W., Kravchenko, A. N., Smucker, A. J. M., and Rivers, M. L. (2011). "Comparison of image segmentation methods in simulated 2D and 3D microtomographic images of soil aggregates." Geoderma, 162(3-4), 231-241.

Wang, Y. H., and Mok, C. M. (2008). "Mechanisms of small-strain shear-modulus anisotropy in soils." J. Geotech. Geoenviron. Eng., 134(10), 1516-1530.

Wongsaroj, J., Soga, K., and Mair, R. J. (2011). "Modelling of long-term ground response to tunnelling under St James's Park, London." Stiff Sedimentary Clays: Genesis and Engineering Behaviour: Géotechnique Symposium in Print 2007, Thomas Telford Ltd., London, UK, 253-268.

Yamashita, S., Kawaguchi, T., Nakata, Y., Mikami, T., Fujiwara, T., and Shibuya, S. (2009). "Interpretation of international parallel test on the measurement of Gmax using bender elements." Soils Found., 49(4), 631-650.

Yimsiri, S., and Soga, K. (2011). "Cross-anisotropic elastic parameters of two natural stiff clays." Géotechnique, 61(9), 809-814.

Yong, R. N., and Silvestri, V. (1979). "Anisotropic behavior of a sensitive clay." Can. Geotech. J., 16(2), 335-350.

Youd, T. L., et al. (2001). "Liquefaction resistance of soil: summary report from the 1996 NCEER and 1998. NCEER/NSF Workshops on Evaluation of Liquefaction Resistance of Soils." J. Geotech. Geoenviron. Eng., 127(10), 817-833.

Yu, C. Y., Chow, J. K., and Wang, Y. H. (2016). "Pore-size changes and responses of kaolinite with different structures subject to consolidation and shearing." Eng. Geol., 202, 122-131.

Yu, P., and Richart, F. E., Jr. (1984). "Stress ratio effects on shear modulus of dry sands." J. Geotech. Eng. Div., 110(GT3), 331-345.

Yuan, S., Liu, X., and Buzzi, O. (2019). "Technical aspects of mercury intrusion porosimetry for clays." Environ. Geotech., 8(4), 255-263.

Zapata-Medina, D. G., Cortes-Garcia, L. D., Finno, R. J., and Arboleda-Monsalve, L. G. (2020). "Stiffness and strength anisotropy of overconsolidated Bootlegger Cove clays." Can. Geotech. J., 57(11), 1652-1663.

Zdravković, L., Potts, D. M., and Hight, D. W. (2002). "The effect of strength anisotropy on the behavior of embankments on soft ground." Géotechnique, 52(6), 447-457.

Zen, K., Umehara, Y., and Hamada, K. (1978). "Laboratory tests and in situ seismic survey on vibratory shear modulus of clayey soils with various plasticity." Proc., 5th Japanese Earthquake Engineering Symp., 721-728.

Zeng, L. L., Cui, Y. J., Conil, N., Zghondi, J., Armand, G., and Talandier, J. (2017). "Experimental study on swelling behaviour and microstructure changes of natural stiff Teguline clays upon wetting." Can. Geotech. J., 54(5), 700-709.

Zeng, X., and Ni, B. (1999). "Stress-induced anisotropic Gmax of sands and its measurement." J. Geotech. Geoenviron. Eng., 125(9), 741-749.

Zentar, R., Karstunen, M., Wiltafafsky, C., Schweiger, H. F., and Koskinen, M. (2002). "Comparison of two approaches for modelling anisotropy of soft clays." Proc., 8th Int. Symp. on Numerical Models in Geomechanics (NUMOG VIII), Rome, Italy, 115-121.

Zhao, Y., Hu, X., and Li, X. (2020). "Analysis of the intra-aggregate pore structures in three soil types using X-ray computed tomography." Catena, 193, 104622.

Zheng, Y., Baudet, B. A., Delage, P., Pereira, J. M., and Sammonds, P. (2022). "Pore changes in an illitic clay during one-dimensional compression." Géotechnique, 1-16.

Zheng, Y., Sun, H., Hou, M., and Ge, X. (2021). "Microstructure evolution of soft clay under consolidation loading." Eng. Geol., 29.